RIKAGAKU KENKYUSHO
the Institute of Physical and Chemical Research
Wako-shi, Saitama Pref., JAPAN

'73

IPCR cyclotron Progress Report 1973

Vol. 7

IPCR Cyclotron Progress Report

Vol. 7

The Institute of Physical and Chemical Research
"RIKAGAKU KENKYUSHO" Wako-shi, Saitama, 351 JAPAN
December, 1973

This volume contains recent information of the IPCR Cyclotron, informal reports and abstracts of papers which will be published at scientific meetings or in publications by staff members, guests, and visitors.

CONTENTS

Page

1. INTRODUCTION 1

2. MACHINE OPERATION 2

3. MACHINE DEVELOPMENT AND ACCELERATOR PHYSICS

3–1. Increase of Maximum Energies of Cyclotron Beams 5

3–2. Study of Composition of Residual Gas in the Cyclotron Chamber 7

3–3. Improvement of the Structure of Septum Holder at the Entrance of Beam Deflection Channel 10

3–4. Improvement of Standard Voltage Source for the Current Stabilizer of Magnet 14

3–5. Trial-Making of a Current Stabilizer for a Quadrupole Magnet 15

4. NUCLEAR PHYSICS
Scattering and Reactions

4–1. DWBA Calculations of Inelastic Scatterings of ^{12}C and ^{14}N 17

4–2. The Finite Range DWBA Analyses of the Reactions $^{52}Cr(^{14}N, ^{13}C)^{53}Mn$ and $^{52}Cr(^{12}C, ^{11}B)^{53}Mn$ 22

4–3. Angular Distributions of Transfer Reactions Induced by Heavy Ions 27

4–4. A Study of Transfer Reactions Induced by ^{14}N and ^{12}C on ^{208}Pb and ^{209}Bi 32

4–5. Angular Distributions and Linear Momentum Transfers of Target Residue in the $^{209}Bi + ^{12}C$ Reaction 37

4–6. Limit of the Cross Section for the Compound Reaction between Complex Nuclei 39

4–7. $(^3He, d)$ Reactions on Cr Isotopes at an Energy of 29.3 MeV 42

4–8. The $(^3He, ^3He)$, $(^3He, ^3He')$, and $(^3He, \alpha)$ Reactions on ^{13}C 46

4–9. Two-Step Process in the $^{12}C(^3He, \alpha)^{11}C$ Reaction 47

4–10. Sum Rule Approach for Isovector Nuclear Vibrations 51

4–11. Momentum Transfer Dependence of the Effective Charge for Electro-excitation 53

4–12. Effects of Monopole Core Polarization 55

4–13. The Splitting of the Isospin and Spin-Isospin Dipole Resonances in ^{12}C 58

4–14. New Giant Resonances 60

4–15. Sum Rules and Nonexchange Force 62

5. NUCLEAR PHYSICS
Nuclear Spectroscopy

5–1. Asymmetric Fission of ^{236}U 65

5–2. Alpha-Decay of ^{215}Fr 69

5–3. Magnetic Moment of the $29/2^+$ State in ^{213}Fr 71

5–4. The Blocking Effect of the M1 Core Polarization Studied from the g-Factor of the $(\pi h_{9/2})^6$ 8^+ State in ^{214}Ra 74

5–5. In-Beam Alpha- and Gamma-Spectroscopy of ^{216}Ra 77

5–6. Measurement of Half-Life in ms Region with a Mechanical Chopper 79

6. NUCLEAR INSTRUMENTATION

6–1. New Data Processing System 83

6–2. Interface between PHA Units and OKITAC 4500C Computer 86

7. ATOMIC AND SOLID-STATE PHYSICS

7–1. Inner-Shell Excitation by N Ions and Alpha-Particles (1) 87

7–2. Inner-Shell Excitation by N Ions and Alpha-Particles (2) 93

7–3. Positron Annihilation in V and Nb 98

7–4. Positron Annihilation in Paramagnetic Nickel Single Crystal 101

7–5. Point Defects in Irradiated Copper and Cu_3Au 103

8. RADIOCHEMISTRY

8–1. Mössbauer Emission Spectroscopy of ^{119}Sn after the EC Decay of ^{119}Sb 105

8–2. Charge States of Ions from ^{18}F Decay 110

9. RADIATION CHEMISTRY AND RADIATION BIOLOGY

9–1. Heavy Ion Radiolysis of Liquid Ketones
Effect of Water on the Radiolysis of Acetone 112

9–2. ESR Studies of Free Radicals Produced in Organic Crystals Irradiated with Heavy Ions 114

9–3. Inactivation of Bacterial Cells by Charged Particles 117

9–4. LET Dependence of DNA-Strand Breaks in E.coli B_{s-1} 122

10. PREPARATION OF RADIOISOTOPES AND LABELED COMPOUNDS

10–1. Measurement of Excitation Curves for the Formation of Medical-Use Radioisotopes 126

10–2. Preparation of ^{18}F-Labelled Compounds 129

10–3. Preparation of ^{119}Sb for Mössbauer Emission Spectroscopy of ^{110}Sn 132

11. RADIATION MONITORING

11–1. Routine Monitoring 134

11–2. Residual Radiation in the Cyclotron Vault after Deuteron Acceleration 136

12. A NEW MACHINE

12–1. Specifications of Variable Frequency Linac 140

12–2. The Variable Frequency Linac Project
Results of Measurements on Model Cavity 1 143

12–3. The Variable Frequency Linac Project
Orbit Dynamics : Radial Acceptance 147

12–4. The Variable Frequency Linac Project
Orbit Dynamics : Phase Oscillation and Energy Resolution 149

12–5. Two Examples of Heavy-Ion Cyclotron with External Injection Provision 151

13. LIST OF PUBLICATIONS 155

14. LIST OF PERSONNEL 158

15. LIST OF OUTSIDE USERS AND THEIR THEMES 161

AUTHOR INDEX 165

1. INTRODUCTION

In this year our cyclotron was operated smoothly as before. Several improvements have been made in the machine itself and its accessory facilities which resulted in more stable and efficient operation.

In all fields of study using the machine a majority of research works have been carried out with heavy ions. A theoretical approach to heavy ion nuclear reactions has started and offered a promissing prospect. A new data processing system with on-line use of a computer has been completed.

A preliminary work has been done in the field of atomic physics in which the inner-shell ionization produced by heavy ion bombardment was investigated by X-ray measurements.

A project of construction of a new heavy ion machine is expected to be supported by the Government and will be realized in this and the next fiscal years. A number of preparatory studies on the basic problems in the construction of the new machine were almost completed during last three years as seen in the foregoing issues of Progress Report. The new machine is a linear accelerator and its performance was designed to yield a beam of heavy ions up to uranium having energy of 1 to 6 MeV/nucleon. We hope that the completion of this machine would be beneficial to research in new fields unworked yet.

H. Hagihara

Hitosi Hagihara, Chairman
The Cyclotron Board

2. MACHINE OPERATION

Machine Group

The cyclotron was operated without any serious machine failure in the period from October 27, 1972, to October 23, 1973, on the 24 h-a-day basis. Statistics of machine operation are shown in Table 1. The recorded working times of the oscillator and the ion source are slightly longer than those of the last year. Beam time for heavy ions continues to rise in spite of necessity of more maintenance work of the ion source than for the acceleration of ordinary light ions. Table 2 shows machine time allotments to various activities in this period. More than 95 % of the schedule was fulfilled. Declaration of loss of machine time due to machine failure was only thrice in this period. The figure had been about 10 for the past few years.

Efforts of improvement of various parts of the cyclotron are being continued : Replacement of insulators which support the shorting device with much sturdy ones, eliminating occurrence of failure due to insulation breakdown : Removal of an old dee-voltage pick-up arm from the center of the accelerating chamber and installation of a new pick-up at the side of east dee, improving the reliability of indication of operating voltage : Renewal of diffusion oil of the 32" pump to one of superior quality and detection and stopping of small vacuum leakage at

Table 1. Machine operation time indicated by working-time meter.

Date	Oscillator	Ion source	Beam
Oct. 27, 1972	27555 (h)	30038 (h)	1698 (h)
Oct. 23, 1973	32976 (h)	35693 (h)	6652 (h)
361 days	5421 (h)	5655 (h)	4954 (h)
Percent of 361 days	62.6 %	65.4 %	57.2 %

Schedule in this period:

Machine time	214 (days)
Overhaul and installation work	41 (days)
Periodical inspection and repair	28 (days)
Vacation, holiday, and Sunday	78 (days)

Table 2. Scheduled machine time and subjects of activity in this period VIII.

Subject	Hours	Percent
Heavy ion reaction	531	Nucl. phys. 53.6 (%)
Direct reaction with light particles	1209	
In-beam spectroscopy with heavy ions	883	
In-beam spectroscopy with light particles	216	
Radioisotope production for nuclear spectroscopy	176	
Nuclear chemistry	310	Fields other than nucl. phys. 21.9 (%)
Radiation chemistry	157	
Radiation biology	269	
Solid state physics	279	
Inner atomic shell excitation study	216	
Nuclear medicine in cooperation with other organizations	185	Outside users 6.5 (%)
Nuclear fuel study	132	
Radio-isotope production	50	
Instrument development and beam channel alignment by use of beam	125	Maintenance operation and engineering 18.0 (%)
Exchange of ion source	66	
Reserved for machine time adjustment and cooling of radiation	148	
Machine inspection and repair	672	
Total	5624	100 (%)

the throat of the main pump resulting in the attainment of better ultimate pressure with less pumping time, and the pressure in the accelerating chamber without gas loading from ion source is 5×10^{-7} Torr normally.[1] These improvements made possible to obtain ions of higher energy than hitherto obtained, for instance, 112 MeV for C and nearly 60 MeV for α particle.[2] Rectified 18V–350A heater power supply for the oscillator tube was manufactured and installed in the oscillator housing in place of the AC supply hitherto used. It is expected to decrease low-frequency ripples of the radiofrequency waveform and to improve beam characteristics in cooperation with increased filtering of high-voltage power supply, made last year.

References

1) Y. Miyazawa, T. Kageyama, and T. Karasawa : IPCR Cyclotron Progr. Rep., 7, 7 (1973).
2) Y. Miyazawa, K. Ogiwara, T. Tonuma, S. Fujita, M. Hemmi, K. Ikegami, T. Inoue, T. Kageyama, S. Kohara, H. Nakajima, A. Shimamura, and O. Terajima : ibid., p. 5.

3. MACHINE DEVELOPMENT AND ACCELERATOR PHYSICS

3-1. Increase of Maximum Energies of Cyclotron Beams

Y. Miyazawa, K. Ogiwara, T. Tonuma, S. Fujita, M. Hemmi,
K. Ikegami, T. Inoue, T. Kageyama, S. Kohara,
H. Nakajima, A. Shimamura, and O. Terajima

In an ordinary cyclotron, the maximum energy of beam is limited depending on the accelerating voltage which can be maintained by the dee without sparking. The limit also changes according to the starting phase of ion leaving the ion source.

In September, 1973, the central region geometry of the cyclotron was improved as follows: The screen[1] that defines the first half turn orbit of beam attached on the ion source for light particles was removed. The removal allowed the beam to have a large positive phase with respect to the rf-field. In other words, it became possible to accelerate the beam leaving the ion source even after the dee voltage had attained a peak. Besides, the width of z-slit was changed to 80 mm from 60 mm to improve the extraction efficiency of the beam at the deflection channel. It clips the height of beam at the first two or three turns within 15 mm.

To eliminate the possibility of break down, the insulators of the moving short were changed to those of a new type and the unused pick-up arm for the dee voltage was also removed. With these improvements, the dee voltage above 85 kV was enabled to reach easily in the oscillation above 8 MHz. Table 1 shows the comparison of accelerating energies before

Table 1. Comparison of beam energies before and after improvement.

Particle	Before improvement Energy (MeV)		After improvement Energy (MeV)	
P	4.5 ~ 17.5	f	4.5 ~ 17.5	f
d	9 ~ 25	V_d	9 ~ 30	V_d
$^3He^{++}$	13 ~ 48	V_d	13 ~ 50	f
$^4He^{++}$	16 ~ 50	V_d	16 ~ 60	V_d

The f and V_d show the maximum energies of beam restricted by the upper frequency or dee voltage limits in the cyclotron, respectively.

and after the improvements were done in the cyclotron. We could get new records of the maximum energies for several kinds of ion beam. The maximum energies of the both proton and $^3He^{++}$ beams were only restricted by the limit of the highest frequency of the oscillation after the improvements. The extracted beam of alpha-particles of 60 MeV was obtained in the nominal dee voltage of 85 kV. Though we did not try to accelerate the deuteron beam, it is sure that the 30 MeV deuteron beam can be accelerated under the same operating conditions of the 60 MeV alpha-beam.

Figure 1 shows the comparison of the operating dee voltages before and after the improvements were done. As seen in the figure, the dee voltage necessary for acceleration of the ions to corresponding energies had decreased after the improvements by about 15 % as compared with that before the improvements.

Heavy ions such as C^{4+} and N^{4+} will also be accelerated to extend the maximum energies in the near future.

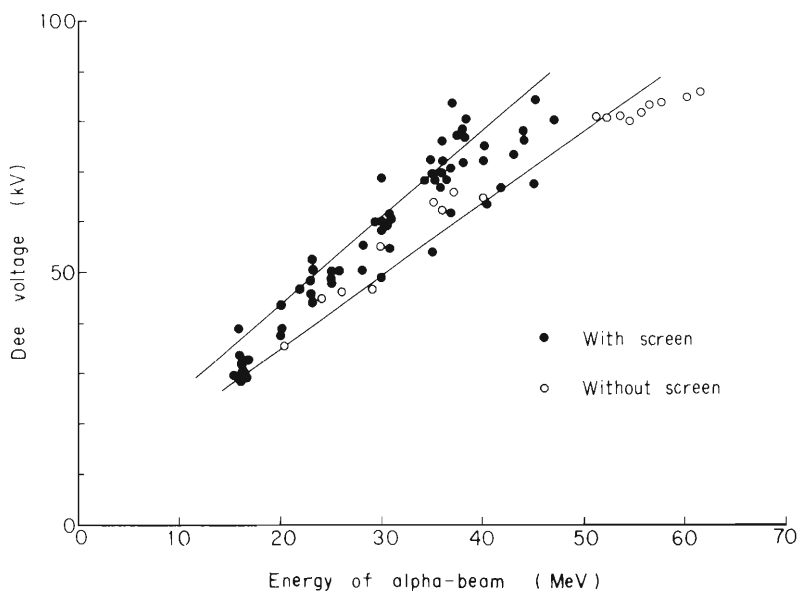

Fig. 1. Comparison of operating dee voltages before and after improvement.

Reference

1) Y. Miyazawa, K. Ogiwara, S. Fujita, M. Hemmi, K. Ikegami, T. Inoue, T. Kageyama, S. Kohara, H. Nakajima, A. Shimamura, O. Terajima, and T. Tonuma : IPCR Cyclotron Progr. Rep., 6, 7 (1972).

3-2. Study of Composition of Residual Gas in the Cyclotron Chamber

Y. Miyazawa, T. Kageyama, and T. Karasawa

The accelerating chamber of the cyclotron[1] has a volume of 1×10^4 liter and the surface area in vacuum of about 140 m^2. The main oil diffusion pump is 32 in. in diam. and connected in series with a 14 in. pump. The pump fluid is the Lion S. The analysis of residual gas in the accelerating chamber was made by using a quadrupole mass filter (M.F). The measurements were done at times of 5, 24, 31, and 290 h after evacuation from the atmosphere.

A typical mass spectrum after the chamber was evacuated for 290 h is shown in Fig. 1. The mass numbers 17 and 18 were assigned to OH and H_2O, respectively. It was shown that the residual gas is mostly consisted of water vapor.[2] The peaks of 28 and 32 were also assigned, for the most part, to be N_2 and O_2, respectively. The existence of N_2 and O_2 gases in the chamber can be regarded as due to the leakage of air in this vacuum system. Firstly, the leakage of the chamber is below 1×10^{-3} Torr liter/sec measured with the pressure rise test and secondly, the leakage of about 2×10^{-3} Torr liter/sec occurred in the top flange of the 32 in. pump. Many peaks of hydrocarbons (C_nH_m) are also seen in the spectrum. The groups of CH_m, C_2H_m, ... , and C_6H_m are detected in the range of mass up to 85. The yields of CH_m and C_2H_m groups could not be determined accurately because those peaks

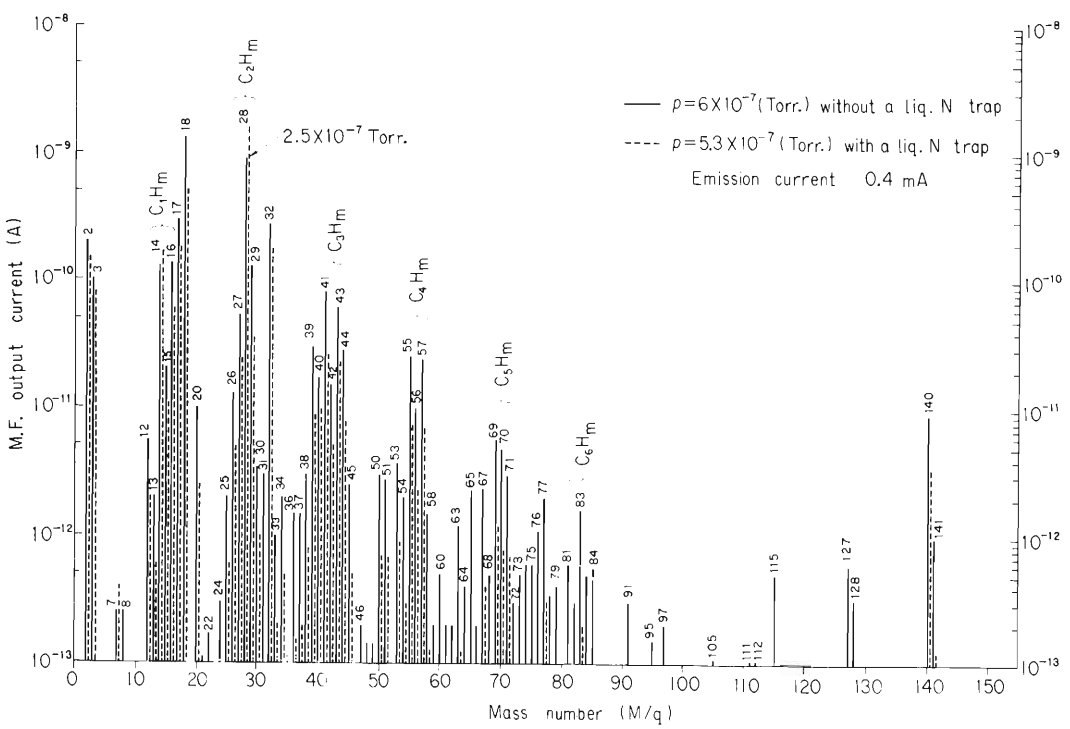

Fig. 1. Residual gas composition in the cyclotron chamber after evacuation for 290 h.

were masked by large yields of N^+ and N_2^+ peaks. Besides, the peak 141[3] characterizing the pump fluid of Lion S was detected in the spectrum. The peaks 2 and 3 are also detected with the relatively large yield. Most part of peak 3 seems to be the DH produced by the deuterium gas (D_2) fed in the ion source.

The results of measurement in using a liquid nitrogen trap on the pump head is shown in Fig. 1. Unfortunately, a small leakage occurred at the bottom of the liquid nitrogen trap when the liquid nitrogen was supplied into the trap. The yields of masses 28 and 14 with the liquid nitrogen are, therefore, increased than those of the case without the liquid nitrogen. The yields of other peaks were reduced to one third or less.

Figure 2 shows the change of the typical peaks with the evacuation time. The yields of the peaks 18, 17, and 2 were almost inversely proportional to the evacuation time. It is seen that the peaks 28 and 32 do not decrease with time because of the air leakage in this system. The yields of hydrocarbons had decreased slowly with time and, especially, the yields of the hydrocarbons with large mass number had hardly changed with time. The peaks measured after 31 h became slightly larger than those after 24 h. This is the effect due to the outgassing in the operation of the cyclotron.

To increase the final vacuum, it is necessary to eliminate both the leakage air and water vapor in this system. Therefore, the use of cryogenic pumps into the chamber will be useful to decrease the pump-down time. Further investigation is in progress.

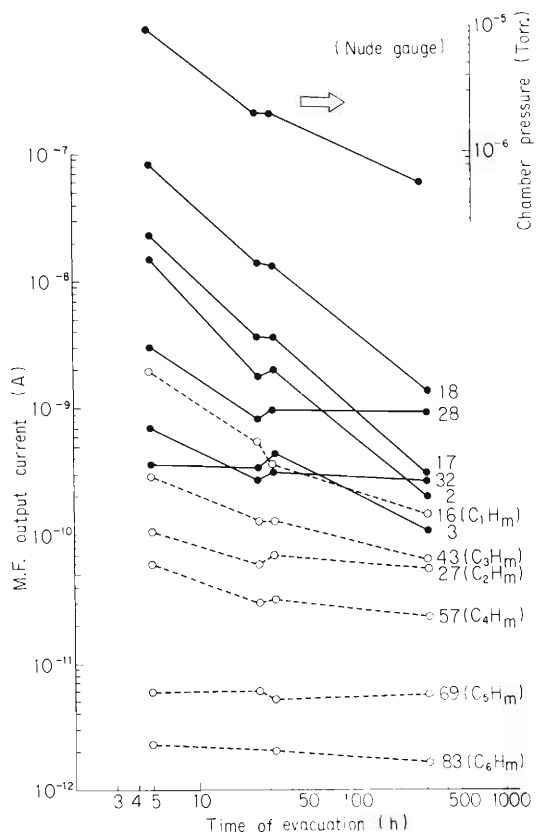

Fig. 2. Change of the typical peaks with the evacuation time.

References

1) T. Tonuma, Y. Miyazawa, K. Yoshida, K. Yada, T. Karasawa, and H. Kumagai : J. Vacuum Soc. Japan, 12, 405 (1969).
2) J. Blears : J. Sci. Instr., Suppl. No. 1, p.36 (1951).
3) Y. Koyama and K. Maeda : J. Vacuum Soc. Japan, 14, 141 (1971).

3-3. Improvement of the Structure of Septum Holder at the Entrance of Beam Deflection Channel

K. Ogiwara and Y. Miyazawa

The structure of the septum holder at the entrance of beam deflection channel has been improved with the objects of increasing the intensity of beam extractable, ensuring the stable operation of the cyclotron, decreasing the necessity of frequent replacement of the septum plate by lengthening the life of the plate against damage by the beam, and reduction of radiation exposure for people doing replacement work by reducing the time they have to take by simplifying the procedure.

The cyclotron has two dees. As shown in Fig. 1, the septum is attached to the side of east dee facing a deflector plate. Ions accelerated by the cyclotron are deflected by the radio-frequency field between this septum and the deflector and extracted to the outside of the accelerating chamber. The distance of the septum from the center of the cyclotron is 741 mm at the entrance and 831 mm at the exit. Total length is 1060 mm extending about 80 degrees of angular width. Tungsten plates 0.5 mm thick and 48 mm high are used as the septum. Initially, the total length was subdivided into three parts ; 160 mm at the entrance, 400 mm at the middle part, and 500 mm at the exit part. It was intended to differentiate the degree of

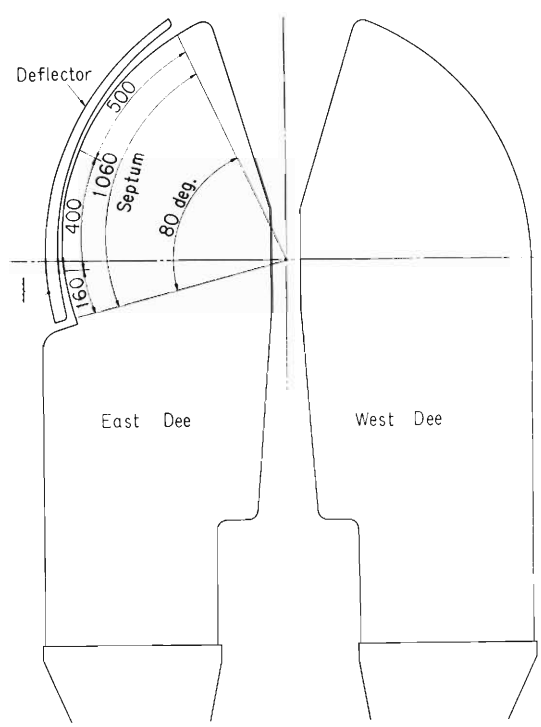

Fig. 1. Plan of the accelerating electrodes showing the position of deflector-septum channel.

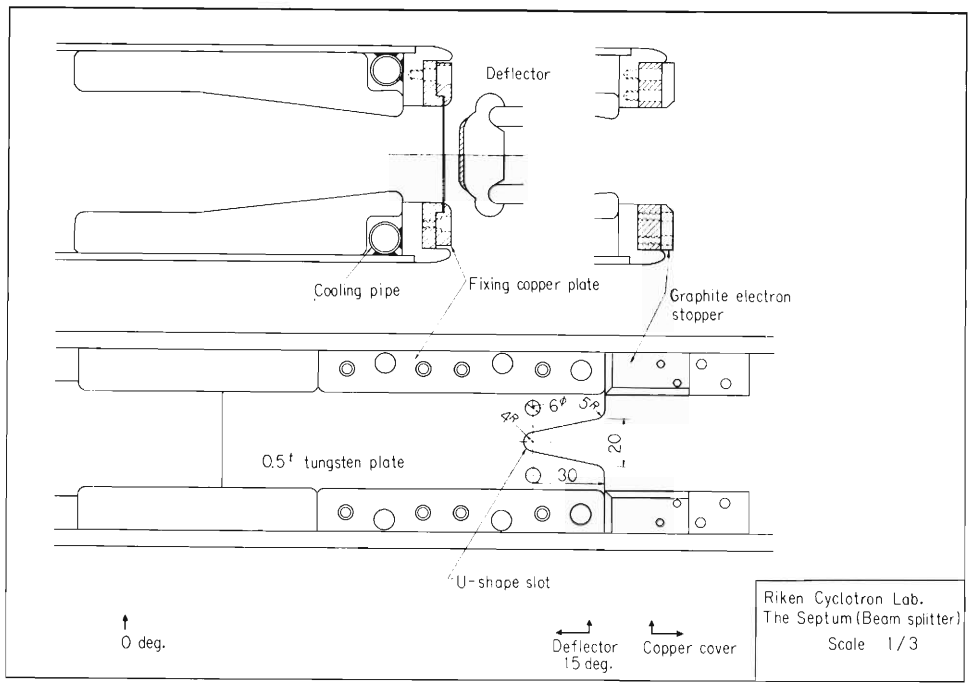

Fig. 2. Details of the structure of septum at the entrance part.

damage of each part and to simplify the manufacture and replacement of the damaged part. Fig. 2 shows the entrance region. Later, it was found that a small step-like form is apt to occur at the junction of the entrance and the middle part and is heated locally by beams resulting in deformation and bulging of the plate. Since then, the entrance and the middle part have been unified into one 560 mm unit. The septum plates are fixed tightly onto the septum mount made of copper by screwing the fixing plates also made of copper. Secondary electron stoppers made of graphite are provided at the entrance part. The stopper will be described in detail later. Following is a brief description of the improvement.

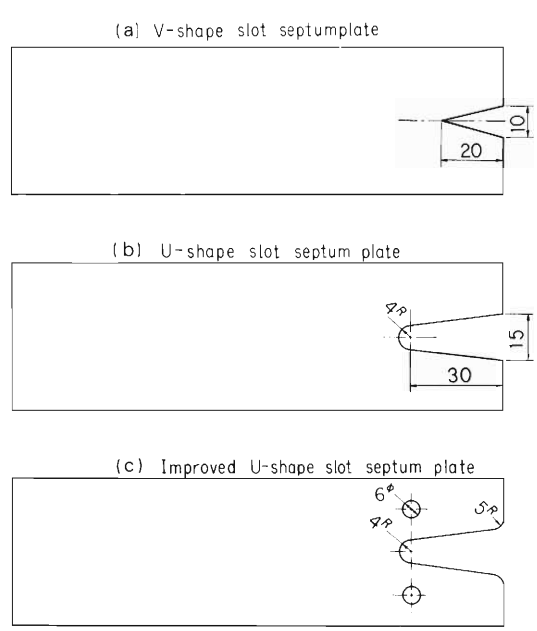

Fig. 3. The shape of septum plate at the septum entrance portion.

(1) The shape of slot cut at the beginning of the septum was changed from V-shaped to U-shaped last year. Heating of the septum by beams was most intense at the cusp of V-slot, bringing about bulging outward. Therefore good extraction condition was impaired and loss of beam at this point increased. The effect was cumulative and the life of the septum plate was about one or two months for this V-cut. By modifying the shape to U the life has been improved by about two-fold, that is, four-month life has been achieved this year. As shown in Fig. 3 (c), several holes were further provided in this period to absorb the thermal stress around the slot, which decreased the deformation of this part notably.

(2) The secondary electron stopper was made of graphite. As seen in Fig. 2, graphite plates were attached before the entrance part of the septum. Formerly, the septum mounts were extended to this region so as to be able to change the position of the initial part of the septum. Thermal electrons generated at the septum slot are accelerated by the combined effect of main magnetic and electric fields between the septum and the deflector plates and can reach the extended part, resulting in the multiplication of electrons by secondary emission. The quantity can be very large when the beam lost at the slot exceeds some threshold value, and causes heating and melting of the extended part of the septum mount under a long time operation. Violent flashover between the earth plate and this heated part is often generated. It is impossible to continue operation of the cyclotron under such condition and the power supply of the oscillator must be switched off to cool down the heated part. Operation must be resumed carefully enough with a limited beam intensity. Melted copper drops on the earth

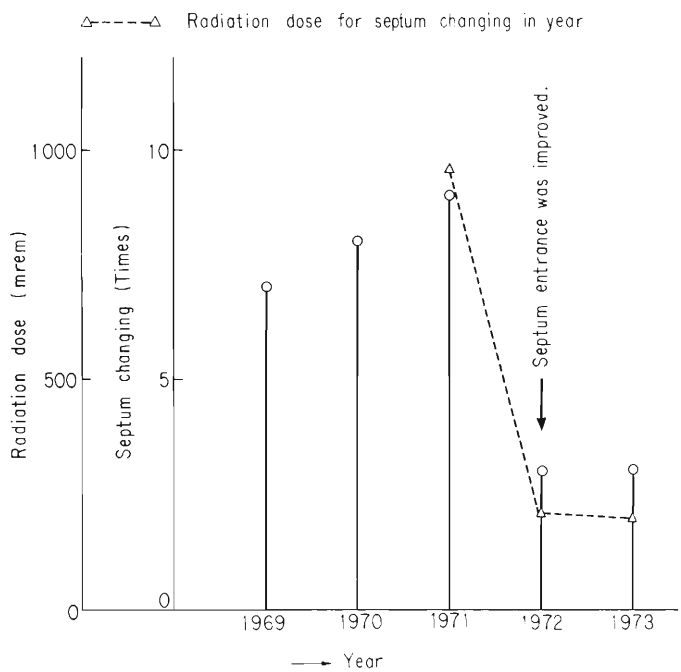

The broken line shows the amount of radiation exposure for persons during the septum replacement in a year.

Fig. 4. Statistics of septum replacement.

plate and the droplets thus formed easily induce a new discharge, which forces the operator to limit the beam intensity within a low level until the dusts are removed. The replacement of this damaged part often met difficulty because of the melting of heads of screws which fix the part to the dee. The work requires about one hour for two men and radiation exposure of each one amounts to as high as 100 mrem at times. This trouble has been removed completely by replacing the septum mount with graphite blocks.

(3) Now, the parts to be replaced are standardized and even an unskilled person can do the job within 20 min. The replacement work is to be done depending on the working conditions of the cyclotron such as the kind of particles, and the energy and intensity required. At present, three times a year seem sufficient for stable operation of cyclotron. Fig. 4 shows the statistics of replacement.

3-4. Improvement of Standard Voltage Source for the Current Stabilizer of Magnet

H. Nakajima

The beam handling system of the cyclotron is operating every day and the magnets in this system are excited by stabilized power supplies. The stabilizers have a power control circuit composed of some transistors and silicon controlled rectifiers (S.C.R.) as well as a standard voltage referring source to detect deviation of the output current.

We have hitherto used a mercury battery as the standard voltage source. But this battery has not a life long enough to be used without frequent care in daily operation. Therefore, we have adopted a solid state reference voltage generator instead of the mercury battery. The circuit is composed of some temperature-compensated zener diodes and transistors. We have replaced the battery with the improved voltage source except for a stabilizer for the SW-II magnet, by which a long life for practical application and excellent performance have been achieved. Particulary for the reaction particle analyzer which requires high stability, we have chosen a temperature compensated zener diode 1N946. In addition, the diode current was stabilized by a circuit to secure the superior quality of this diode. By this means, we have realized a stability of the output voltage with an accuracy better than 1×10^{-5} at 5.2 V for 24 h.

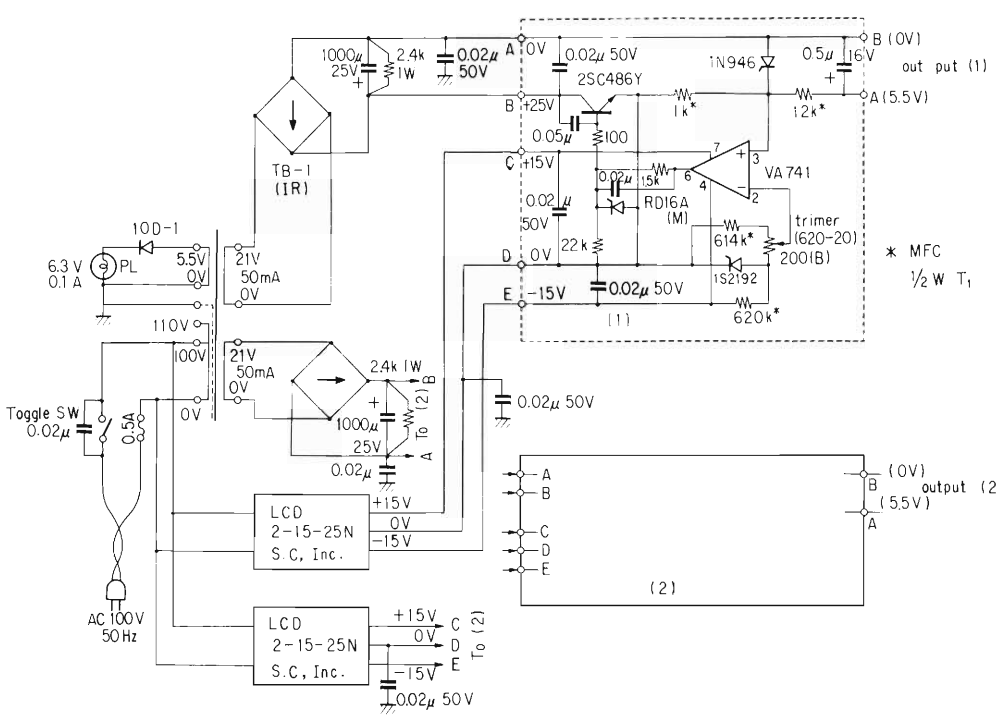

Fig. 1. Schematic circuit of the standard voltage source for reaction particle analyzer.

3-5. Trial-Making of a Current Stabilizer for a Quadrupole Magnet

H. Nakajima and M. Hemmi

Many quadrupole magnets are installed and in operation at the beam handling system of the cyclotron. These Q-magnets are classified into two groups with respect to dimensions of their aperture. The resistance of coil is about 6.5 Ω and the maximum excitation current is 20 A. We have trially made and tested a current stabilizer for the Q-magnet.

1) Outline of circuit design

We choose 7 Ω as the load resistance for the stabilizer in view of the average resistance of the Q-magnet and 20 A as the largest output current. Then the maximum output voltage is 140 V. We take 0.01 % as an acceptable deviation of output current for 10 % line voltage variation, and 0.1 % for its stability for 12 h. We designed a feed-back loop suitable for slow response of load, and also cared for the problems of trouble shooting and maintenance. Integrated circuits and some hybrid circuits are adopted to decrease the quantity of parts.

The circuit is composed of two feed-back loops, one is a controller of output current and the other is collector voltage compensator for a series transistor. A standard voltage generator and a power source are combined with the main circuit, and a power limiter protects the transistor from over-dissipation. The block diagram of the current stabilizer is shown in Fig. 1.

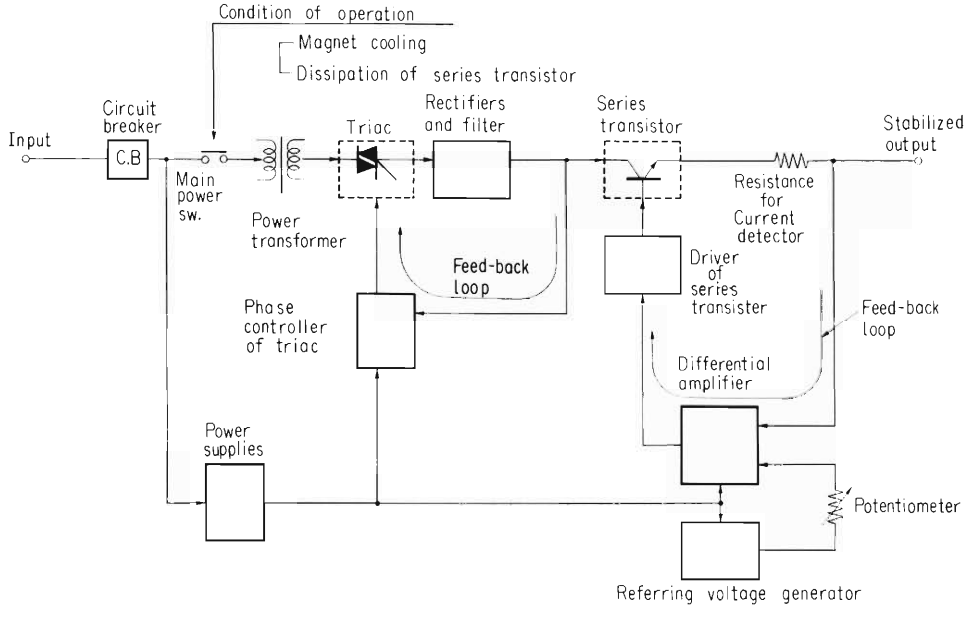

Fig. 1. Block diagram of current stabilizer.

2) Result

Stability of output current was measured at several different currents each for 24 h. Damping and rising characteristics were not measured. An example of stability of output current is shown in Fig. 2. The results of running test were generally satisfactory, but modification of the circuit and change of value of a resistor for current detection were found to decrease ripple and noise further. Simplification of the circuit seems possible and is in progress.

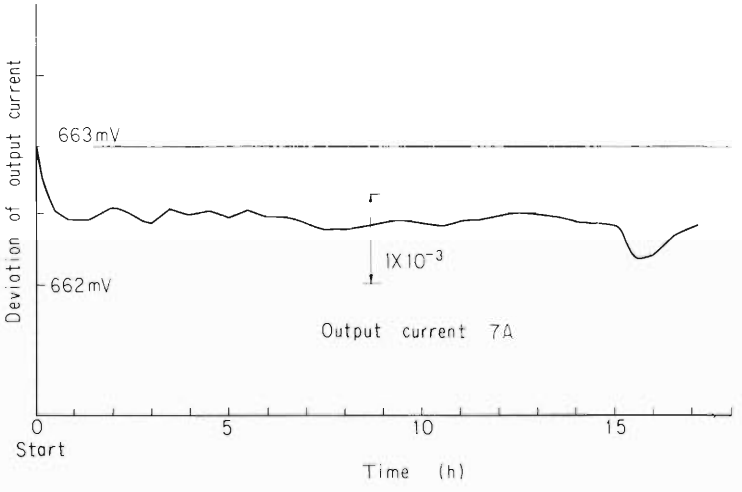

Fig. 2. Stability of output current at 7 A.

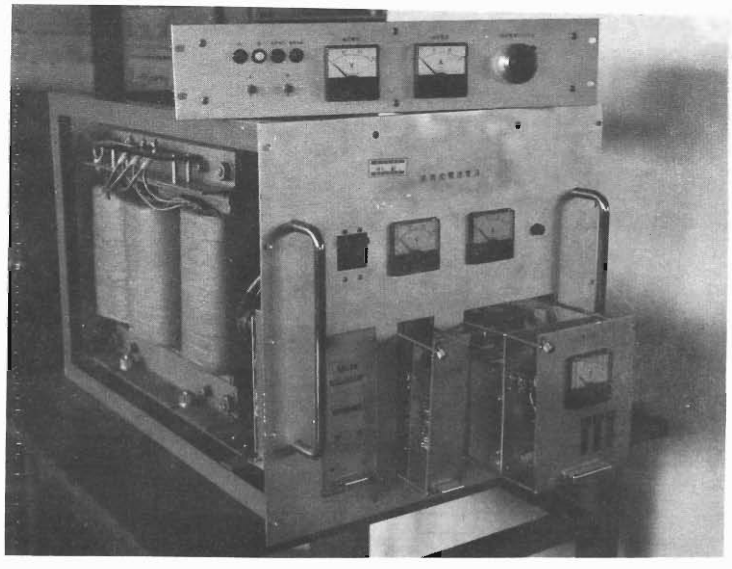

Fig. 3. Photograph of the stabilizer.

4. NUCLEAR PHYSICS
Scattering and Reactions

4-1. DWBA Calculations of Inelastic Scatterings of ^{12}C and ^{14}N

I. Kohno

Experimental results of elastic and inelastic scatterings of ^{12}C and ^{14}N and an optical model analysis of the elastic scatterings were reported previously.[1)]

The experimental differential cross sections of the inelastic scatterings were analyzed by the DWBA method assuming collective excitation. The collective excitation of colliding fragments are described in terms of a non-spherical optical potential where the departure from sphericity is contained in the radius parameter $R(\Omega')$:

$$V(r, \Omega') = -V_0\left[1+\exp\{(r-R(\Omega'))/a\}\right]^{-1} \tag{1}$$

$$R(\Omega') = R_0^{(1)}\left[1+\sum_{kq}\alpha_{kq}^{(1)}Y_{kq}(\Omega^{(1)\prime})\right]+R_0^{(2)}\left[1+\sum_{kq}\alpha_{kq}^{(2)}Y_{kq}(\Omega^{(2)\prime})\right]$$

$$= R_0^{(1)}+R_0^{(2)}+\delta R^{(1)}+\delta R^{(2)} = R_0+\delta R \tag{2}$$

Here α_{kq} are the usual collective coordinates, Ω' refer to the body-fixed axes, and suffixes (1) and (2) show projectile and target nuclei respectively.

A Taylor expansion of the potential about $R=R_0$ yields the series :

$$V = V(r-R_0)+\sum_{n>0}\frac{(-1)^n}{n!}(\delta R)^n\frac{d^n}{dr^n}V(r-R_0) \tag{3}$$

In the case of single excitation of target or projectile $\delta R = \delta R^{(1)}$ or $\delta R^{(2)}$, if the other fragments are supposed to be spherical, and the DWBA analysis can be treated equally as in the inelastic scatterings of p, d, and α particles.

When the excitation is a single excitation with transition of angular momentum L between the initial spin state J_A and the final spin state J_B, the differential cross section can be represented by the INS DWBA I code* using the reduced cross section $\sigma_L(\theta)$ as follows:

$$\frac{d\sigma}{d\Omega} = \frac{2J_B+1}{2J_A+1}\times\frac{(2L+1)^{-1}}{5.093\times10^3}\times\frac{\beta_L^2R_0^{(p)2}V_0^2}{a^2}V_L(\theta)\ \left(\frac{mb}{sr.}\right) \tag{4}$$

Here β_L is the deformation parameter, V_0 and a are the real part of strength and diffusivity parameters of the optical potential, respectively, and $R_0^{(p)}$ is $R_0^{(1)}$ or $R_0^{(2)}$ following the single excitation of projectile or target nucleus. In the calculation of DWBA, the effect of Coulomb potential in the outer region of nucleus was considered besides the nuclear excitation, because the Coulomb excitation was expected not to be neglected in heavy ion scattering. The calculations were done by the code which was modified by Yamaji so as to be able to treat higher partial wave (ℓ_{max}=200) than in the INS DWBA I code.

* T. Udagawa, H. Yoshida, K. Kubo, and G. Yamaura : INS. DWBA I code.

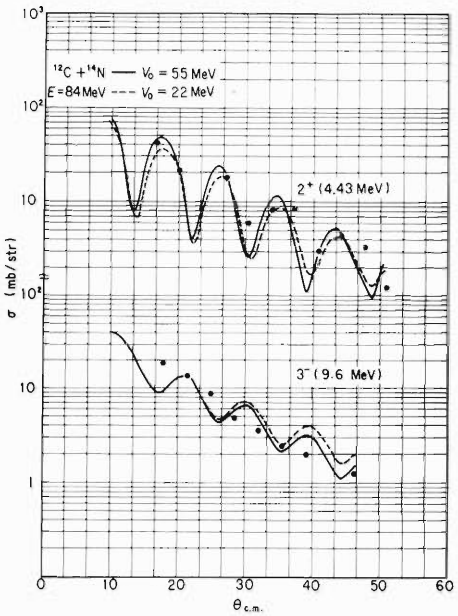

Fig. 1. DWBA predictions for the excitations of 2^+ (4.43 MeV) and 3^-(9.6 MeV) states of ^{12}C by ^{14}N particles at the energy of 84 MeV compared with the data. Solid lines show DWBA predictions using the optical experimental parameters with a deep real potential and dashed curve the shallow potential.

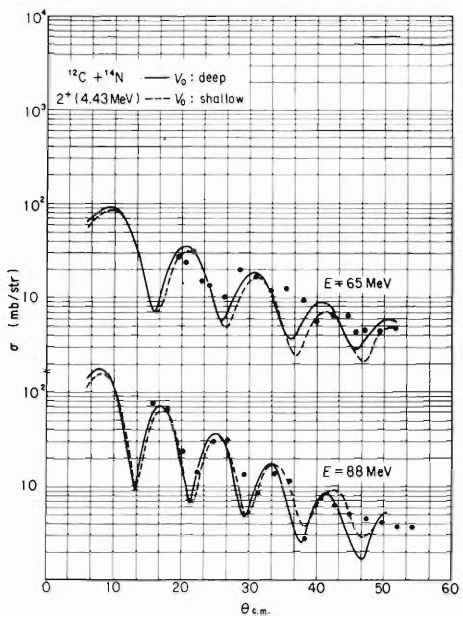

Fig. 2. DWBA predictions for the excitation of 2^+ (4.43 MeV) state of ^{12}C by ^{14}N particles at the energies of 65 and 88 MeV compared with the data. Solid lines show DWBA predictions using the optical experimental parameters with a deep real potential and dashed curve the shallow potential.

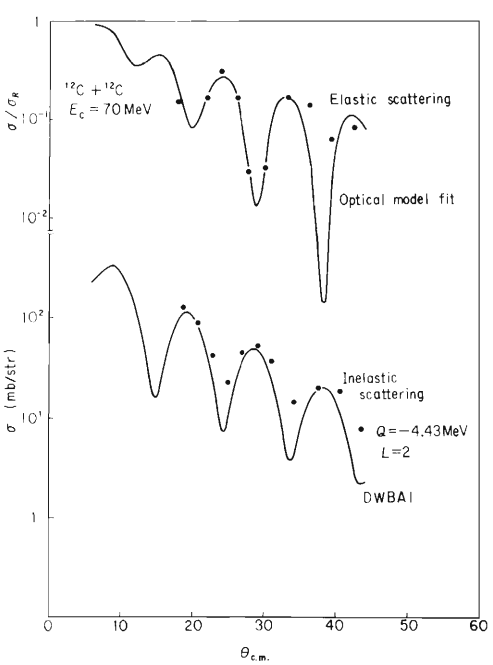

Fig. 3. a) Optical model fit to the elastic scattering of 70 MeV ^{12}C form ^{12}C and DWBA prediction of 2^+ (4.43 MeV) state compared with the experimental data. Parameters of the optical potential are given in Table 1 in Ref. 1)

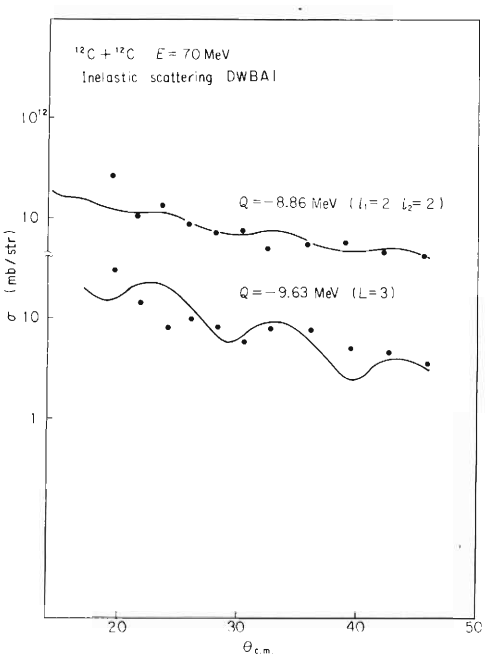

Fig. 3. b) DWBA predictions for the excitation of 3^-(9.6 MeV) state of ^{12}C by ^{12}C and for the mutual excitation of ^{12}C particles to their 4.43 MeV 2^+ states compared with the experimental data.

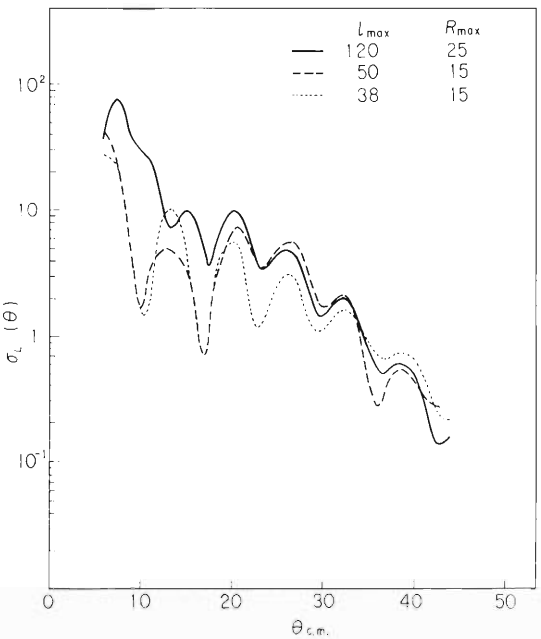

Fig. 4. Calculated angular distribution of inelastic scattering of ^{12}C projectile to 2^+ state (1.78 MeV) on ^{28}Si varying the values of R_{max} and ℓ_{max}.

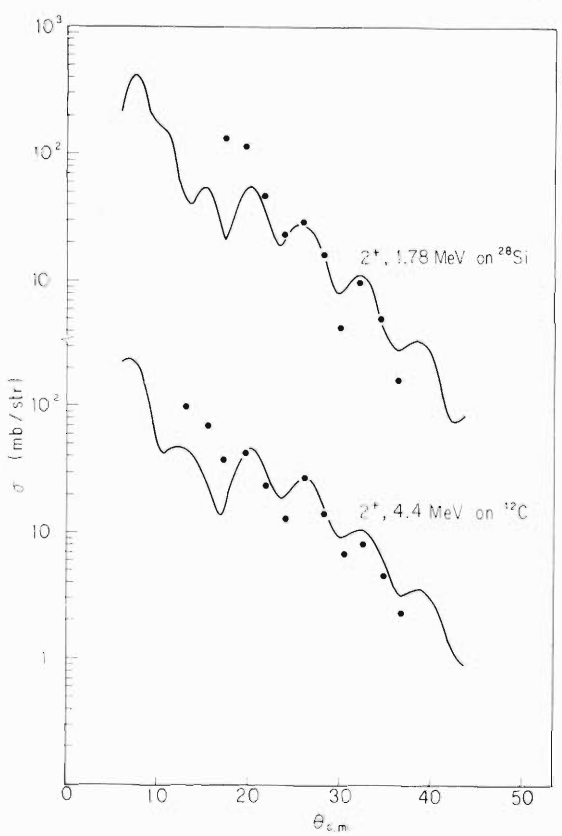

Fig. 5. a) DWBA predictions for the excitations of 1.78 MeV 2^+ state of ^{28}Si and 4.43 MeV 2^+ state of ^{12}C in collision between ^{12}C projectile and ^{28}Si target at the energy of 70 MeV compared with the data.

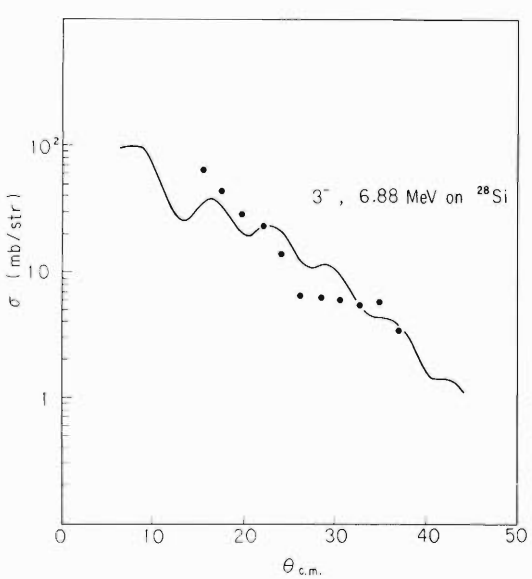

Fig. 5. b) DWBA prediction for the excitation of 6.88 MeV 3^-state of ^{28}Si by ^{12}C particles at the energy of 70 MeV compared with the data.

The differential cross sections obtained for $^{12}C + ^{14}N$ and $^{12}C + ^{12}C$ are shown in Figs. 1~3 in comparison with the experimental data. As the effect of Coulomb excitation was large in $^{28}Si + ^{12}C$ at 70 MeV, partial waves with large ℓ values and large value of R_{max} which limits the region of integration must be considered. In Fig. 4 the calculated angular distributions of inelastic scattering to 2^+ state (1.78 MeV) of ^{28}Si are represented for various values of R_{max} and ℓ_{max}. From these calculations it was found that ℓ_{max} value above 120 and R_{max} value above 25 fm which is nearly 4 times R_0, were necessary to include completely the effect of Coulomb excitation. In $^{12}C + ^{14}N$, $\ell_{max}=45$ and $R_{max}=2R_0$ were satisfactory for making DWBA calculation. The calculated differential cross sections of inelastic scatterings of ^{12}C to 2 + state (1.78 MeV) of ^{28}Si, 2 + state (4.43 MeV) of ^{12}C, and 3 - state (6.88 MeV) of ^{28}Si at $^{28}Si + ^{12}C$ are shown in Fig. 5.

The differential cross sections of mutual excitation (4.4 MeV state of projectile and target ^{12}C) at $^{12}C + ^{12}C$ were calculated using the Eqn. (5) following Bassel et al.[3]:

$$\frac{d\sigma}{d\Omega}(0\rightarrow\ell_1,\ 0\rightarrow\ell_2)=\frac{1}{4\pi}\left(\frac{\mu}{2\pi\hbar^2}\right)^2\frac{K_b}{K_a}\left(\frac{\beta\ell_1\beta\ell_2 R_0^{(1)}R_0^{(2)}V_0}{a}\right)^2$$

$$\times\sum_L <\ell_1\ell_2 OO|LO>^2 \sum_M\left|\frac{d}{dR_0}B_L^M\right|^2. \qquad (5)$$

Here μ is the reduced mass of the system, K_a and K_b the wave numbers of incident and outgoing channels, and ℓ_1 and ℓ_2 multipolarities of final states of nuclei 1 and 2. dB_L^M / dR_0 is a differential of B_L^M which is a transition amplitude of single excitation. In this case, nuclei 1 and 2 were both ^{12}C and $\ell_1=\ell_2=2$, and the values of B_L^M were calculated by DWBA for single excitation of 2 + state of ^{12}C at $^{12}C + ^{12}C$. The results of calculation are shown in Fig. 3 (b) and the feature of angular distribution seems to become less diffraction-like compared with that of single excitation, and to reproduce the experimental results.

In Table 1 the deformation parameters β_ℓ and the deformation length $\beta_\ell R$ for 2 + and 3 - levels of both ^{12}C and ^{28}Si obtained from DWBA analyses of the inelastic scatterings are summerized. The calculated values of β_2 for 2 + level of ^{12}C are scattered between 0.4 and 0.9, but these values are close to ones obtained from other heavy ion inelastic scatterings : Bassel et al.[3] obtained the values of 0.56 to 0.9 from DWBA analyses of $^{12}C + ^{12}C$ and $^{12}C + ^{16}O$, and Oertzen et al.[4] obtained 0.3 ± 0.1 from DWBA analyses of $^{12}C + ^{14}N$. The agreement of β_ℓ for 2 + and 3 - levels of ^{28}Si with the values[5] obtained from the inelastic scatterings of p, n and α particles are not necessarily good.

Table 1. The deformation lengths $\beta_\ell R$ and the deformation parameters β_ℓ obtained from DWBA prediction.

Reaction	Transition	β_ℓ	$\beta_\ell R$(fm)	E(MeV)
$^{12}C + ^{12}C$	$0 \rightarrow 2, 0 \rightarrow 0$	0.50	1.35	70.0
$^{12}C + ^{12}C$ a)	$0 \rightarrow 2, 0 \rightarrow 2$	0.716	1.94	70.0
$^{12}C + ^{14}N$	$0 \rightarrow 2$	0.492	1.37	88.0
$^{12}C + ^{14}N$ *	$0 \rightarrow 2$	0.466	1.39	88.0
$^{12}C + ^{14}N$	$0 \rightarrow 2$	0.405	1.13	84.0
$^{12}C + ^{14}N$ *	$0 \rightarrow 2$	0.381	1.14	84.0
$^{12}C + ^{14}N$	$0 \rightarrow 2$	0.450	1.26	65.0
$^{12}C + ^{14}N$ *	$0 \rightarrow 2$	0.607	1.82	65.0
$^{28}Si + ^{12}C$	$0 \rightarrow 0, 0 \rightarrow 2$	0.932	2.20	70.0
$^{28}Si + ^{12}C$ b)	$0 \rightarrow 2, 0 \rightarrow 0$	0.664	2.07	70.0
$^{12}C + ^{12}C$	$0 \rightarrow 3, 0 \rightarrow 0$	0.534	1.45	70.0
$^{12}C + ^{14}N$	$0 \rightarrow 3, 0 \rightarrow 0$	0.35	0.97	84.0
$^{12}C + ^{14}N$ *	$0 \rightarrow 3, 0 \rightarrow 0$	0.39	1.17	84.0
$^{28}Si + ^{12}C$	$0 \rightarrow 3, 0 \rightarrow 0$	0.705	2.20	70.0

* shallow potential

a) Mutual excitation

b) Single excitation of 1.78 MeV 2^+ on ^{28}Si

References

1) I. Kohno, S. Nakajima, T. Tonuma, and M. Odera : IPCR Cyclotron Progr. Rep., 3, 15 (1969).

2) R. H. Bassel, G. R. Satchler, and R. M. Drisko : Nucl. Phys., 89, 419 (1966).

3) W. V. Oertzen, M. Liu, C. Caverzasio, J. C. Jacmart, F. Pougheon, M. Riou, J. C. Royntette, and C. Stephan : ibid., A143, 34 (197).

4) H. Sherif and J. S. Blair : ibid., A140, 33 (1970) ;
J. Kokame, K. Fukunaga, and H. Nakamura : Phys. Lett., 20, 672 (1963) ;
R. H. Stelson, R. L. Robinson, H. J. Kim, J. Rapaport, and G. R. Satchler : Nucl. Phys., 68, 97 (1965).

4-2. The Finite Range DWBA Analyses of the Reactions $^{52}Cr(^{14}N,^{13}C)^{53}Mn$ and $^{52}Cr(^{12}C,^{11}B)^{53}Mn$

S. Nakajima

The finite range DWBA analyses are being performed for the single-proton transfer reactions induced by 90 and 70 MeV ^{14}N ions and 60 MeV ^{12}C ions on a ^{52}Cr target. A report on details of the experiments is under preparation. The calculations utilize the program INS-DWBA-4[1] written by H. Yoshida and adapted by S. Yamaji to the FACOM 230-60 computer of the IPCR. This code treats exactly the six-dimensional integral and includes accurately the recoil effect.

The calculated cross sections are shown in Figs. 1 and 2 together with experimental values obtained in this laboratory. The optical potential parameters used for calculation were of Woods-Saxon type and are shown in Table 1. The same parameters were used for the exit

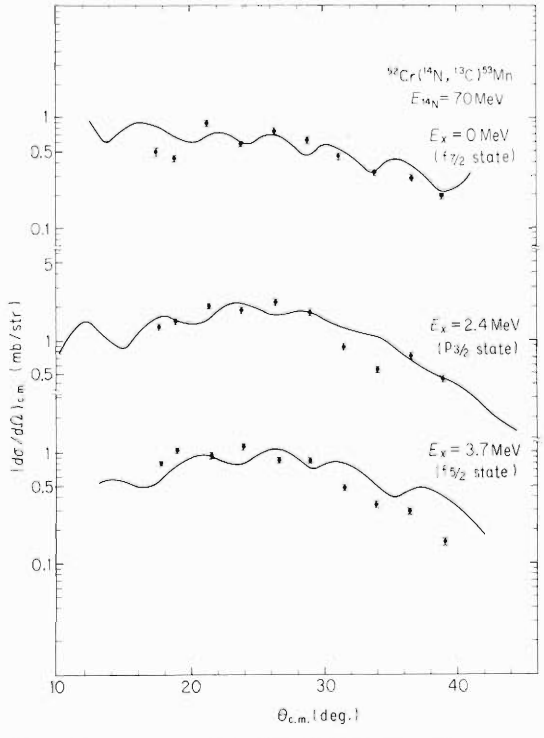

Fig. 1. Angular distributions of $^{52}Cr\ (^{14}N,\ ^{13}C)^{53}Mn$ at $E_{\ell ab}$ = 70 MeV for transitions to the ground ($7/2^-$), 2.4 MeV ($3/2^-$) and 3.7 MeV ($5/2^-$) excited states. The solid curves are those of the finite range DWBA calculations normalized arbitrarily to fit to the data.

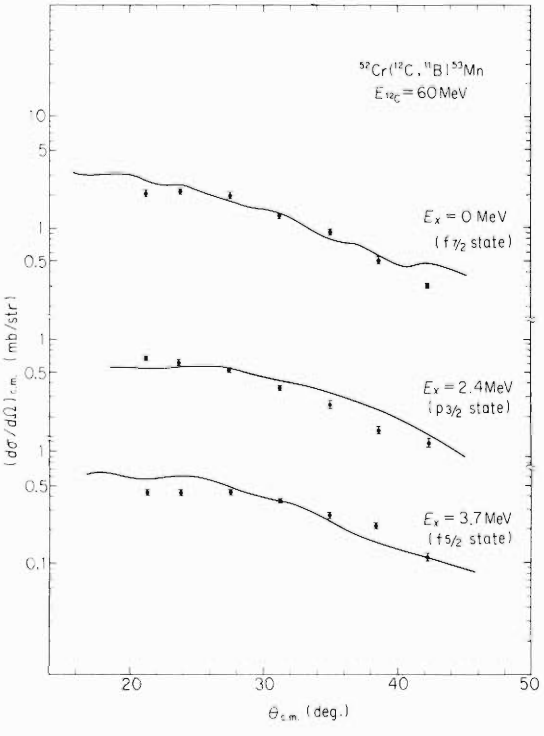

Fig. 2. Angular distributions of $^{52}Cr\ (^{12}C,\ ^{11}B)^{53}Mn$ at $E_{\ell ab}$ = 60 MeV for transitions to the ground, 2.4 MeV and 3.7 MeV excited states. The solid curves are those of the finite range DWBA calculations normalized arbitrarily to fit to the data.

channel. Bound state wave functions were solved in a Woods-Saxon potential with a = 0.67 fm and r_0 = 1.27 fm. The calculations of Cohen and Kurath[2] were used for the spectroscopic factor of an incident particle S(a→b+x). The values of $(2\ell+1)\,W^2(\ell_a j_a \ell_b j_b; s\ell)\,S(a\rightarrow b+x)$ are shown in Table 2. The calculated angular distributions and absolute cross sections do not

Table 1. Optical potential parameters for the elastic scattering of ^{14}N on ^{52}Cr at 70 MeV and ^{12}C on ^{52}Cr at 60 MeV.

	V(MeV)	W(MeV)	r_0(fm)	a_0(fm)	r_I(fm)	a_I(fm)
$^{12}C + ^{52}Cr$	60.0	18.25	1.04	0.739	1.04	0.516
$^{14}N + ^{52}Cr$	60.6	11.1	1.03	0.700	1.16	0.516

Table 2. Spectroscopic amplitude $(2\ell + 1)\,W^2(\ell_a j_a \ell_b j_b; s\ell)\,S(a\rightarrow b+x)$. Spectroscopic factor of an incident particle S (a→b+x) is taken from the calculation of Cohen and Kurath. That of a residual nucleus S(B→A+x) is not multiplied in this table.

$(2\ell + 1)\,W^2(\ell_a j_a \ell_b j_b; s\ell)\,S(^{14}N \rightarrow {}^{13}C+P)$

Transition	$\ell = 4$	$\ell = 3$	$\ell = 2$	$\ell = 1$	$\ell = 0$
$p\frac{3}{2} \rightarrow f\frac{7}{2}$	0.0005	0.0007	0.0007		
$\rightarrow f\frac{5}{2}$	0.0013	0.00056	0.00015		
$\rightarrow p\frac{3}{2}$			0.0008	0.0008	0.0003
$p\frac{1}{2} \rightarrow f\frac{7}{2}$	0.258	0.086			
$\rightarrow f\frac{5}{2}$		0.152	0.191		
$\rightarrow p\frac{3}{2}$			0.287	0.057	

$(2\ell + 1)\,W^2(\ell_a j_a \ell_b j_b; s\ell)\,S(^{12}C \rightarrow {}^{11}B+P)$

Transition	$\ell = 4$	$\ell = 3$	$\ell = 2$	$\ell = 1$	$\ell = 0$
$p\frac{3}{2} \rightarrow f\frac{7}{2}$	0.381	0.534	0.509		
$\rightarrow f\frac{5}{2}$	0.916	0.396	0.113		
$\rightarrow p\frac{3}{2}$			0.59	0.59	0.24

necessarily agree with the data. But, slightly changing the bound state or the optical potential parameters in the exit channel, it may be possible to reproduce the data.

The recoil effect is investigated and the results are shown in Figs. 3 and 4. In these figures, the $\ell = 1$ and the $\ell = 3$ transfers have an unnatural parity which is not allowed in a no-recoil DWBA theory. As the incident energy increases, the $\ell = 1$ transfer becomes larger in magnitude, that is, the recoil effect becomes more significant. Moreover, the angular distributions with even parity are in phase to each other, but are out of phase with opposite parity. When an unnatural parity transfer is comparable in magnitude with a natural parity transfer, the sum of them will show a damping of diffraction oscillation as pointed out by Dodd and Greider.[3] In our case, however, the recoil effect does not necessarily play an important role because of the smallness of their spectroscopic amplitude $(2\ell+1)\, W^2(\ell_a j_a \ell_b j_b ; s\ell)$ S (a→b+x) S (A→B+x) or the calculated DWBA amplitude.

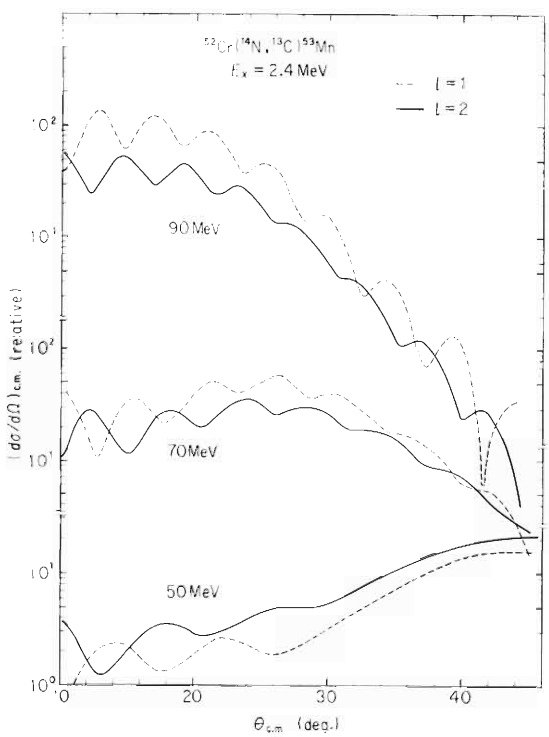

Fig. 3. Comparison of the magnitude and its energy dependence between the $\ell = 2$ and the $\ell = 1$ transfers in the reaction ^{52}Cr(^{14}N, ^{13}C) ^{53}Mn leading to the 2.4 MeV excited state in ^{53}Mn.

Spectroscopic amplitudes are neglected in the calculation. These weighting factors are 5 and 1 for $\ell = 2$ and $\ell = 1$, respectively.

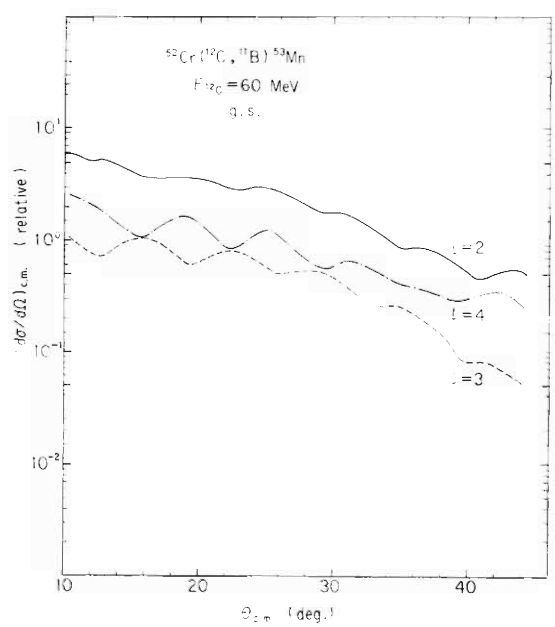

Fig. 4. Contribution of the angular momentum transfers $\ell = 2$, 3 and 4 to the cross section in the reaction ^{52}Cr(^{12}C, ^{11}B) ^{53}Mn leading to the ground state in ^{53}Mn. The sum of these curves gives the final cross sections.

The dependence of the angular distribution on the optical parameters is seen in Fig. 5. Change of the optical parameter set influences the absolute magnitude and the shape of the curve. Several parameter-sets can reproduce the elastic scattering, but few of them is able to fit to transfer reactions.

Because of strong absorption, the distorted waves are only sensitive to the nuclear surface and the interior of the nucleus does not contribute to the transition amplitude. Then, it is possible to cut off a lower radius or lower partial waves in the DWBA calculation. Fig. 6 illustrates a radial cut-off effect in the calculation using the imaginary part of the optical potential W = 11 MeV. Difference is not distinct in two curves of the angular distribution. The effect of the cut-off of lower partial waves is illustrated in Fig. 7. It is seen that a suitable cut-off of them scarcely affects the absolute magnitude and the form of the angular distribution. The time necessary for calculation can be reduced with such a cut-off.

Further investigation is in progress for extracting the spectroscopic factors of the residual nucleus and the dependence of the reaction amplitude on the kinematic conditions.

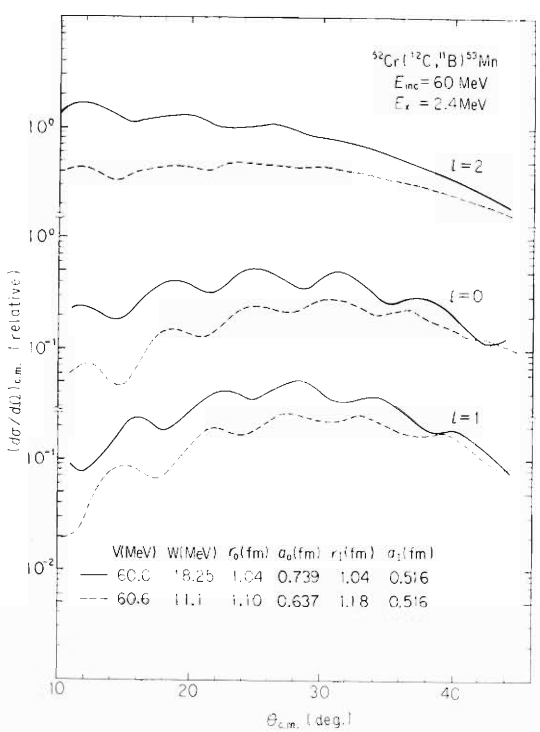

Fig. 5. The dependence of the angular distribution on the optical parameter in the reaction $^{52}Cr(^{12}C, ^{11}B)^{53}Mn$ leading to the 2.4 MeV excited state in ^{53}Mn at E_{lab} = 60 MeV.

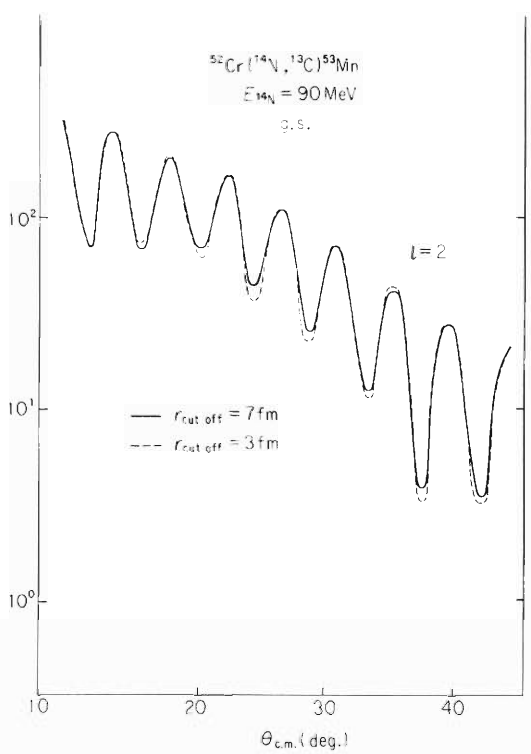

Fig. 6. The dependence of the angular distribution on the lower radial cut-off in the reaction $^{52}Cr(^{14}N, ^{13}C)^{53}Mn$ leading to the ground state in ^{53}Mn at E_{lab} = 90 MeV.

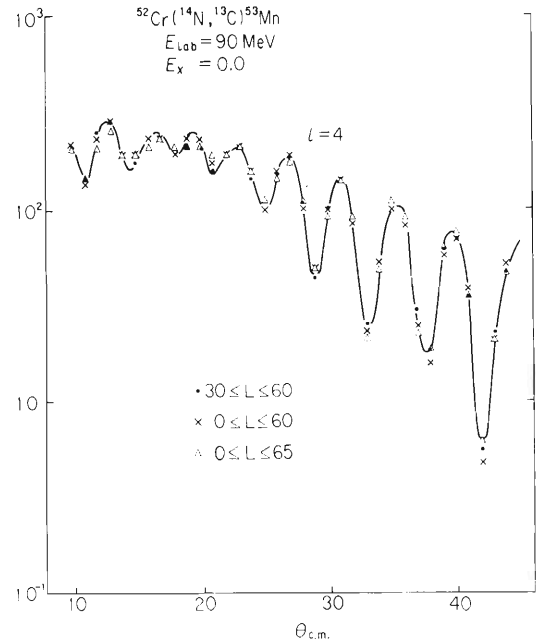

Fig. 7. The influence of cut-off of lower partial waves in the calculation of the reaction $^{52}Cr(^{14}N, ^{13}C)^{53}Mn$ leading to the ground state in ^{53}Mn at E_{lab} = 90 MeV.

References

1) H. Yoshida : Reference Manual for INS-DWBA-4, Institute of Nuclear Study, University of Tokyo (1972).

2) S. Cohen and D. Kurath : Nucl. Phys., A101, 1 (1967).

3) L. R. Dodd and K. R. Greider : Phys. Rev., 180, 1187 (1969).

4-3. Angular Distributions of Transfer Reactions Induced by Heavy Ions

M. Yoshie, K. Katori, I. Kohno, S. Nakajima,
T. Motobayashi, T. Mikumo, and H. Kamitsubo

Transfer reactions studied using the beams of ^{14}N and ^{12}C on the (fp) shell[1] and heavy nuclei[2] showed various patterns in their angular distribution. We note here qualitative features of these patterns and intend to interpret these angular distributions theoretically based on the model of peripheral collisions developed by Strutinsky.[3),4)]

We present here two cases; (1) ^{52}Cr + ^{14}N at 90 and 70 MeV and (2) ^{208}Pb + ^{14}N at 90 MeV. In both cases, for single nucleon transfer reactions the yield concentrated at states near the ground state, and for multi-nucleon stripping reactions the energy spectra showed broad bumps, whose shapes varied with the bombarding energies and the number of transferred nucleons.

For the stripping reactions induced by 90 MeV ^{14}N ions on ^{52}Cr, the angular distributions of products integrated over whole energy spectra peak forward in the angular range from

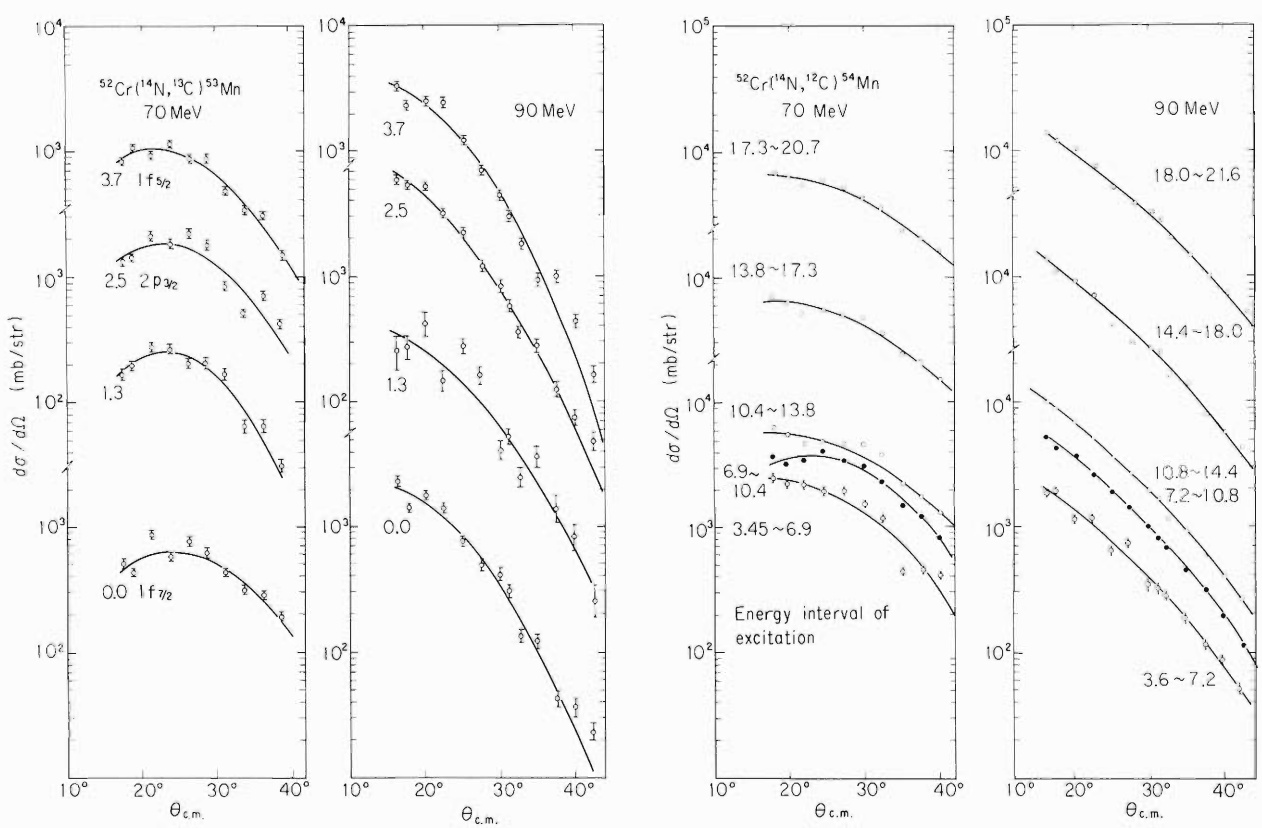

Fig. 1. Angular distributions of ^{13}C and ^{12}C from ^{52}Cr + ^{14}N at 90 and 70 MeV. For ^{13}C, those of some selective peaks are shown, and for ^{12}C, those of integrated cross sections over energy intervals of 3.5 MeV are shown. The solid curves are obtained by calculation with the Strutinsky model fitting to the data.

θ_{cm}=16° to θ_{cm}=45.° Fig. 1 shows some angular distributions of ^{13}C and ^{12}C emerging from ^{52}Cr + ^{14}N at 90 and 70 MeV. In the case of ^{13}C, angular distributions of a few selective peaks corresponding to energy levels of ^{53}Mn are shown. Angular distributions of ^{12}C yields integrated over about 3 MeV energy intervals are shown in Fig. 1. In each case, the shapes of angular distributions do not depend strongly on excitation energies or transferred angular momenta.

At 70 MeV, the cross section maxima are observed at θ_{cm}=24° for ^{13}C, and a bump appeared at θ_{cm}=24° for ^{12}C.

For multi-nucleon stripping reactions $\frac{d\sigma}{d\Omega} = e^{-K\theta}$ holds approximately. The slope diminishes as the mass of the observed particles becomes smaller.

In Fig. 2 are also shown the angular distributions of ^{13}C, ^{12}C, ^{12}B, and ^{10}B from ^{208}Pb + ^{14}N reactions at 90 MeV. They all have maxima at θ_{cm}=70~80°.

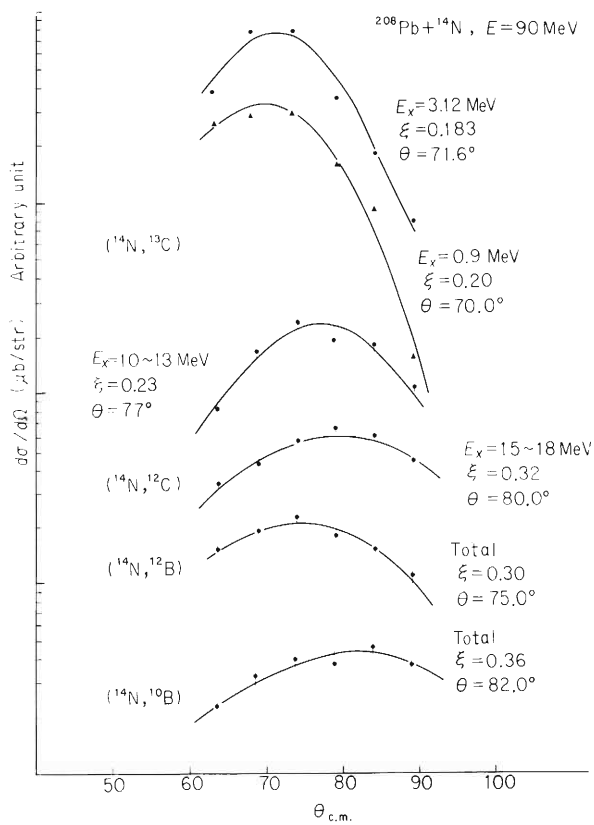

Fig. 2. Angular distributions of ^{13}C, ^{12}C, ^{12}B, and ^{10}B from ^{208}Pb + ^{14}N at 90 MeV. The upper two data are those of specific levels, and others are those of integrated cross sections over energy intervals indicated on the figure. The solid curves are obtained by calculation with the Strutinsky model fitting to the data.

Strutinsky gave an expression for the differential cross section as

$$\frac{d\sigma}{d\Omega} = \frac{d\sigma(0^\circ)}{d\Omega} \frac{2}{\pi \ell_0 \sin\vartheta} \exp\left(\frac{\vartheta^2}{\xi^2}\right) \times \left[ch\left(\frac{2\theta\vartheta}{\xi^2}\right) + \sin\left\{\left(\frac{2\ell_0+1+\theta\xi_r^2}{\xi}\right)\vartheta\right\}\right],$$

where $\xi = (\xi_q^2 + \xi_r^2)^{1/2}$ is the total angular dispersion determined by the quantal dispersion coefficient $\xi_q = \sqrt{2}/\Delta\ell$ and by the dynamic quantity $\xi_r = \sqrt{2}K\Delta\ell$.

Neglecting the second term in the parentheses which oscillates rapidly with angle, parameters ξ and θ were found by fitting the data to the formula. Normalization was made rather arbitrarily. Results of the fitting are also shown in Figs. 1 and 2 and parameters are presented in Figs. 3 and 4.

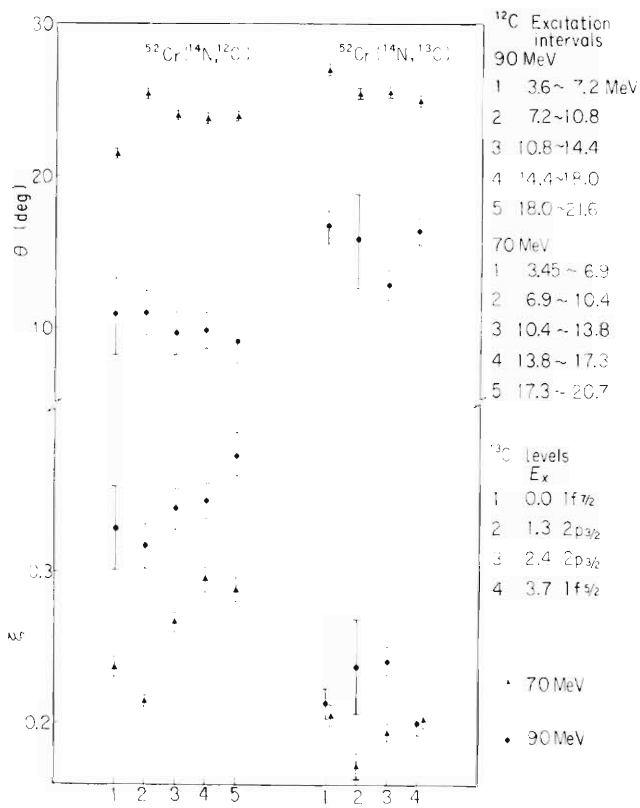

Fig. 3. Strutinsky's parameters obtained from the experimental differential cross sections of ^{13}C and ^{12}C projectiles from the reaction ^{52}Cr + ^{14}N at energies of 90 and 70 MeV (see Fig. 1 (a) and (b)). The numbers on the abscissa indicate the excitation intervals of summation for ^{12}C, and the levels of ^{53}Mn for ^{13}C as defined in the figure.

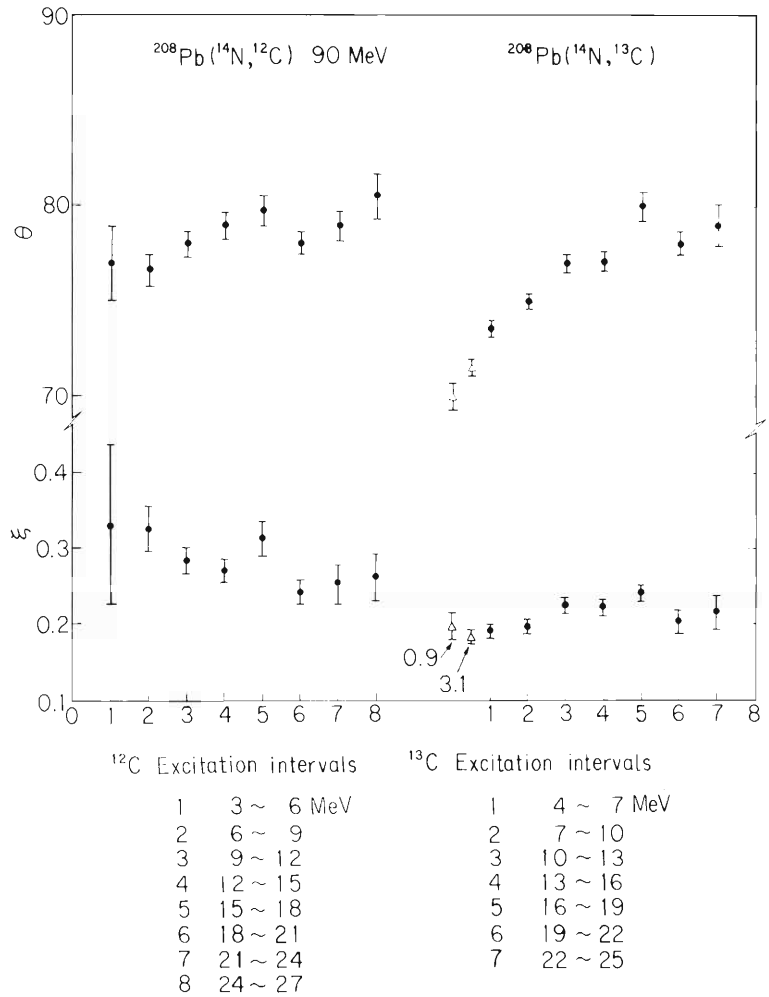

Fig. 4. Strutinsky's parameters obtained from the experimental differential cross sections of ^{13}C, ^{12}C, ^{12}B, and ^{10}B projectiles from the reaction $^{208}Pb + ^{14}N$ at 90 MeV (see Fig. 2). The numbers on the abscissa indicate the excitation intervals of summation. The parameters of two specific levels are also given.

We obtained some characteristic features on the parameters : First, for $^{52}Cr + ^{14}N$

(1) θ decreases and ξ remains constant as bombarding energy increases ;

(2) θ remains constant and ξ increases as excitation energy increases ;

(3) θ decreases and ξ increases as stripped mass increases.

Secondly for $^{208}Pb + ^{14}N$, ξ is slightly larger in the case of ^{12}C than in the case of ^{13}C. For ^{13}C, parameters which fit the data of specific levels and of unresolved part in the energy spectra are given in Fig. 4. The parameters vary continuously.

The DWBA theory can account for the (^{14}N, ^{13}C) data for specific levels of both $^{52}Cr + ^{14}N$ and $^{208}Pb + ^{14}N$ qualitatively.

Strutinsky's phenomenologically introduced parameters can be interpreted in connection with the DWBA theory. When the number of transferred nucleons increases, and when the

bombarding energy increases, there is systematic deviation in the values of parameter from those obtained for single nucleon transfer.

This suggests the existence of a new mechanism in heavy ion reactions, which becomes more important at high energies.

References

1) I. Kohno, S. Nakajima, I. Yamane, M. Yoshie, M. Odera, and H. Kamitsubo : IPCR Cyclotron Prog. Rep., 6, 23 (1972) ; S. Nakajima, I. Kohno, I. Yamane, M. Yoshie, H. Kamitsubo, M. Odera, and T. Mikumo : ibid., p. 27 (1972).
2) T. Motobayashi, I. Kohno, S. Nakajima, M. Yoshie, K. Katori, T. Mikumo, and H. Kamitsubo : ibid., 7, 32 (1973).
3) V. M. Strutinsky : JETP, 19, 1401 (1964).
4) V. M. Strutinsky : Phys. Lett., 44B, 245 (1973).

4-4. A Study of Transfer Reactions Induced by ^{14}N and ^{12}C on ^{208}Pb and ^{209}Bi

T. Motobayashi, I. Kohno, S. Nakajima, M. Yoshie,
K. Katori, T. Mikumo, and H. Kamitsubo

A study of the transfer reactions induced by ^{14}N and ^{12}C on (fp) shell nuclei at energies 2 or 3 times higher than the Coulomb barrier has been reported previously.[1] In these experiments, the energy spectra of the emitted particles showed a large "bump" at multi nucleon transfer and selective peaks which correspond to several levels of the residual nuclei only at one nucleon transfer reaction, and the angular distributions showed forward peaks. These features are very different from experimental results of other transfer reactions on (fp) shell nuclei at the energy near the Coulomb barrier.[2),3)] In these cases, "bumps" were very small or not found, and the angular distributions showed a simple "bell shape" which had a broad peak at the grazing angle. In order to study what features are found in the transfer reactions on the heavy targets at the

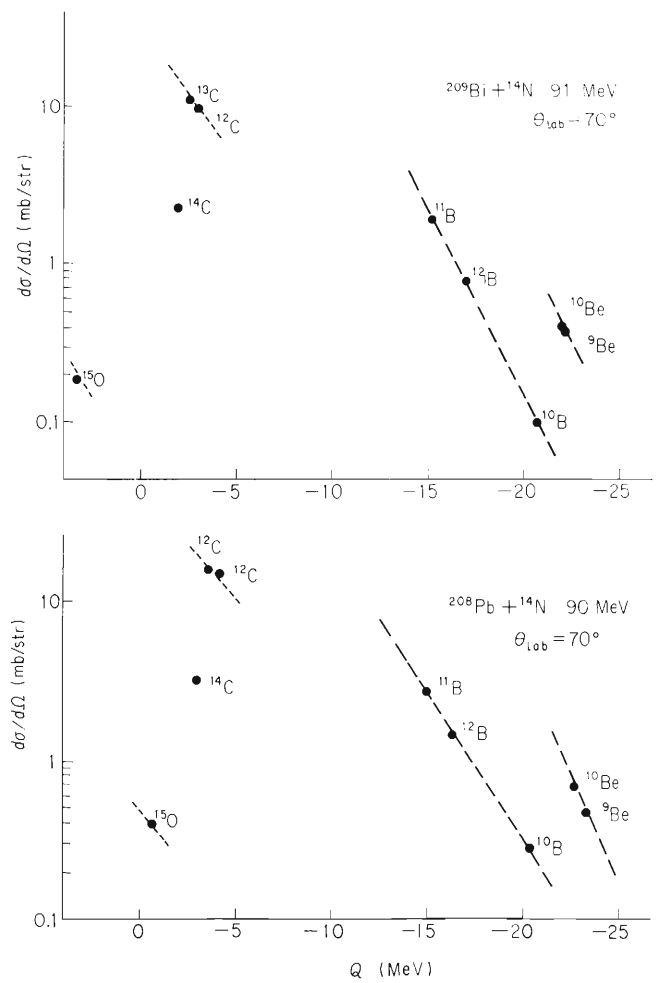

Fig. 1. Differential cross sections at θ_{max} (70° in this case) plotted v.s. ground state Q values of the corresponding reactions.

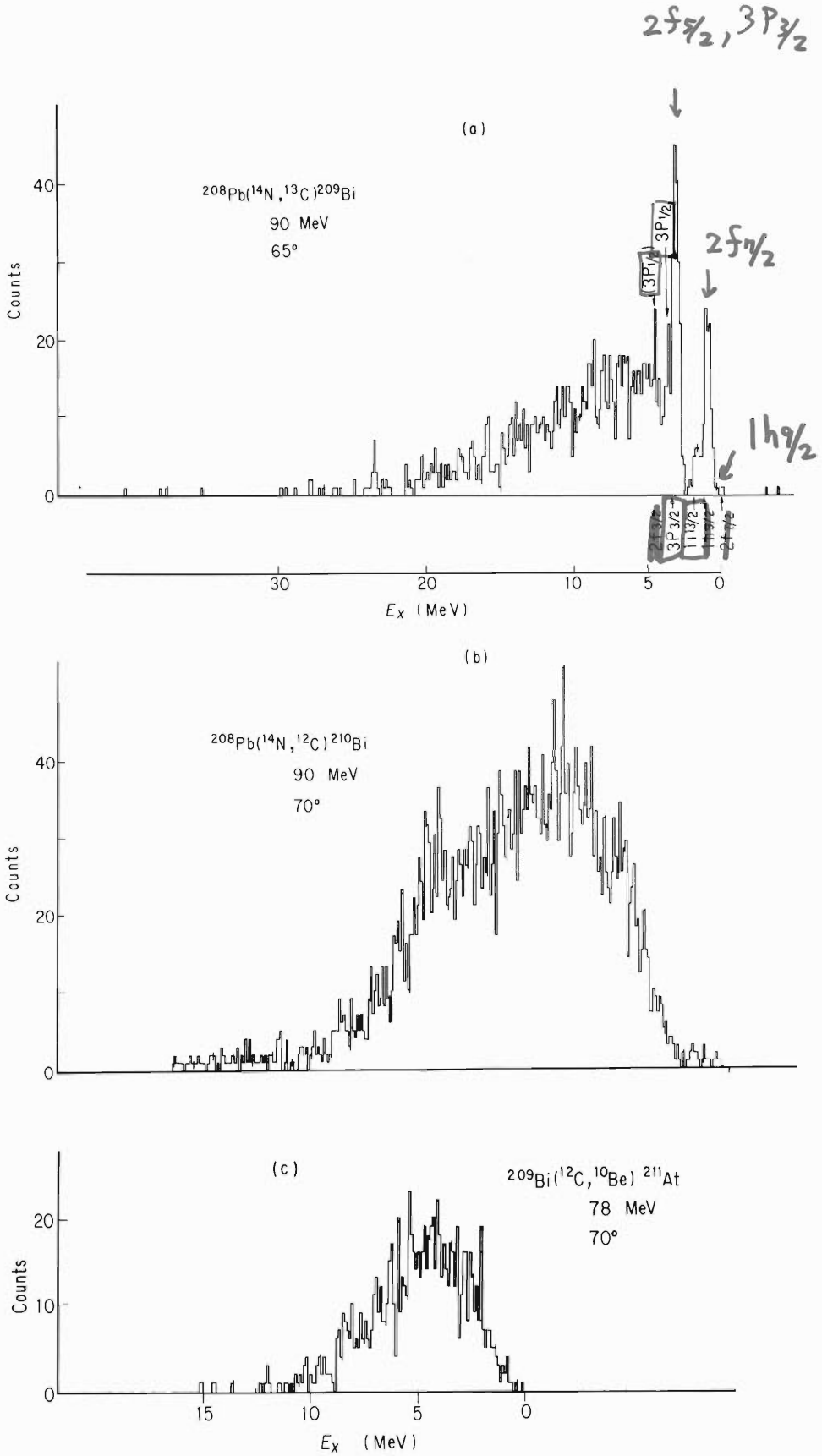

Fig. 2. (a) and (b) ^{13}C and ^{12}C spectra due to 90 MeV ^{14}N reactions on ^{208}Pb, (c) ^{10}Be spectrum due to 78 MeV ^{12}C reaction on ^{209}Bi. For ^{13}C spectrum, the known proton single-particle states are labeled according to their shell model orbits.

energy above the Coulomb barrier, we have done experiments of the transfer reactions induced by ^{14}N and ^{12}C on ^{208}Pb and ^{209}Bi at energies of 90 MeV (^{14}N) and 78 MeV (^{12}C). Experimental procedure has been described in a previous report.[4] The thickness of targets was about $400\mu g/cm^2$.

Experimental results

(1) The differential cross sections $(d\sigma/d\Omega)_{\theta max}$ for all emitted particles have the same regularities as that reported by Dubuna group.[5] For the same atomic number of the emitted particles, the regularity is represented by relation $\log(d\sigma/d\Omega)_{\theta max}$=const. Qgg as shown in Fig. 1, where $(d\sigma/d\Omega)_{\theta max}$ means the differential cross section at the angle, at which the angular distribution has a maximum value, and Qgg is the ground state Q-value for each transfer reaction.

(2) In the energy spectra of multi-nucleon transfer reactions, typical bumps were found as seen in the transfer reaction on (fp) shell nuclei at higher energies. Examples of these bumps are shown in Fig. 2(b) and (c). However, the width of bumps is smaller and the peak position of them is nearer to Ex=0 compared with the bumps found in the case of the transfer reaction on (fp) shell nuclei.

In the energy spectrum of one-proton transfer reaction on ^{208}Pb, some selectively excited peaks corresponding to the single proton levels of ^{209}Bi and a small bump at higher Ex are observed as shown in Fig. 2(a).

In case of selective peaks it is well known that the transfer yields have strong Q- and L-dependencies, which are reproduced by the classical picture. We have tried to understand these Q- and L- dependencies for some selective peaks of this experiment by calculating the

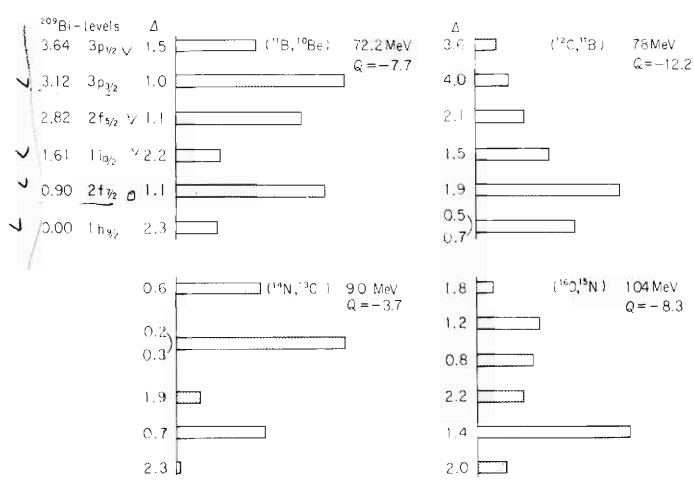

Fig. 3. Comparison of the calculated values of Δ (the degree of mismatching) and the relative intensities of six known single-proton states of ^{209}Bi. The $3p_{3/2}$ and $2f_{5/2}$ states in (^{14}N, ^{13}C) reaction are mixed by poor resolution. It is assumed that the spin of transferred proton is not flipped.

momentum- and angular momentum-mismatching classically. When the classical trajectories are assumed both in incident and exit channels of the transfer reactions and the transfer process takes place at the periphelion of the orbit, the angular momentum mismatch $\Delta L=K\Delta D$ can be calculated. Here K is the relative momentum of the bulk motion and $\Delta D=D_f-D_i-\Delta D_{recoil}$ where D_i and D_f are the distances of closest approach in initial and final channels respectively,[6] and ΔD_{recoil} is the change in the distance between centers of mass of two nuclei before and after the transfer of a nucleon. Linear momentum mismatch of transfered nucleon is given by $\Delta k=k-\lambda_1/R_1-\lambda_2/R_2$ following Brink's condition.[7] According to the semiclassical theory, $\Delta L\leq 2$ and $\frac{1}{2}R\Delta k\leq\pi$ are the conditions under which the transfer probability is large,[7] and then $\Delta = [(R\Delta k/2\pi)^2 + (K\Delta D/2)^2]^{1/2} \leq\sqrt{2}\simeq 1.4$. The calculated values of Δ are compared with the relative intensities of several peaks in the reaction $^{208}Pb(^{14}N, ^{13}C)^{209}Bi$ and other reactions $^{208}Pb(^{16}O, ^{15}N)^{209}Bi$, $^{208}Pb(^{12}C, ^{11}B)^{209}Bi$[8] and $^{208}Pb(^{11}B,^{10}Be)^{209}Bi$[9] in Fig. 3. In this figure in

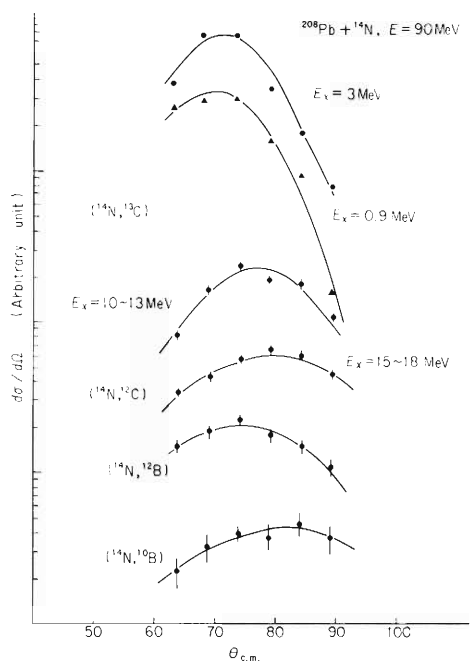

Fig. 4. Angular distributions of various reactions induced by 90 MeV ^{14}N on ^{208}Pb. Solid lines result from calculations by Strutinsky model fitting to the data. For (^{14}N, ^{12}C) and one of the (^{14}N, ^{13}C) reactions, the cross sections are integrated over the energy range indicated. The cross sections of $^{10,12}B$ are totally integrated over the energy spectra.

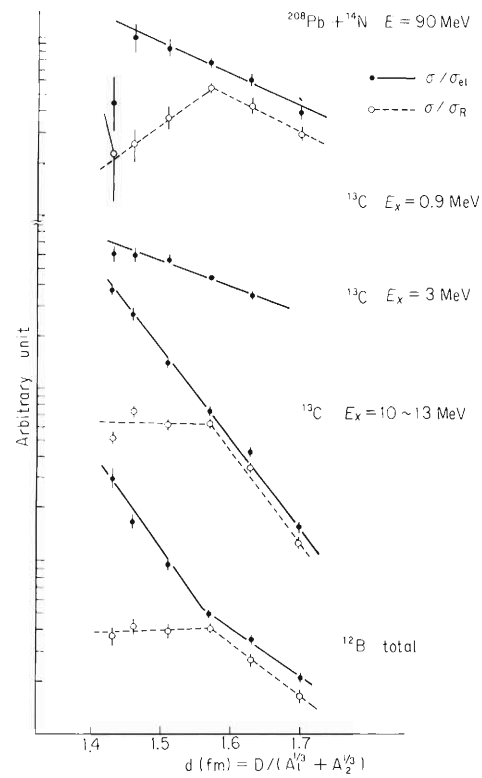

Fig. 5. The cross sections of various reactions induced by 90 MeV ^{14}N on ^{208}Pb plotted v.s. $d=D/(A_1^{1/3}+A_2^{1/3})$, where D is the distance of closest approach for the Rutherford trajectory. The cross sections are divided by the Rutherford cross sections (dashed lines) and by the elastic cross sections of the initial channel (Solid lines).

general the smaller Δ value shows the more enhanced yield of the peak.

(3) The angular distributions obtained show a typical bell shape as shown in Fig. 4. Solid lines are the differential cross sections calculated by Strutinsky model[10] that fits to the data. The analysis by Strutinsky model are described elsewhere[11] in this Cyclotron Progress Report.

Figure 5 shows the differential cross sections of transfer reactions divided by the Rutherford cross sections (σ/σ_R) and those divided by the elastic scattering cross sections of the initial channel (σ/σ_{el}) as a function of the distance of closest approach D. In cases of (^{14}N, ^{13}C) reactions, for a larger distance σ/σ_R becomes smaller because of the smaller overlap of the wave function of the transferred nucleons, and for a smaller distance σ/σ_R becomes smaller because of the absorption of the incident and outgoing waves. As for σ/σ_{el} the absorption is compensated and the lines of $\log(\sigma/\sigma_{el})$ v.s. D become straight. However in case of (^{14}N, ^{12}B) reaction, for small distance the curve of σ/σ_R v.s. D becomes flat as already seen in our previous data of $^{52}Cr(^{14}N, ^{12}C)^{54}Mn$ reaction at the energy of 90 MeV.[12] This suggest that the reaction mechanism of multinucleon transfer reaction which makes the "bump" in energy spectrum is different from the mechanism of one nucleon transfer reaction.

References

1) I. Kohno, S. Nakajima, I. Yamane, M. Yoshie, M. Odera, and H. Kamitsubo : IPCR Cyclotron Progr. Rep., 6, 23 (1972).
2) F.D. Becchetti, P. R. Christensen, V.I. Manko, and R. J. Nickles : Phys. Lett., 43B, 279 (1973).
3) M. C. Lemaire : Phys. Rep., 7C, 280 (1973).
4) S. Nakajima, I. Kohno, I. Yamane, M. Yoshie, M. Odera, and H. Kamitsubo : IPCR Cyclotron Progr. Rep., 6, 89 (1972).
5) A. G. Artukh, V. V. Ardeichikov, J. Erö, G. F. Gridnev, V. L. Mikheev, V. V. Volkov, and J. Wilczynski : Nucl. Phys., A160, 511 (1971).
6) P. R. Christensen, V.I. Manko, F.D. Becchetti, and R. J. Nickles : ibid., A207, 33 (1973).
7) D. M. Brink : Phys. Lett., 40B, 37 (1972).
8) D. G. Kovar, F. D. Becchetti, B. G. Harvey, F. Pühlhofer, J. Mahoney, D. W. Millor, and M. S. Zisman : Phys. Rev. Lett., 29, 1023 (1972).
9) J.L.C. Ford, Jr., K. S. Toth, D. C. Hensley, R. M. Caedke, P. J. Riley, and S. T. Thornton : Proc. of Symp. on Heavy Ion Transfer Reactions at Argonne, Argonne Physics Division Informal Report, PHY-1973B, 495 (1973).
10) V. M. Strutinsky : Phys. Lett., 44B, 245 (1973).
11) M. Yoshie, K. Katori, I. Kohno, S. Nakajima, T. Motobayashi, T. Mikumo, and H. Kamitsubo : IPCR Cyclotron Progr. Rep., 7, 27 (1973).
12) H. Kamitsubo, M. Yoshie, I. Kohno, S. Nakajima, I. Yamane, and T. Mikumo : Proc. of Symp. on Heavy Ion Transfer Reactions at Argonne, Argonne Physics Division Informal Report, PHY-1973B, 549 (1973).

4-5. Angular Distributions and Linear Momentum Transfers of Target Residue in the $^{209}Bi + ^{12}C$ Reaction

K. Hiruta, T. Nomura, M. Yoshie,
and O. Hashimoto

Angular distributions of residual nuclei produced in the $^{209}Bi + ^{12}C$ reaction were measured to distinguish the reaction products due to (^{12}C,αxn) from those due to (^{12}C,xn). A selfsupporting ^{209}Bi target of about 100 $\mu g/cm^2$ in thickness was bombarded with 80 MeV ^{12}C-ions supplied from the cyclotron. In Fig. 1, the reaction products recoiled from the target were caught by an aluminum foil and alpha-decays emitted therefrom were detected with a Si surface-barrier diode placed about 1.5 cm under the stopper to identify the reaction products. A slit of 0.5 cm in diameter was set between the catcher foil and the Si-detector so that α-particles and reaction products from the target could not enter the detector. The catcher foil was made rotatable around the target on the horizontal plane including the beam axis. The distance between the target and stopper was 12.5 cm.

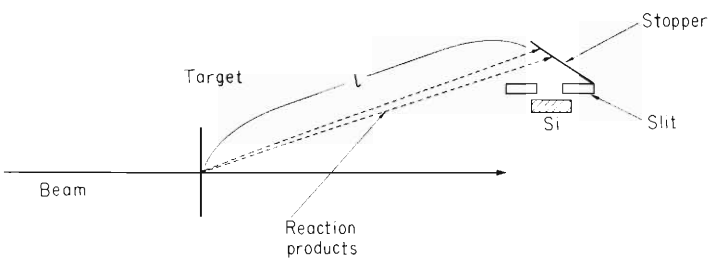

Fig. 1. Experimental set-up.

The measured angular distributions for various reaction products at 80 MeV are shown in Fig. 2. The following points are to be noted:

(1) The angular distributions of ^{217}Ac (and also its decay product ^{213}Fr) and ^{218}Ac, which were produced in the (^{12}C, 4n) and (^{12}C, 3n) reactions, respectively, increase monotonously as the angle decreases. A possible maximum must lie near 0°

(2) The angular distribution of ^{215}Fr, which was produced in the (^{12}C,α2n) reaction, shows a broad maximum at about 15°, being completely different from those of ^{217}Ac and ^{218}Ac.

(3) The angular distribution of ^{214}Fr has also a peak at 15°, but shows a rapid increase in the neighborhood of 0°. If we subtract the yield of ^{218}Ac from that of ^{214}Fr, the resultant can be considered to represent the yield of $^{209}Bi(^{12}C,\alpha 3n)^{214}Fr$ reaction. As seen in Fig. 2 this angular distribution is very similar to that of ^{215}Fr.

Recoil velocities of ^{217}Ac and ^{215}Fr were measured by the time-of-flight method (See Fig. 1)

and were determined to be V=(1.866±0.032)×10^{8}cm / sec (E_r = 3.91 MeV) for ^{217}Ac and V = (1.706 ± 0.026) × 10^{8}cm / sec (E_r = 3.25 MeV) for ^{215}Fr. The recoil energy experimentally determined for ^{217}Ac agrees very well with the value E_r (cal) = 4.12 MeV calculated on the assumption of full momentum transfer, indicating that ^{217}Ac is produced in the compound reaction. It is interesting to note that the experimental recoil energy for ^{215}Fr is far from the value E_r (cal) given above. This comes from the recoil effect of α-particle emission in the (^{12}C,α2n) reaction, which is considered to be either due to the α-particle evaporation from the compound nucleus or due to the Be^8 transfer from projectile to target.[1] A further measurement of recoil velocities is being planned to clarify this point.

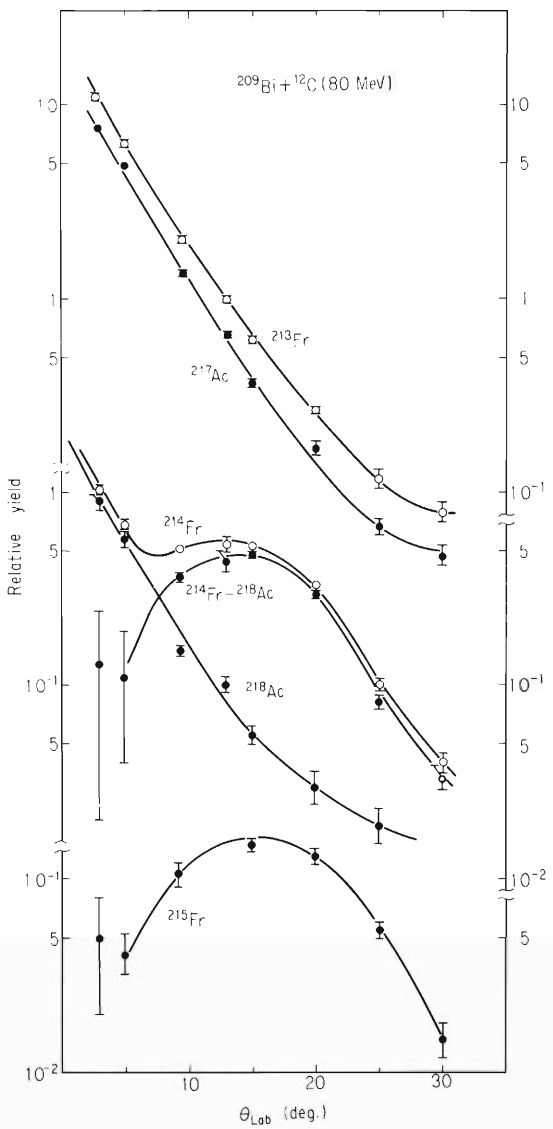

Fig. 2. Angular distributions of ^{209}Bi + ^{12}C reaction products.

Reference

1) R. Bimbot, D. Gardes, and M. F. Rivet : Nucl. Phys., A189, 193 (1972).

4-6. Limit of the Cross Section for the Compound Reaction between Complex Nuclei

T. Nomura

In heavy-ion induced reactions the ratio of the cross section for the compound reaction, σ_{cf}, to the total reaction cross section, σ_R, decreases as the incident energy increases. This is usually interpreted as the effect of the increasing maximum angular momentum brought into a compound nucleus. Let us define a critical angular momentum, J_{cr}, of a nucleus at a given excitation energy as the maximum spin that the nucleus can possess. Then partial waves whose angular momenta exceed J_{cr} of a compound nucleus do not contribute to the formation of the compound nucleus. Based on this idea the value of J_{cr} has been experimentally deduced to be around 40 – 50 $\hbar$ at E≈100 MeV in the case of rare earth nuclei. Theoretically the critical angular momentum has been calculated from the concept of yeast levels or from the stability of a nucleus against fissions.[1)]

Recently, experiments have been done about the measurement of the compound reaction cross section under the condition that the same compound nucleus was made at the same excitation energy using different projectiles.[2),3)] If we deduce the critical angular momentum from the relation

$$\sigma_{cf}/\sigma_R = (J_{cr} + 1)^2 / (J_{max} + 1)^2$$

obtained in the sharp cut-off model, the value of J_{cr} should be nearly the same, being independent of entrance channels. The above experiments have shown, however, quite different values of J_{cr} for different combinations of projectile and target. This cannot be explained solely by the concept of the critical angular momentum and suggests that the compound reaction cross section depends on the dynamical process of fusion between two interacting nuclei. Then a question arises: what kind of physical quantity determines the limit of σ_{cf} ?

We have found a systematics which indicates that the relative velocity of the colliding nuclei seems to play an important role for this problem. Fig. 1 shows experimental values of σ_{cf}/σ_R plotted vs. a kinetic energy per nucleon in the vicinity of the collision. It is clear that there is a strong correlation between these values. This correlation suggests that the limit of σ_{cf} is determined not only by the critical angular momentum but also by the relative velocity of the system. The latter may have connection with the nuclear viscosity.

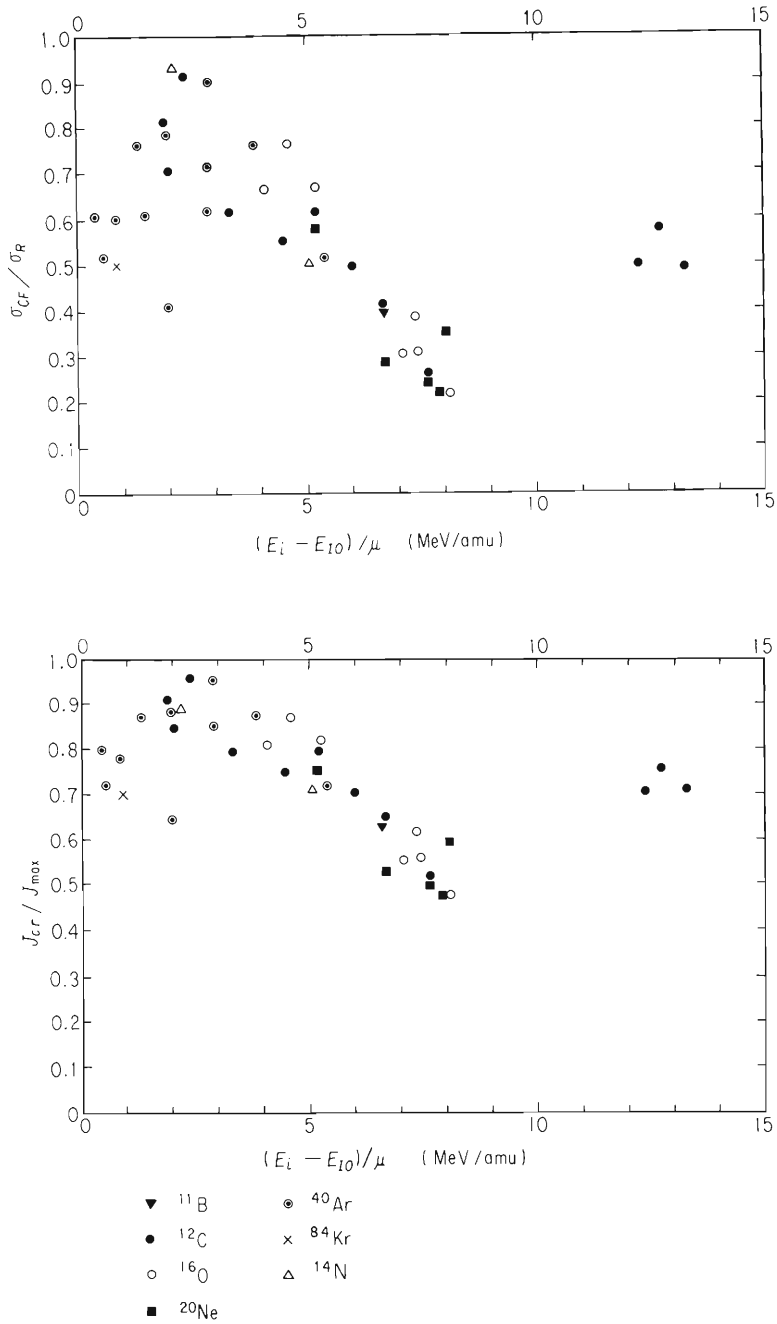

Fig. 1. Upper : Experimental values of the ratio of the compound reaction cross section to the total reaction cross section plotted vs. the relative kinetic energy per nucleon in the vicinity of the collision, where E_i is the incident kinetic energy in the c.m. system, E_{I0} the interaction barrier for S-wave and μ the reduced mass. Lower : Ratio of J_{cr} to J_{max} plotted vs. the same quantity mentioned above. J_{max} is the maximum angular momentum brought into the compound nucleus. J_{cr} and J_{max} are calculated from the sharp cut-off model. Data are taken from the compilation in Ref. 3).

References

1) S. Cohen, F. Plasil, and W. J. Swiatecki : Proc. 3rd Conf. on Reactions between Complex Nuclei (Univ. Calif. Press, Berkeley 1963), p. 325 (1963).

2) A. M. Zebelman and J. M. Miller: Phys. Rev. Lett., 30, 27 (1973).

3) M. Lefort, Y. Le Beyec, and J. Peter : "On the Fusion Reactions between Complex Nuclei", IPNO-RC-73-04 (1973), presented at the XI Winter Meeting on Nuclear Physics, Villars, Jan. (1973).

4-7. (^{3}He, d) Reactions on Cr Isotopes at an Energy of 29.3 MeV

N. Nakanishi, S. Takeda,* H. Ohnuma, S. Yamada, H. Sakaguchi,
M. Nakamura, S. Takeuchi,** and K. Koyama

Angular distributions of differential cross section were measured on the reactions ^{50,52,54}Cr(^{3}He, d)^{51,53,55}Mn at an incident energy of 29.29 MeV. Figs. 1 ~ 3 show deuteron spectra for these reactions. Remarkable features may be seen in these spectra ; many unbound analogue states, continuous spectrum in the highly excited region and a few strongly excited levels (ℓ_p= 1). Some angular distributions of ^{54}Cr(^{3}He, d)^{55}Mn are shown in Fig. 4, as an example. The upper portion is on an Ex = 0.127 MeV $J^\pi = 7/2^-$ level of ^{55}Mn nucleus and the middle and lower portions are on an Ex = 1.527 MeV $J^\pi = 3/2^-$ level and Ex = 12.3 MeV level (IAS of ^{55}Cr), respectively. These experimental curves indicate typical patterns corresponding to ℓ_p = 3, ℓ_p = 1, and unbound IAS, respectively. In the figure, solid and broken lines are preliminary predictions of DWBA calculation (DWUCK) using the deeper and shallower real parts of optical potential of ^{3}He particle, respectively. These optical model parameters which are indicated in the figure are obtained by an automatic search procedure (SEARCH) to give the best fit to the experimental result of ^{52}Cr(^{3}He, ^{3}He)^{52}Cr at the same

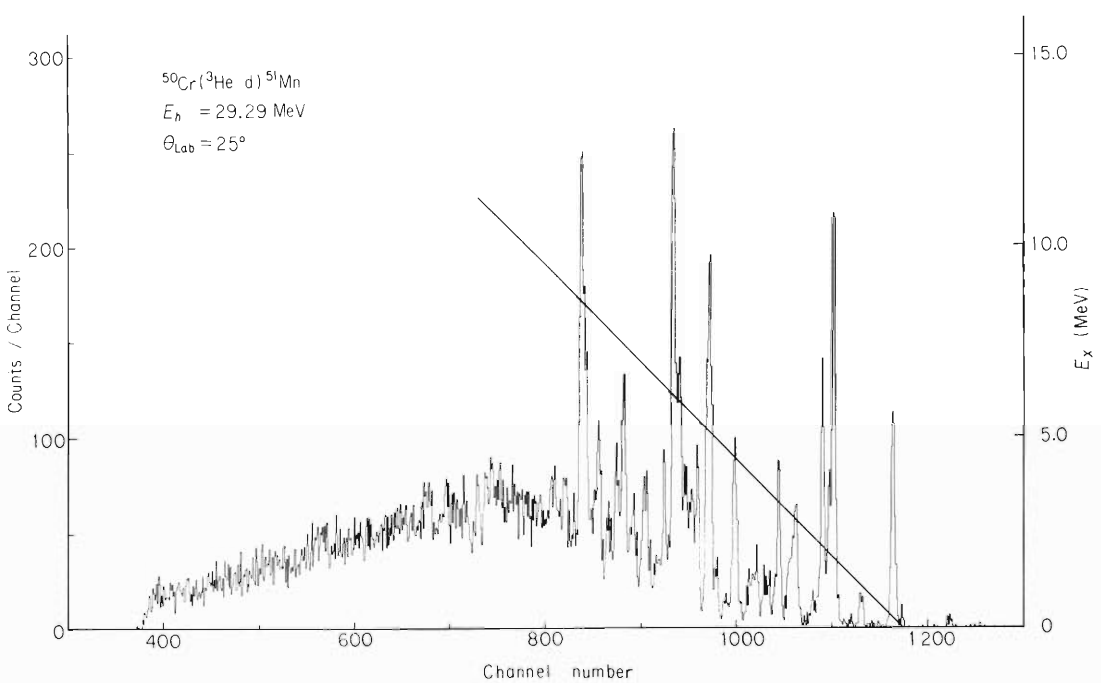

Fig. 1. Energy spectrum of deuteron of ^{50}Cr(^{3}He, d)^{51}Mn reaction.

* Present address, National Laboratory for High Energy Physics .
** Kyoto University.

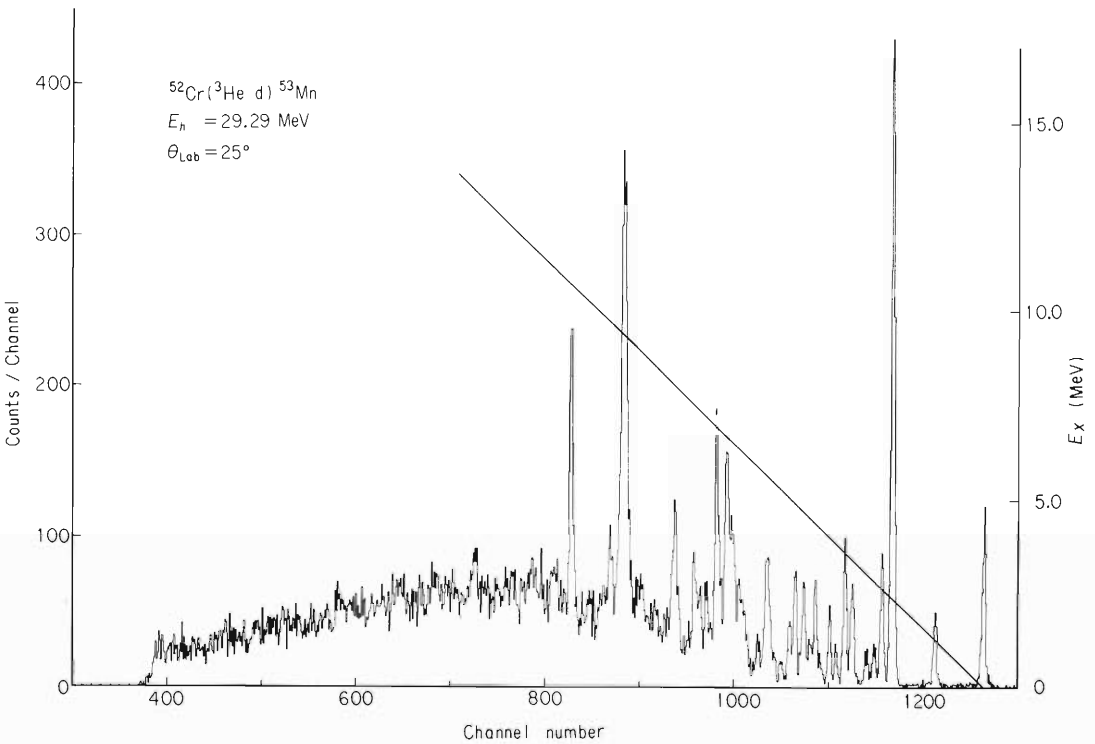

Fig. 2. Energy spectrum of deuteron of ^{52}Cr (^{3}He, d) ^{53}Mn reaction.

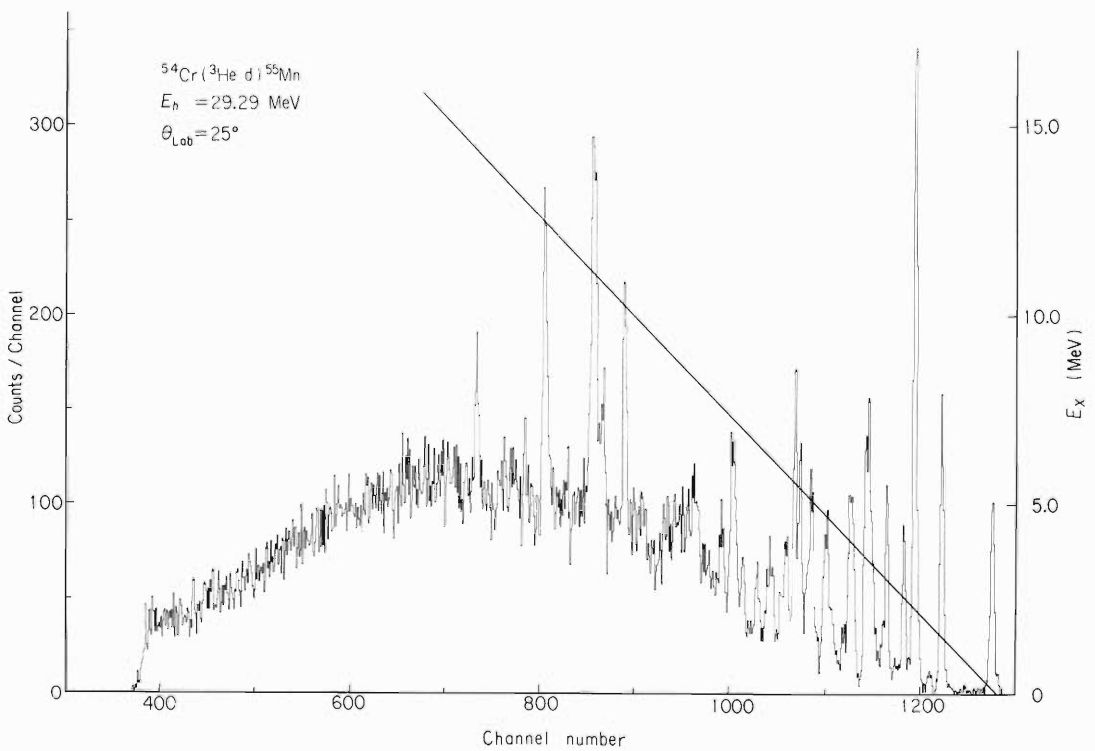

Fig. 3. Energy spectrum of deuteron of ^{54}Cr (^{3}He, d) ^{55}Mn reaction.

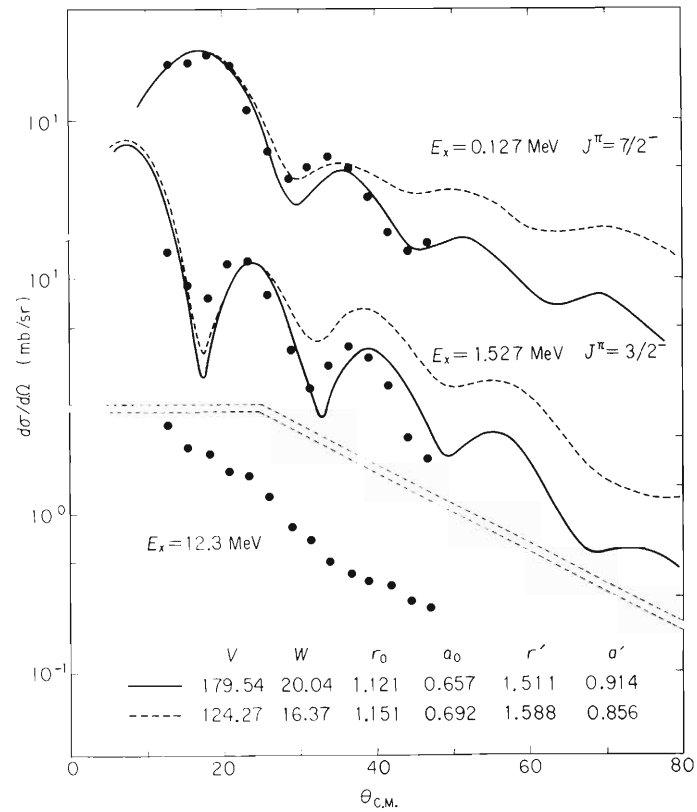

Fig. 4. Typical angular distribution of ^{54}Cr (^{3}He, d)^{55}Mn reaction. Dots are experimental points and lines are DWBA curves.

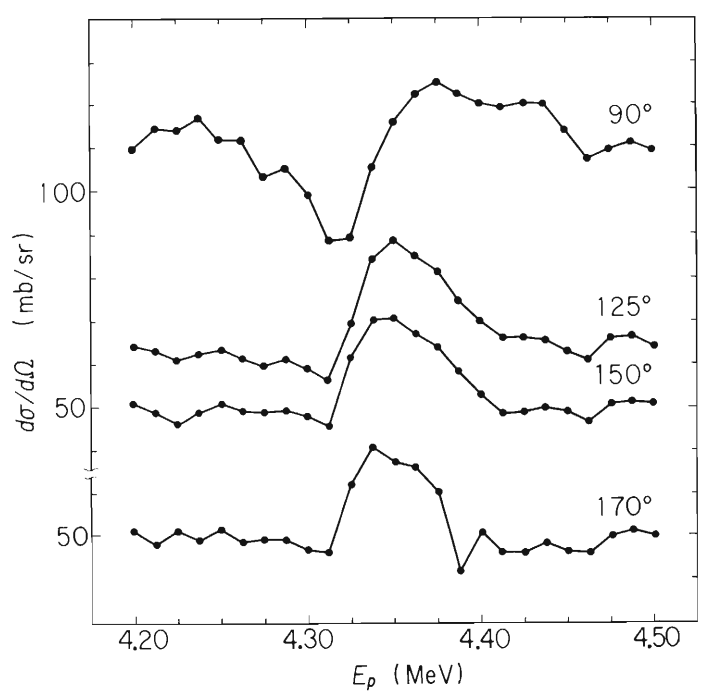

Fig. 5. Excitation curves of ^{54}Cr (p, p)^{54}Cr scattering.

energy. It may be seen from the agreement between them that the deeper potential family is more suitable than the shallower one. As for the type of the imaginary part of the optical potential, the difference is not recognized between the volume and surface types.

Some of the unbound analogue states were established by proton elastic and inelastic scattering on Cr isotopes.[1] We also performed the same experiment with proton in a higher energy range using the 10 MV tandem Van de Graaff accelerator at the Kyoto University. An example of the resonance scattering of protons by ^{54}Cr is shown in Fig. 5. The resonance behavior corresponds to the Ex = 12.4 MeV unbound isobaric analogue state.

Reference

1) J. D. Moses, H. W. Newson, and E. G. Bilpuch : Nucl. Phys., A175, 556 (1971).

4-8. The (^{3}He,^{3}He), (^{3}He,^{3}He′), and (^{3}He, α) Reactions on ^{13}C

T. Fujisawa, H. Kamitsubo, T. Wada,
M. Koike, Y. Tagishi, and T. Kanai

Differential cross sections of (^{3}He, ^{3}He), (^{3}He, ^{3}He′), and (^{3}He,α) reactions on ^{13}C have been measured at incident energies of 29.2, 34.7, and 39.6 MeV. The target used was a self-supporting foil with thickness of about 700 μg/cm^2 whose the purity of ^{13}C was 90 %. The reaction products were observed with a ΔE-E counter telescope consisting of two silicon surface barrier units. In Fig. 1 the typical energy spectra of ^{3}He and α-particle are shown. Analyses of them are being carried out.

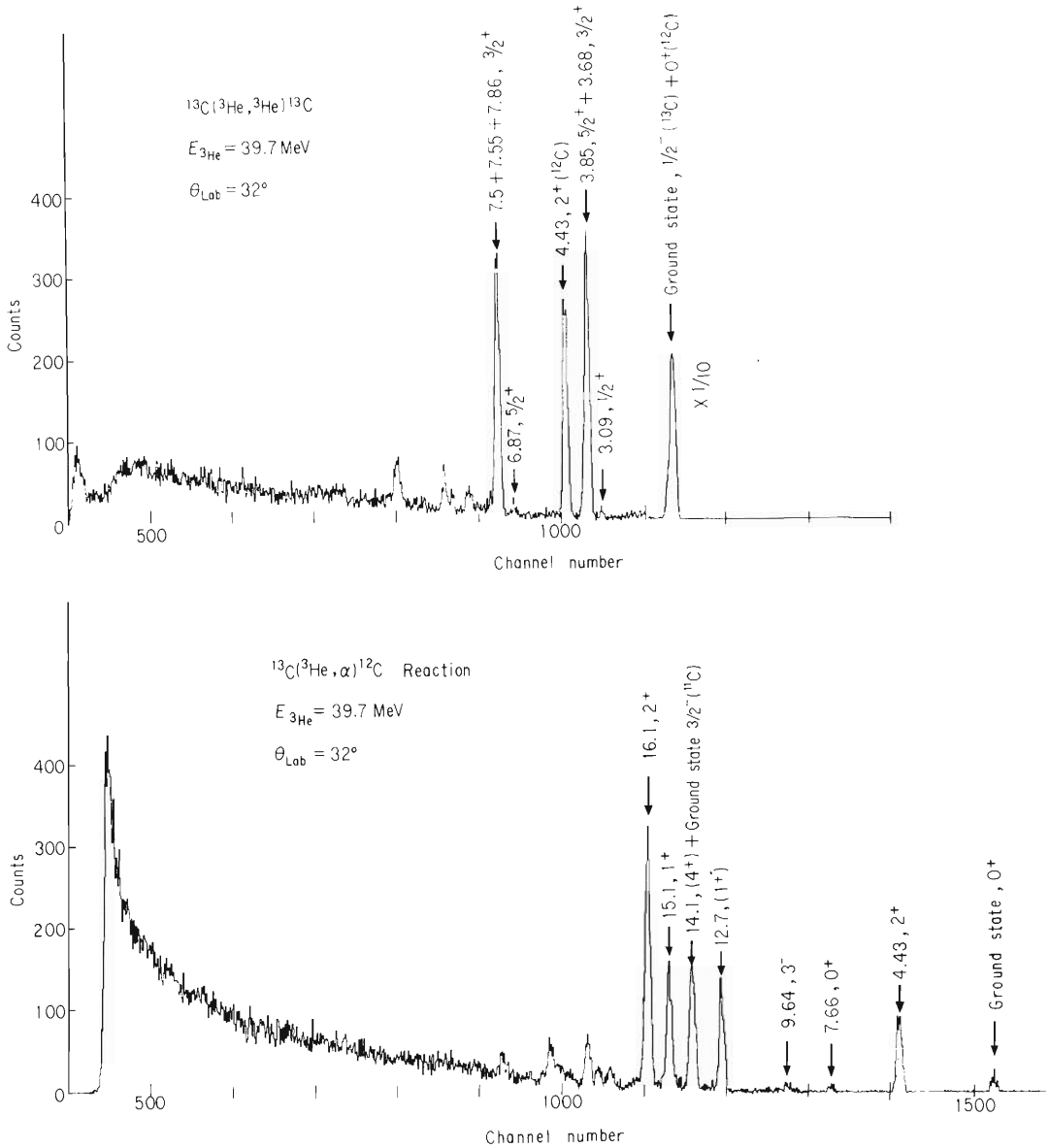

Fig. 1. Typical energy spectra of ^{3}He and α-particle in the ^{13}C(^{3}He, ^{3}He′) and ^{13}C(^{3}He, α)^{12}C reactions.

4-9. Two-Step Process in the $^{12}C(^3He,\alpha)^{11}C$ Reaction

S. Yamaji, T. Fujisawa, S. Motonaga, F. Yoshida,
H. Sakaguchi, and K. Masui

Previously the reaction $^{12}C(^3He,\alpha)^{11}C$ was studied at the bombarding energies of 24.0, 29.2, 34.7, and 39.6 MeV[1] and differential cross sections were analyzed in DWBA and CCBA. The large strength of shell-model-forbidden transition to the $5/2^-$ state can be explained by the two-step process. The reaction $^{12}C(^3He,\alpha)^{11}C$[2)~4)] was also extensively studied in other laboratories to examine the reaction mechanism. In lower energies (below 28 MeV)[2),3)] the shell-model-forbidden transitions are said to be mainly knock-on reactions, while at a higher energy (42 MeV)[4)] they are found to be two-step processes.

The coupled channel Born approximation (CCBA) calculations were carried out by

Table 1. Optical parameter.

	Incident Energy	V_0 (MeV)	r_R (fm)	a_R (fm)	W_0 (MeV)	r_D (fm)	a_D (fm)	r_C (fm)
$^{12}C+^3He$	24.0	142.3	1.1	0.718	13.43	1.314	0.823	1.4
	29.2	135.0	1.1	0.700	14.34	1.097	0.907	1.4
	34.7	129.3	1.1	0.751	14.72	1.205	0.834	1.4
	39.6	123.0	1.1	0.823	17.00	1.416	0.657	1.4
$^{11}C+\alpha$		200.0	1.3	0.7	12.5	1.3	0.7	1.3

$$V(r) = -\{V_0 f(X_R) - i4W_0 \frac{d}{dX_D} f(X_D)\} \qquad f(X_i) = [1+\exp(X_i)]^{-1}$$

$$X_i = (r - r_i Z^{1/3})/a_i$$

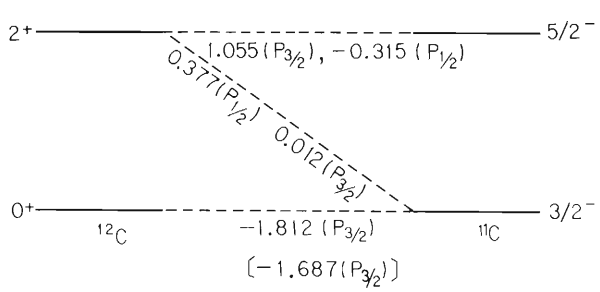

The number in Parentheses is the spectroscopic amplitude of Cohen and Kurath.

Fig. 1. Spectroscopic amplitude.

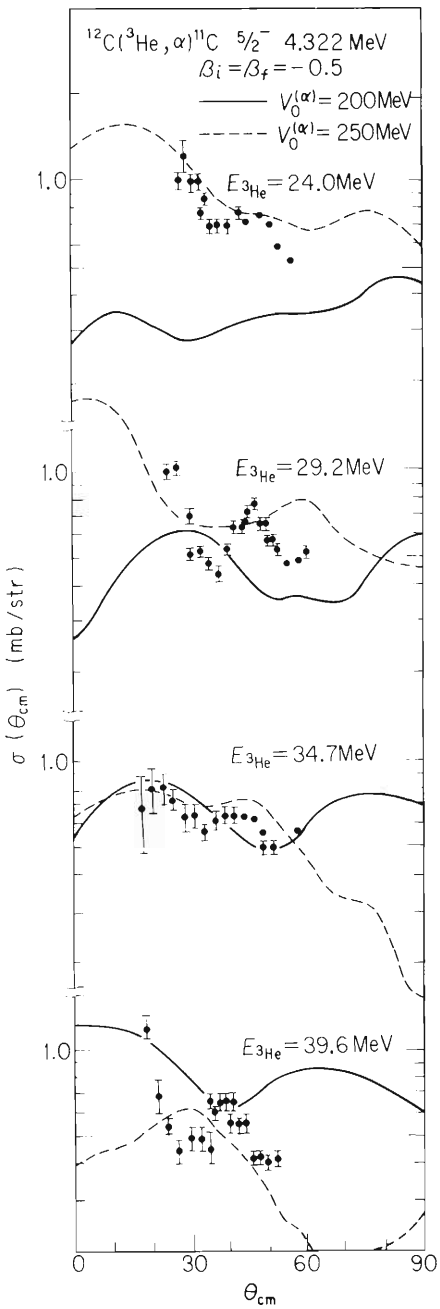

Fig. 2. The CCBA analysis of the reaction $^{12}C(^3He, \alpha)^{11}C$ ($5/2^-$, 4.322 MeV). The strength of the interaction V_{n^3He} is 100 MeV for the case of $V_0^{(\alpha)}$ = 200 MeV and 120 MeV for the case of $V_0^{(\alpha)}$ = 250 MeV, where $V_0^{(\alpha)}$ is the depth of the real optical potential of the α particle. The depth of the imaginary potential is reduced by 20% in the calculation of the two-step process.

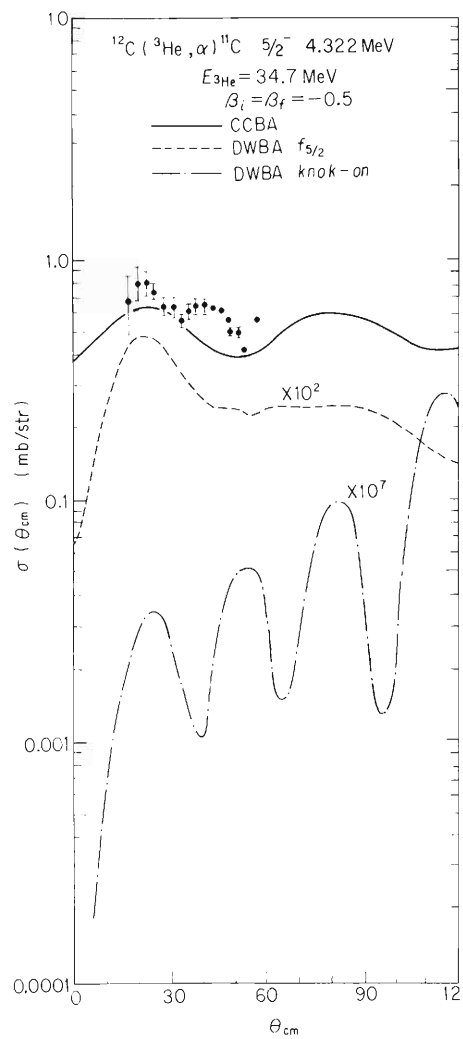

Fig. 3. Contributions of one-step pick-up process, knock-on process, and two-step process.

Ascuitto and Glendenning[5] and Tamura et al.[6] We made the CCBA code based on the JUPITOR-1* and checked it by comparing our results with those calculated by the code MARS.[7]

The optical parameters of ^{3}He on ^{12}C were searched[8] and are shown in Table 1. The experimental data of the elastic scattering of α on ^{12}C[9] were used to obtain the optical parameters of α on ^{11}C shown in Table 1. We used the spectroscopic amplitude in Fig. 1 which is obtained by Clegg's wave function.[4),10]

The calculated results are shown in Fig. 2. The interaction $V_{n^{3}He}$ is taken to be of a Gaussian type with the range of 2.52 fm. The strength is adjusted to give the right magnitude for the ground state transition at the bombarding energy of 34.7 MeV. The calculated cross sections can reproduce the order of magnitude fairly well. However, their angular distribution depends on the depth of the optical potential of α-particle.

We also examined the possibility of knock-on process in the case of 34.7 MeV. The spectroscopic amplitudes for the devision of ^{11}C into ^{8}Be and ^{3}He and that of ^{12}C into ^{8}Be and α are taken from the work of Honda et al.[11] The ground state of ^{12}C and the second excited state of ^{11}C are assumed to be $[44]^{11}S_0$ and $[43]^{22}D_{5/2}$ respectively. The finite-range DWBA calculation of the cross section of the knock-on process[12] was carried out by using the code INS-DWBA-4.** The interaction between ^{3}He and α was taken to be the same as the interaction $V_{n^{3}He}$. The cross section for the knock-on process was found to be very small as can be seen in Fig. 3. If the transition is considered to be caused by the pick-up of the orbit $f_{5/2}$ and the spectroscopic amplitude of Kurath's[13),14] calculation 0.022 is used, the magnitude of the calculated cross section is smaller than that of the experimental cross section by a factor of 100.

References

1) T. Fujisawa, H. Kamitsubo, S. Motonaga, K. Matsuda, F. Yoshida, H. Sakaguchi, and K. Masui : IPCR Cyclotron Progr. Rep., 4, 46 (1970).
2) T. J. Gray, H. T. Fortune, W. Trost, and N. R. Fletcher : Nucl. Phys., A144, 129 (1970).
3) H. Fuchs and H. Oeschler : ibid., A202, 363 (1973).
4) R. N. Singh, N. De. Takacsy, S. I. Hayakawa, R. L. Hutson, and J. J. Kraushaar : ibid., A205, 97 (1973).
5) R. J. Ascuitto and N. K. Glendnning : Phys. Rev., 181, 1376 (1969).
6) T. Tamura, D. R. Bes, R. A. Broglia, and S. Landowne : Phys. Rev. Lett., 25, 1507 (1970) ; ibid., 26, 156 (1971).
7) T. Tamura and T. Udagawa : Tech. Rep. Center Nucl. Stud., Univ. Texas, No. 30 (1972).

* T. Tamura : Computer Program Jupitor-1 for Coupled-Channel Calculation, ORNL-4152 (1967).

** H. Yoshida : Reference Manual for INS-DWBA-4, Inst. Nucl. Stud. Univ. of Tokyo (1972).

8) T. Fujisawa, S. Yamaji, K. Matsuda, S. Motonaga, F. Yoshida, H. Sakaguchi, and K. Masui : J. Phys. Soc. Japan, 34, 5 (1973).

9) T. Mikumo, H. Yamaguchi, I. Nonaka, M. Odera, Y. Hashimoto, M. Kondo, and T. Maki : J. Phys. Soc. Japan, 15, 1158 (1960); T. Mikumo : ibid., 16, 1066 (1961).

10) A. B. Clegg : Nucl. Phys., 38, 353 (1962)

11) T. Honda, H. Horie, Y. Kudo, and H. Ui : ibid., 62, 561 (1965).

12) S. Yamaji and S. Yoshida : Progr. Theor. Phys., 44, 125 (1970).

13) D. Kurath: in Proc. 1967 Summer Inst. in Physics, (ed. B. Margolis and C. S. Lam) Benjamin (1968).

14) S. Cohen and D. Kurath : Nucl. Phys., A101, 1 (1967).

4-10. Sum Rule Approach for Isovector Nuclear Vibrations

T. Suzuki

The purpose of the present article is to show that the restoring force parameter and mass parameter for isovector nuclear vibration are obtained by making use of the generalized sum rules.

The relation between the isovector density and the average nuclear field is given by the nuclear symmetry potential, which is usually expressed in the form:

$$V_{sym}=\frac{1}{4}V_1\frac{N-Z}{A}\tau_3=\frac{1}{4}V_1\frac{\rho_n-\rho_p}{\rho_0}\tau_3,\ (V_1\approx 100\mathrm{MeV}), \tag{1}$$

where $\tau_3 = +1$ for neutron and $\tau_3 = -1$ for proton. The variation of the isovector density ($\rho_n - \rho_p$ in isovector λ -pole vibration is uniquely determined from the sum rule for isovector density operator and the classical energy weighted sum rule. If we use the Gaussian matter distribution, it is expressed by

$$\delta(\rho n-\rho p)=\frac{4}{V_1}X_\lambda\sum_\mu\beta_{\lambda\mu}r^\lambda Y_{\lambda\mu}(\hat{r})\rho_0(r),\quad(\lambda\geq 1). \tag{2}$$

$$\beta_{\lambda\mu}=\sum_{i=1}^{A}r_i^\lambda Y_{\lambda\mu}(\hat{r}),\quad X_\lambda=\frac{5V_1}{8R^2}\frac{8\pi}{(2\lambda+1)A<r^{2\lambda-2}>}.$$

utilizing Eqns. (1) and (2), the variation of the isovector average nuclear field under the λ -pole vibration is obtained as

$$\delta V(r)=X_\lambda\sum_\mu\beta_{\lambda\mu}r^\lambda Y_{\lambda\mu}(\hat{r})\tau_3. \tag{3}$$

Hence, the total nuclear potential for isovector λ -pole oscillation can be written in the form:

$$V=\sum_{i=1}^{A}\frac{m\omega_0^2}{2}r_i^2+\frac{1}{2}X_\lambda\sum_\mu\sum_{i,j}(r_i^\lambda Y^*_{\lambda\mu}(\hat{r}_i)\ \tau_3^i)(r_j^\lambda Y_{\lambda\mu}(\hat{r}_j)\tau_3^j), \tag{4}$$

where harmonic oscillator potential is taken as the average nuclear field independent of isospin variable. Denoting the mass parameter and eigenfrequency for λ -pole vibration by B_λ and ω_λ, respectively, the above equation may be described as

$$\frac{B_\lambda\omega_\lambda^2}{2}\sum_\mu\beta^*_{\lambda\mu}\beta_{\lambda\mu}=\left\{\frac{B_\lambda(n\omega_0)^2}{2}+\frac{X_\lambda}{2}\right\}\sum_\mu\beta^*_{\lambda\mu}\beta_{\lambda\mu}, \tag{5}$$

yielding

$$\omega_\lambda=(n\omega_0)\left\{1+\frac{X_\lambda}{(n\omega_0)^2B_\lambda}\right\}^{1/2}, \tag{6}$$

in which $n\omega_0$ is the eigenfrequency of the λ -pole states in the harmonic oscillator potential.

On the other hand, the mass parameter B_λ is determined by the relation between the zero-point energy and the classical energy weighted sum rule value, and has a value of

$$B_\lambda = \frac{4\pi m}{A\lambda\ (2\lambda+1)<r^{2\lambda-2}>}. \tag{7}$$

Employing Eqns.(6) and (7), one can find the eigenfrequency of the isovector λ -pole vibration in the form:

$$\omega_\lambda = (n\omega_0)\left\{1+\frac{V_1}{(n\omega_0)^2}\frac{5\lambda}{4mR^2}\right\}^{1/2}, \quad (\lambda>0). \tag{8}$$

When we take into account the exchange effect in the nuclear interaction, the nucleon mass m in Eqn.(8) reads as $m^* \approx m/1.4$.

Examples:

(1) Dipole resonance ($\lambda = 1$, $n = 1$)

$$\text{Theor.}\quad \omega_1 = \begin{cases} 1.77\omega_0 \approx 72.6/A^{1/3}(\text{MeV}) & \text{for m,} \\ 2.00\omega_0 \approx 82\ /A^{1/3}(\text{MeV}) & \text{for m*,} \end{cases}$$

$$\text{Exp.}\quad \omega_1 \approx 80/A^{1/3}(\text{MeV}).$$

($\omega_1 = 1.77\ \omega_0$ has been also obtained by Bohr and Mottelsson in the other approach.[1])

(2) Quadrupole resonance ($\lambda = 2$, $n = 2$)

$$\text{Theor.}\quad \omega_2 = \begin{cases} 2.88\omega_0 \approx 118/A^{1/3}(\text{MeV}) & \text{for m,} \\ 3.16\omega_0 \approx 130/A^{1/3}(\text{MeV}) & \text{for m*,} \end{cases}$$

$$\text{Exp.}\quad \omega_2 \approx 130/A^{1/3}(\text{MeV}).$$

In the same way, as for the $\lambda(>0)$-pole vibration, the eigenfrequency of the isovector monopole oscillation is predicted to be

$$\omega = 2\omega_0\left(1+V_1\cdot\frac{5}{8m\omega_0^2R^2}\right)^{1/2} = \omega_2,$$

which is different from the one obtained in the other approach.[2]

References

1) A. Bohr and B. R. Mottelson : in Proc. of neutron capture gamma-ray spectroscopy, Studsvik, IAEA, Vienna, P. 3 (1969).

2) T. Suzuki : Nucl. Phys. (1973), to be published.

4-11. Momentum Transfer Dependence of the Effective Charge for Electro-excitation

T. Suzuki

It is naturally expected that the effective charge for electro-excitation depends on the value of momentum transfer, since it mainly comes from the effect of the core polarization as shown schematically in Fig. 1. Fig. 1(a) represents a diagram for the bare single-particle transition, while Fig. 1(b) and (c) show the transition of the particle state coupling with the vibrational states (wavy line) of the core. The matrix elements corresponding to the last two diagrams, which are considered as the additional charge (effective charge) for the single particle transition (Fig. 1(a)), need not have the same momentum transfer dependence as the one for the first diagram.

The purpose of the present article is to study the effective charge and its momentum transfer dependence in electro-excitation in the framework of the particle-vibration coupling model. The excitation energy for the electric λ-pole vibrational state of the core is estimated in the self-consistent field theory and sum rule approach. It is shown that the momentum transfer(q) dependence of the isoscalar E_λ effective charge can be written in the form:

$$e_{\mathrm{eff}}^{(\lambda)}(q)=\frac{Z}{A}e\left(\sum_n \frac{\alpha_{n\lambda}}{n^2-\alpha_{n\lambda}}\right)\frac{(j_2\|r^\lambda Y_\lambda\|j_1)}{R^\lambda}\frac{j_\lambda(qR)}{(j_2\|j_\lambda(qr)Y_\lambda\|j_1)}, \tag{1}$$

for the single particle transition from $|j_1)$ to $|j_2)$. In the above expression, n comes from $n\omega_0$ which is the excitation energy of the λ-pole states, in the harmonic oscillator potential, carrying $\alpha_n \times 100$ % of the classical energy weighted sum rule value. In the limit of $(q \to E_x)$, Eqn.(1) leads to the effective charge for photo-reaction:

$$e_{\mathrm{eff}}^{(\lambda)}(q=Ex)=\frac{Z}{A}e\sum_n \frac{\alpha_{n\lambda}}{n^2-\alpha_{n\lambda}}. \tag{2}$$

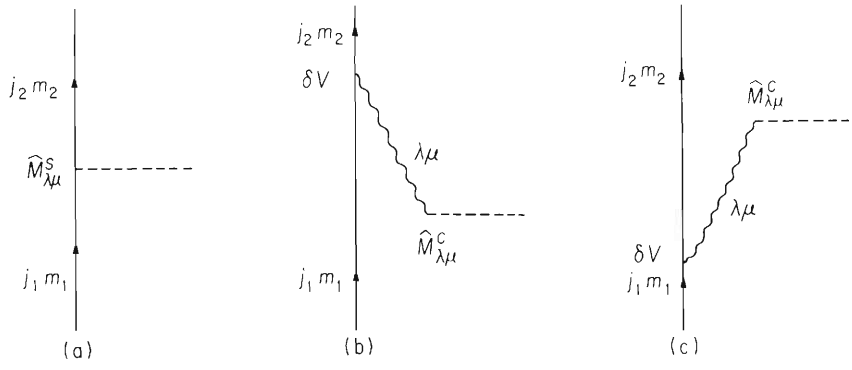

Fig. 1. The effect of core polarization. The first diagram represents the bare single particle transition, while the remaining diagrams show contributions of the core polarization to the effective charge up to the first order in perturbation theory.

For example, we obtain $e_{eff}^{(2)}(q=Ex) = eZ/A$ for $n = 2$, $\lambda = 2$, and $\alpha_2 = 1$, which is the well-known value of the effective charge for E2 transition.[1)]

In Fig. 2 is shown the momentum transfer dependence of the E2 effective charge given in Eqn.(1) for various transitions, where we choose the following nuclear radius and harmonic oscillator length parameters:

R = 3.36 (fm), b = 1.73 (fm) for (0p) and (0s, 0d) shells,

R = 4.65 (fm), b = 2.02 (fm) for (1p, 0f) shell.

It is predicted that in the (0f → 0f) transition the value of the effective charge for E2 transition decreases with increasing momentum transfer and changes drastically at about $q = 3.34/R(fm^{-1})$ [$(dj_2(x)/dx)_{3.34} \approx 0$]. The most recent experiments for ^{51}V[2)] are consistent with the present results.

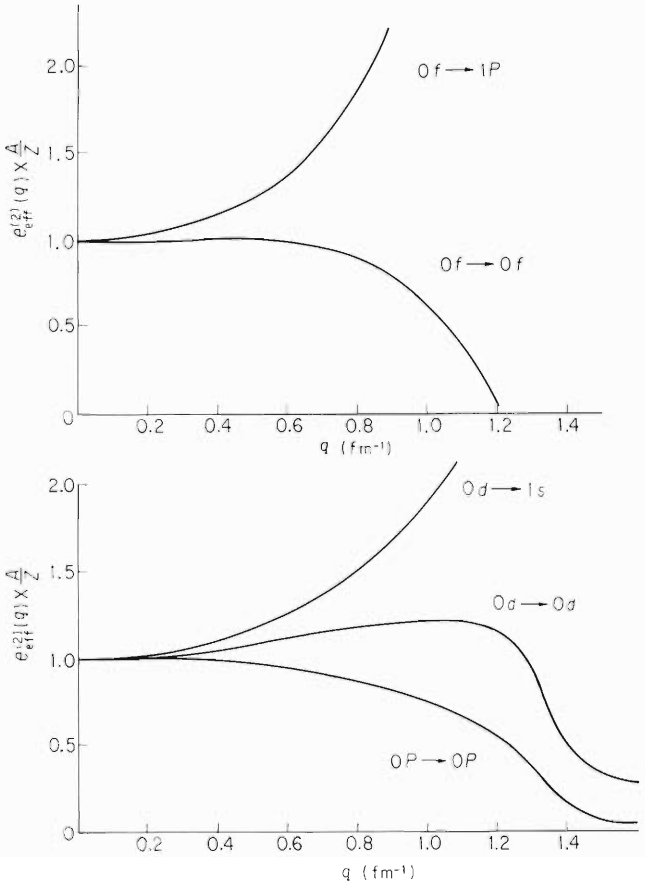

Fig. 2. The calculated values of the E2 effective charge versus momentum transfer.

References

1) A. Bohr and B. R. Mottelson : Nucl. Structure, Benjamin, New York, 1, 334 (1969).

2) G. A. Peterson, K. Hosoyama, M. Nagao, A. Nakada, and Y. Torizuka: Phys. Rev., C7, 1028 (1973).

4-12. Effects of Monopole Core Polarization

T. Suzuki

It is the purpose of this paper to study the effects of the isoscalar and isovector monopole core polarization. The Excitation energies for the monopole resonances of the core are estimated by making use of the sum rules.[1),2)] The less model dependent forms of the variation of the matter density under nuclear vibrations and the interaction Hamiltonian between a single particle and the core are also obtained by utilizing the sum rules.[1),2)]

(1) Isotope shift

When a neutron is added to the core, only the monopole mode of the core excitation affects the charge radius to the first order in the density change. Hence, the isotope shift is described as:

$$\delta\langle r_p^2\rangle = \langle r_p^2\rangle_{A+1} - \langle r_p^2\rangle_A$$
$$= -\frac{2}{Z}\frac{1}{\omega_s}(j|\delta V|(\omega_s j)j)((\omega_s j)j|\int \delta\rho_p^s r^2 d\vec{r}|j), \tag{1}$$

where $|(\omega_S j)j)$ represents the neutron state, $|j)$, coupling with the isoscalar monopole vibration of the core, $|\omega_S)$, with the eigen-frequency $\omega_S = \sqrt{2}\omega_0$.[3)] Interaction Hamiltonian, δV, in the harmonic oscillator shell model, and the variation of the charge density, $\delta\rho_p^S$, are written as:

$$\delta V(r) = -\frac{m\omega_0^2}{2}\frac{1}{A\langle r^2\rangle}\alpha_s(r^2 - \langle r^2\rangle), \quad (\alpha_s = \sum_{i=1}^{A} r_i^2 - A\langle r^2\rangle), \tag{2}$$

$$\delta\rho_p^s = -\frac{1}{2A\langle r^2\rangle}\alpha_S\frac{1}{r^2}\frac{d}{dr}\left\{r^3\rho_p(r)\right\}. \tag{3}$$

By inserting Eqns.(2) and (3) into Eqn.(1) and using the classical energy weighted sum rule value for α_S, one can find the isotope shift to be of the form:

$$\delta\langle r_p^2\rangle = \frac{1}{A}\left\{\langle j|r^2|j\rangle - \langle r^2\rangle\right\}$$
$$\approx \frac{1}{A}\frac{1}{3}\langle r^2\rangle \tag{4}$$

which is about one half of the standard unit.[4)] The effect of the isovector monopole core polarization is about 20 ~ 50 % of the one from the isoscalar mode.

(2) Isospin impurity

Since isospin impurity of the nuclear ground state is caused by the mixing of the isovector monopole state through the Coulomb interaction, it can be obtained by calculation:

$$P(T=1) = \frac{1}{\omega_V^2}\left|(\omega_V|\int \delta\rho_p^V Vc\, d\vec{r}|)\right|^2, \tag{5}$$

where $W_V = 2.88\ \omega_0$[2] is the eigenfrequency of the isovector monopole vibration of the core and $\delta\rho_p^V$ is given by[2]

$$\delta\rho_p^V = -\frac{25}{6AR^4}\alpha_V \rho_p(r)(r^2 - \langle r^2\rangle),\ (\alpha_V = \sum_{i=1}^{A}(r_i^2 - \langle r^2\rangle)\tau_3^i). \tag{6}$$

As the Coulomb matrix element can be estimated as follows:

$$(\omega_V|\int \delta\rho_p^V V_C\, d\vec{r}\,|) = \frac{Ze^2}{4R^3}(\omega_V|\alpha_V|), \tag{7}$$

we obtain the T = 1 impurity, by employing the classical energy weighted sum rule value,

$$P(T=1) = \frac{1}{\omega_V{}^3}\frac{3A(Ze^2)^2}{40mR^4} \approx 3.00\times 10^{-6} Z^{8/3}, \tag{8}$$
$$(R = 1.2A^{1/3}(\mathrm{fm})).$$

It is interesting to notice that in the two-fluid hydrodynamic model the T = 1 impurity are predicted[4] to be

$$P(T=1) = 5.55\times 10^{-7} Z^{8/3}. \tag{9}$$

The lowest level in the hydrodynamic model has the eigenfrequency of 4.12 ω_0 MeV and carries only 49 % of the classical energy weighted sum rule value.

(3) Coulomb energy correction

Isospin impurity of the core produces the symmetry potential which acts differently on protons and neutrons. Therefore, it gives rise to a correction to the Coulomb energy difference between the analog states. In the particle-vibration coupling model, Coulomb energy correction for the system of the core plus one particle is expressed by

$$\Delta E = \left(-\frac{4}{\omega_V}\right)(j|\delta V|((\omega_V j)j))|((\omega_V j)j|\int \delta\rho_p^V V_C\, d\vec{r}\,|j), \tag{10}$$

where $|(\omega_V j)j)$ stands for the last particle coupling with the isovector monopole vibration of the core. The Coulomb matrix element and ω_V are given in Section (2), while the coupling term δV, can be obtained, by using the sum rules,[2]

$$\delta V(r) = \frac{25}{24}\frac{V_1}{AR^4}\alpha_V(r^2 - \langle r^2\rangle)\tau_3,\ (V_1 = 100\ \mathrm{MeV}). \tag{11}$$

Then, by calculating Eqn.(10), one can find

$$\Delta E = \frac{5}{4}\frac{1}{\omega_V^2}\frac{V_1}{m}\frac{Ze^2}{R^5}\{(j|r^2|j) - \langle r^2\rangle\}. \tag{12}$$

The ratio of ΔE to the so-called direct term of the Coulomb energy difference is roughly given as

$$\frac{\Delta E}{(j|V_C|j)} \approx 6 \sim 9\,\% \tag{13}$$

which is large enough to explain the Nolen-Schiffer effect.[5]

References

1) T. Suzuki and C. Hinohara : IPCR Cyclotron Rep., No. 29 (1973).
2) T. Suzuki : ibid., No. 32 (1973).
3) T. Suzuki : Nucl. Phys., (1973), to be published.
4) A. Bohr and B. R. Mottelson : Nuclear Structure, Benjamin, New York, 1 (1969).
5) J. A. Nolen and J. P. Schiffer : Ann. Rev. Nucl. Sci., 19, 471 (1969).

4-13. The Splitting of the Isospin and Spin-Isospin Dipole Resonances in ^{12}C

T. Suzuki and C. Hinohara*

Two electric dipole modes are known in nuclear motion. One of them is the isospin dipole ($\tau-$) mode that is an oscillation of all protons against all neutrons in the nucleus. The other is the spin-isospin dipole ($\sigma\tau-$) mode that is an oscillation of the spin-up protons and spin-down neutrons against the spin-down protons and spin-up neutrons.

In ^{12}C the double splitting of the isospin dipole resonance is well known in the photo-reaction, the first main peak near the excitation energy of 23 MeV being higher than the second peak near 26 MeV. Recent measurements of the cross section for electro-excitation of ^{12}C[1] have shown that the spin-isospin dipole resonance is also split into two peaks in the same way as the isospin dipole resonance.

As discussed by many authors,[2] in the axially symmetric deformed even nuclei the isospin dipole states are separated into two groups according to their excitation energy; one consisting of the $K^\pi = 1^-$ states with excitation energy $\omega_\perp$, and the other of the $K^\pi = 0^-$ states with ω_Z. The total strength for excitation of the isospin mode states at $\omega_\perp$ is twice that for the isospin-mode states at ω_Z. Employing the SU(2) symmetry in the axially symmetric deformed potential,

Table 1. Electric dipole states in the axially symmetric deformed potential.

Excitation energy	τ-mode		$\sigma\tau$-mode	
	K-Band	Strength	K-Band	Strength
$\omega_\perp$	$K=1^-$	$2S_\tau$	$K=1^-$ $K=0^-$	$2S_{\sigma\tau}$
ω_Z	$K=0^-$	S_τ	$K=1^-$	$S_{\sigma\tau}$

$$S_\tau = \frac{NZ}{A}, \quad S_{\sigma\tau} \approx \frac{A}{4}\{1+\frac{1}{3A}\sum_{i=1}^{A}(0|\vec{\ell}_i\vec{\sigma}_i|0)\}$$

it is shown that the spin-isospin dipole states are also classified into two groups in such nuclei. One is composed of the $K^\pi = 1^-$ and $K^\pi = 0^-$ spin-isospin mode states with $\omega_\perp$, while the other of the $K^\pi = 1^-$ states with ω_Z. The total strength of the spin-isospin dipole oscillations with $\omega_\perp$ is twice that of the one with ω_Z according to the degree of freedom of the oscillation (Table 1).

* Tohoku University.

We have performed a detailed calculation of the excitation energies of the electric dipole states of ^{12}C and the cross section for their photo- and electro-excitation based on the oblately deformed nuclear shell model. The wave function of the dipole state is constructed in the adiabatic approximation, where the intrinsic wave function is composed of lp (N=2)–lh(N=1) states in the Nilsson potential (η=–4, κ=0.05). The particle-hole pair scattering is assumed to be caused by the usual phenomenological effective interaction. The characteristic features of the cross section for photo- and electro- excitation are well reproduced by the present theory[3] which could not be explained by previous studies.[4]

References

1) G. Ricco, H.S. Caplan, R.M. Hutcheon, and R. Malvano : Nucl. Phys., A114, 685 (1968); A. Yamaguchi, T. Terasawa, K. Nakahara, and Y. Torizuka : Phys. Rev., C3, 1750 (1971).
2) M. Danos : Bull. Am. Phys. Soc., 1, 136, 246 (1956); K. Okamoto : Progr. Theor. Phys., 15, 75 (1956); B. R. Mottelson and S. G. Nilsson : Nucl. Phys., 13, 281 (1959).
3) T. Suzuki and C. Hinohara: ibid., A204, 289 (1973).
4) N. Vihn Mau and G. E. Brown: ibid., 29, 89 (1962); F. H. Lewis, Jr. and J. D. Walecka : Phys. Rev., 133, B849 (1964); M. Kamimura, K. Ikeda, and A. Arima : Nucl. Phys., A95, 129 (1967); F. J. Kelly and H. Uberall : Phys. Rev., 175, 1235 (1968).

4-14. New Giant Resonances

T. Suzuki

Recent studies of the nuclear continuum region have demonstrated the existence of the giant resonances due to the new modes other than electric isospin dipole one.[1),2)] Especially, the new giant resonance at Ex $\approx 60/A^{1/3}$ MeV has been systematically observed in (e,e′), (p,p′), (τ,τ') and (α,α') experiments[2)] and it is suggested to be due to isoscalar monopole and/or quadrupole oscillations. A broad resonance at Ex $\approx 130/A^{1/3}$ MeV is also observed in (e,e′) experiments and is interpreted to be isovector monopole and/or quadrupole resonances. It is the purpose of this paper to investigate the eigenfrequencies of these collective monopole and quadrupole states, whose excitation strengths exhaust the classical energy weighted sum rule values. The nuclear potential for these oscillations is obtained from the harmonic oscillator shell model, taking into account the condition as proposed by Bohr and Mottelson.[3)] On the other hand, the mass parameters can be determined by the classical energy weighted sum rule values. The obtained restoring force parameters and mass parameters are listed in Table 1 for each dynamic variable of the vibration. In Fig. 1, the present results are compared with the experimental values of the excitation energy for giant multipole resonances. For reference, in Fig. 1 are also shown the experimental and calculated values for giant dipole resonance.[3)]

Table 1 The calculated mass and restoring force parameters of the giant resonance state.

	Mode of resonance	Dynamic variable	Mass parameter	Restoring force parameter	Eigen-frequency
Isoscalar	Monopole	$\alpha_0^S = \sum_{i=1}^{A} (r_i^2 - \langle r^2 \rangle)$	$\frac{m}{4A\langle r^2\rangle}$	$\frac{m\omega_0^2}{2A\langle r^2\rangle}$	$\sqrt{2}\omega_0$
Isoscalar	Quadrupole	$\alpha_{2\mu}^S = \sum_{i=1}^{A} r_i^2 Y_{2\mu}(\hat{r}_i)$	$\frac{2\pi m}{5A\langle r^2\rangle}$	$\frac{4\pi m\omega_0^2}{5A\langle r^2\rangle}$	$\sqrt{2}\omega_0$
Isovector	Monopole	$\alpha_0^V = \sum_{i=1}^{A} (r_i^2 - \langle r^2 \rangle)\tau_3^i$	$\frac{m}{4A\langle r^2\rangle}$	$\frac{m}{4A\langle r^2\rangle}\left(4\omega_0^2 + \frac{35V_1}{4mR^2}\right)$	$\sim\sqrt{19}\omega_0$
Isovector	Quadrupole	$\alpha_{2\mu}^V = \sum_{i=1}^{A} r_i^2 Y_{2\mu}(\hat{r}_i)\tau_3^i$	$\frac{2\pi m}{5A\langle r^2\rangle}$	$\frac{2\pi m}{5A\langle r^2\rangle}\left(4\omega_0^2 + \frac{7V_1}{2mR^2}\right)$	$\sim\sqrt{10}\omega_0$

$\omega_0 = 41.1/A^{1/3}$ (MeV), $R = 1.2A^{1/3}$ (fm), $V_1 = 100$ (MeV)

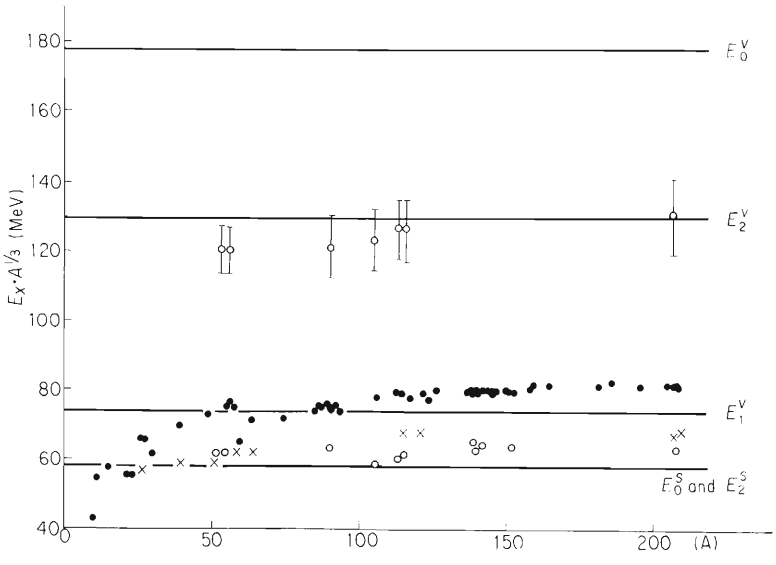

Fig. 1. Systematics of the excitation energies for giant multipole resonances. The experimental data are taken from Ref. 2) The black circles are for E1. The crosses and open circles are for E2 or E0, in which the former was obtained from (p, p′) reactions and the latter from electron scattering. The straight lines represent the calculated values of the excitation energies.

The systematics of the excitation energies for the observed new giant resonances are well explained by the simple model.

References

1) T. Suzuki : Nucl. Phys., A204, 289 (1973).
2) L. W. Fagg : Proc. Intern. Conf. Photonuclear Reactions and Applications, Asilomar, (1973);
Y. Torizuka : idem;
M. B. Lewis : idem.
3) A. Bohr and B. R. Mottelson : Proc. Neutron Capture Gamma-ray Spectroscopy, Studsvik, IAEA, Vienna (1969).

4-15. Sum Rules and Nonexchange Force*

T. Suzuki and C. Hinohara**

The purpose of this short note is to show that the form of the nonexchange residual interaction in the harmonic oscillator shell model is determined by utilizing the sum rules for multipole operators and nuclear transition density.

The well-known classical energy weighted sum rule[1] can be written in the natural unit:

$$\sum_{n}\omega_n<|\beta^{*}_{\lambda 0}|\omega_n><\omega_n|\beta_{\lambda 0}|>=\frac{A}{8\pi m}\lambda(2\lambda+1)<r^{2\lambda-2}>,\ (\lambda\geq 1), \tag{1}$$

where ω_n represents the eigenfrequency of the nuclear state, $|\omega_n>$, and

$$\beta_{\lambda\mu}=\sum_{i=1}^{A} r_i^{\lambda} Y_{\lambda\mu}(\hat{r}).$$

On the other hand, the sum rule for nuclear density is expressed in the form[2]:

$$\sum_{n}\omega_n<|\hat{\rho}(\vec{r})|\omega_n><\omega_n|\beta_{\lambda 0}|>=-\frac{1}{2m}\lambda r^{\lambda-1}Y_{\lambda 0}(\hat{r})\frac{d\rho_0(r)}{dr},\ (\lambda\geq 1), \tag{2}$$

denoting the isoscalar density operator and the nuclear matter distribution in the ground state as $\hat{\rho}(\vec{r})$ and $\rho_0(r)$, respectively. If the classical energy weighted sum rule value is carried by a single λ-pole state, $|\omega_\lambda>$, the above two equations provide the model independent form of the nuclear transition density:

$$<|\hat{\rho}(\vec{r})|\omega_\lambda>=\frac{X_\lambda}{2}<|\beta_{\lambda 0}|\omega_\lambda>r^{\lambda-1}Y_{\lambda 0}\frac{d\rho_0(r)}{dr}, \tag{3}$$

$$X_\lambda=-\frac{8\pi}{A(2\lambda+1)<r^{2\lambda-2}>}$$

Since Eqn. (3) indicates that the point r in $\rho_0(r)$ goes into the point:

$$r\rightarrow r\left(1-\frac{X_\lambda}{2}\beta_{\lambda 0}r^{\lambda-2}Y_{\lambda 0}(\hat{r})\right) \tag{4}$$

under the λ-pole distortion, the one-body potential V(r) can be written in the form:

$$V(r)=V_0(r)+\frac{X_\lambda}{2}\beta_{\lambda 0}r^{\lambda-1}Y_{\lambda 0}(\hat{r})\frac{dV_0(r)}{dr}, \tag{5}$$

assuming the self-consistency between the nuclear density and the average nuclear field. Hence, if $V_0(r)$ is taken to be a harmonic oscillator potential, the total nuclear potential can be expressed as

$$V=\sum_{i=1}^{A}\frac{m\omega^2}{2}r_i^2+\frac{1}{2}\frac{m\omega^2}{2}\sum_{\lambda,\mu}X_\lambda\sum_{i,j}r_i{}^{\lambda}Y^{*}_{\lambda\mu}(\hat{r}_i)\,r_j{}^{\lambda}Y_{\lambda\mu}(\hat{r}_j),\ (\lambda\geq 1). \tag{6}$$

* T. Suzuki and C. Hinohara: Phys. Rev. C., (to be published).

** Tohoku University.

In case of $\lambda = 0$, the sum rules are described as

$$\sum_n \omega_n < |\beta_0| \omega_n > < \omega_n |\beta_0| > = \frac{2A}{m} < r^2 >, \tag{7}$$

$$\sum_n \omega_n < |\hat{\rho}(\vec{r})| \omega_n > < \omega_n |\beta_0| > = -\frac{1}{m} \frac{1}{r^2} \frac{d}{dr} \left\{ r^3 \rho_0(r) \right\}, \tag{8}$$

$$(\beta_0 = \sum_{i=1}^{A} r_i^2).$$

Using the above equations and assuming the self-consistency, one can find the nuclear potential for a breathing mode in the harmonic oscillator shell model :

$$V = \sum_{i=1}^{A} \frac{m\omega^2}{2} r_i^2 - \frac{1}{2} \frac{m\omega^2}{2} \frac{1}{A < r^2 >} \sum_{i,j} r_i^2 \cdot r_j^2. \tag{9}$$

Finally, we note the following three points. Firstly, the nuclear potential for $\lambda = 2$ given in Eqn. (6) has the same form as the one with Q-Q interaction derived on the other approach by B. R. Mottelson in calculating the isoscalar E2-effective moment.[3] Secondly, the interaction Hamiltonian used in the particle-vibration coupling model is given in Eqn.(5), which has a different r-dependence from the one in the particle-"surface vibration" coupling model.[3] Thirdly, if β_0 and β_2 are considered to be dynamic variables for nuclear E0 and E2 vibrations, respectively, the eigenfrequency of these vibrations is obtained as

$$\omega_0 = \omega_2 = \sqrt{2}\omega \approx 58/A^{1/3} (\mathrm{MeV}), \tag{10}$$

utilizing the nuclear potentials given in Eqns.(9) and (6).[4] This value is comparable with excitation energy for newly observed giant resonance which is interpreted to be isoscalar monopole and/or quadrupole mode.[5]

References

1) A. M. Lane : "Nuclear Theory", Benjamin, New York (1965).
2) E. I. Kao and S. Fallieros : Phys. Rev. Lett., 25, 827 (1970);
   T. J. Deal and S. Fallieros : Phys. Rev., C7, 1709 (1973);
   J. V. Noble : Ann. Phys., 67, 98 (1971);
   H. Ui and T. Tsukamoto : Contribution to Intr. Conf. on Nucl. Structure Studies using Electron Scattering and Photoreaction, Sendai (1972).
3) B. R. Mottelson : Nikko Summer School Lectures (1967), Nordita Publication, No. 288.
4) T. Suzuki : Nucl. Phys, 217, 182 (1973).
5) Y. Torizuka : Proc. Intern. Conf. Nucl. Structure Studies Using Electron Scattering and Photoreaction, Sendai (1972);
   E. Spamer : idem;

Y. Torizuka : Proc. Intern. Conf. Photonuclear Reaction and Application, Asilomar (1973);
M. B. Lewis : idem ;
Th. Walcher : Proc. Intern. Conf. Nucl. Phys., Munich (1973).

5. NUCLEAR PHYSICS
Nuclear Spectroscopy

5-1. Asymmetric Fission of ^{236}U

A. Iwamoto,* S. Suekane,** S. Yamaji,
and K. Harada*

One of the most characteristic features of the low energy fission of medium to heavy actinide nuclei is the mass asymmetry of the fragments. In addition, the development of experimental techniques has made it possible to determine the fission barrier heights with good accuracy.[1] We have calculated the total potential energy surface for the fission of ^{236}U and could reproduce the features rather well.

Assuming the fission process to be adiabatic, we calculate the total intrinsic energy of the system according to Strutinsky's prescription.[2] The total energy E is then expressed as

$$E = E_{LDM} + E_{sc} + E_{pc} \quad , \tag{1}$$

where E_{LDM} is the liquid drop energy, E_{sc} is the shell correction energy, and E_{pc} is the pairing correction energy. To calculate E_{sc}, we use the two-center shell model, generalized to asymmetric deformations.[3] This model is especially suited for the description of whole fission process. A fourth order correction term similar to that of Ref. 3) is used in the neck region and ℓ-dependent term is defined in terms of stretched coordinate. The values of κ and μ are taken from Ref. 4). The averaged energy which is needed in the Strutinsky's method was calculated using the six-order curvature corrections and the smearing width of $1\hbar\omega$. The pairing correction E_{pc} was calculated following the method of Bolsterli et al.[5] For the liquid drop energy, the Groote-Hilf's mass formula[6] was used, which consists of the surface and curvature energies, and for the Coulomb energy, uniform charge distribution was assumed. Nuclear surface shape used in the liquid drop calculation was assumed to be the equipotential surface of the two-center Hamiltonian.

Imposing the volume conservation and other conditions, four independent shape parameters were finally left. These are z_0 (center separation of the two potentials), δ_1, δ_2 (deformation parameters of each fragment), and α(volume ratio of the two fragments). The parameter z_0 is approximately considered to be the distance between two fragments.

In order to investigate the mass asymmetry, we first show in Fig. 1 the energy surface of the symmetric case. Symmetry means that $\alpha = 1$ and $\delta_1 = \delta_2 = \delta$. From Fig. 1 we see the following :

(1) the ground state lies at about $z_0 = 0.0$fm. and $\delta = 0.2$;

(2) the second minimum (2.0 MeV relative to the ground state) lies at about $z_0 = 4.0$fm.

* Japan Atomic Energy Research Institute.

** Osaka City University.

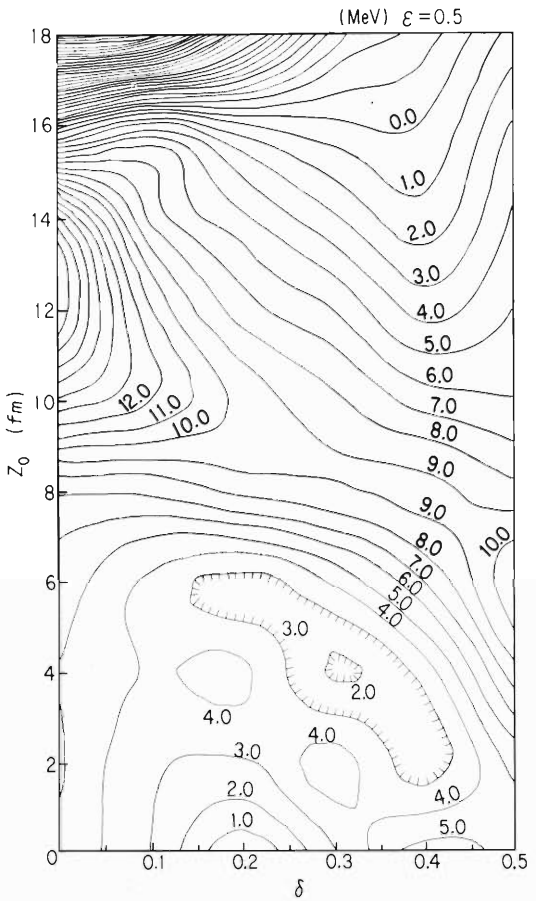

Fig. 1. Potential energy surface for ^{236}U in the symmetric two-center model. Energies are in MeV and LDM energy is normalized to zero at the spherical state (δ = 0.0 and z_0 = 0.0).

and δ = 0.3, in contrast to the results of the usual Nilsson model calculations (z_0 = 0.0);

(3) the first barrier is about 4.0 MeV in height and lies at about z_0 = 2.7fm. and δ = 0.235;

(4) the second barrier is about 9.0 MeV in height and lies at about z_0 = 8.5fm, and δ = 0.3 $\simeq$ 0.4.

These features are quite different from the liquid drop energy surface and are mainly due to the shell correction.

To see the effects of mass asymmetry, we then vary the parameter α from 1.0 at several points including the first barrier, the second minimum and the second barrier. Parameters, z_0 and δ_1 are assumed to be the same as those of the symmetric case. Calculations show that at the first barrier and the second minimum, the energy increases monotonously as α increases. This means that at these points the symmetric deformation is preferred. In Fig. 2, the height of the second barrier is illustrated as a function of mass asymmetry. The solid line, which represents the total energy, decreases as the mass ratio increases, and after the passage of a

minimum point it begins to increase. The mass ratio corresponding to the minimum total energy is between 138/98 and 148/88. The energy gain from the symmetry to the most probable asymmetry is about 3.5 MeV, which lowers the height of the second barrier from 9.0 MeV to 5.7 MeV. The calculated barrier height is in good agreement with the experimental value, but the mass ratio is somewhat larger than the experimental one (140/96). The discrepancy could be resolved if the most probable asymmetry was determined not at the second suddle point but at the later stage of the fission process. However, we do not try it here, because many difficulties remain concerning the method of shell corrections and pairing correction at such two-center-like deformations.

From Fig. 2, it can be seen that preference for mass asymmetry is due to shell correction. This fact is checked from the single particle energy spectrum at these deformations. At the second barrier, the level density of the spectrum near the Fermi surface decreases as the mass ratio increases from 1.0. This might be the consequence of the shell structure arising from nascent fragments.

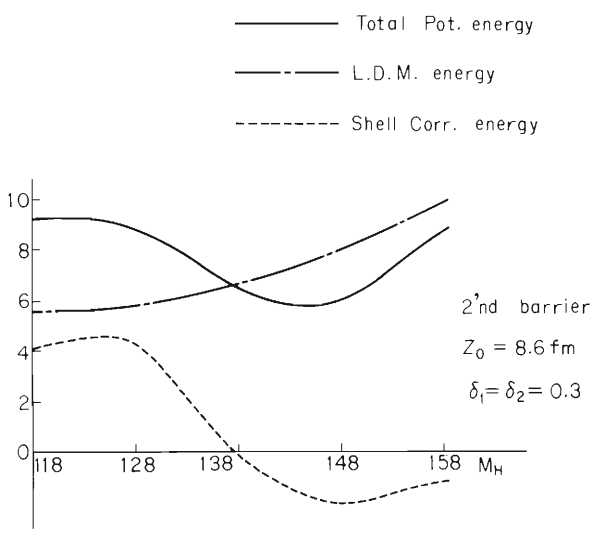

Fig. 2. Energies at the second barrier (z_0 = 8.6fm. and $\delta_1 = \delta_2 = 0.3$) as a function of mass asymmetry. The abscissa is the fragment mass and 118 means the symmetric shape. The solid line represents the total potential energy, the dot-and-dash line, the liquid drop energy, and the dotted line, the shell correction energy. The liquid drop energy is normalized to zero at the spherical state ($\delta = 0.0$, $z_0 = 0$, and $\alpha = 1$)

References

1) B. B. Brack, H. C. Britt, J. D. Garrett, O. Hansen, and B. Lerouce : Third Symposium on the Physics and Chemistry of fission, Preprint (1973).
2) M. Brack, J. Damgard, A. S. Jensen, H. C. Pauli, V. M. Strutinsky, and C. Y. Wong : Rev. Mod. Phys., 44, 320 (1972).
3) J. Maruhn and W. Greiner : Z. Physik, 251, 431 (1972); M. G. Mustafa, U. Mosel, and H. W. Schmidtt : Phys. Rev., C7, 1519 (1973).
4) C. Gustafson, I. L. Lamm, B. Nilsson, and S. G. Nilsson : Ark. Phys., 36, 613 (1967); D. A. Arseniev, A. Sobiczewsky, and V. G. Soloviev : Nucl. Phys., A139, 269 (1969).
5) M. Bolsterli, E. O. Fiset, J. R. Nix, and J. L. Norton : Phys. Rev., C5, 1050 (1972).
6) H. V. Groote and E. Hilf: Nucl. Phys., A129, 1 (1966).

5-2. Alpha-Decay of ^{215}Fr

K. Hiruta, T. Nomura, M. Yoshie, and O. Hashimoto

The α-decay of ^{215}Fr has been studied by the pulsed-beam method reported in our recent papers.[1)~3)] The francium isotope ^{215}Fr was produced in the bombardment of ^{209}Bi with 72~81 MeV ^{12}C-ions from the cyclotron and its lifetime was measured between the beam bursts of the

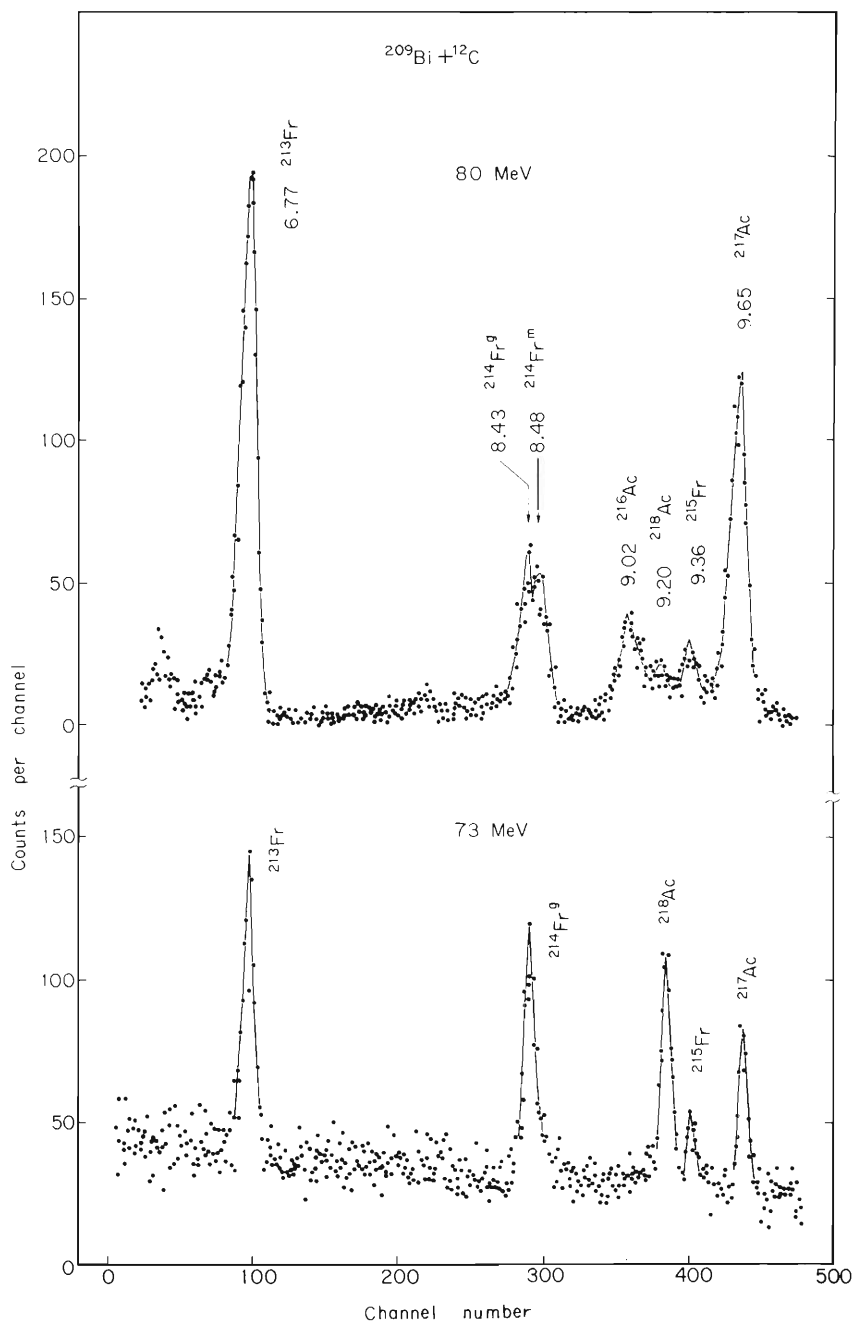

Fig. 1. An α-particle spectrum resulting from bombardment of ^{209}Bi with 80 and 73 MeV

cyclotron. Fig. 1 shows a typical delayed α-spectra from the $^{209}Bi + ^{12}C$ reaction. The ground state of ^{215}Fr has been found to decay with $E_\alpha = (9.355 \pm 0.020)$ MeV and $t_{1/2} = (0.12 \pm 0.02)$ μs. The mass assignment of ^{215}Fr was made on the basis of its excitation function, angular distribution, α-decay energy, lifetime, and α-decay chain relation.

The experimental and theoretical reduced α-widths of N=128 isotones from ^{212}Po to ^{218}Th are shown in Fig. 2. The experimental reduced width was deduced from $\gamma_\alpha^2 = \frac{\hbar\lambda}{2P}$, where λ is the decay constant and P the barrier penetrability calculated for S-wave α-particles and for a pure Coulomb potential with $R = 1.57A^{1/3}$ fm. The theoretical values of the reduced width were obtained from a shell-model calculation,[4] in which we assumed ^{208}Pb as an inert core and put valence nucleon into the lowest shell-model orbitals outside the core, i.e., the $1h_{9/2}$ orbital for protons and $2g_{9/2}$ for neutrons. The reduced α-width of ^{215}Fr fits very well to the general trend of N=128 isotones and agrees with the calculated value. This also justifies the assumption that the decay of ^{215}Fr proceeds mainly via S-wave. In consequence, the spin and parity of the ground state of ^{215}Fr are the same as those of the ground state of ^{211}At, which is $(9/2)^-$.

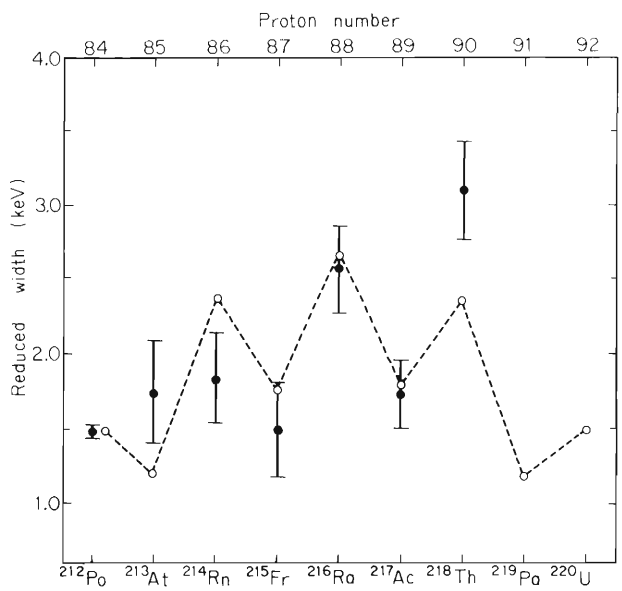

Fig. 2. Experimental (solid circles) and theoretical reduced α-widths for the ground state decay of N=128 isotones. The theoretical values are normalized on the experimental value of ^{212}Po.

References

1) T. Nomura, K. Hiruta, T. Inamura, and M. Odera : Phys. Lett., 40B, 543 (1972).
2) K. Hiruta, T. Nomura, T. Inamura, and M. Odera : ibid., 45B, 244 (1973).
3) T. Nomura and K. Hiruta : Nucl. Instr., 108, 61 (1973).
4) H. J. Mang : Phys. Rev., 199, 1069 (1960).

5-3. Magnetic Moment of the $29/2^+$ State in ^{213}Fr

E. Recknagel, Y. Yamazaki, O. Hashimoto,
S. Nagamiya, and K. Nakai

The level structure of the neutron-closed ^{213}Fr nucleus (N = 126) was recently studied by Maier et al.[1] and the existence of the isomeric $29/2^+$ state ($T_{1/2}$ = 0.5 μs) was discovered as shown in Fig. 1. The main configuration of this state was assigned to be $[(\pi h^4_{9/2})8^+ \otimes \pi i_{13/2}]\cdot 29/2^+$. Measurement of the g-factor of this state will give a good check of the above assignment. If the assignment was found to be valid, this state would be very suitable for deduction of effective orbital g-factor.

A liquid metallic target of enriched ^{204}Hg was bombarded with 94 MeV ^{14}N beams from the cyclotron to populate the $29/2^+$ isomeric state via the $^{204}Hg(^{14}N, 5n)^{213}Fr$ reaction. The 680 keV ($29/2^+ \rightarrow 23/2^-$) gamma-ray was detected with two NaI(Tl) counters placed at ± 135° to the beam axis, in order to observe the n = 2 storoboscopic resonance. The result shown in Fig. 2 gives g(uncorr) = 1.04 ± 0.01. If a correction 0.0 ± 1.0 % is made for the Knight shift and diamagnetism, we obtain

$$g(\text{corr}) = 1.04 \pm 0.02.$$

There exists appreciable enhancement in the B(E3) value from the $29/2^+$ state to the $23/2^-$ state in ^{213}Fr as well as in the corresponding transitions in ^{211}At and ^{210}Po. If these enhancements are ascribed to the admixture of the core-excited 3^- state in ^{208}Pb, we can deduce the mixing amplitudes by use of the weak coupling model, as shown in Table 1. After the correction due to this admixture, we obtain

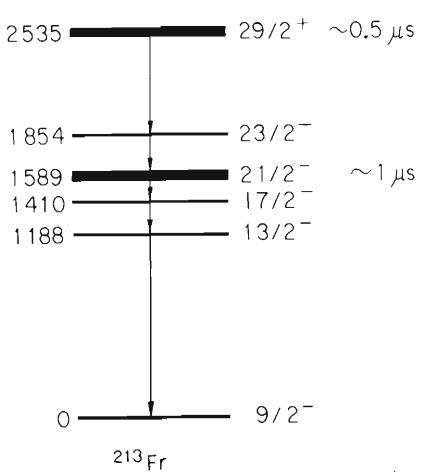

Fig. 1. Energy levels of ^{213}Fr proposed by Maier et al. [1]

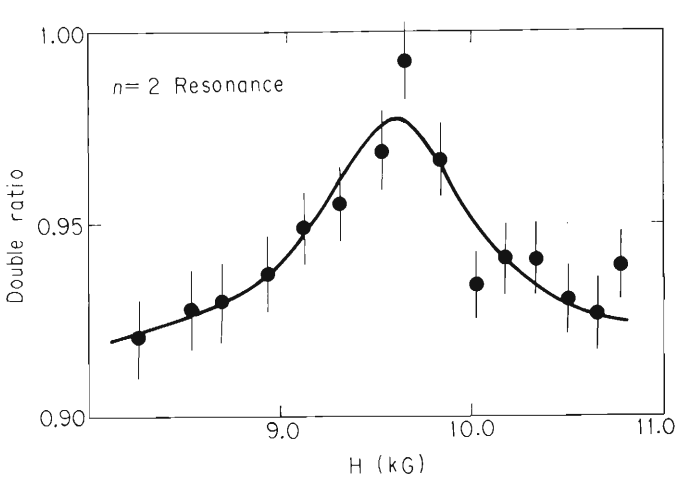

Fig. 2. The n = 2 storoboscopic resonance. Solid curve gives the best fit assuming a Lorentzian line shape.

$$g([(\pi h^4_{9/2})\,8^+ \otimes \pi i_{13/2}]\,29/2^+) = 1.05 \pm 0.03.$$

In Table 2, the g-factors of the $(\pi h_{9/2})^{n-1} \otimes \pi i_{13/2}$ states are listed, where the value for ^{210}Po has been calculated from the experimental g-factors by use of the additivity relation. The agreement of these g-factors supports the configuration assignment by Maier et al.[1]

The effective g_ℓ-factor can be obtained by use of the following equation, because the g-factor in question is insensitive to the ambiguity of the effective g_s-factor and the first order configuration mixing $\delta\mu_{1st}$.

$$g(29/2^+) = g_\ell - \frac{5}{319}(g_s - g_\ell) + \frac{2}{29}[\delta\mu_{1st}(i_{13/2}) + \delta\mu_{1st}[(h^4_{9/2})\,8^+)].$$

Table 1. B(E3) values of $11^- \rightarrow 8_2^+$ in ^{210}Po and $29/2^+ \rightarrow 23/2^-$ in ^{211}At and ^{213}Fr.

	B_{exp}(E3)* in e^2fm^6	$B_{s.p.}(E3, \pi i_{13/2} \rightarrow \pi f_{7/2})$**	a^2 ***
^{210}Po	46000 ± 10000	5000	0.10 ± 0.04
^{211}At	51000 ± 7000[6]	5000	0.10 ± 0.06
	40000 ± 10000[5]		
^{213}Fr	35000 ± 9000	5000	0.06 ± 0.03

* The experimental values for ^{210}Po and ^{213}Fr were measured by Fant[4] and by Maier et al,[1] respectively, The difference between the values reported by Bergström et al.[6] and by Maier et al.[5] for ^{211}At was due to the difference in the estimation for the branching ratio.

** This single particle value was calculated by use of the radial matrix element $<f_{7/2}|r^3|i_{13/2}> = 196$ fm^3.[6]

*** Squares of mixing amplitudes of the collective 3^- state were deduced by use of the weak coupling model.

Table 2. The g-factors of $(\pi h_{9/2})^{n-1} \otimes \pi i_{13/2}$ states and the deduced anomalous orbital g-factors.

Nucleus	J^π	g_{exp}	$g([\pi h_{9/2} \pi i_{13/2}]\,11^-)$*	$g([(\pi h_{9/2})^{n-1} \otimes \pi i_{13/2}]\,29/2^+)$*	δg_ℓ
^{210}Po	11^-	1.107 ± 0.019	1.15 ± 0.03	1.09 ± 0.03**	0.13 ± 0.03
^{211}At	$29/2^+$	1.03 ± 0.04		1.05 ± 0.05	0.10 ± 0.05
^{213}Fr	$29/2^+$	1.04 ± 0.02		1.05 ± 0.03	0.10 ± 0.03

* These values are corrected for the mixing of the collective 3^- state.

** Calculated by use of the additivity relation from $g(\pi h_{9/2}) = 0.910$.[8]

If we use the value obtained from the blocking effect[2] as the first order configuration mixing $\delta\mu_{1st}$, we obtain

$$\delta g_{\ell} = 0.10 \pm 0.03,$$

which is in good agreement with the previously reported value.[3]

References

1) K. H. Maier, J. R. Leigh, F. Pühlhofer, and R. M. Diamond: Suppl. J. de Physique, 32, C6-211 (1971).
2) Y. Yamazaki, O. Hashimoto, H. Ikezoe, S. Nagamiya, K. Nakai, and T. Yamazaki: IPCR Cyclotron Progr. Rep., 7 74 (1973).
3) T. Yamazaki, T. Nomura, S. Nagamiya, and T. Katou: Phys. Rev. Lett., 25, 547 (1970).
4) B. Fant: Physica Scripta, 4, 175 (1971).
5) K. H. Maier, J. R. Leigh, F. Pühlhofer, and R. M. Diamond : Phys. Lett., 35B, 401 (1971).
6) I. Bergström, B. Fant, C. J. Herrlander, K. Wikström, and J. Blomqvist : Physica Scripta, 1, 243 (1970).

5-4. The Blocking Effect of the M1 Core Polarization Studied from the g-Factor of the $(\pi h_{9/2})^6$ 8^+ State in ^{214}Ra

Y. Yamazaki, O. Hashimoto, H. Ikezoe, S. Nagamiya,
K. Nakai, and T. Yamazaki

In the past few years, a number of magnetic moments of isomeric states have been measured in the lead region. Among them, g-factors of $(\pi h_{9/2})^n$ states measured so far have agreed well within experimental errors, as expected from the additivity. According to the configuration mixing theory of Arima and Horie,[1] however, a correction due to the core polarization of $(\pi h_{11/2}^{-1} \pi h_{9/2})1^+$ type is proportional to the number of holes in the $h_{9/2}$ orbital, so that the g-factor of the $(\pi h_{9/2})^n$ state decreases as the number of protons in the orbital increases. By observing this so-called blocking effect, we can study the mechanism of the core polarization.

Recently, Maier et al.[2] have found an isomeric 8^+ state ($T_{1/2}$ = 67 μs) in ^{214}Ra, whose main configuration is considered to be $(\pi h_{9/2})^6$ 8^+. This state is one of the most suitable states for the study of the above problem. In addition, the measurement of the g-factor of this state presents another interesting problem as to whether the nuclear alignment is preserved over a few 10 μsec or not.

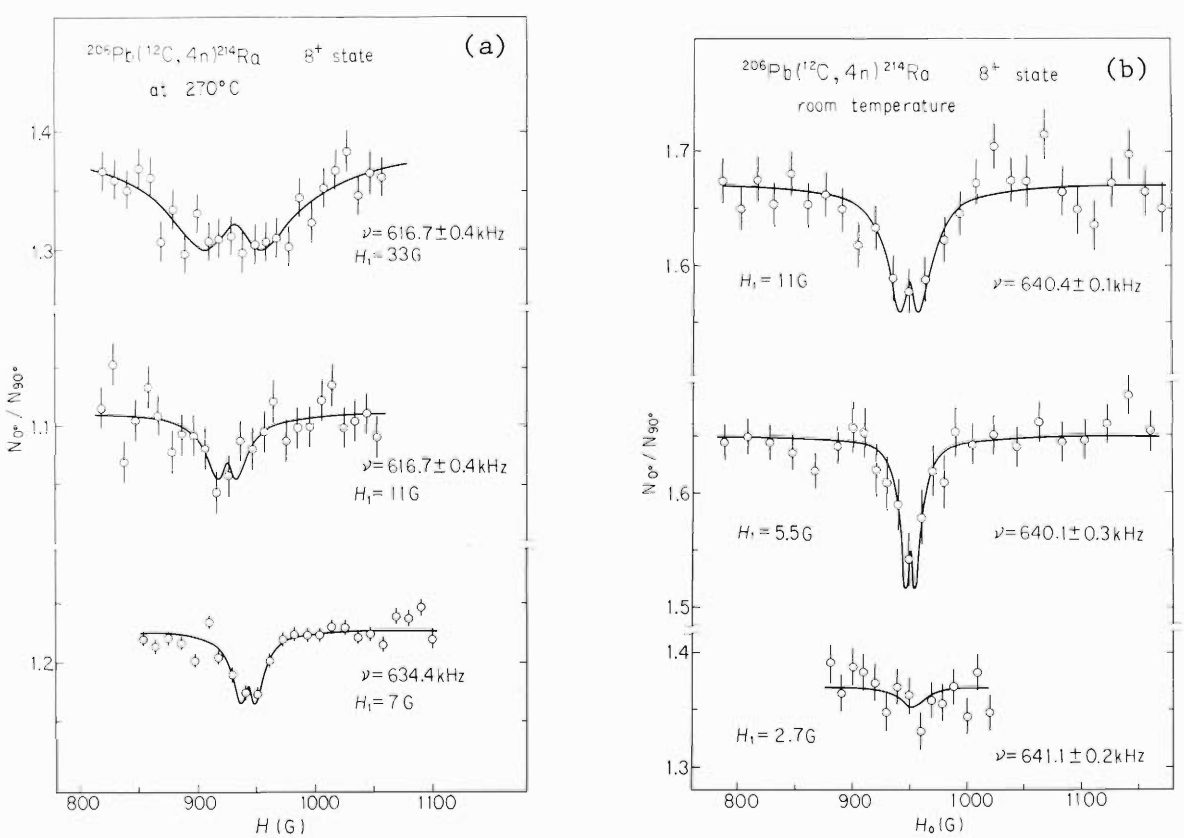

Fig. 1. Typical NMR patterns for the 8^+ state in ^{214}Ra.

The measurement was carried out by use of the in-beam γ-ray NMR method (NMR/PAD). The state was populated via the ^{206}Pb (^{12}C, 4n)^{214}Ra reaction with the 90 MeV ^{12}C beam from the cyclotron. The γ-rays followed by the reaction was detected by two NaI(Tl) detectors placed at 90° and 0° with respect to the beam direction. A static external magnetic field H_0 was applied parallel to the beam direction and its strength was varied automatically. An rf-field with fixed frequency was applied perpendicularly to H_0, and the ratio N(0°)/N(90°) was observed at two different temperatures, 270°C and room temperature. Typical NMR patterns obtained are shown in Fig. 1, where the solid curves are those fitted by the theoretical function by Matthias et al.[3] No significant difference was observed between the two temperatures. In addition, the present NMR experiments indicate that the relaxation time is about 300 μs or even longer at room temperature, while the relaxation time due to the interaction with conduction electrons is estimated to be 150 μs from the data of ^{207}Pb in the Pb metal. The above two facts suggested the small effect due to quadrupole interaction by the radiation damage.

The g-factor obtained is

$$g(\mathrm{corr}) = 0.881 \pm 0.006,$$

where the correction of 0.0 ± 0.5 % was made for the Knight shift and diamagnetism, because they are expected to cancel out each other approximately.[4),5)]

The g-factors of the $(\pi h_{9/2})^n$ states will decrease linearly with the particle number n as given by the following equation:

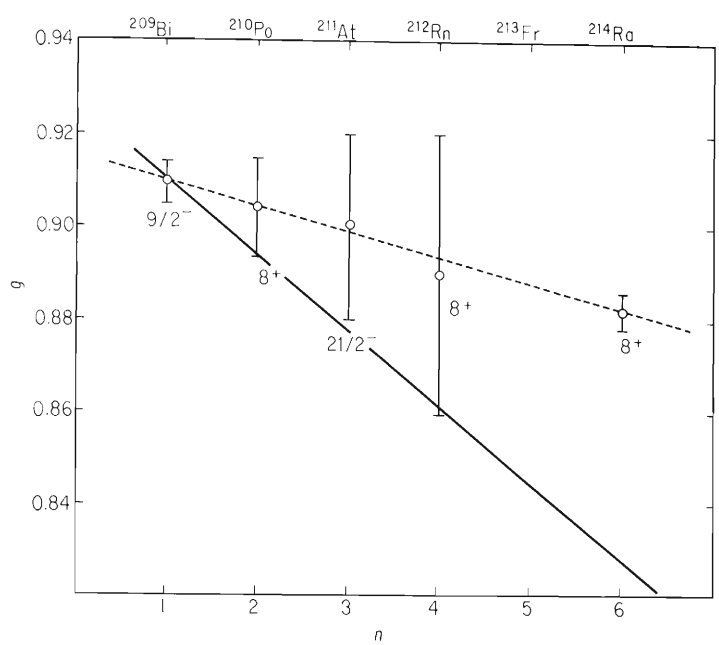

Fig. 2. The g-factors of the $(\pi h_{9/2})^n$ states. The dotted line gives the best fit for the experimental data, and the solid line shows the theoretical prediction by Arima and Horie.[1)]

$$g = g_{\text{Schmidt}} + \frac{\ell + 1}{\ell + 1/2}\delta g_{\ell} + \frac{9 - n}{8}\delta g_{\text{core}}(p) + \delta g_{\text{core}}(n) + \delta g_{\text{other}},$$

where δg_{ℓ} is the anomalous part of the orbital g-factor,[6] $\delta g_{\text{core}}(p)$ and $\delta g_{\text{core}}(n)$ are corrections due to proton and neutron core polarization in the n = 1 case, respectively, and δg_{other} is the other possible corrections such as the anomalous part of the g_s-factor due to mesonic exchange current or the higher order configuration mixings. The third term of the above equation represents the blocking of the proton core polarization of $(\pi h_{11/2}^{-1}\pi h_{9/2})1^+$ type. From the data of the g-factors of the states in question summarized in Fig. 2, we can deduce the $\delta g_{\text{core}}(p)$ to be

$$\delta g_{\text{core}}(p) = 0.05 \pm 0.01 \quad .$$

Possible isotone dependence of the δg_{other} will reduce the blocking effect.*,** By taking this dependence into account, we obtain

$$\delta g_{\text{core}}(p) = 0.07 \pm 0.02 \quad .$$

This value is about one half of the theoretical predictions.[1),7),8)] Since the value δg_{ℓ} is known to be 0.13,[6] we obtained $\delta g_{\text{core}}(n) + \delta g_{\text{other}} = 0.12 \pm 0.02$. One of possible interpretations of this fact will be given by assuming that $\delta g_{\text{core}}(p)$ is comparable to $\delta g_{\text{core}}(n)$. The calculation performed very recently by Arita* seems to support this assumption.

References

1) A. Arima and H. Horie : Progr. Theor. Phys., 12, 623 (1954).
2) K. H. Maier, J. R. Leigh, F. Pühlhofer, and R. M. Diamond : J. de Physique, 32, C6-211 (1971).
3) E. Matthias, B. Olsen, D. A. Shirley, J. E. Templeton, and R. M. Steffen : Phys. Rev., A4, 1626 (1971).
4) L. E. Drain : Met. Rev., 12, 195 (1967).
5) F. D. Feriock and W. R. Johnson : Phys. Rev. Lett., 21, 785 (1968).
6) T. Yamazaki, T. Nomura, S. Nagamiya, and T. Katou : ibid., 33B, 574 (1970); S. Nagamiya and T. Yamazaki : Phys. Rev., C4, 1961 (1971); T. Yamazaki : Suppl. J. Phys. Soc. Japan, 34, 17 (1973).
7) H. A. Mavromatis and L. Zamick : Nucl. Phys., A104, 17 (1967).
8) J. Blomqvist, N. Freed, and H. O. Zetterstrom : Phys. Lett., 18, 47 (1965).

* K. Arita: Private communication (1973)

** K. Ogawa: ibid.

5-5. In-Beam Alpha- and Gamma-Spectroscopy of ^{216}Ra

T. Nomura, K. Hiruta, M. Yoshie, and O. Hashimoto

By means of the in-beam alpha- and gamma-spectroscopy, we have investigated the level structure of ^{216}Ra, about which nothing is known at present. Delayed alpha- and gamma-transitions were measured in the ^{208}Pb(^{12}C, 4n)^{216}Ra reaction by the pulsed beam method using natural beam bursts of the cyclotron. The results obtained are listed in Table 1. These alpha- and gamma-transitions were assigned to ^{216}Ra on the basis of their excitation functions and found to have the same lifetime of about 7 ns. This indicates the existence of an

Table 1. Delayed α- and γ-transitions in the ^{208}Pb (^{12}C, 4n)^{216}Ra reaction.

E_α (keV)	Q_α (keV)	ΔQ_α (keV)	Relative intensity
9349 (6)*	9525 (7)	0	1
9551(14)	9731(15)	206(10)	1.0×10^{-2}
10182(20)	10374(21)	849(16)	1.6×10^{-3}
10491(10)	10689(11)	1164 (6)	2.5×10^{-3}
10823(10)	11027(11)	1502 (6)	5.6×10^{-3}
11027(10)	11235(11)	1710 (6)	8.7×10^{-3}
11345(24)	11559(25)	2034(20)	9.6×10^{-4}
11640(30)	11860(31)	2335(30)	3×10^{-4}

E_γ (keV)	Relative intensity	Multipolarity**
203.7	0.97	Q
309.3	1.06	D
314.8	1	Q
343.9	2.07	Q
475.8	1.37	Q
613.4	1.04	D
688.0	1.12	Q

* The ground-state decay.

** Q : quadrupole transition; D : dipole transition.

isomeric state in ^{216}Ra with $t_{1/2} \approx 7$ ns. Angular distribution measurements were carried out for gamma-rays to assign their multipolarity.

The proposed level scheme of ^{216}Ra is shown in Fig. 1.

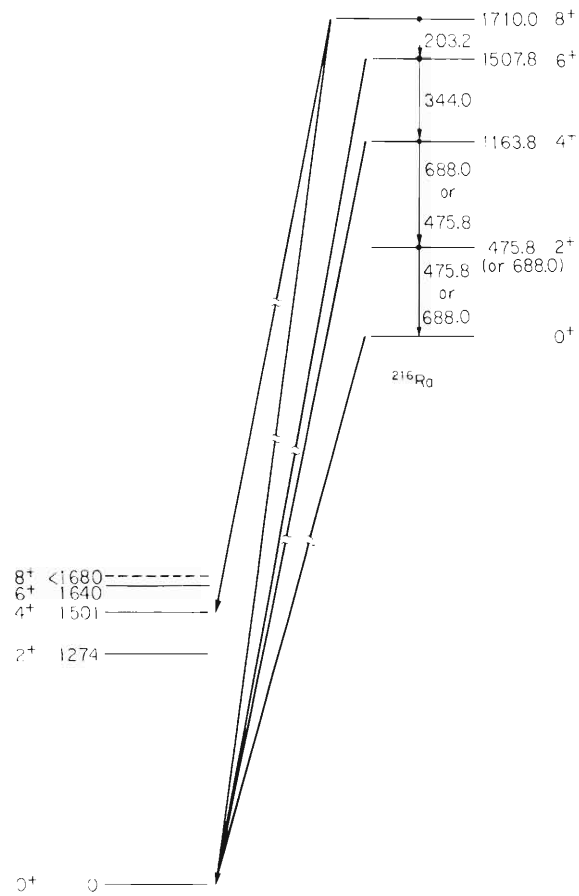

Fig. 1. A proposed level scheme in ^{216}Ra.

5-6. Measurement of Half-Life in ms Region with a Mechanical Chopper

A. Hashizume, Y. Tendow, T. Katou, and H. Kumagai

For the study of half-life in the millisecond region, some improvements have been made in the mechanical beam chopper previously reported.[1] The time base depended on the rotational speed of a DC motor. But instability of the speed prevented very accurate measurement. The block diagram of the new system is shown in Fig. 1. The time base generator consists of a 10 kHz quartz-oscillator and a frequency divider which is controlled by external start-stop pulses. The time interval of output pulses defines the time resolution of this system.

At the time of beam passage, the start pulse from a photo-transistor is applied to a time base generator. The output pulses of this generator advance the 4-bit binary scaler. Parallel output signals of this scaler are coupled directly to the multichannel analyzer and the time base is determined. On the other hand, the linear gate for signals from the Ge(Li) detector is opened by the output pulse of the binary scaler after some delay from the start pulse, which is defined by the time base generator. When the binary scaler was overflowed, a stop pulse from the scaler is applied to the generator and to the linear gate, and these gates are closed until the next cycle begins. Thus we can obtain a two-dimensional spectrum with time and energy base.

The half-life of 2.757 MeV (7 or 8^-) state in ^{132}Xe excited by the ^{130}Te(α,2n) reaction has been determined. The spectrum is shown in Fig. 2 and each peak was processed with a computer by fitting Gaussian distribution and decay curves obtained were analyzed by the method of least squares fitting. A representative decay curve is shown in Fig. 3 with the fitted curve. The weighted mean of half-life of 538, 600, 773, and 668 keV γ-rays is 8.39 ± 0.11 ms.

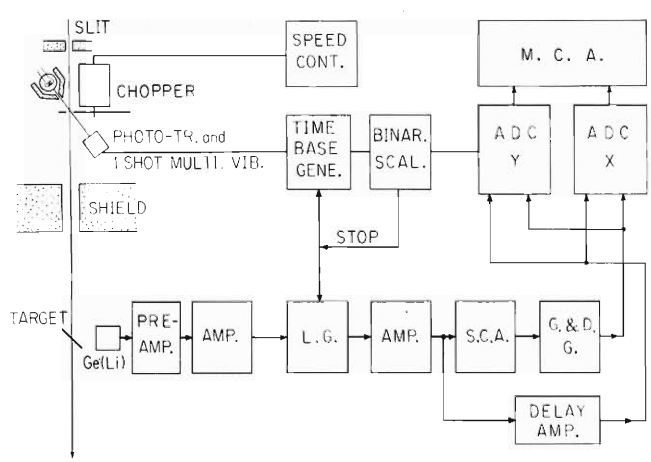

Fig. 1. Schematic diagram to study the half-life in millisecond region.

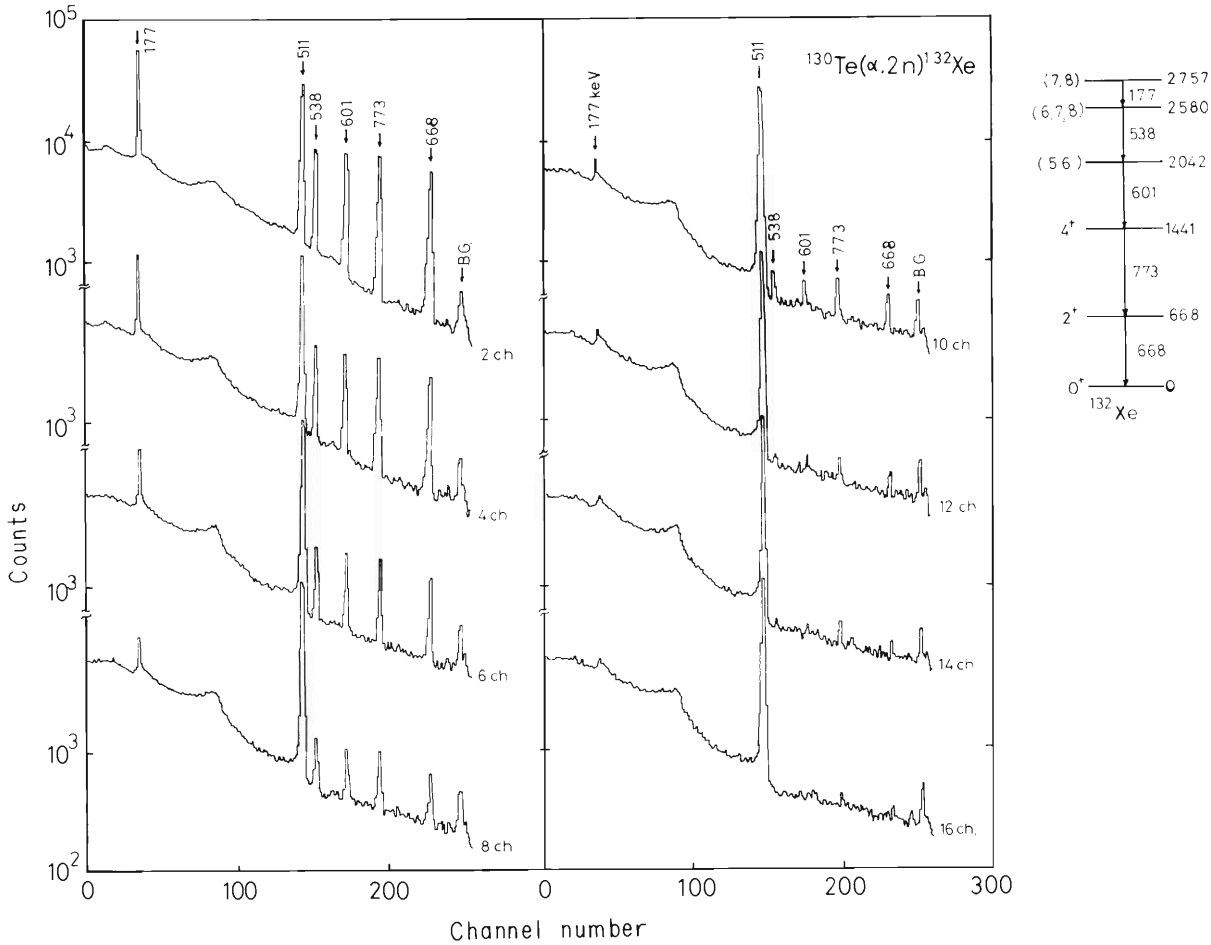

The time base of Y-coordinate is 5 ms/channel.

Fig. 2. Delayed γ-ray spectra between 15 ms to 85 ms after bombardment.

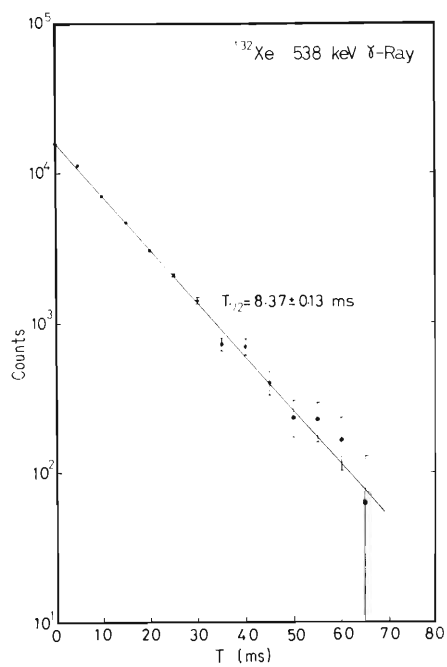

Fig. 3. An example of the decay curve of de-exciting γ-rays in ^{132}Xe.

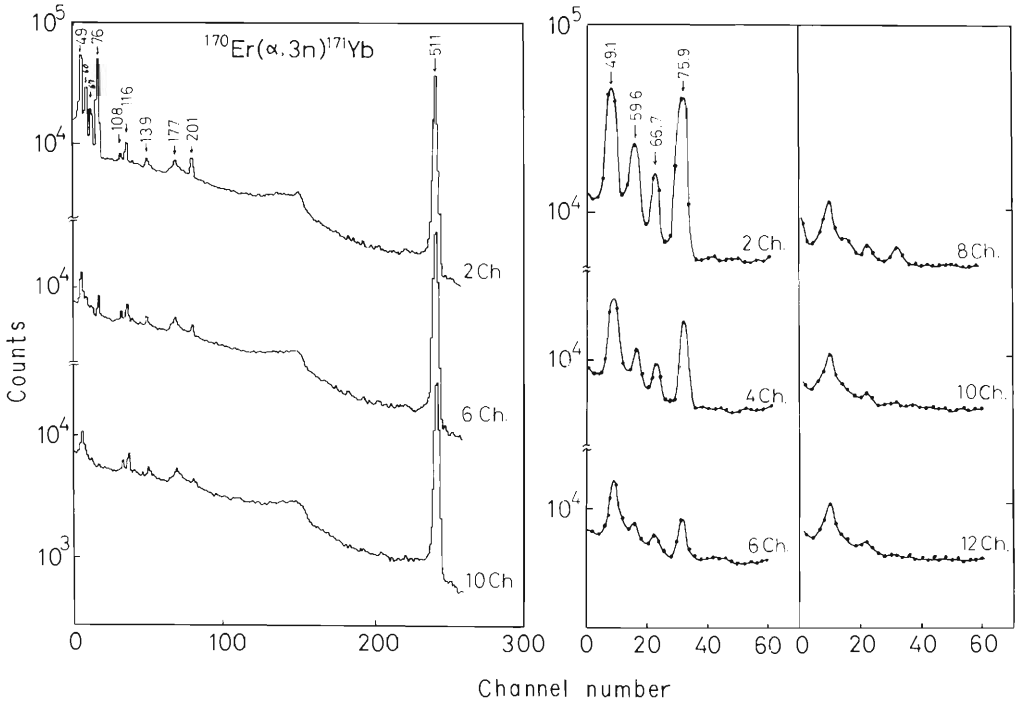

The time base is 5 ms/channel.

Fig. 4. Delayed γ-ray spectra emitted from the ^{170}Er(α, 3n)^{171}Yb reaction.

The isomer in 95.2 keV ($7/2^+$ [633]) state in ^{171}Yb is expected because of large change of K-quantum number to de-excite to the 75.9 keV ($5/2^-$[521]) state. This state de-excites to the ground state with 9.2, 66.7, and 75.9 keV γ-rays. There was only one private report[2] presenting a value 5 ms without citing any error. ^{170}Er enriched to 96 % was bombarded with 38 MeV α-particles and this isomeric state was excited by the ^{170}Er(α,3n) reaction. The spectra and a decay curve are shown in Figs. 4 and 5. The half-life was determined to be 5.25 ± 0.24 ms. The 19.4 keV isomeric transition is reported to be pure E1 from L-subshell ratios.[3] Following the selection rule of asymptotic quantum numbers for E1 transitions, the above isomeric transition is expected to be highly forbidden because of $|\Delta K| = 3$ and $\Delta\Lambda = -2$. Comparing with the Weisskopf's estimate, the hindrance factor is 2×10^8.

The 257 keV γ-ray corresponding to the transition from 0.382 MeV state to 0.125 MeV state in ^{90}Nb decays with 6.19 ± 0.08 ms half-life as shown by the curve c in Fig. 6. The half-life previously reported was 10 to 20 ms.[4] The 0.232 and 0.443 MeV γ-rays decay with $T_{1/2}$ = 14 ms. These γ-rays are not yet determined from which nucleus they emitted. It is necessary to measure excitation functions for mass assignment.

It was observed that 366 and 380 keV γ-rays decayed with half-life of 9.7 ms from the study of the γ-ray spectra obtained from the Au target by bombarding with 90 MeV ^{12}C ions. In the γ-ray spectra taken in the time interval from 5 to 85 ms after the bombardment, the 608, 425, 515, and 683 keV γ-rays were observed. These energies agree with those studied by the decay of ^{204}At by Dairiki[5] and can be attributed to the (4 or 5^-) → 6^+ → 4^+ → 2^+ →

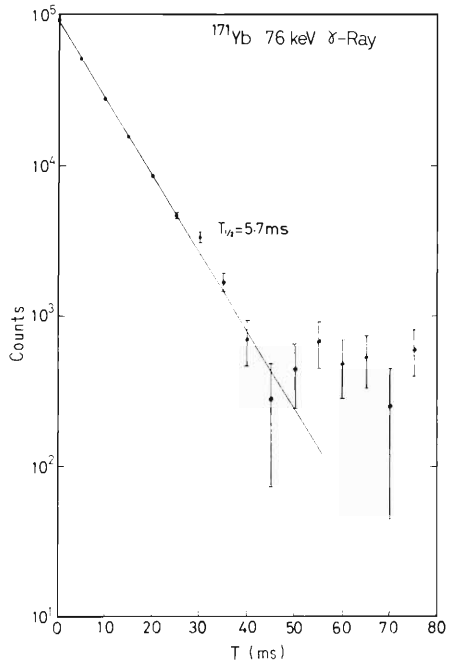

Fig. 5. Decay curve of 76 keV γ-ray.

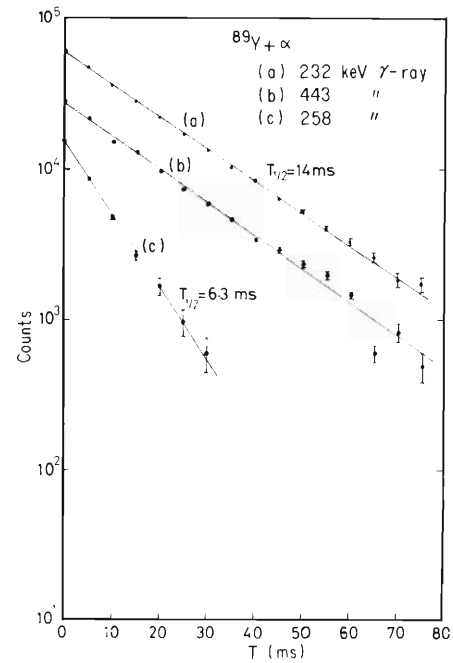

Fig. 6. Decay curves of (a) 232 keV, (b) 443 keV, and (c) 258 keV γ-rays.

0^+ transition in ^{204}Po with the order mentioned above. The excitation functions of these γ-rays also show a character of (^{12}C, 6n) reaction. The excitation function of the delayed γ-rays almost agrees with that of the (^{12}C, 6n) reaction. And we propose the existence of a new isomer in ^{204}At or ^{205}At with a half-life of 9.7 ms. Further experiment is in progress.

References

1) A. Hashizume and H. Kumagai : IPCR Cyclotron Progr. Rep., 5, 72 (1971).
2) J. Radeloff, J. N. Buttler, K. W. Kesternich, and E. Bodenstedt : Frühjahrstagung Bad Byrmont, Fachausschuss Kernphysik, (1967).
3) G. Kaye : Nucl. Phys., 86, 241 (1966).
4) H. B. Mathur and E. K. Hyde : Phys. Rev., 98, 79 (1955).
5) J. M. Dairiki : UCRL 20412 (1970).

6. NUCLEAR INSTRUMENTATION

6-1. New Data Processing System

T. Wada, T. Nomura, H. Kamitsubo,
Y. Chiba, and F. Yoshida

Since an on-line PHA system[1] was installed in 1965 for the experiments with the IPCR cyclotron, a new computer with higher speed and larger memory capacity is needed as the detector system has been developed. A new on-line PHA system with OKITAC 4500C computer has been installed for this need. It includes a hard-ware memory increment and list functions. With these functions and large capacity of disk storage, it can be used for high-speed data acquisition. A large memory capacity enables data processing during the data acquisition.

The brief specifications of OKITAC 4500C computer are as follows;

Word length

16 bits + parity,

Memory

16 kW, 0.6 μsec. cycle time,

Page

256 words, memory protection is in page unit,

Speed

Adding	1.4 μsec	Floating point adding	3.5 μsec
Multiplying	6.1 μsec	Floating point multiplying	10.7 μsec,

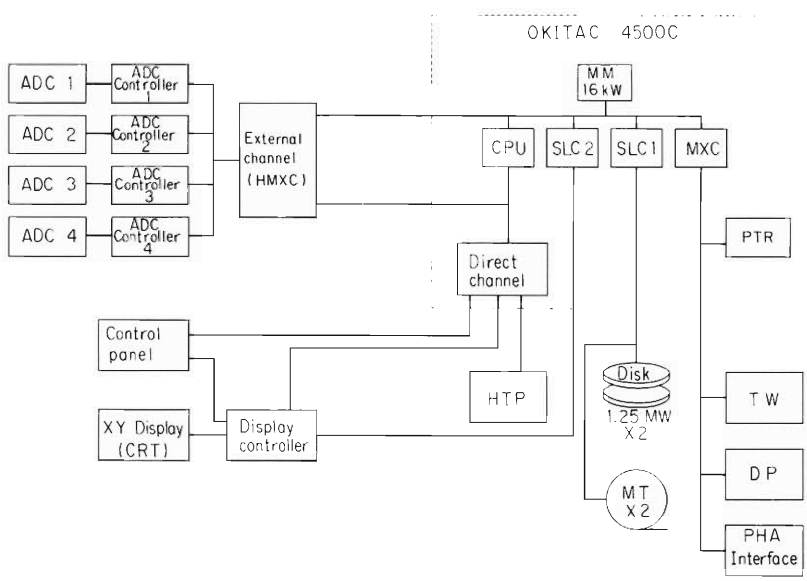

Fig. 1. OKITAC 4500C PHA system configuration.

Interrupt level

16 levels.

I/O speed

1.7 mega bytes/sec (max).

Figure 1 shows a block diagram of the whole system. There are four ADCs connected with the computer and the following five coincidence modes can be selected;

(1) PHA 1 A (I/L), B (I/L), C (I/L), D (I/L)

(2) PHA 2 A (I/L), B (I/L), C-D (I/L)

(3) PHA 3 A-B (I/L), C-D (I/L)

(4) PHA 4 A (I/L), B-C-D (L)

(5) PHA 5 A-B-C-D (I/L)

where the four ADCs are named A,B,C, and D, the hyphen (-) shows the coincidence pair and I/L shows the selection of increment/list mode. In the list mode the external channel (HMXC) transfers the data from ADCs into the computer memory independently the CPU program and sends interrupt signals only when a preset number of words are transfered, and then the computer dumps the words of the area on the disk storage. The disk storage has two disk plates of fixed and cartridge type. The system programs are written in the fixed plate and the experimental data are stored in the cartridge type plate.

There are switches and push buttons on the control panel simulating a wired PHA unit.

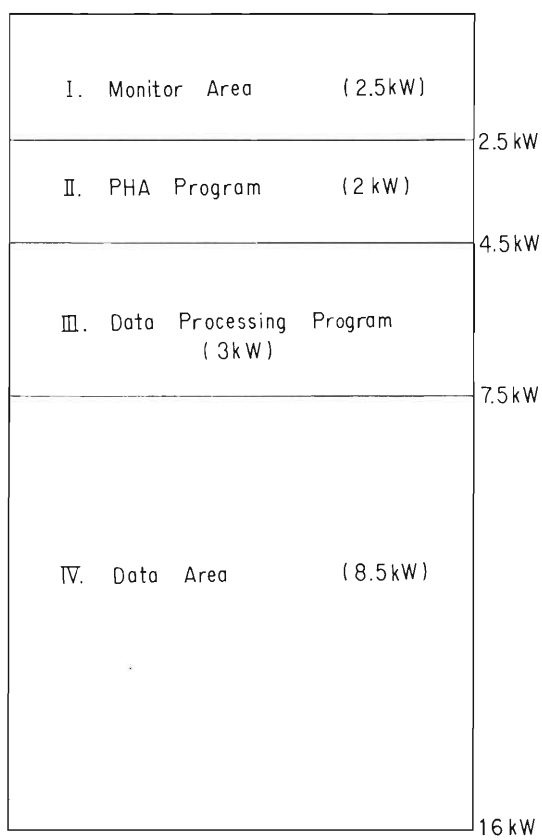

Fig. 2. OKITAC 4500C memory allocation.

These are used to select the memory region to display on the CRT or to change vertical scale for and to start/stop of data acquisition or data transfer, etc.

Figure 2 shows the memory allocation. In the area III stored are the programs for data manipulation, transfer of data, background subtraction, peak area integration and so on. The programs are called from the disk storage into this memory area. The execution of these programs has higher priority than the display program. The previous DDP-124 system will be used for off-line data analysis and for a variety of scientific computations.

Reference

1) T. Wada, Y. Chiba, K. Matsuda, and M. Yoshimizu : IPCR Cyclotron Progr. Rep., 1, 62 (1967).

6-2. Interface between PHA Units and OKITAC 4500C Computer

T. Wada, S. Takeda, and H. Kamitsubo

An interface between PHA units and the new OKITAC 4500C on-line computer has been constructed. Fig. 1 shows a schematic diagram of this interface. The interface controls four PHA units and up to ten scalers for start/stop data acquisition, and transfers the data stored in these units to the computer.

(1) Data acquisition

In order to be used for two independent measuring systems, four PHA units and the scalers can be divided into two groups. Any units can be selected to belong to one of the two groups or to be off-line, by a three-position change-over switch. If the start/stop button on one of these units or on the panel of this interface is pushed, all other units in the same group are started/stopped. The on-line computer is also regarded as a PHA unit in this case. The computer sends and receives two pairs of signals of start/stop. There are two pairs of start/stop buttons on the panel of this interface corresponding to two groups.

(2) Data transfer

The following data are transfered to the computer : (i) the status of group selection switches (one for each unit), (ii) the status of power on/off of all units, (iii) the status of six four-digit digital switches, (iv) contents of each scaler, and (v) contents of the core memory of the four PHA units. The contents of each PHA unit are read out through the parallel printer channel. The data flow is one-way.

There are two transfer-start push buttons on the panel for the two groups. When the button is pushed, the interrupt signal is sent to the computer. The computer first reads the panel data ((i)–(iii)), and analyzing the data (i) and (ii) by software, transfers the contents of the selected scalers and PHA units.

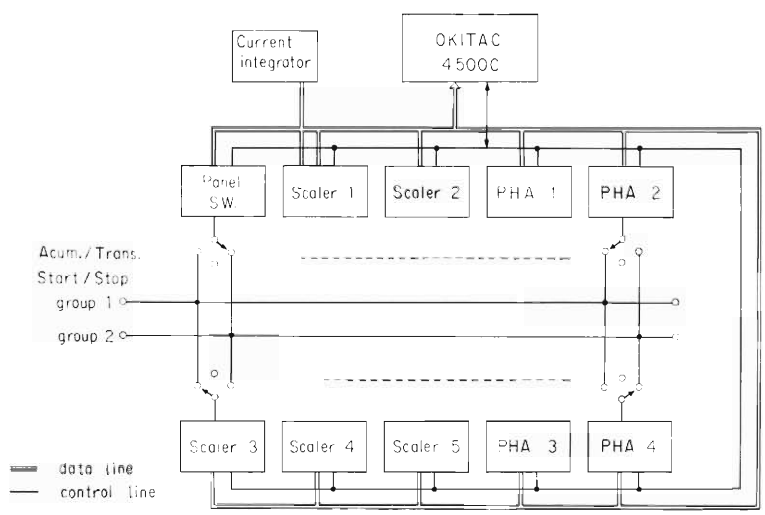

Fig. 1. Schematic diagram of the interface between PHA units and the OKITAC 4500C computer.

7. ATOMIC AND SOLID-STATE PHYSICS

7-1. Inner-Shell Excitation by N Ions and Alpha Particles (1)

Y. Awaya, T. Hamada, M. Okano, A. Hashizume,
T. Takahashi, K. Izumo, Y. Tendow, and T. Katou

Studies on the inner-shell electron excitation by heavy ion bombardment have been made by many authors in these several years. Most of the experimental results obtained for the low energy region of projectiles have been explained on the electron promotion mechanism where formation of the molecular orbit between a projectile and a target atom is assumed. If the projectile energy becomes of the order of MeV/nucleon, the excitation mechanism is considered to be different from that in the low energy region. The Coulomb interaction between a projectile and an electron seems to play an improtant role,[1),2)] but experiments in this energy region have been reported in a few cases. The present experiment was intended to obtain information about the inner-shell excitation mechanism in the high energy region.

The characteristic K and L X-rays from various elements excited by bombarding the target atoms with 5 MeV/nucleon N^{4+} ions and α-particles have been measured with a high resolution Si(Li) detector. Target elements studied were $_{24}$Cr, $_{26}$Fe, $_{29}$Cu, $_{38}$Sr, $_{47}$Ag, $_{56}$Ba, $^{142}_{60}$Nd, $_{71}$Lu, $_{82}$Pb, and $_{83}$Bi. The targets of Cr, Fe, Cu, Ag, Pb, and Bi were made by evaporating these metallic elements on the backing, while the others were made by sedimentation of their insoluble compounds. Mylar film of 4 μm was used as the backing except Ag, for which a thinner Formvar film was used. Thickness of the target materials ranged from about 20 for Cr to about 350 $\mu g/cm^2$ for Bi.

Only the K X-rays were measured for elements lighter than Sr. In order to check contributions of the nuclear Coulomb excitation to the X-ray spectrum, γ-ray spectra were also measured with a Ge(Li) detector. The target was inclined at 45° with respect to both the particle beam and the exit window of X-rays, and the X-rays emerging at 90° to the beam were detected. Between the target and the detector, there were two 50 μm Be foils, i.e. a window of the target chamber and that of the detector, in addition to air of about 7 mm. The relative efficiency of the Si(Li) detector was determined in the same source-detector arrangement by using X-rays and γ-rays from radioisotopes, ^{54}Mn, ^{57}Co, ^{65}Zn, ^{109}Cd, ^{137}Cs, and ^{203}Hg. The effects on the efficiency of absorption of X-rays in the materials mentioned above and of back-scattering from the backing were thus eliminated. The relative efficiency curve obtained is shown in Fig. 1.

The energy shift of X-rays was estimated by comparing the peak positions in the spectra of the X-rays from the particle-excited target atoms and those from the radioisotopes, ^{54}Mn, ^{57}Co, ^{65}Zn, ^{88}Y, ^{109}Cd, ^{137}Cs, ^{143,144}Pm, ^{175}Hf, and ^{207}Bi. The daughters of these isotopes emit

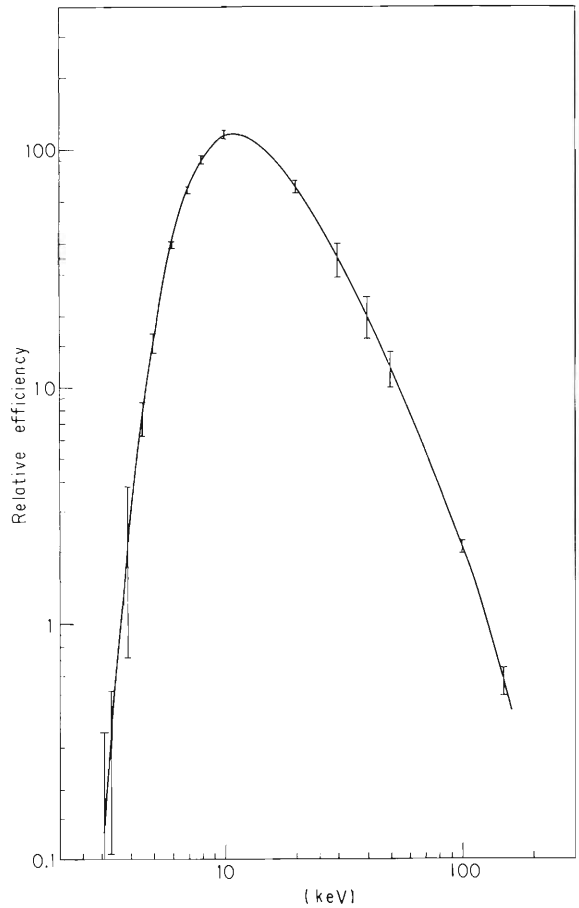

Fig. 1. Relative efficiency curve of the Si(Li) detector. Geometrical factors are included.

the same characteristic X-rays as those from the corresponding target elements but for Bi. The peak position was determined by using the code of chi-square-fit assuming the pattern of a peak to be Gaussian. Unresolved peaks were also separated by the same code. In case of L X-rays that consist of many components, the peak separation was made by referring to the transition probabilities calculated by Scofield.[3] Typical spectra of K and L X-rays obtained by N ion and α-particle bombardments and those from the radioisotopes are presented in Fig. 2.

The amounts of the energy shift of X-rays observed in the N ion bombardment are shown in Figs. 3 and 4. The shifts in $K\alpha_1$ and $K\alpha_2$ lines are the same when these peaks can be separated. The shift of $K\beta_1$ X-ray, which is dominantly affected by the number of vacancies in L-shell, becomes maximum at $Z \simeq 38$. This may reflect the fact that the vacancy production cross section for the L-shell becomes maximum when the condition $Em_e/Mu_L \simeq 1$ is satisfied, where, E is energy of the projectile; M: mass of the projectile; m_e: electron mass; and u_L: binding energy of L-shell electron. This condition has been derived from the binary encounter model[4] in which it is assumed that the interaction leading to the inner-shell excitation is the Coulomb interaction. No shifts were observed in the case of α-particle bombardment within the error of measurements.

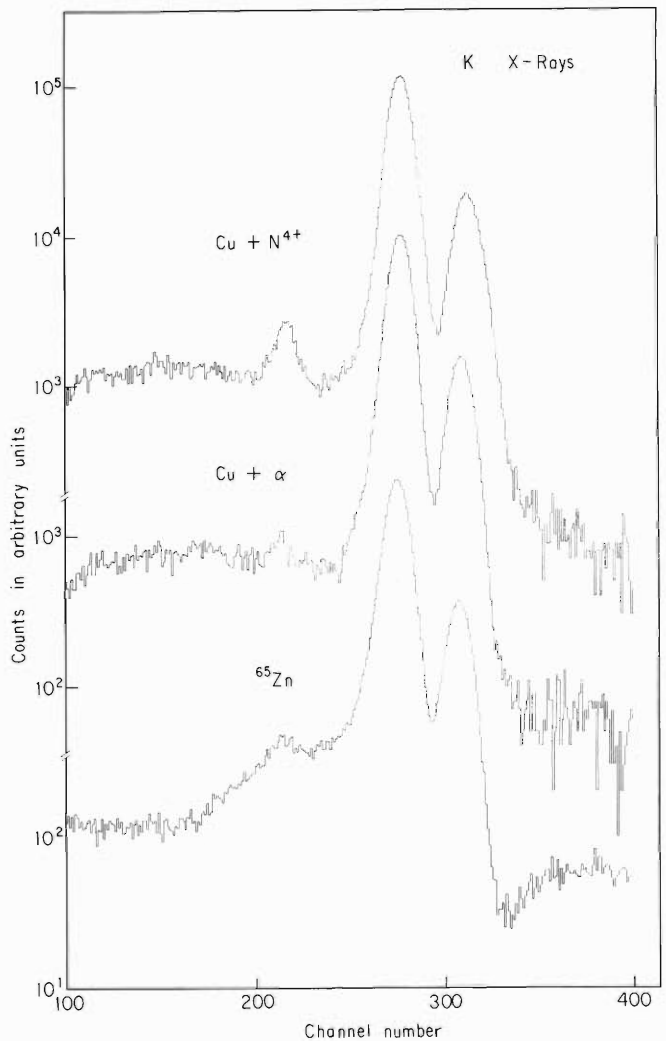

Fig. 2. (a) Spectra of K X-rays obtained by N ion and α-particle bombardments on Cu target and by the decay of ^{65}Zn.

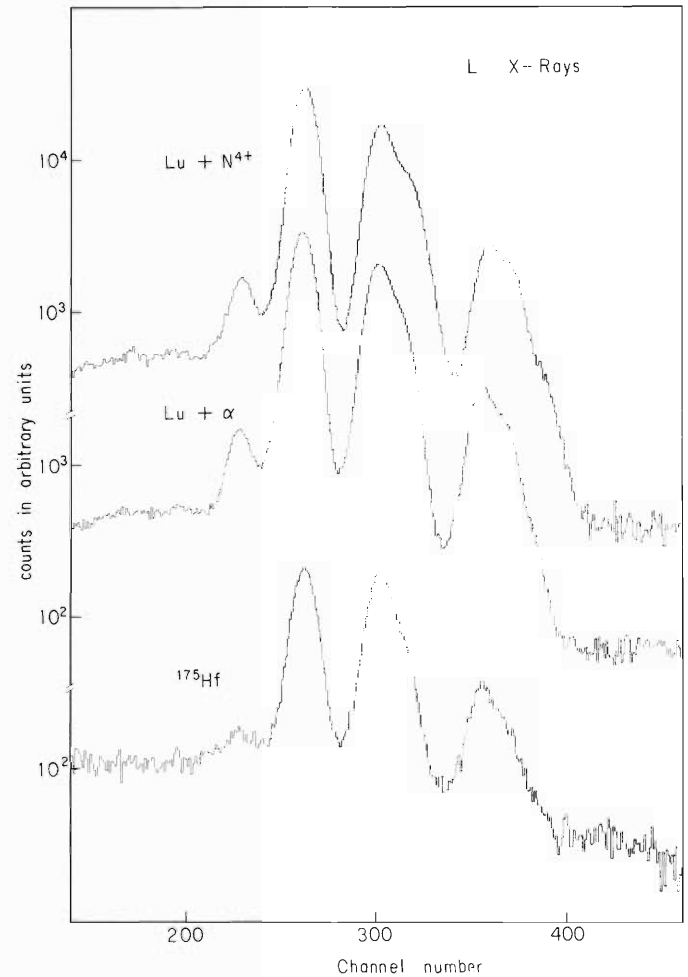

Fig. 2. (b) Spectra of L X-rays obtained by N ion and α-particle bombardments on Lu target and by the decay of ^{175}Hf.

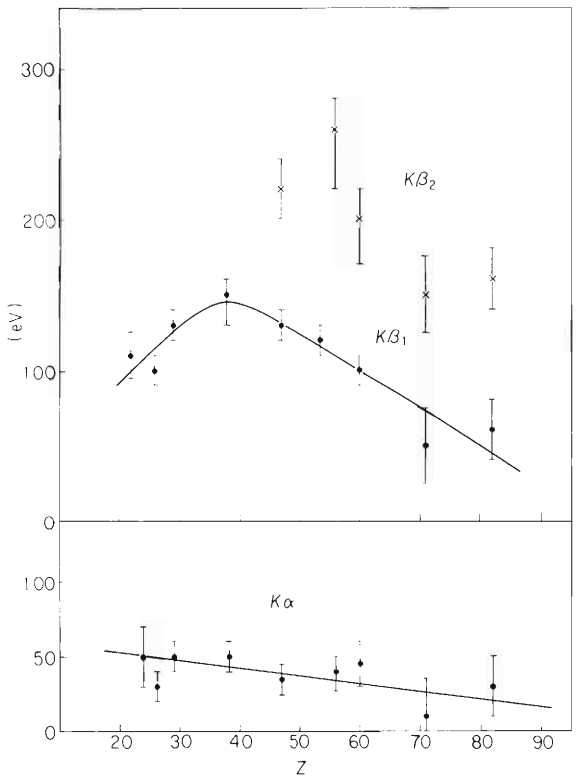

Fig. 3. Energy shift of Kα, Kβ1 and Kβ2 X-rays.

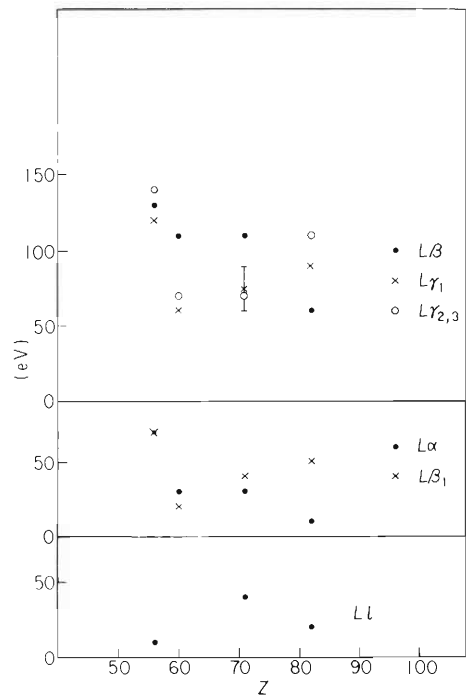

Fig. 4. Energy shift of L X-rays.

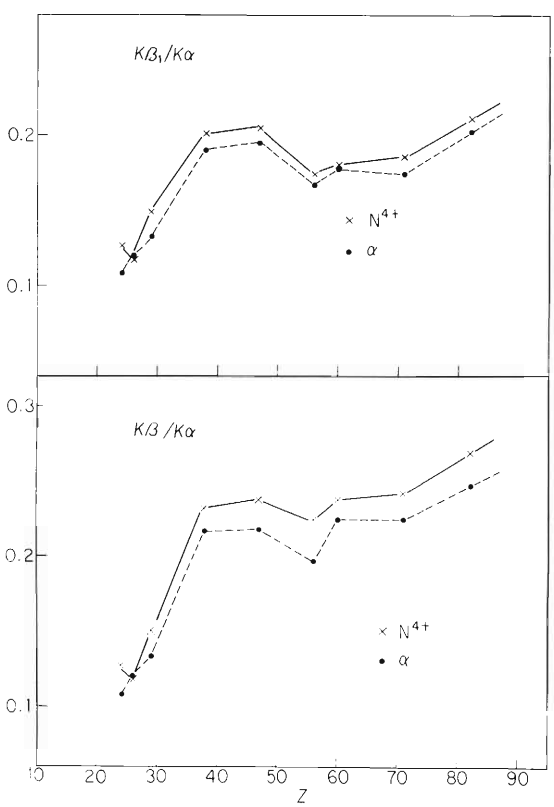

Fig. 5. Kβ/Kα values obtained by N-ion and α-particle bombardments.

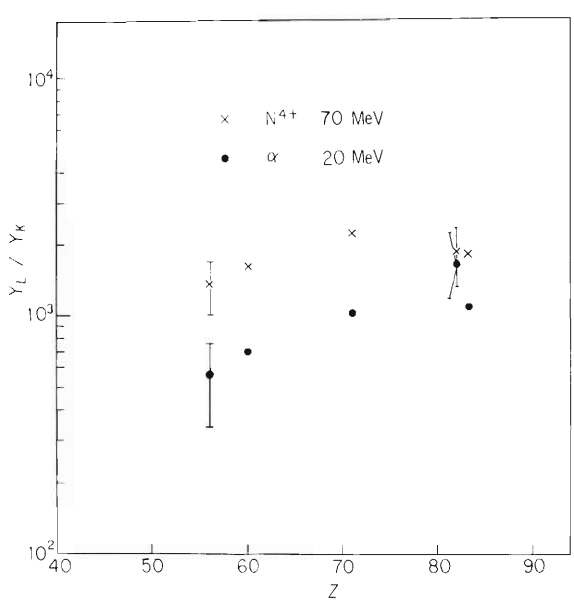

Fig. 6. Intensity ratio of K and L X-rays obtained by N ion and α-particle bombardments.

The variations of intensity ratios Kβ/Kα with the atomic number are shown in Fig. 5. A similar tendency of variation is found for the N-ion and α-particle bombardment. The ratios of K and L X-ray yields for N ions and α-particles are shown in Fig. 6.

The ratio of the K X-ray yields obtained for N-ion and α-particle bombardments is shown in Fig. 7. As the charge of N ion changes in the target, it is difficult to estimate its effective charge at the Faraday cup exactly. But, when the work on the charge exchange done by Tonuma et al.[6] and the thickness of the targets are taken into account, it may be concluded that it is not so different from the equilibrium charge state, 6.9?) Assuming the fluorescence yields for both cases to be the same, this intensity ratio means the ratio of K-shell vacancy production cross sections. If the atomic Coulomb interaction causes the inner shell excitation, the cross section will show the z_p^2-dependence,[4),5)] where z_p is the atomic number of the projectile. Then the value of z_N^2/z_α^2 becomes 12.25. The result expressed in Fig. 7 shows that, roughly speaking, the inner-shell excitation in this energy region is mainly due to the Coulomb interaction.

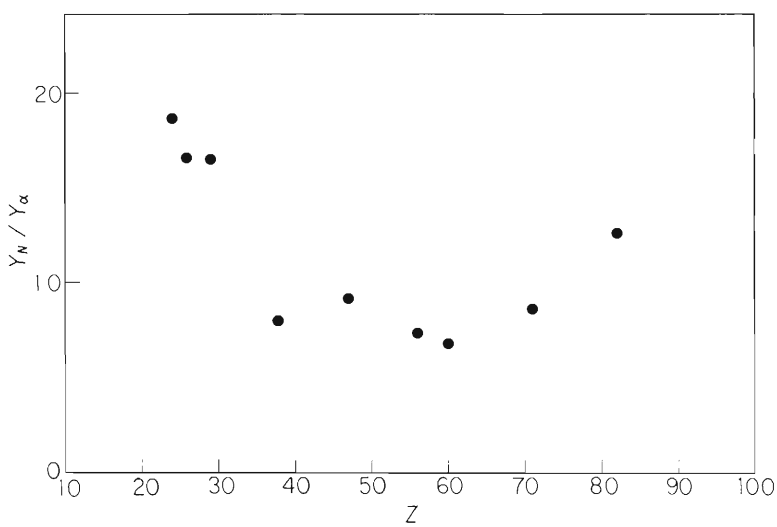

Fig. 7. Ratio of K X-ray yields obtained by N-ion and α-particle bombardments.

The present experimental results are the preliminary ones to which some corrections should be made. These corrections and the theoretical analysis of the results are now in progress.

References

1) M. J. Saltmarsh, A. vander Woude, and C.A. Ludemann : Phys. Rev. Lett., 29, 329 (1972).
2) J. M. Hansteen and O. P. Mosebekk : ibid., 29, 1361 (1972).
3) J. H. Scofield : Phys. Rev., 179, 9 (1969).
4) J. D. Garcia : ibid., A 1, 280 (1970).

5) E. Merzbacker and H. W. Lewis : Handbuch der Physik, Springer-Verlag, Berlin, 34, 166 (1958).

6) T. Tonuma, I. Kohno, Y. Miyazawa, F. Yoshida, T. Karasawa, T. Takahashi, and S. Konno: J. Phys. Soc. Japan, 34, 148 (1973).

7) A. B. Wittkower and H. D. Betz : Atomic Data, Academic Press, New York and London, 5, 113 (1973).

7-2. Inner-Shell Excitation by N Ions and Alpha Particles (2)

K. Izumo, Y. Tendow, Y. Awaya, T. Katou, M. Okano,
A. Hashizume, T. Takahashi, and T. Hamada

In the study of inner-shell excitation of atoms bombarded with high-energy ions, a continuous energy distribution of photons is always observed as a background in the low energy region of X-ray spectra.[1] Watson et al.[2] ascribed this continuum mainly to bremsstrahlung arising from accelerated electrons produced by ionization of target atoms, but no further detail has been given in his paper.

The experimental results obtained for X-rays emitted from various target materials bombarded with alpha-particles or N-ions, some examples of which are presented in Fig. 1 (a)~(d), show the following features in the above-mentioned continuum:

(1) The spectral distribution of photons falls off rather rapidly with increasing energy and its end-point energy is quite low compared with the projectile energy.

(2) The end-point energy is almost independent of the atomic number of the target material and also of the species of projectiles provided that their energies per nucleon are the same.

These findings lead us to an anticipation that the continuum would be due to bremsstrahlung from recoil electrons (delta-rays) created by the projectiles within the target. To confirm this, we have made a rough estimation of the contribution from the bremsstrahlung to the X-ray spectra, assuming the following procedures:

(i) an incident ion collides with electrons in the target;

(ii) the recoil electrons radiate bremsstrahlung when they are passing through the electric fields of the target atoms;

(iii) a fraction a(k) of the radiated photons having a momentum k goes through the target itself, the backing material if any, the windows of the target chamber and the detector, and the air between these two windows;

(iv) photons having a momentum k are detected by the Si(Li) detector with an efficiency $\varepsilon(k)$.

Then the momentum distribution of the photons dc(k)/dk is expressed by the following equation :

$$\frac{dc(k)}{dk} = I_0 \int \sigma_{sc}(E_i, E_e)\, \rho_e \cdot \sigma_B (E_e, k)\, \rho_a\, dE_e \cdot a(k)\varepsilon(k),$$

where I_0 : flux of the incident particles of energy E_i ;

$\sigma_{sc}(E_i, E_e)$: scattering cross section in which an incident ion of energy E_i transfers an energy E_e to an electron;

$\sigma_B (E_e, k)$: radiation cross section in which a photon of momentum k is emitted by

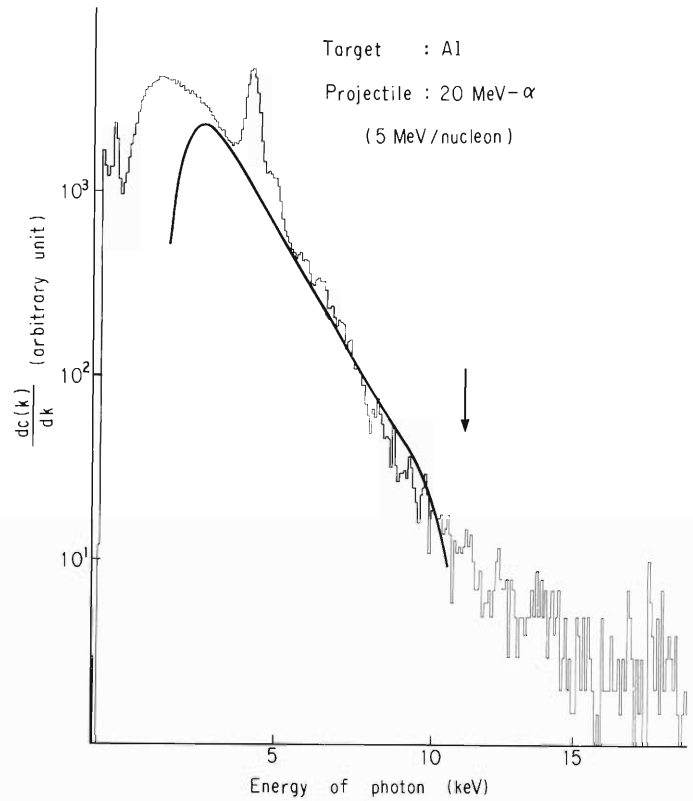
Target : Al
Projectile : 20 MeV-α
(5 MeV/nucleon)
10^3
10^2
10^1
$\frac{dc(k)}{dk}$ (arbitrary unit)
5
10
15
Energy of photon (keV)

Fig. 1(a)

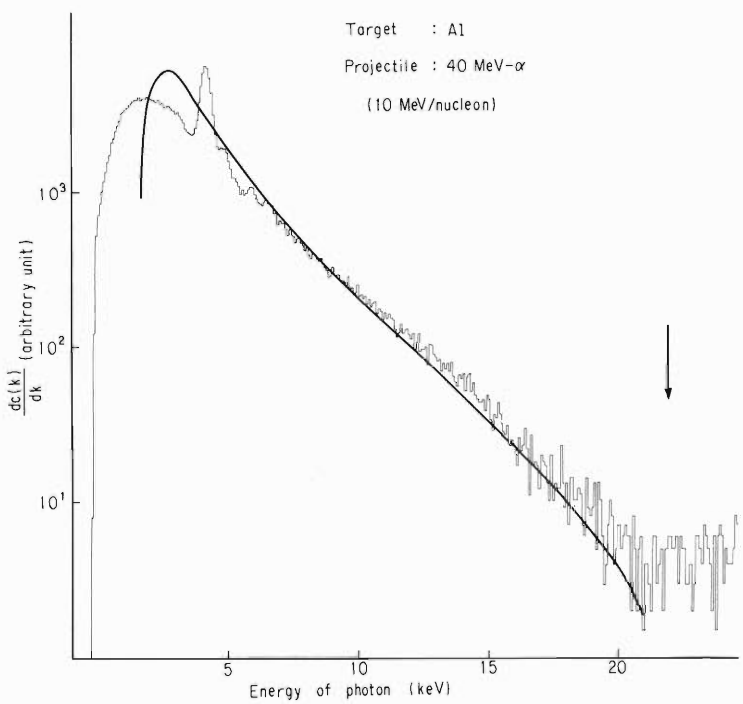
Target : Al
Projectile : 40 MeV-α
(10 MeV/nucleon)
10^3
10^2
10^1
$\frac{dc(k)}{dk}$ (arbitrary unit)
5
10
15
20
Energy of photon (keV)

Fig. 1(b)

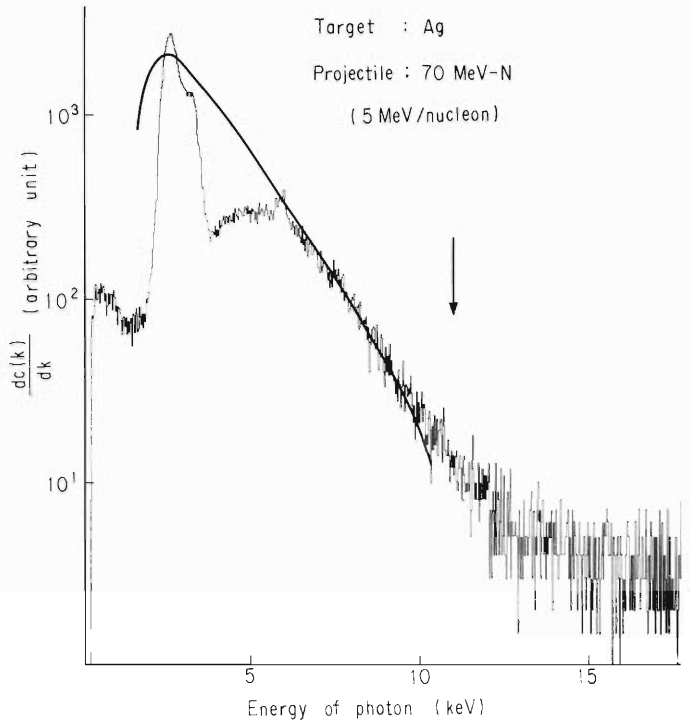

Fig. 1(c)

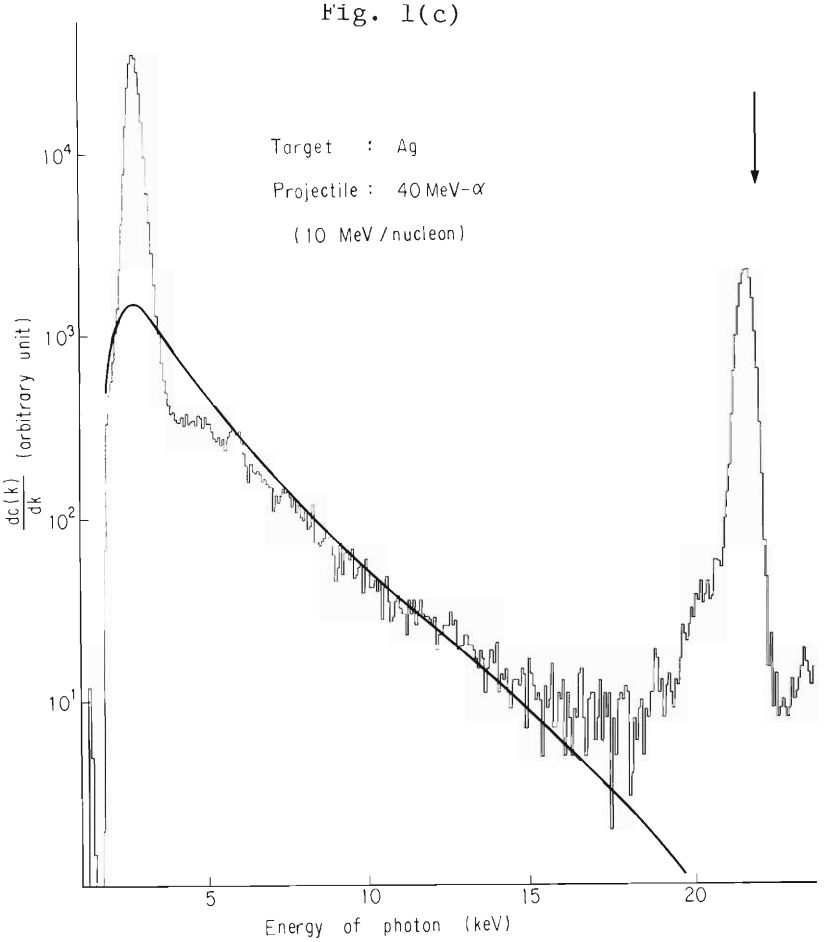

Fig. 1(d)

Fig. 1 (a) ~ (d) X-ray spectra obtained for various conditions of ion bombardment as indicated in each figure. The calculated energy distribution of bremsstrahlung photons is represented by solid lines. An arrow mark in each figure shows the position of end-point energy expected by our estimation.

an electron of energy E_e;

ρ_e, ρ_a : number of electrons and that of target atoms per unit area of the target, respectively.

We have neglected the binding energy of electrons on account of large momentum of the incident particles and effects of finite thickness of the target materials. Electrons are treated here as non-relativistic.

In our case the Rutherford cross section[3] is represented by

$$\sigma_{sc}(E_i, E_e) = \frac{\pi (z_i e^2)^2}{E_i} \cdot \frac{m_i}{m_e} \cdot \frac{1}{E_e^2}$$

and the non-relativistic σ_B is written by the equation:[4]

$$\sigma_B(E_e, k) = \frac{16}{3} \cdot \alpha Z^2 r_0^2 \left(\frac{m_e C}{p_e}\right)^2 \cdot \frac{1}{k} \cdot \ell n \frac{p_e + p_e'}{p_e - p_e'},$$

where α : fine structure constant;

z_i and m_i : charge state and mass of incident particle, respectively

Z : atomic number of target atom;

p_e and p_e' : momentum of a recoil electron before and after photon emission, respectively;

r_0 : classical radius of electron.

Now we consider only a relative behavior of dc(k)/dk. After simple calculations, we get

$$\frac{dc(k)}{dk} \propto \frac{1}{k^3} \left\{ \frac{2}{3}\left(\frac{p'}{p}\right) + \frac{1}{6}\frac{1}{p^2}\left(\frac{p'}{p}\right) - \frac{1}{4}\frac{1}{p^4} \ell n \frac{p+p'}{p-p'} \right\} a(k)\varepsilon(k),$$

where

$$p = \sqrt{k_{max}/k}$$

$$p' = \sqrt{p^2 - 1}$$

$$ch\, k_{max}\,(\text{in keV}) = 2.2E_0,$$

and E_0 : energy of incident particle in MeV per nucleon.

The product of a(k) and ε(k) has been obtained experimentally and its energy dependence is shown in Fig. 1 of the preceding paper.[1] In the lower energy region, however, it is very difficult to find appropriate photon sources for calibration. So, we used the efficiency curve only above 10 keV. In the lower energy region we assumed $\varepsilon(k) = 1$ and estimated a(k) for absorption by the two beryllium windows and air between the target and the detector.

Our results for the energy distribution of the bremsstrahlung photons are shown graphically in Fig. 1(a)~(d) as well as the experimental ones, where the theoretical curves shown as solid lines have been adjusted up and down to fit the experimental distribution best in the slope region, and an arrow mark in each figure shows the position of end-point energy expected by our estimation.

Considering the simplicity of our estimation the agreement between the estimated distribution and the experimental one is fairly good in each case. For the end-point energy

and the slope of higher energy side the agreement is quite sufficient. Remarkable discrepancy in the extremely low energy part should be attributed to some other factors not considered here. Especially, in case of the Ag-target, it will be explained in terms of absorption of photons in the target material.

References

1) Y. Awaya, T. Hamada, M. Okano, A. Hashizume, T. Takahashi, K. Izumo, Y. Tendow, and K. Katou : IPCR Cyclotron Progr. Rep., 7, 87 (1973).
2) R. L. Watson, J. R. Sjurseth, and R. W. Howard : Nucl. Instr. Methods, 93, 69 (1971).
3) E. Gerjuoy : Phys. Rev., 148, 43 (1966).
4) J. M. Jauch and F. Rohrlich : "The Theory of Photons and Electrons", Addison-Wesley (1954); W. Heitler : "The Quantum Theory of Radiation", 3rd ed., Oxford Press (1954).

7-3. Positron Annihilation in V and Nb

N. Shiotani, T. Okada,
H. Sekizawa, and T. Mizoguchi

As a part of systematic studies of the electronic structure of transition metals, we have measured the angular distributions of two γ-rays resulting from annihilation of positrons in V and Nb.

The angular distribution curves were taken using a parallel-slit system. The geometrical angular resolution was 0.70 milliradian. An about 300 milliCurie ^{58}Co source was used. The electronic coincidence counting system used was a standard one with a resolving time of 100 nsec. The coincidence counting rate $N(\theta)$ was measured at an angle θ, and due corrections were made on it for the decay of the source and the accidental coincidence. The final counting rate as a function of the angle was obtained by summing up the counting rates of several runs with proper weights. A vanadium single crystal of 99.999 % purity and a niobium single crystal of 99.99 % purity were cut normal to the [100], [110], and [111] directions of crystals. The surfaces of these crystals were chemically etched to remove distortions introduced during mechanical cutting and then finished by electropolishing. All measurements were done at room temperature.

The experimental results on vanadium and niobium are shown in Figs. 1 and 2, respectively. These curves show the annihilation rate as a function of the photon momentum perpendicular to the γ-rays, P_z. They are not deconvoluted with the angular resolution functions of the system and of the thermal motion of positrons. The area under each curve is normalized to a constant. The smoothed curves drawn through the experimental points were obtained by a procedure equivalent to evaluating at θ_i the least-squares polynomial of degree 3 relevant to the five successive points $(N(\theta_{i+k}), \theta_{i+k})$, (k=−2, −1, -----, 2). The positions of the first Brillouin zone boundaries along the [100], [110], and [111] directions are indicated by the letters H, P, and N, respectively in Figs. 1 and 2. The anisotropy in the electronic structure is clearly manifested in the angular distributions. When the angular distribution curves are normalized to the same area, there are little difference between V and Nb except for the fine structures on the [100] curve of Nb near $P_z = 0$. At $P_z = 0$, the [110] curve is the highest in counting rate, followed by the [111] curve, and the [100] curve is the lowest. There is a concavity at H on the [100] curve. But no visible concavity is found at N or at P on the [110] and the [111] curves, respectively. Beyond the zone boundaries there exsist some anisotropies.

According to the energy band structures of V calculated by Wakoh and Yamashita,* the first conduction band is completely filled, the second band has a closed hole pocket, and the

* S. Wakoh and J. Yamashita : Private communication.

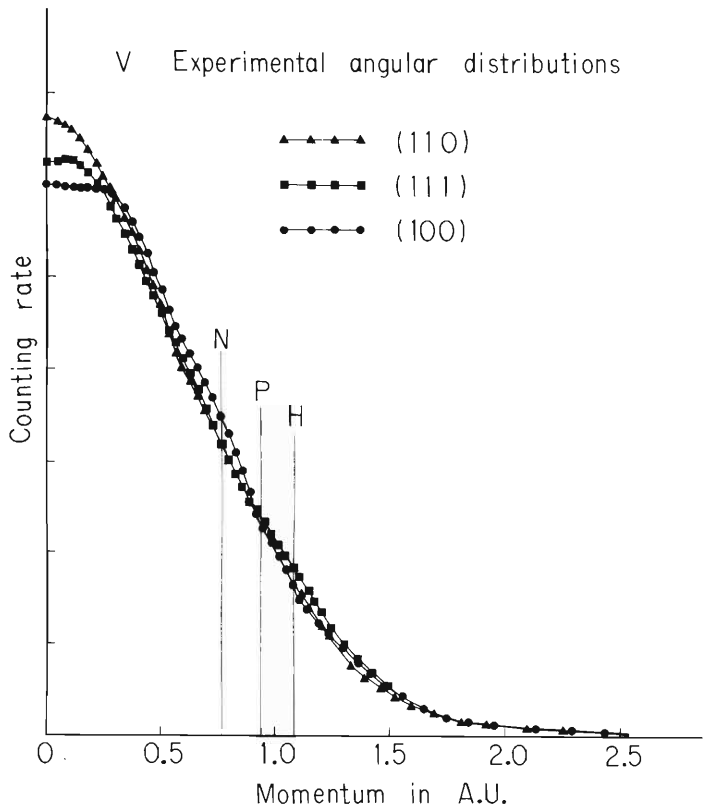

Fig. 1.

Experimental angular distributions in V along three principal axes of the crystal. N, P, and H indicate the positions of the first Brillouin zone boundaries along [110], [111], and [100] directions, respectively. The angle θ is converted to the momentum $P_z = mc\,\theta$ and indicated on the abscissa in atomic unit.

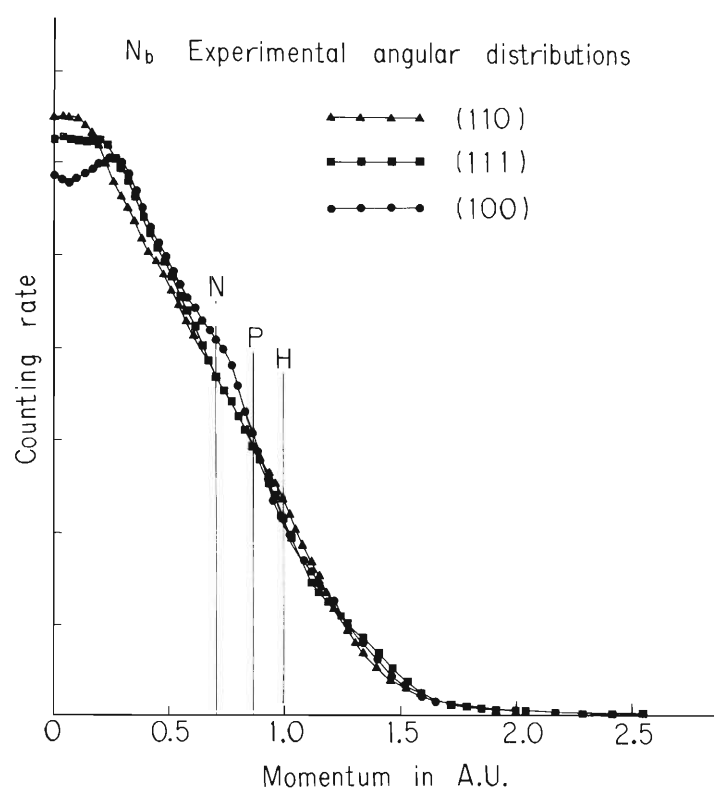

Fig. 2.

Experimental angular distributions in Nb along three principal axes of the crystal. N, P, and H indicate the positions of the first Brillouin zone boundaries along [110], [111], and [100] directions, respectively.

third band has a set of hole surfaces which are in distorted ellipsoidal shape and a multiply connected jungle-gym hole surfaces consisting of interconnecting arms along [100] directions.

Based on the above mentioned band structures of V, we have proposed a tentative explanation for the observed anisotropies in the angular distribution curves.[2] The shape of the distribution curves are for the most part determined by the filled band. The partly filled d-bands add fine structures to the curves. In particular, the presence of the jungle-gym hole arms along [100] directions and hole surfaces is reflected on the shapes of the angular distribution curves, especially the flat top and the concavity on the [100] curve.

Reference

1) N. Shiotani, T. Okada, H. Sekizawa, T. Mizoguchi, and S. Wakoh : 3rd Int. Conf. on Positron Annihilation, Otaniemi, Finland (1973).

7-4. Positron Annihilation in Paramagnetic Nickel Single Crystal

T. Okada, H. Sekizawa, T. Mizoguchi, and N. Shiotani

Recently, we investigated the angular correlation of positron annihilation in ferromagnetic nickel at room temperature, and the results have been reported already elsewhere.[1)]

The study has been extended to the paramagnetic state, i.e., above the ferromagnetic Curie temperature of 358°C. The experimental apparatus was almost the same as in the previous report[1)] except high-temperature specimen holder. The (110) nickel single crystal disc was mounted on a heat-insulated plate with a heater and fixed in an evacuated holder having a window of 5 μm stainless steel foil. The positron source was put just outside the window facing the crystal. Two glass-covered windows on both sides of the holder were provided for the emitted γ-rays. A conventional combination of two long-slit scintillation counters and an electronic circuit system for coincidence was employed for the detection of 511 keV γ-rays.

The angular correlation curve obtained at 360°C is shown in Fig. 1 along with the curves at room temperature with the external magnetic field applied parallel or antiparallel to the positron beam. Deconvolution procedures to take account of the finite instrumental resolution are not yet applied to these curves. The decrease in resolution due to the thermal effect would be much pronounced for the paramagnetic curve. However, a rough estimation of the effect revealed that it cannot account for the remarkable change in the shape of the paramagnetic curve compared with the ferromagnetic ones. We have tried[1)] to explain the shapes of the ferromagnetic curves based on the shapes of the Fermi surfaces of nickel calculated by

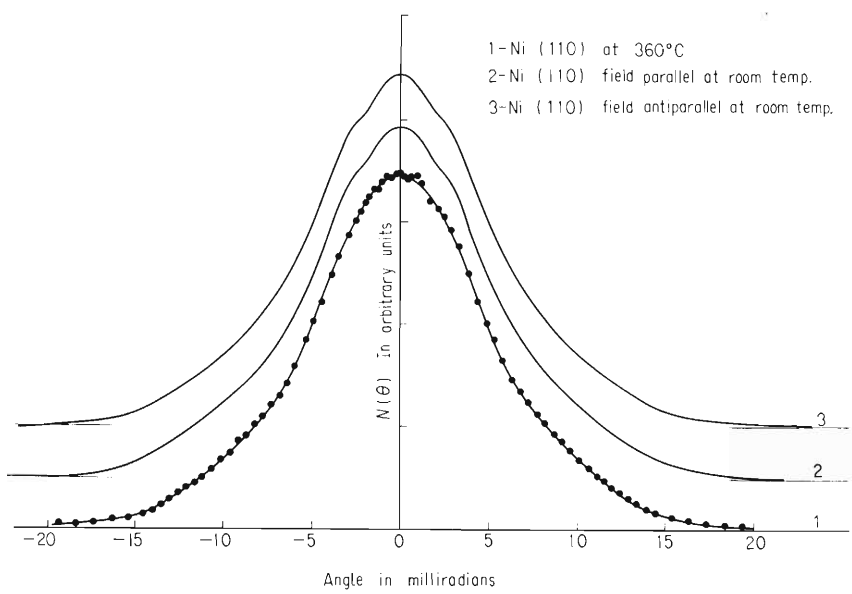

Fig. 1. The angular correlation curves of (110) nickel single crystal at 360°C and at room temperature.

Connolly,[2] but without much success. Elaborate calculation of the matrix elements dominating the momentum dependence of the positron annihilation processes based on the calculation of electron and positron wave functions would be indispensable for further discussions.

Further experiments on crystals with orientations other than (110) and detailed theoretical considerations are in progress.

References

1) N. Shiotani, T. Okada, H. Sekizawa, T. Mizoguchi, and T. Karasawa : J. Phys. Soc. Japan, 35, 456 (1973).

2) J. W. Connolly : Phys. Rev., 159, 415 (1967).

7-5. Point Defects in Irradiated Copper and Cu_3Au

H. Sakairi, E. Yagi, A. Koyama,
T. Karasawa, and R. R. Hasiguti

The purpose of this study is the identification of point defects contributing to annealing stages appearing on metals damaged by irradiation. A series of experiments on copper and ordered Cu_3Au alloy were already performed.

This year, the annealing of disordered Cu_3Au alloy irradiated at liquid helium temperature was experimented. Initial specific resistivities of disordered Cu_3Au specimens used in two irradiation runs were 9.995 and 9.649 $\mu\Omega$·cm respectively. Each was irradiated by 17 MeV alpha particles from the cyclotron, together with a pure copper specimen for comparison. Results of irradiation and stage I annealing are listed in Tables 1 and 2. The increase of resistivity of disordered Cu_3Au is about three times as large as that of Cu. However, the amount of the stage I recovery of the alloy is smaller than that of Cu. That is, the stage I annealing of disordered Cu_3Au is suppressed compared with that of Cu. The origin of the difference between $\Delta\rho^{I}(Cu_3Au)$ for two runs are not certain. It may be ascribed to the difference of the initial degree of disorder shown by the difference between initial specific resistivities of two specimens.

These results support the explanation of the annealing process with the conversion-two-interstitial model,[1] in which the stages I and III annealings are supposed to be caused by the migration of crowdion type metastable interstitials and split type stable ones, respectively.

Table 1. Resistivity increase by irradiation.

	Dose ($10^{-15}\alpha/cm^2$)	$\Delta\rho$ (Cu_3Au) (10^{-8} ohm·cm)	$\Delta\rho$ (Cu) (10^{-8} ohm·cm)
Run I	1.45	4.4	1.46
Run II	1.56	5.1	1.70

Table 2. Resistivity decrease by stage I annealing.

	$\Delta\rho^{I}(Cu_3Au)$ (10^{-8} ohm·cm)	$\Delta\rho^{I}(Cu)$ (10^{-8} ohm·cm)
Run I	0.40	0.92
Run II	0.14	0.96

With this model, the suppression of the stage I annealing in disordered Cu_3Au can be explained by the conversion of metastable crowdions into stable and less mobile interstitials because of the unsymmetrical atomic configuration in disordered alloy.

Reference

1) W. Bauer, A. Seeger, and A. Sosin : Phys. Lett., 24A, 195 (1967).

8. RADIOCHEMISTRY

8-1. Mössbauer Emission Spectroscopy of ^{119}Sn after the EC Decay of ^{119}Sb

F. Ambe, S. Ambe, and N. Saito

We have been studying the valence state of ^{119}Sn after the EC decay of ^{119}Sb in a variety of matrices by the nuclear gamma-ray resonance (Mössbauer effect) of the 23.8 keV transition of ^{119}Sn.[1)~5)] In this period much amelioration has been attained in the procedures for producing the source nuclides (^{119}Sb and ^{119m}Te),[6)] in the counting system of the resonant gamma-rays, and also in the computer program for analysis of the spectra obtained. Under the

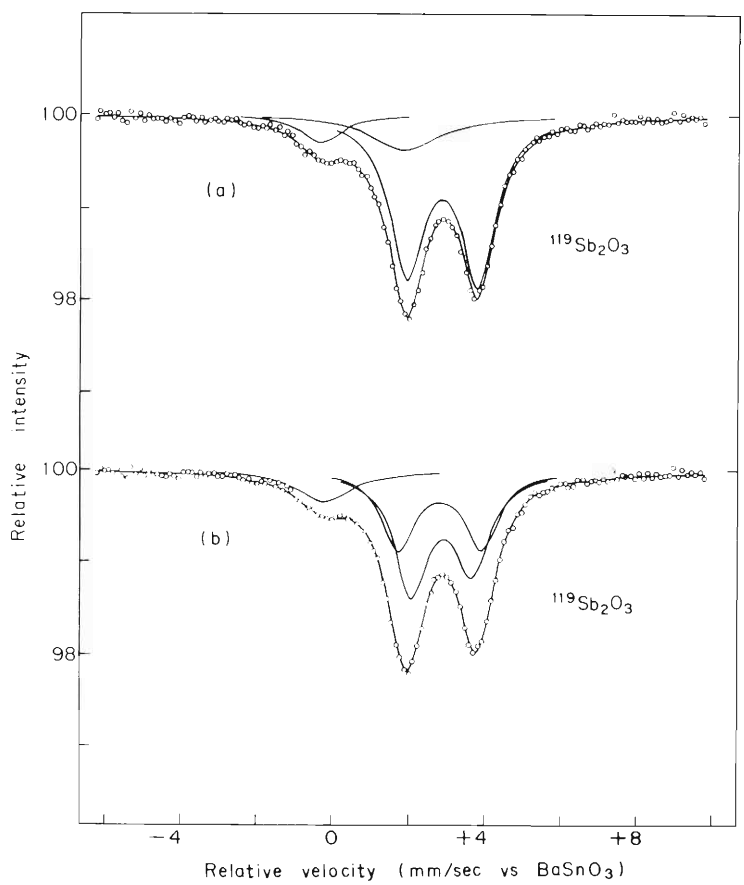

(a) Decomposition into two singlets and a doublet with the same width.

(b) Decomposition into a singlet and a pair of doublets each with the same width.

Fig. 1. Typical results of the computer fitting of the emission spectra of $^{119}Sb_2O_3$.

improved conditions, the emission spectra of the metals, oxides, and chalcogenides of antimony and tellurium were redetermined and analyzed, and, at the same time, the object of the study was extended to other matrices such as halides, compounds with complex ligands and materials containing tin as a macro-component. Some results obtained are described briefly below.

The emission spectrum of $^{119}Sb_2O_3$ was reported already without detailed analysis.[3] Computer decomposition of the spectrum showed that the dominant doublet attributed tentatively to the Sn(II) state is asymmetric both in area and width. Since the Sn(II) ions are in the non-magnetic $^1S_0$ state, asymmetry in area but not in width can be expected for a quadrupole doublet of the Sn(II) species in an isotropic powder sample due to the anisotropy of the Debye-Waller factor. Least-squares fitting of the observed doublet to a pair of Lorentzians with the same width discloses a line with an isomer shift of about 1.9 mm/sec versus $BaSnO_3$ (Fig. 1(a)). The valence assignment of the fourth line is not straightforward on the basis of the Mössbauer data accumulated so far on tin compounds, though the isomer shift suggests metallic tin, sp^3 type Sn(IV) species or an Sn(III) state. Alternately the apparent doublet can be decomposed into two sets of doublets, each with the same width, assuming two different sites of ^{119}Sn atoms in the Sb_2O_3 lattice (Fig. 1(b)).

Reproducibility was finally attained in the emission spectra of $^{119}Sb_2Se_3$[3] as a result of an improvement of the purity of the ^{119}Sb metal used as the starting material. A typical spectrum obtained is shown in Fig. 2. Thus a simple relation was established between the valence distribution of ^{119}Sn and the electronegativity of the ligand for the series of antimony chalcogenides ($^{119}Sb_2S_3$(sublimed samples),[2] $^{119}Sb_2Se_3$, and $^{119}Sb_2Te_3$[2,4]): the fraction of ^{119}Sn in the Sn(II) state increases with the decrease of the electronegativity of the chalcogenide ligands.

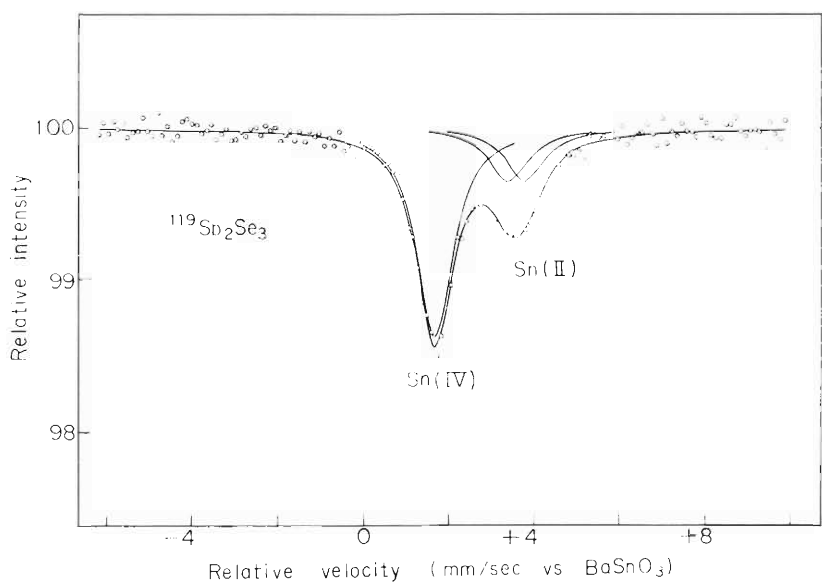

Fig. 2. ^{119}Sn-Mössbauer emission spectrum of $^{119}Sb_2Se_3$ at 78±1 K against $BaSnO_3$. In the abscissa a velocity of approach is taken negative.

The spectra of $^{119}SbI_3$ consisted of two resonance lines assignable to the Sn(II) and Sn(IV) states respectively, as shown in Fig. 3. The result presents an interesting contrast with that of the corresponding chalcogenide, $^{119}Sb_2Te_3$, for which no line was detected in the Sn(IV) region.[2),4)]

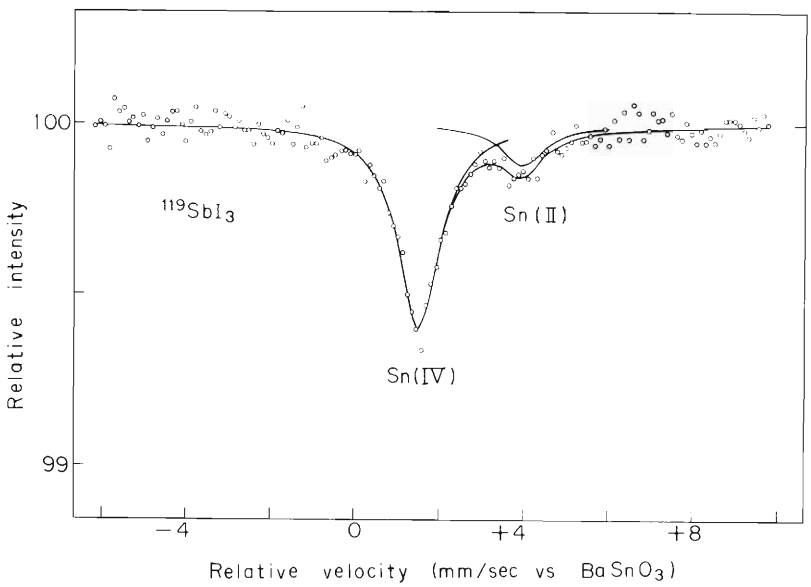

Fig. 3. ^{119}Sn-Mössbauer emission spectrum of $^{119}SbI_3$ at 78± 1 K against $BaSnO_3$. In the abscissa a velocity of approach is taken negative.

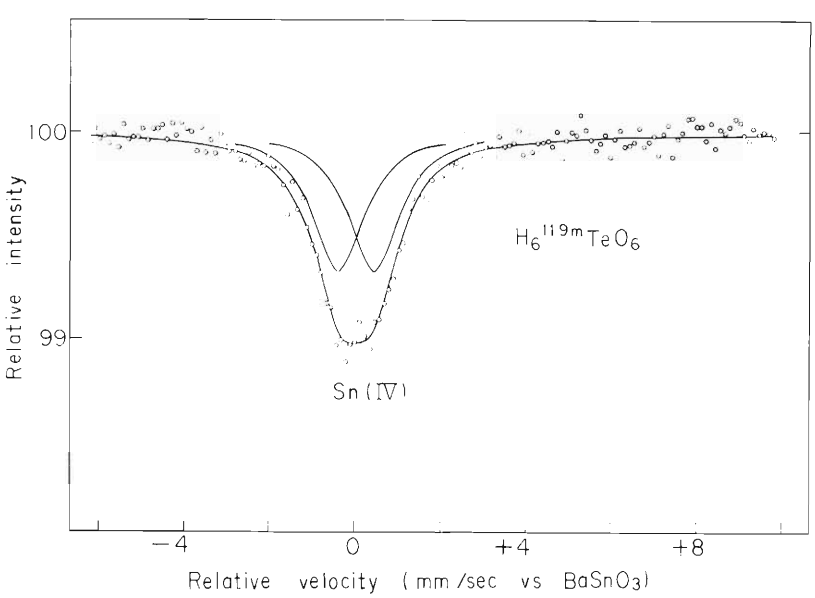

Fig. 4. ^{119}Sn-Mössbauer emission spectrum of $H_6{}^{119m}TeO_6$ at 78± 1 K against $BaSnO_3$. In the abscissa a velocity of approach is taken negative.

Use of ^{119m}Te, a parent nuclide of ^{119}Sb, makes possible studying the valence state of ^{119}Sn produced in matrices with hexavalent cations. Measurements were made on $H_6{}^{119m}TeO_6$ and a typical result is shown in Fig. 4. The spectra are composed of a broad peak centered near the zero relative velocity versus $BaSnO_3$, which may be identified as an unresolved quadrupole doublet of Sn(IV). We have already reported that the ^{119}Sb atoms are distributed between the Sb(III) and Sb(V) states in the ratio of 5 to 95 after the EC decay of ^{119m}Te in $H_6{}^{119m}TeO_6$.[7] Taken together, the change of the valence following the successive EC decays of ^{119m}Te in telluric acid is summarized as follows:

$$^{119}\text{Sn(IV)}\ 100\ \% \begin{cases} \leftarrow\ ^{119}\text{Sb(V)} \quad 95\ \% \leftarrow H_6{}^{119m}\text{Te(VI)}O_6 \\ \leftarrow\ ^{119}\text{Sb(III)} \quad 5\ \% \end{cases}$$

It was also reported already that the ^{119}Sn atoms produced in $Sb_2{}^{119m}Te_3$ are in a different chemical state from those in $^{119}Sb_2Te_3$.[2),5)] A study of this type of defect atoms has further been extended to matrices containing tin as a macro component. A result on $Sn^{119}Sb$* is shown in Fig. 5, together with the absorption spectrum of SnSb. As seen in the figure, it can be concluded that the ^{119}Sn atoms produced in $Sn^{119}Sb$ are in a defect state, whose electronic structure is different from that of the tin atoms in the normal lattice site.

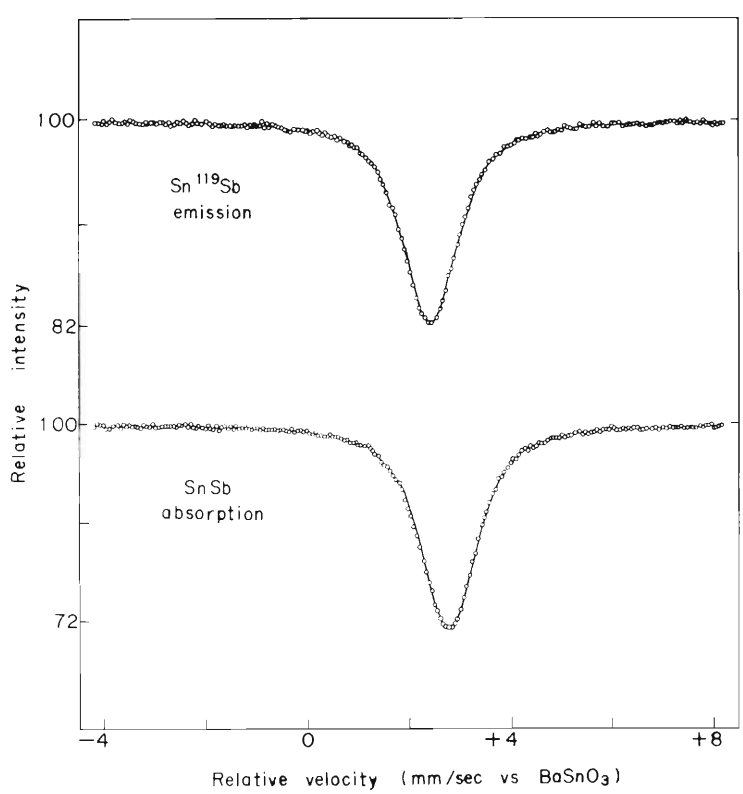

Fig. 5. ^{119}Sn-Mössbauer emission spectrum of $Sn^{119}Sb$ and absorption spectrum of SnSb at 78± 1 K. In the abscissa a velocity of approach is taken negative and positive respectively.

* Tin metal depleted in ^{119}Sn (^{120}Sn 98.39 %, ^{119}Sn 0.39 %) was used in the preparation of the samples to decrease the resonant self-absoption of the Mössbauer gamma-rays in the samples.

References

1) F. Ambe, H. Shoji, S. Ambe, M. Takeda, and N. Saito : IPCR Cyclotron Progr. Rep., 4, 115 (1970).
2) F. Ambe, H. Shoji, S. Ambe, M. Takeda, and N. Saito : ibid., 5, 85 (1971).
3) F. Ambe, S. Ambe, and N. Saito : ibid., 6, 102 (1972).
4) F. Ambe, H. Shoji, S. Ambe, M. Takeda, and N. Saito : Chem. Phys. Lett., 14, 522 (1972).
5) F. Ambe and S. Ambe : Phys. Lett., 43A, 399 (1973).
6) S. Ambe and F. Ambe : IPCR Cyclotron Progr. Rep., 7, 132 (1973) ; F. Ambe, S. Ambe, and H. Shoji : Radiochem. Radioanal. Lett., 15, 349 (1973).
7) S. Ambe, F. Ambe, and N. Saito : IPCR Cyclotron Progr. Rep., 6, 104 (1972) ; Radiochim. Acta, in press.

8-2. Charge States of Ions from ^{18}F Decay

M. Aratani

The charge states of ions from ^{18}F decay were studied by means of a charge spectrometer. It was previously reported that 8+, 7+, and 6+ peaks were "big three" in the charge spectrum of ions from the decay of ^{18}F trapped on metal surfaces. One of the best results recently obtained with a copper surface is shown in Fig. 1. As may be seen, each peak is a doublet. The doublet at the 7+ peak, revealed by the measurement in higher resolution is shown in Fig. 2. According to the values of coil current, the narrow and broad lines are attributed to $^{18}O^{7+}$ and $^{16}O^{6+}$, respectively. $^{18}O^{n+}$ ions are considered to have been derived from ^{18}F atoms just decayed, as was previously reported.[1] ^{16}O species, however, cannot be radiogenic in the present case. ^{16}O atoms have possibly been trapped on the surface of the source during the preparation[2] of ^{18}F by the nuclear reaction, ^{16}O (^{3}He, p)^{18}F. Mechanism of formation of $^{16}O^{n+}$ ions is not yet clear. A series of expetiments will be made on the effect of oxygen on the charge states of recoils from ^{18}F decay.

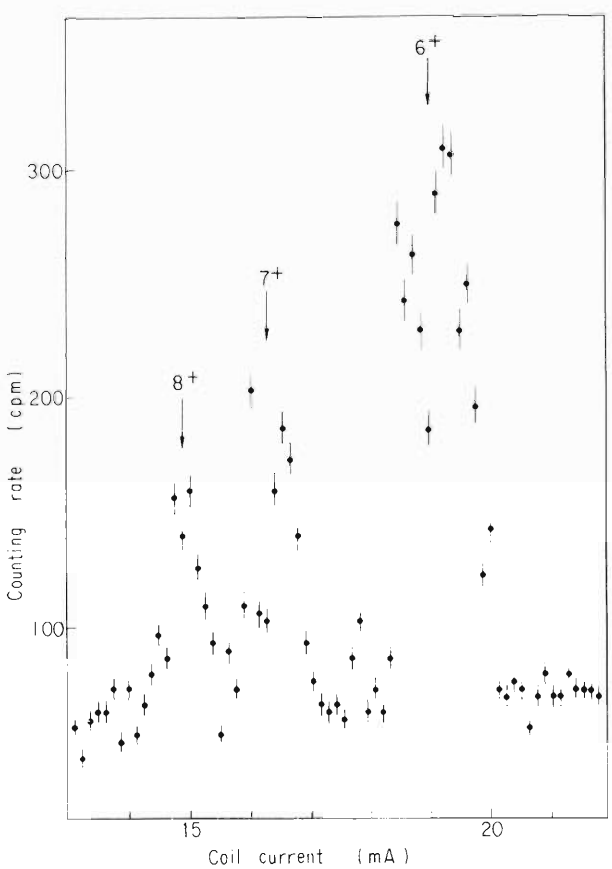

Fig. 1. Highly charged ions from ^{18}F decay.

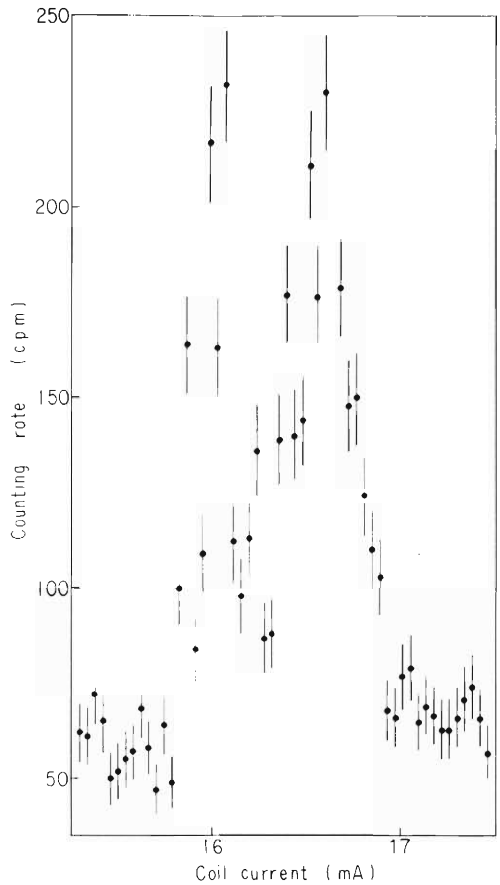

Fig. 2. A doublet at the 7^+ peak.

References

1) S. Yokoi, M. Aratani, and T. Nozaki : IPCR Cyclotron Progr. Rep., 5, 88 (1971).

2) M. Aratani : ibid., 6, 99 (1972).

9. RADIATION CHEMISTRY AND RADIATION BIOLOGY

9-1. Heavy Ion Radiolysis of Liquid Ketones

Effect of Water on the Radiolysis of Acetone

M. Matsui, M. Imamura, and T. Karasawa

The object of this series of heavy-ion radiolysis is to elucidate the characteristic interactions of energetic heavy ions with liquid organic compounds. The heavy ions which have very high LET were shown to induce unique chemical reactions in the radiolysis of liquid compounds in a previous report,[1] in which acetone was dealt with.

Similar results have also been obtained with methyl ethyl and diethyl ketones. For these ketones the yields of H_2 and CO increase with increasing LET and reach maxima in the vicinity of LET = 50 ~ 70 eV/Å. These significant results were explained to be due to the decomposition of ketone molecules inside the reaction zone of a fixed radius. The thermal-spike effect in the track core of the heavy ions was also suggested from the fact that the ratios of $G(H_2)$ to G(CO) increase with increasing LET.

This year we have carried out similar radiolysis experiments with acetone containing a small amount (2 wt %) of water to confirm the above conclusion. Water added to acetone has been known to give rise to an increase of $G(H_2)$ in the γ-radiolysis owing to its reaction

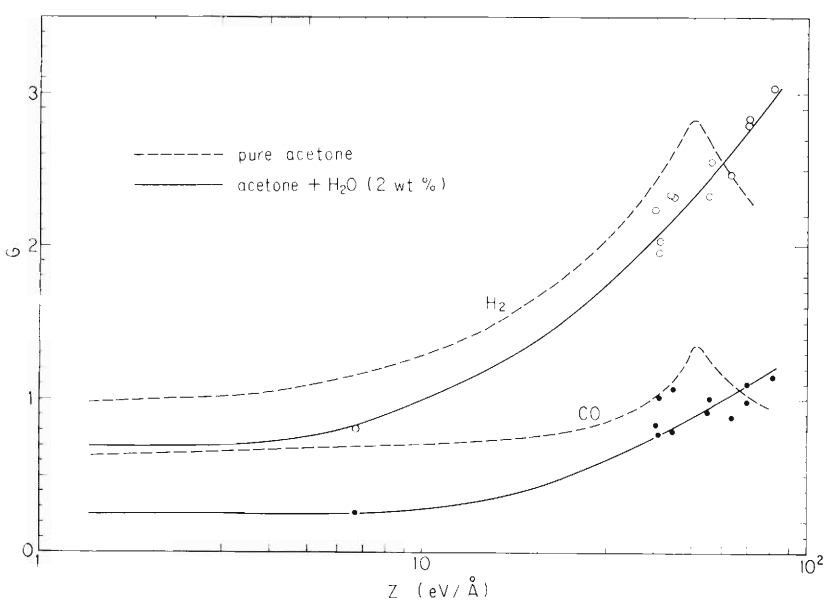

Broken lines show the variation for pure acetone which was reported in Ref. 1).

Fig. 1. Variations with LET of $G(H_2)$ and G(CO) from acetone containing 2 wt% H_2O (solid lines).

with radical cations produced in the radiolysis of acetone. It is also considered that water may form hydrogen bond with acetone molecules, resulting in the transfer of excess energy outside from the core and therefore the disappearance of the peaks of $G(H_2)$ and G(CO).

Since the results of γ-radiolysis revealed that the increase in $G(H_2)$ is invariant between 2 and 5 wt% H_2O, the heavy-ion radiolysis was carried out with acetone containing 2 wt% H_2O. Heavy ions used were ^4He, ^{12}C, and ^{14}N ions, which had energies of 18.9, 30.0 ~ 66.4, and 18.0 ~ 47.5 MeV, respectively.

The results are shown in Fig. 1, where $G(H_2)$ and G(CO) are plotted as a function of the energy-loss parameter defined by $Z = (1/E)\int_0^E (-dE/dx)dE$. (The variations for pure acetone[1] are also illustrated with broken lines.) Both $G(H_2)$ and G(CO) are lower than those for pure acetone in the high LET region below LET $\simeq$ 60 eV/Å and they continue to increase up to the highest LET investigated. The ratio $G(H_2)/G(CO)$ also increases with increasing LET qualitatively similarly as in pure acetone.

The present results seem to indicate that the added water plays a role in enlarging the size of the reaction zone by transferring excitation energy, lowering $G(H_2)$ and G(CO) and probably shifting the peak LET to a much higher value. However, the thermal-spike effect is regarded as being still important considering the increases in $G(H_2)$, G(CO), and their ratio with increasing LET, since, as assumed previously, excess hydrogen in the high LET region is believed to result from thermal decomposition of free radicals produced from acetone.

Some other liquid organic compounds are being subjected to heavy-ion irradiation to confirm the thermal-spike effect in the radiolysis, and the results will be reported in a succeeding paper.

Reference

1) M. Matsui, M. Imamura, and T. Karasawa : IPCR Cyclotron Progr. Rep., 5, 90 (1971); M. Matsui and M. Imamura : Bull. Chem. Soc. Japan, in press.

9-2. ESR Studies of Free Radicals Produced in Organic Crystals Irradiated with Heavy Ions

K. Kimura, M. Matsui, T. Karasawa, and M. Imamura

Electron-spin-resonance studies have been carried out on the heavy-ion irradiated malonic acid and sodium acetate crystals. Along with previous results with eicosane,[1] these results serve to elucidate the distribution of free radicals and the characteristic interaction of heavy ions with matter. Irradiation was carried out with 23.3 MeV He-ions and 85 MeV C-ions as well as with ^{60}Co γ-rays at 77°K. ESR spectra were recorded at 77°K and higher temperatures.

(1) ESR spectra and their power saturation for malonic acid crystal

Figure 1 shows ESR spectra observed at 77°K for the sliced single crystal of malonic acid irradiated with C-ions (a) and γ-rays (b), the static magnetic field being perpendicular to the [100] plane of the crystal. The ESR spectrum for C-ion irradiation is regarded as being due to

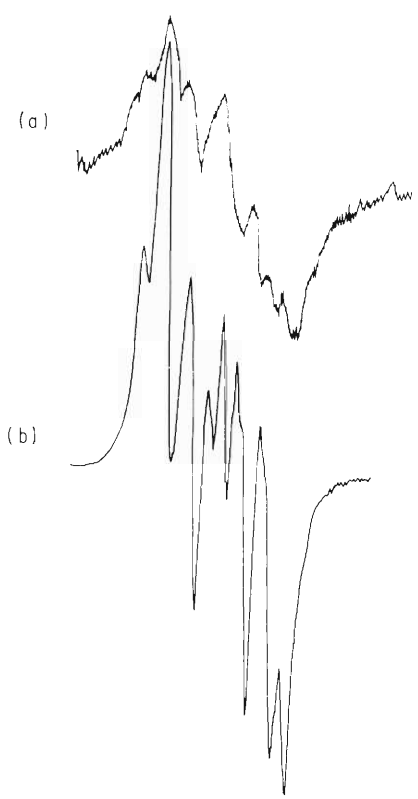

a : Carbon ions at a dose of 1.3×10^{19} eV/g;
b : γ-Rays at a dose of 7.8×10^{19} eV/g.

Fig. 1. ESR spectra of irradiated single crystals of malonic acid. Irradiation and ESR determinations were carried out at 77°K.

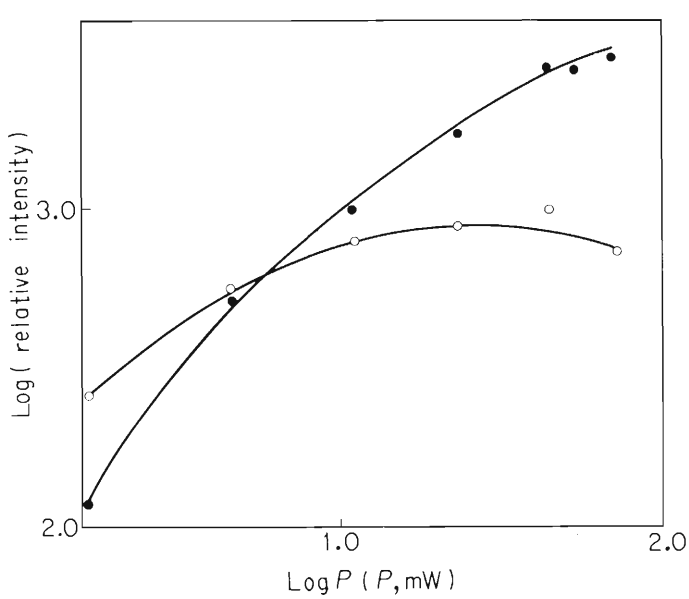

Irradiation and ESR determinations were carried out at 77°K.
● : Carbon ions; ○ : γ-Rays.

Fig. 2. Curves of ESR power saturation of irradiated single crystals of malonic acid.

CH_2COOH and $CH(COOH)_2$ radicals on the basis of its similarity to that for γ-ray irradiation where the formation of these two radicals has been confirmed. The broader line widths of the C-ion spectra may indicate the strong spin-spin interaction between radicals located closely. This assumption is supported by the fact that the ESR spectrum for the C-ion irradiation appears to saturate at a higher microwave-power than that for the γ-irradiation as shown in Fig. 2.

(2) ESR spectra for sodium acetate crystals

In the γ-radiolysis at 77°K, the methyl radical is a principal paramagnetic species in crystalline $CH_3COONa \cdot 3H_2O$,[2] while, in the anhydrous powders, CH_2COO^- and other radicals are

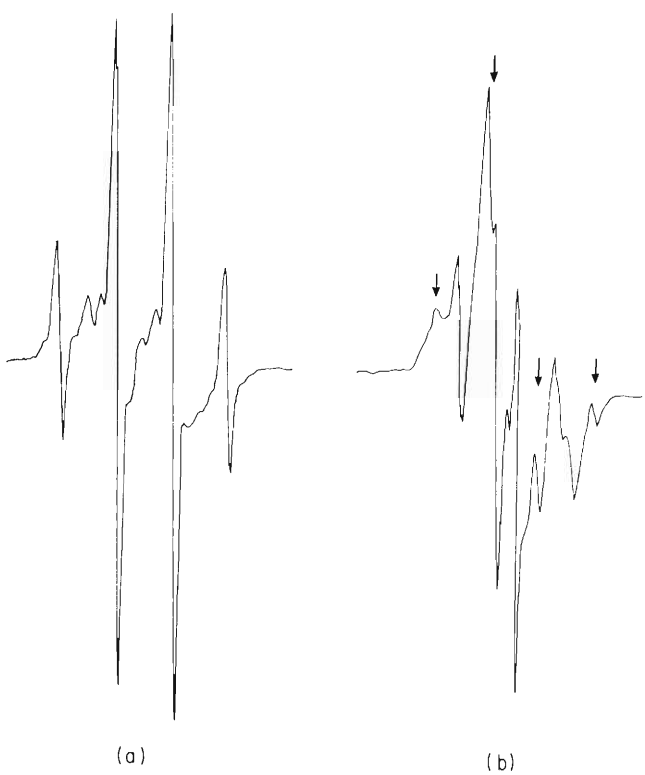

Irradiation and ESR determinations were carried out at 77°K. Arrows indicate the peaks of CH_3 radical.
a : Crystalling $CH_3COONa \cdot 3H_2O$;
b : CH_3COONa

Fig. 3. ESR spectra of γ-irradiated sodium acetate.

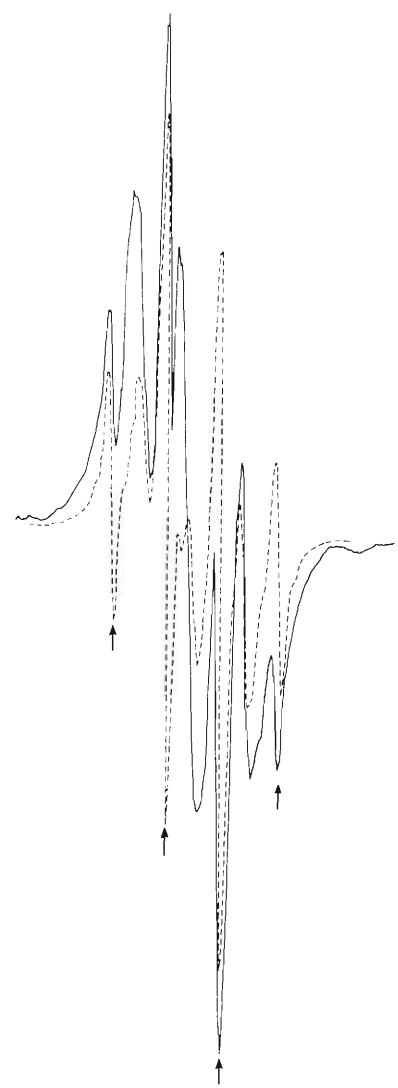

Irradiation and ESR determinations were carried out at 77°K. Arrows indicate the peaks of CH_3 radical.
·····: He ions ; ——: C ions

Fig. 4. ESR spectra of irradiated $CH_3COONa \cdot 3H_2O$ crystals.

produced and CH_3 radical production is reduced as shown in Fig. 3. These results seem to indicate a significant effect of hydration on the nature of radicals produced with γ-rays.

ESR spectra obtained with crystalline $CH_3COONa \cdot 3H_2O$ at 77°K by He- and C-ion irradiations are shown in Fig. 4. A triplet is seen together with a sharp quartet of CH_3 radicals in either case, the relative intensity of the former being lower in the He-ion irradiation though. The triplet absorption has an intensity ratio of 1 : 2 : 1 and a hf splitting constant of about 20 gauss, which is assignable to the absorption due to CH_2COO^- radicals.

The LET dependence of the radical production in sodium acetate crystals is an interesting subject in relation to the hydration effect and further studies are in progress.

References

1) K. Kimura, M. Kikuchi, M. Matsui, T. Karasawa, M. Imamura, Y. Tabata, and K. Oshima: IPCR Cyclotron Progr. Rep., 6, 110 (1972).

2) M. T. Rogers and L. D. Kispert : J. Chem. Phys., 46, 221 (1967).

9-3. Inactivation of Bacterial Cells by Charged Particles

A. Matsuyama, T. Takahashi, and F. Yatagai

B. subtilis spores, E. coli B_{s-1}, and E. coli B/r were bombarded with α-particles and carbon, nitrogen, and oxygen ions to study the LET dependence of these bacterial cells. The samples spread on a membrane filter (Millipore filter type HA) were exposed to charged particles of different energies in air.[1] Dosimetry was performed by the nuclear electronic method as previously described.[2] All survival curves determined in this study were exponential. From the viewpoint of the target theory, this means that the inactivation of a sensitive target in the bacterial cells is a single lethal-hit process. Effective inactivation cross section (effectiveness per particle), S_{eff}, was calculated using these survival curves expressed by $N/N_0 = \exp(-S_{eff} \cdot \phi)$, where N/N_0 is the surviving fraction for given fluence ϕ. The 37 % dose, D_{37}, is given by $D_{37} = L\phi_{37}$, where ϕ_{37} is the corresponding fluence and L the total LET of the bombarding particles.

(1) B. subtilis spores

For α-particles, S_{eff} increased with LET to reach a saturation level (S_α^{sat}) of 0.145 μ^2 as shown in Fig. 1. This value was evaluated from the mean values of S_{eff} obtained for α-particles of the total LET higher than 18.0 eV/Å. Using the S_α^{sat} values, the LET dependence of S_{eff} for α-particles was analyzed by essentially the same method as used by Pollard et al.,[3] Barendsen[4] and Oda et al.[5] A cut-off energy of 200 eV was employed for δ-rays according to Barendsen.[4] To estimate the number of primary activations or ionizations, n, which have to be produced within a critical length of a particle track to result in damage to the reproductive capacity of the spores, the experimental curve of Fig. 2 was compared with theoretical curves derived from the equation:

$$S_{eff} = S_\alpha^{sat} \left(1 - \sum_{j=0}^{n-1} f_j \right), \qquad (1)$$

where f_j is the probability that an incident particle gives j ionizations within a critical length t, and f_j is the Poisson distribution given by $(j)^{-1} \times (t\, L_{core}/W)^j \times \exp(-t\, L_{core}/W)$, where L_{core} is the track core LET.[4] Assuming an average energy (W) of 35 eV required to form an ion pair,[4] the best fit of Eqn. 1 to experimental data was obtained for n=6~7 and t=27~31 Å from a least-square analysis. According to Barendsen,[4] the steepest rise in effectiveness per particle must correspond to a LET, whereby the average number of ions produced within the critical length of the track equals the number of n ionizations required for damage. From Fig. 2, this steepest rise occurs at a track-core LET of about 7 eV/Å. Thus, the critical track lengths were calculated to be 30 and 35 Å for n=6 and 7, respectively. These t values thus obtained are consistent with those obtained by the least-square analysis. This fact seems to assure the validity of such estimation. The values of S_{eff} for heavy ions were found to be

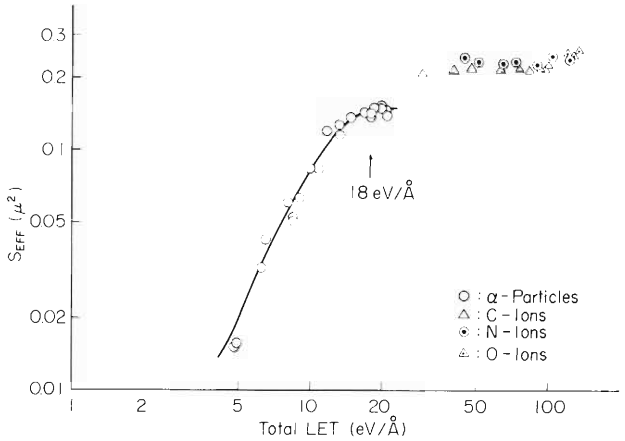

Fig. 1. Relation between S_{eff} and the total LET in B. subtilis spores.

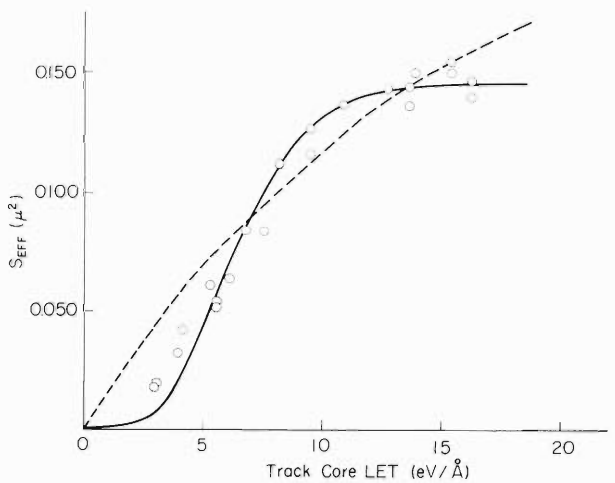

Solid and broken lines show the results of least-square analysis to fit Eqn. 1 for the experimental data, when saturation levels are chosen to be 0.145 and 0.24μ^2, respectively (see text).

Fig. 2. Relation between S_{eff} and the track core LET of α-particles in B. subtilis spores.

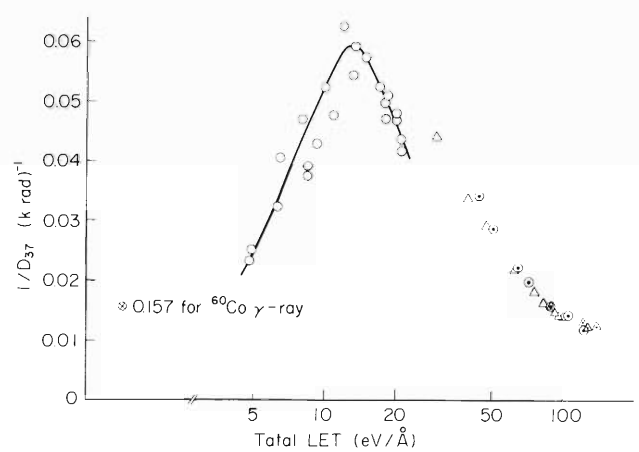

Fig. 3. Relation between RBE ($1/D_{37}$) and the total LET in B. subtilis spores.

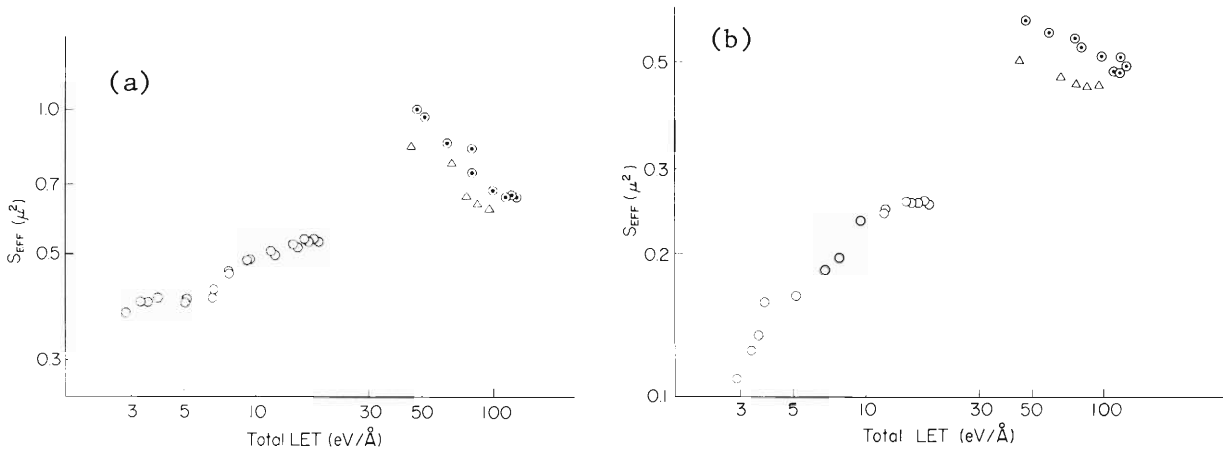

Fig. 4. Relation between S_{eff} and the total LET in E. coli B_{s-1} (a) and E. coli B/r (b).

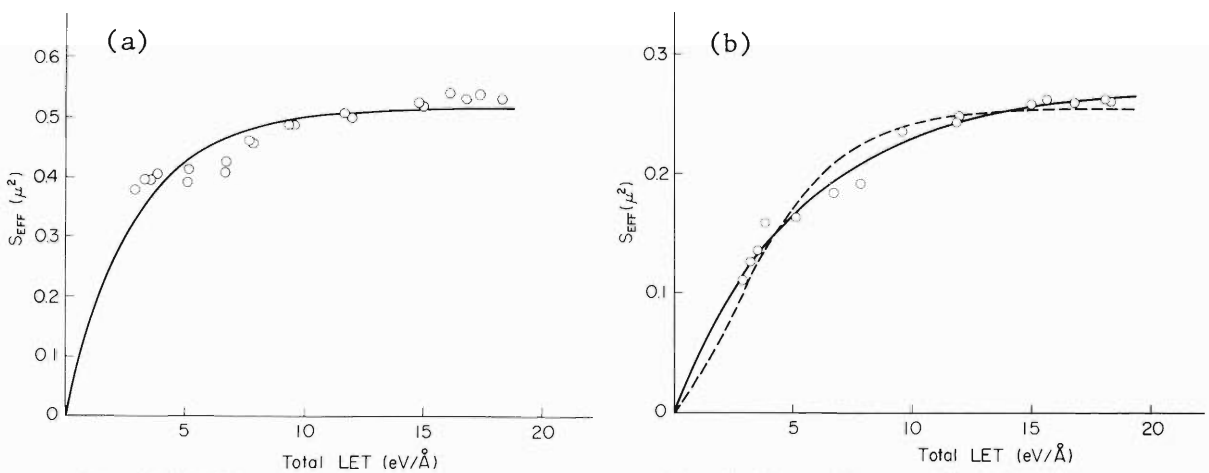

(a) Solid line shows the result of least-square analysis.

(b) Solid and broken lines show the results of least-square analysis assuming n = 1 and 2, respectively (see text).

Fig. 5. Relation between S_{eff} and the total LET of α-particles in E. coli B_{s-1} (a) and E. coli B/r (b).

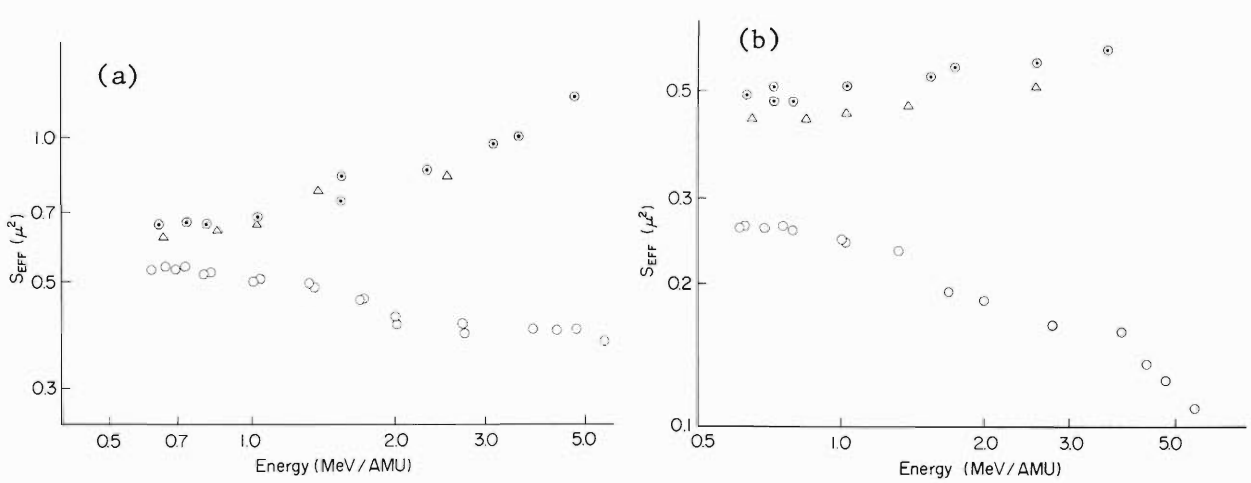

Fig. 6 Relation between S_{eff} and energy in E.coli B_{s-1} (a) and E.coli B/r (b).

higher than S_{α}^{sat} and increased in the order of carbon, nitrogen, and oxygen ions (Fig. 1). Energy dependence of S_{eff} for each heavy ion was scarcely observed. Attempts have been made to interpret the discrepancy between S_{α}^{sat} and S_{eff} for heavy ions in terms of the effect of high energy δ-rays, utilizing the theories developed by Dolphin and Hutchinson[6] and Oda et al.[5] However, such attempts failed mainly because S_{eff} values for heavy ions are almost independent of energies.* Furthermore, the least-square analysis using Eqn. 1 cannot explain the characteristic LET dependence for α-particles, if the saturation level of S_{eff} be assumed to be 0.24 μ^2 in the LET region of heavy ions (broken line in Fig. 2). These facts seem to suggest the necessity of adding another term to Eqn. 1, which should be negligible in the LET region of α-particles and become appreciable in the LET region of heavy ions to account for the present experiment. As seen in Fig. 3, the maximum RBE was found at an LET of 12 eV/Å. The mean values of S_{eff} for carbon, nitrogen, and oxygen ions were found to be 0.220, 0.233, and 0.256 μ^2, respectively (Fig. 1).

The discrepancy between S_{α}^{sat} and S_{eff} for heavy ions may be due to the difference in the repair capacity of the target between α-particle and heavy-ion bombardments. An alternative view is that another type of target different from DNA is involved in the inactivation mechanism of spores on heavy-ion bombardments, as suggested by Haynes.[8] It remains open to a criticism that the discrepancy may be ascribed to long-range effects (e.g. thermal spike effect) of bombarding particles of extremely high LET as suggested by Norman,[9] Kondo,[10] and Platznan and Frank,[11] though details of such theories are not yet well-examined.

(2) E. coli B_{s-1} and E. coli B/r

Although an attempt has not yet been made to distinguish the effect of the track core of particles and that of δ-rays, the following results were obtained by using almost the same method as in B. subtilis spores. The values of S_{eff} for α-particles increase with increasing LET's, reaching the stationary level, S_{α}^{sat}, of 0.537 and 0.261 μ^2 for E. coli B_{s-1} and E. coli B/r, respectively (Fig. 4). The analysis of LET dependence revealed that the number of primary activations required to produce one lethal-hit within a very short length of the particle track is 1 and 1~2 for E. coli B_{s-1} and E. coli B/r, respectively (Fig. 5). The discrepancy between S_{α}^{sat} and S_{eff} for heavy ions was also observed in these bacterial cells (Fig. 6). The S_{eff} value for each heavy ion increases with increasing energy and this fact suggests the necessity to take the effect of high-energy δ-rays into consideration.

(3) Inactivation pattern

Based on the above data, the inactivation patterns for different bacteria are classified into three types as indicated in Table 1.

* Katz theory also seems to be difficult to apply in our present analysis since Fig. 20 of Ref. 7 shows considerable dependence of S_{eff} values on $Z^2/\kappa\beta^2$ which varies with energies of bombarding particles.

Table 1. Inactivation pattern of bacteria on bombardment with charged particles.

Inactivation pattern	Strains	n	$S_{\alpha}^{sat}(\mu^2)$	$S_{eff}(\mu^2)$	δ-ray effect
1	E. coli B_{s-1}	1	0.537	0.630 (C) 0.662 (N)	+
2	E. coli B/r	1 or 2	0.261	0.446 (C) 0.490 (N)	+
3	B. subtilis spore	6 or 7	0.145	0.220 (C) 0.233 (N) 0.256 (O)	±

References

1) A. Matsuyama, T. Karasawa, S. Kitayama, and R. Takeshita : IPCR Cyclotron Progr. Rep., 3, 101 (1969).
2) T. Karasawa, H. Seki, M. Imamura, A. Matsuyama, and M. Matsui : "The Uses of Cyclotrons in Chemistry, Metallurgy and Biology", (Ed. C.B. Amphlett), Butterworths, London, p. 76 (1970).
3) E.C. Pollard, W.R. Guild, F. Hutchinson, and R. B. Setlow : Progr. Biophys. Chem., 5, 72 (1955).
4) G.W. Barendsen : Int. J. Radiat. Biol., 8, 453 (1964).
5) N. Oda : "Biophysical Aspects of Radiation Quality", TRS No. 58, IAEA, Vienna, p. 165 (1966).
6) G. W. Dolphin and F. Hutchinson : Radiat. Res., 13, 403 (1960).
7) R. Katz, S.C. Sharma, and M. Homayoonfar : "Topics in Radiation Dosimetry", (Ed. F.H. Attix), Academic Press, New York, London, p.317 (1972).
8) R.H. Haynes : Radiat. Res. Suppl., 6, 1 (1966).
9) A. Norman : ibid., 7, 33 (1967).
10) S. Kondo : Butsuri, 16, 584 (1961).
11) R.L. Platzman and J. Frank: "Symposium on Information Theory", (Ed. N. Yockey), Pergamon Press, New York, p.262 (1958).

9-4. LET Dependence of DNA-Strand Breaks in E. coli B_{s-1}

K. Igarashi, F, Yatagai, T. Takahashi, and A. Matsuyama

In order to measure the LET dependence of DNA-strand breaks in bacterial cells, log-phase cells of E. coli B_{s-1} labelled with ^{3}H-TdR were bombarded in air at room temperature (~20°C) with α-particles and carbon- and nitrogen-ions, as described previously[1),2)], and sedimentation profiles of DNA were determined by the method of McGrath and Williams[3)] using alkaline sucrose gradients. For inhibiting the DNA repair during irradiation, bacterial cells were suspended in a 0.01M Tris buffer containing 0.02M EDTA and an 0.02-m*l* aliquot of the cell

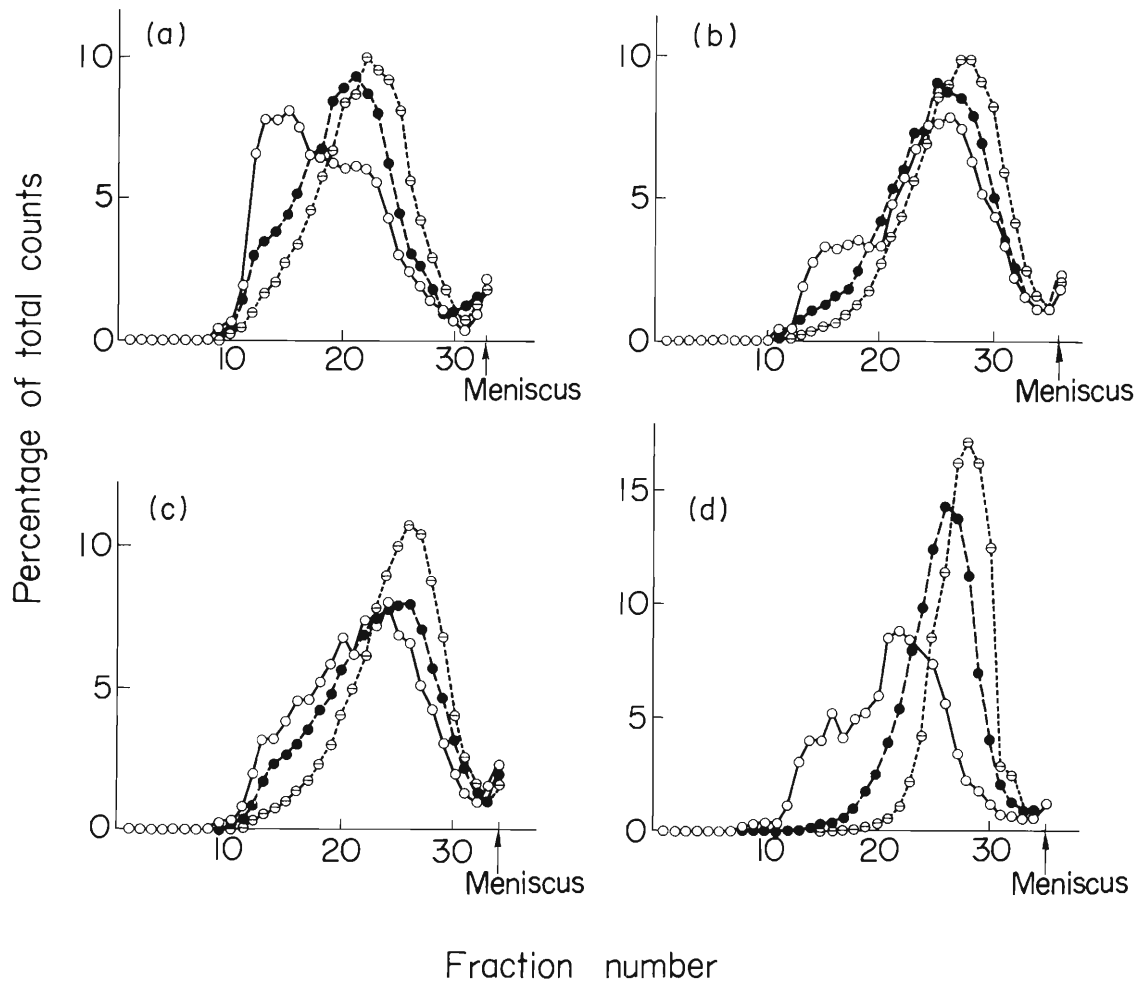

(a) α-particles (0.628 MeV/amu) ○ 61.7 krad ● 93.1 krad ⊖ 123 krad
(b) C ions (2.39 MeV/amu) ○ 97.3 krad ● 146 krad ⊖ 195 krad
(c) N ions (1.73 MeV/amu) ○ 80.9 krad ● 121 krad ⊖ 163 krad
(d) ^{60}Co γ-rays ○ 27 krad ● 36 krad ⊖ 54 krad

Fig. 1. Sedimentation patterns of ^{3}H-DNA from irradiated E. coli B_{s-1}.

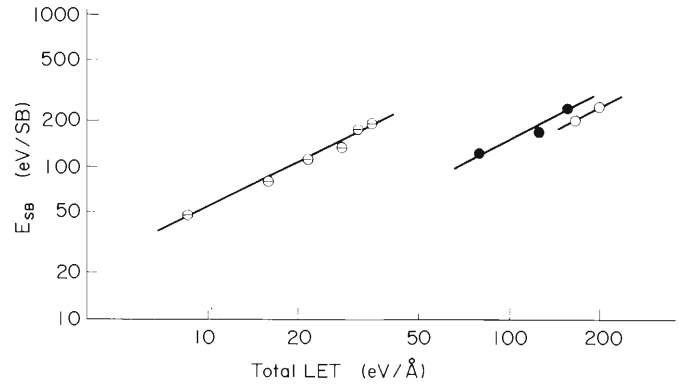

○ α-particles, ● C ions, ⊖ N ions

(LET values in this report refer to energy absorbed in DNA per unit length.)

Fig. 2. LET dependence of the efficiency of DNA single-strand breakage, E_{sb}.

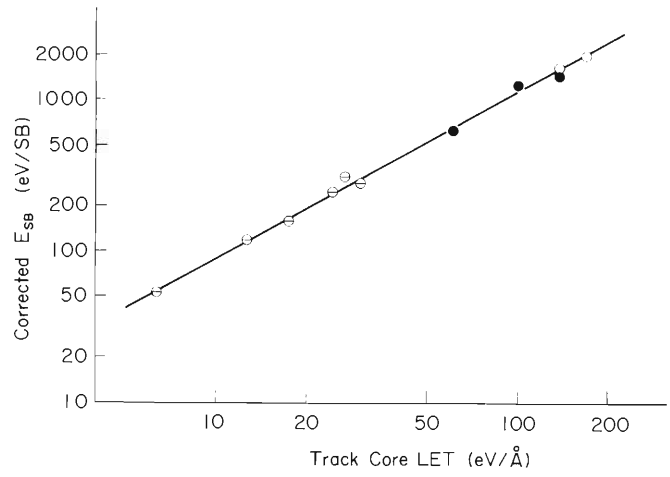

Fig. 3. The relation of E_{sb} corrected for δ-rays and track-core LET.

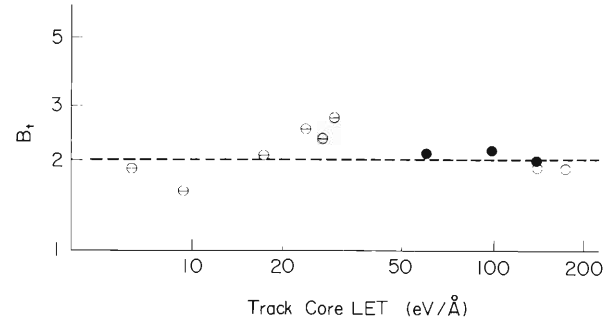

Fig. 4. The number of DNA single-strand breaks by the track-core effect of a single particle-traversal, B_t.

suspension was fed on a membrane filter (Millipore filter Type GS). Some examples of the sedimentation profiles of E. coli B_{s-1} DNA are illustrated in Fig. 1.

From sedimentation profiles, the number-average molecular weight of DNA was calculated[4] and the efficiency for single-strand break production, E_{sb}, was estimated. The value of E_{sb} for each particle was found to increase with increasing total LET as shown in Fig. 2. This LET dependence of E_{sb} reveals the possibility that an excessive energy might be required to produce a single-strand break in such a high LET region as compared with X- or γ-rays. In Fig. 2, the discontinuous increase of E_{sb} was also observed in the overlapping LET region obtained by different kinds of charged particles. This fact suggests the necessity of taking the δ-ray effect into consideration. After an appropriate correction for the δ-ray effect, one can expect that the increase of E_{sb} with increasing track-core LET in the high-LET region is expressed by the same linear relationship for different particles, since the DNA-strand breakage would always take place by the energy dissipation of a high-LET particle when it traverses through the DNA strand. The trial of the δ-ray effect correction for the data indicated in Fig. 2 was made on the following assumptions : (1) The rate of single-strand breakage induced by δ-rays is identical with that by ^{60}Co γ-rays (Fig. 1), E_{sb} = 40 eV/break, which is calculated by the same method as that for charged particles; (2) a cut-off energy of 500 eV is employed to separate the δ-ray effect from the track-core effect; (3) dividing the DNA volume, $2.4 \times 10^{-3} \mu^3$,[5] by the projected area of the cellular nuclear region, $1.1\mu^2$, determined from the electron micrograph, the mean particle traverse length through the DNA strand is estimated to be 22 Å.

As a result, a linear relationship between E_{sb} corrected for δ-rays and the track-core LET was obtained (Fig. 3). The number of single-strand breaks in DNA formed by the track-core effect of a single particle-traversal, B_t, was calculated with the above δ-ray correction. As can be seen in Fig. 4, the values of B_t were found to be about 2, almost independent of the LET of bombarding particles. This fact suggests that the DNA strand in bacterial cells may be on the average distributed as a monolayer and that the traversal of a single particle of high LET through the DNA strand results in a double-strand break.

To examine the contribution of DNA single-strand breakage for the inactivation of cells, the number of DNA single-strand breaks by the absorbed dose of D_{37}, denoted by B_{37}, was

Table 1. Model of inactivation of bacterial cells by charged particles.

particles	α-particles						C-ions			N-ions	
Total LET* (eV/Å)	8.76	16.0	21.2	27.7	31.0	34.0	81.2	128	160	168	200
B_{37} B_{37}^t	7.53	5.31	5.61	4.26	3.22	3.78	3.12	2.63	2.68	3.09	2.18
B_{37} B_{37}^δ	3.64	4.33	4.66	4.48	4.43	4.26	17.4	16.8	17.2	27.7	18.8
P_{37}	2.74	2.28	2.22	2.05	2.08	2.04	1.50	1.22	1.36	1.45	1.18

* In DNA (ρ=1.71)

also calculated with this δ-ray correction. The values of B_{37}^{t} and B_{37}^{δ} shown in Table 1 are B_{37} for the effect of track core and δ-rays, respectively, and $B_{37} = B_{37}^{t} + B_{37}^{\delta}$. The values of B_{37}^{t} decrease with increasing LET approaching a value of 2, while B_{37}^{δ} is not so affected by LET but its level becomes higher for heavier ions. This tendency of B_{37} may reveal the difficulty to account for the inactivation of cells by the DNA single-strand breakage and the DNA single-strand breakage by δ-rays seems to be very ineffective.

The average number of particles (P_{37}) passing through the DNA strand for an absorbed dose of D_{37} was also calculated. It was found that P_{37} decreases toward the unity with increasing LET as shown in Table 1. The values of P_{37} appear to be consistent with the effective inactivation cross section (effectiveness per particle) of E. coli B_{S-1} observed in our separate experiments. This fact suggests the possibility that lethal damage on the cells might be explained by the number of heavy charged particles traversing through the DNA strand rather than the number of DNA single-strand breaks. According to Freifelder,[6] there are two principal types of lethal damage in X-ray irradiated double-strand DNA phage; (1) double-strand breakage which is O_2-independent and occurs at ca. one-half the rate of production of lethal hits and (2) an O_2-dependent damage which is thought to be of alternation of the nucleotide bases. Taking account of O_2-independent inactivation of the cells by high-LET particles,[7] the DNA double-strand breakage induced by the charged particle-traversals might be regarded as an important event for the cell inactivation. The LET dependence of the DNA double-strand breakage on such charged particle bombardment will be discussed elsewhere.

References

1) A. Matsuyama, T. Karasawa, S. Kitayama, and R. Takeshita : IPCR Cyclotron Progr. Rept., 3, 101 (1969).
2) T. Karasawa, H. Seki, M. Imamura, A. Matsuyama, and M. Matsui : "The Uses of Cyclotron in Chemistry, Metallurgy and Biology", (Ed. C.B. Amphlett), Butterworths, London, p.76 (1970).
3) R.A. McGrath and R.W. Williams : Nature, 212, 534 (1966).
4) S. Kitayama and A. Matsuyama : Agr. Biol. Chem., 35, 644 (1971).
5) S. Cooper and C. E. Helmstetter : J. Mol. Biol., 31, 519 (1968).
6) D. Freifelder, S. T. Donta, and R. Goldstein : Virology, 50, 516 (1972).
7) P. Todd : Radiat. Res. Suppl., 7, 196 (1967).

10. PREPARATION OF RADIOISOTOPES AND LABELED COMPOUNDS

10-1. Measurement of Excitation Curves for the Formation of Medical-Use Radioisotopes

T. Nozaki, T. Karasawa, M. Okano,
M. Iwamoto, and T. Hara

The excitation curves for the following reactions were measured: (1) Ne + d → ^{18}F, (2) Ne + ^{3}He → ^{18}F, and (3) ^{197}Au (d, 2n) ^{197m}Hg. The thick target yields of ^{18}F in various reactions were calculated, and the reactions were compared in view of the practical production of ^{18}F in various useful physical and chemical states. Details of the comparison will be published elsewhere in the near future. The excitation curves for the formation of ^{48}Cr and ^{48}V in the ^{3}He bombardment of titanium are now under measurement.

Neon was sealed in target-gas containers which were metal cylinders of 60 mm in diameter and exactly 25 mm in height and with bases of aluminum foils 13 μm thick. From 5 to 15 of these containers were lined up closely in series to make a target assembly, and several such assemblies were bombarded with particle beams of various incident energies. For the ^{197}Au (d, 2n) ^{197m}Hg reaction, the ordinary stacked foil technique was used.

The results are shown in Figs. 1 and 2, and the thick target yields of ^{18}F for various reactions are shown in Figs. 3 and 4. The excitation curves of the ^{3}He reactions to give ^{18}F show that : in energy regions over 15 MeV, neon gives a much higher ^{18}F activity than does oxygen; under 10 MeV, only oxygen gives a sufficiently high ^{18}F yield. The following bombardment, thus, can offer anhydrous ^{18}F and aqueous ^{18}F simultaneously in good yields: ^{3}He particles of an incident energy over 20 MeV is caused first to pass through a neon target layer of such a thickness as to reduce their energy down to about 15 MeV and then to enter a water target.

Although the bombarded neon contains some activity of ^{7}Be and ^{22}Na, they are not incorporated in final products of synthetic processes of ^{18}F labelling.

As is obvious from Fig. 2, carrier-free ^{197m}Hg can be obtained in good yield by deuteron bombardment of a gold plate. A simple chloride-volatilization method has been devised for the separation of the ^{197m}Hg. This nuclide has proved to be useful for lung tumor scanning. It is much more effective than ^{197}Hg because of suitable energy of its γ-ray.

In the ^{3}He bombardment of water for the production of an aqueous ^{18}F solution, a titanium foil is used as the beam extraction window. We intend to separate ^{48}Cr formed in this window, whose thickness has been chosen from the consideration of the excitation curves. The chemical separation technique of this nuclide is also under study.

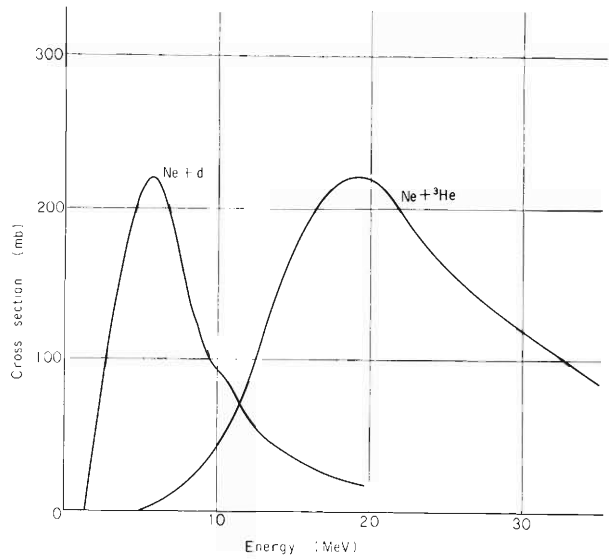

Fig. 1. Excitation curves for the reactions of Ne + d → ^{18}F and Ne + ^{3}He → ^{18}F.

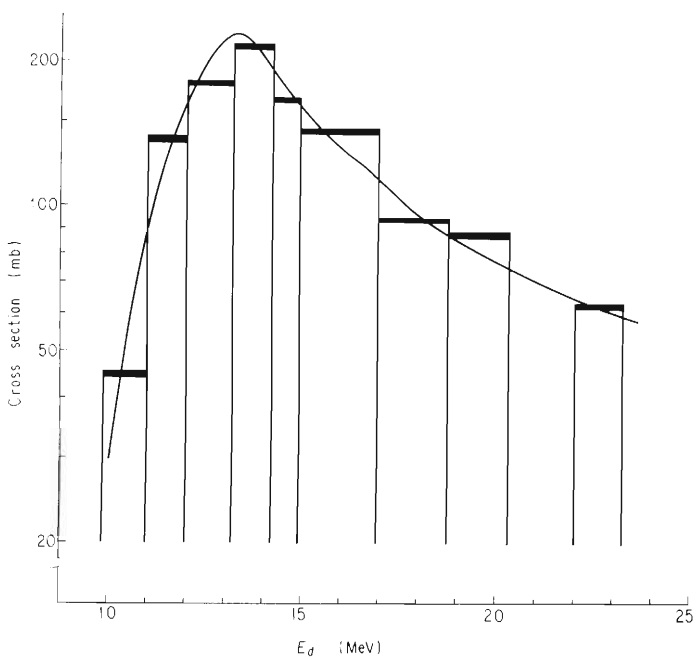

Fig. 2. Excitation curve for the reaction of ^{197}Au (d, 2n) ^{197m}Hg.

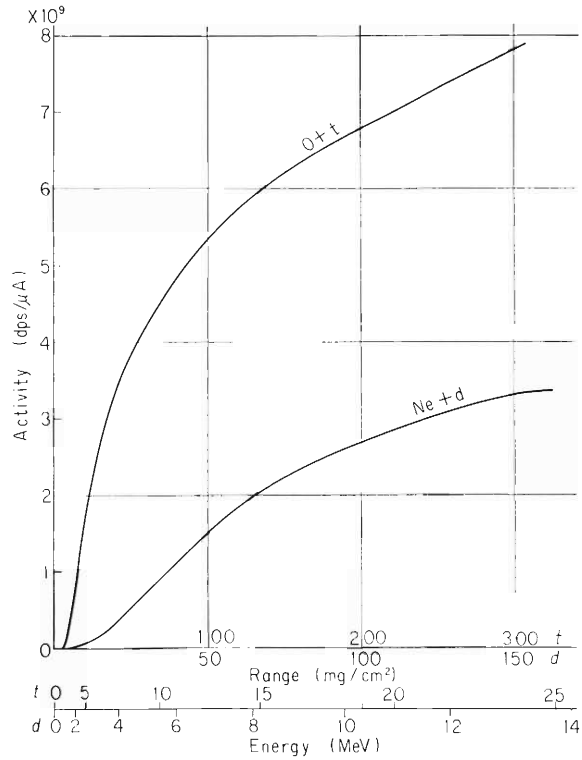

Fig. 3. Thick target yields of ^{18}F for the triton reaction on oxygen and deuteron reaction on neon.

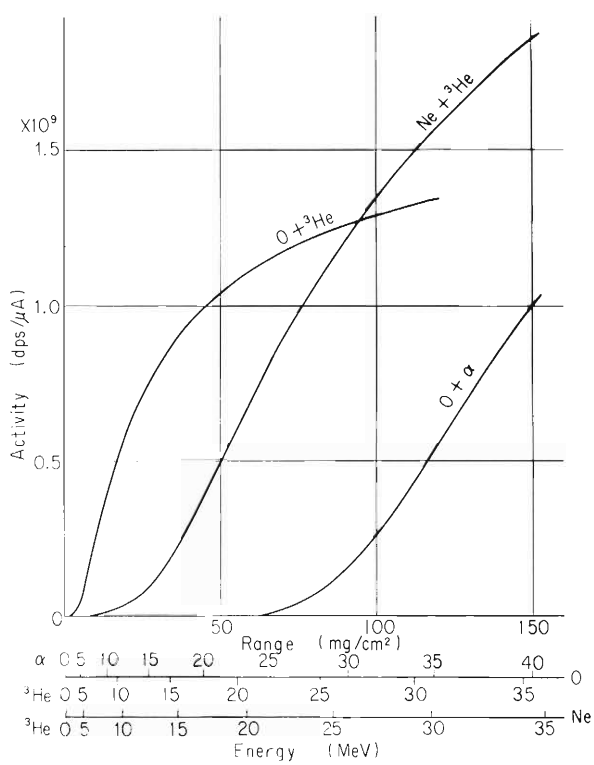

Fig. 4. Thick target yields of ^{18}F for the ^{3}He reactions on neon and oxygen and of α-particle reaction on oxygen.

10-2. Preparation of ^{18}F-Labelled Compounds

T. Nozaki, Y. Ohtsuka, A. Tahara, S. Ambe,
T. Ido, K. Fukushi, and Y. Kasida

We previously reported the synthesis of ^{18}F-labelled cholesteryl fluoride (Compd 1) and its distribution in experimental animals.[1),2)] This fluorosteroid, however, is highly hydrophobic, showing a slow clearance from blood. With less hydrophobic fluorosteroids, more valuable information will be able to be obtained. We synthesized 3β-acetoxy-6β-fluorocholestane-5α-ol-^{18}F (Compd 2) by the reaction of $B^{18}F_3$ with 3β-acetoxy-5α, 6α-epoxycholestane (Compd 3),[3)] and injected it into rats to measure its distribution in their body.

By modifying the synthetic method reported by Henbest and his coworkers,[4)] we attempted to prepare Compd 2 in a higher yield and shorter time. In our cold experiment under a small scale, the ^{18}F yield was increased to 61 % with an organic yield of 51 % under the optimum condition (BF_3-etherate, 0.28 eq. mol; operation time, 100 min). However, different conditions, such as shown in Table 1, had to be used in the actual labelling experiment, because a part of the BF_3-etherate was decomposed by moisture in the preparation of $B^{18}F_3$-etherate.

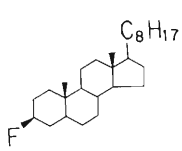

Compd 1

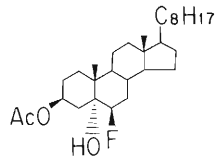

Compd 2

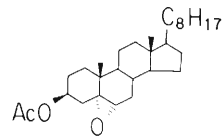

Compd 3

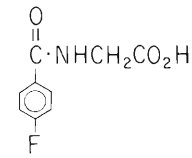

Compd 4

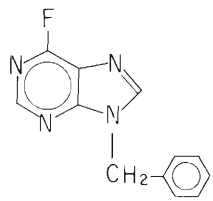

Compd 5

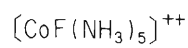

Compd 6

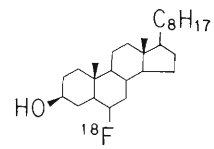

Compd 7

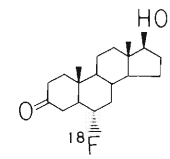

Compd 8

Table 1. Yield of ^{18}F-labelled fluorosteroid (Compd 2).

Exp. No.	BF_3-etherate used(eq. mole)	Org. yield (%)	Inorg. yield (%)	Radiochem. yield (%)*	Operation time (min)
1	3.313	38.5	3.9	4.3	145
2	1.125	48.0	14.2	9.8	126
3 ~ 5	1.75	25.0	4.77	5.7	91

$$* \frac{(\text{dps of the product}) \times 100}{(\text{dps of the } B^{18}F_3\text{-etherate})}$$

The epoxysteroid, Compd 3, (100 mg) was added to a benzene solution of $B^{18}F_3$-etherate prepared by isotopic exchange between BF_3-etherate (50 ~ 60 mg) in benzene (20 mℓ) and ^{18}F adsorbed on the inside wall of a bombardment box in which neon or oxygen had been bombarded. The mixture was stirred for 10 ~ 15 min at room temperature. After the addition of water (several drops) and alumina containing gypsum (10 g), the mixture was filtered. The filtrate was evaporated and the crystalline residue subjected to preparative thin layer chromatography on alumina, the developing solvent being benzene-chloroform (3 : 1). The objective band was extracted and the solvent evaporated to give the crystalline ^{18}F-labelled fluorosteroid, Compd 2, (26 ~ 50 mg). The entire synthesis was carried out within a relatively short time (90 ~ 100 min).

The product, Compd 2, was injected with the aid of an emulsifier into rats and the distribution of the ^{18}F-activity in them was measured with its time change. The results are shown in Fig. 1. Also, the change of ^{18}F-concentration in bile secreted from rats injected with Compd 1 or Compd 2 was followed. The results are shown in Fig. 2.

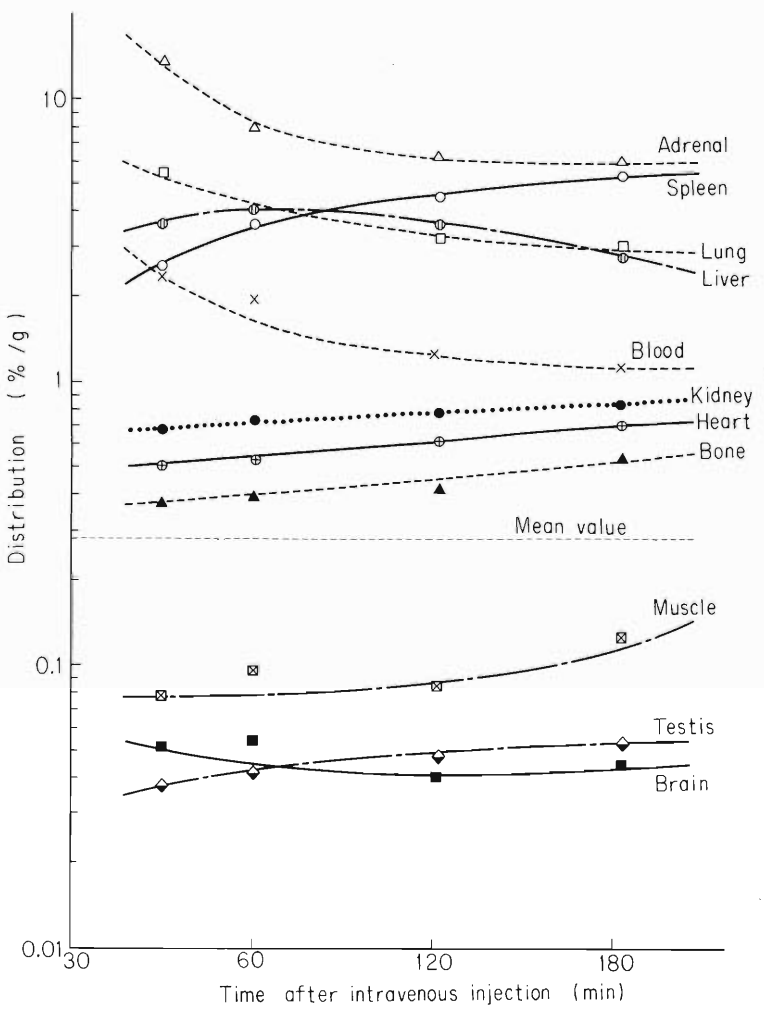

Fig. 1. Distribution of 3β-acetoxy-6β-fluorocholestane-5α-ol in rats and its change with time.

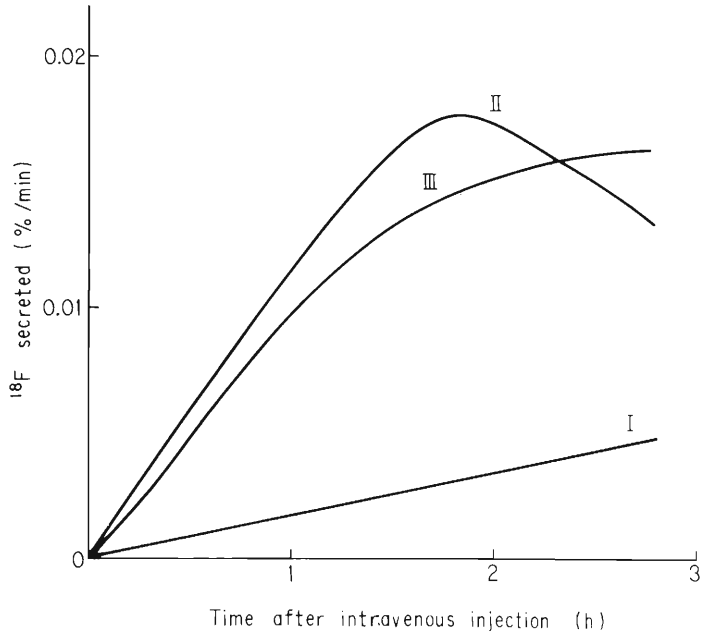

I : Cholesteryl fluoride, normal rats.

II : 3β-Acetoxy-6β-fluorocholestane-5α-ol, normal rats.

III : 3β-Acetoxy-6β-fluorocholestane-5α-ol, polychlorobiphenyl-treated rats (per os, 0.5 μg/g body).

Fig. 2. Secretion velocity of fluorosteroids into bile.

p-Fluorohippuric acid (Compd 4) was synthesized by the Schiemann reaction with a ^{18}F-yield of about 10 % and injected into rats. This compound showed a very rapid clearance into urine. ^{18}F-labelled 6-fluoro-9-benzylpurine (Compd 5) has been synthesized by halogen interchange from 6-chloro-9-benzylpurine and Ag^{18}F. The behavior in vivo of this compound is now going to be studied.

Fluoropentamminecobalt (III) complex ion (Compd 6) was found to be labelled with ^{18}F by isotopic exchange in an aqueous solution. The compound also showed a rapid clearance from rats into their urine. Detailed study of this isotopic exchange is now under way.

Efforts are being made for the elevation of specific activity of the products in general. We intend to prepare, in the near future, ^{18}F-labelled 6-fluorocholesterol (Compd 7) and fluorotestosterone (Compd 8).

References

1) T. Nozaki, A. Shimamura, and T. Karasawa : IPCR Cyclotron Progr. Rep., 2, 156 (1968).

2) T. Nozaki, T. Karasawa, M. Okano, A. Shimamura, M. Iwamoto, T. Ido, and Y. Makide : ibid, 6, 127 (1972).

3) P. A. Plattner, Th. Petrzilka, and W. Lung : Helv. Chim. Acta, 27, 513 (1944).

4) H. B. Henbest and T. I. Wrigly : J. Chem. Soc., 1957, 4765.

10-3. Preparation of ^{119}Sb for Mössbauer Emission Spectroscopy of ^{119}Sn

S. Ambe and F. Ambe

A series of Mössbauer emission studies have been under way in our laboratory on ^{119}Sn after the EC decay of ^{119}Sb.[1)~3)] This report describes the procedure developed for producing ^{119}Sb by proton irradiation of tin followed by radiochemical separation and purification.

The ^{119}Sb was produced by the ^{119}Sn(p,n)^{119} Sb and ^{120}Sn(p, 2n)^{119}Sb reactions. The targets were water-cooled metallic tin plates of natural isotopic abundance. The thickness of the tin plates was 1 mm and an effective area of ca. 20 cm^2 of them was exposed to a dispersed 15 MeV proton beam accelerated in the Cyclotron. A sketch of the target assembly employed is given in Fig. 1. The beam current was usually about 15 μA. An irradiation with 200 mCoulomb of 15 MeV protons makes it possible to accumulate about 4×10^6 counts of the 23.8 keV γ-rays in each of the 400 channels of the Mössbauer spectrometer, if an overall yield of more than 60 % is assumed in the separation of ^{119}Sb and the preparation of source materials.

In a one-liter beaker cooled by water and covered with a watch glass, the irradiated target

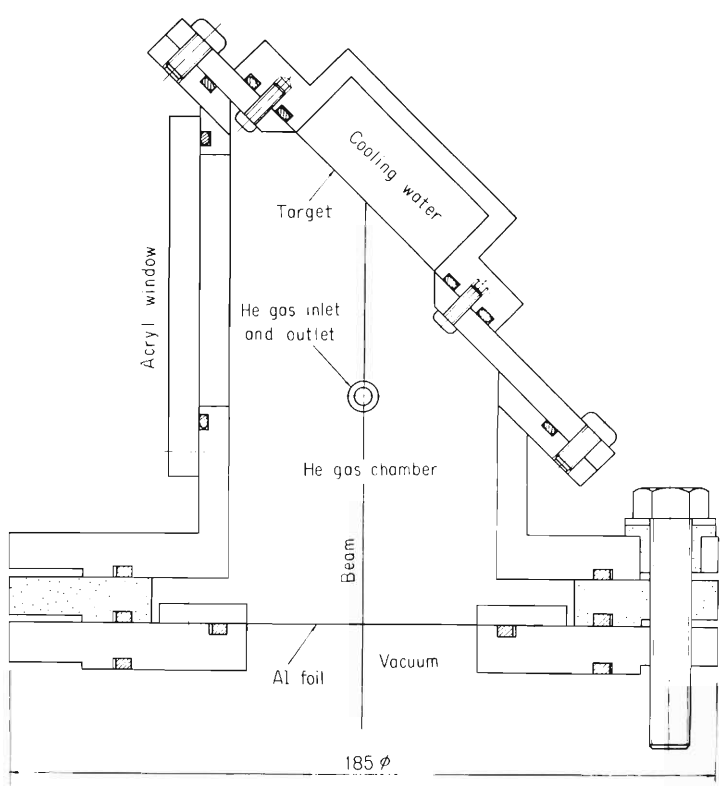

Fig. 1. The target assembly employed for the irradiation of tin targets.

(about 14 g) is dissolved in 75 mℓ of conc. HCl with the aid of 25 mℓ of conc. HNO_3 added slowly in small portions. Unless carrier-free ^{119}Sb is required, addition of a few mg of Sb_2O_3 as a carrier at this stage is recommended. When the greater part of the tin plate has been dissolved, all the contents of the beaker are transferred to a porcelain evaporating-dish, and the solution is evaporated almost to dryness at about 100°C. (Complete drying-up of the solution makes redissolution of the residue extremely difficult.) After cooling, the residue is dissolved in 200 mℓ of 9 M HCl, and a few mℓ of 9 M HCl saturated with chlorine are added to the solution to ascertain the oxidation of ^{119}Sb to Sb(V). The ^{119}Sb(V) in the solution is extracted twice with 100 mℓ each of a 3 : 1 mixture of isopropylether and benzene. The organic phases are collected together and washed four times with 100 mℓ each of 9 M HCl to which a few mℓ of 9 M HCl saturated with chlorine are added. The ^{119}Sb is back-extracted from the organic phase three times with 5 mℓ each of 3 M LiOH. The aqueous phases are collected together and an equal volume of 6 M HCl is added to the solution to yield a 1.5 M HCl – 1.5 M LiCl solution of ^{119}Sb(V). After a few mℓ of 1.5 M HCl–1.5 M LiCl solution saturated with chlorine are added, the solution is passed through a column of a strongly basic anion exchanger, Diaion SA # 100 (6mℓ), pretreated with 1.5 M HCl–1.5 M LiCl. The ^{119}Sb(V) left on the resin phase is washed out with 30 mℓ of 1.5 M HCl–1.5M LiCl. All the eluants are collected together and heated almost to boiling and the ^{119}Sb(V) in the solution is reduced to Sb(III) with 1 g of Na_2SO_3. After cooling, the solution is passed through a column of Diaion SA# 100 (3mℓ) pretreated with 1.5 M HCl–1.5 M LiCl. The resin is washed successively with 15 mℓ each of 1.5 M HCl-1.5 M LiCl, 1.5 M HCl and 0.5 M HCl. Finally, the ^{119}Sb(III) adsorbed on the resin bed is stripped with 15 mℓ of 0.5 M LiOH.

Whole the chemical procedure can be completed within 12 h. The yield of ^{119}Sb amounts to about 90 % and the decontamination factor of tin is more than 5×10^6.

References

1) F. Ambe, H. Shoji, S. Ambe, M. Takeda, and N. Saito : IPCR Cyclotron Progr. Rep., 4, 115 (1970); ibid., 5, 85 (1971) ; F. Ambe, S. Ambe, and N. Saito : ibid., 6, 102 (1972).
2) F. Ambe, H. Shoji, S. Ambe, M. Takeda, and N. Saito : Chem. Phys. Lett., 14, 522 (1972).
3) F. Ambe and S. Ambe : Phys. Lett., 43A, 399 (1973).

11. RADIATION MONITORING

11-1. Routine Monitoring

K. Koda, I. Sakamoto, and I. Usuba

Results of the routine monitoring and related measurements on the IPCR cyclotron obtained from January to December 1972 are described.

As a result of several improvements made on the machine and the accessory facilities, the machine time in this year reached as much as 270 days. In spite of such a hard schedule of the machine operation, the accumulated dose to the workers decreased as described below.

(1) Residual radioactivities on the machine

The radiation level measured around the machine 12 days after machine's shutdown was as follows :

Location	Dose rate (mR/h)
ca.10 cm apart from septum covered with 2mm Pb	300
" deflector	40
at ion source flange	12
at beam exit	200
at slit box	40

Several short-lived radioactive nuclides which account for the majority of residual activities and have a dominant contribution to exposure of the workers during the short period after deuteron acceleration have been identified. They are:

^{11}C (half life, 20 min), ^{24}Na (15 h), ^{56}Mn (2.58 h), ^{64}Cu (12.8 h), and ^{187}W (24 h).

There would still remain some other radionuclides left unidentified.

(2) Surface contamination

The surface contamination of the floor of the cyclotron room, the underground passage, and the experimental area was kept below $10^{-6} \sim 10^{-7}$ $\mu Ci/cm^2$ in terms of beta and gamma activities. The contamination was wiped off twice a year.

(3) Personnel monitoring

The rule of work in the cyclotron vault has been revised this year in order to reduce exposure of the operators and engineers to radiations. The revised points are :

(a) Setting-up of the heavy-ion source to the machine must be begun at least 24 h after the shutdown of deuteron acceleration.

(b) When deuterons have been accelerated over 6 h enough interval for "cooling" should be taken before entering the cyclotron room.

Exposure of the personnel anticipated for various operations under the normal condition of the cyclotron was :

	Working time (min)	Dose rate at work place (mR/h)	Max. exposure expected (mrem)
Replacement of filament of p,d,α-ion source	20	less than 15	5
Replacement of ion source itself	60	" 7	7
Replacement of cone of p,d,α-ion source	30	" 10	5
Inspection of oscillator	20	30	10

(c) Workers to whom a dose over 300 mrem has been accumulated during any 6 months period should be warned and exempted from operations involving a high exposure.

Application of the revised rule has resulted in a remarkable decrease of exposure of the workers during this year. Details will be described in the next report.

Exposure of workers during the replacement of septum was measured simultaneously at their right-hand finger and breast. The result is as follows :

Worker	G	H	I
Breast	20	25	20
Finger	100	80	40

(in mrem)

Similar measurements were made for operation of treating an irradiated zirconium target for ^{90}Nb production. The exposure was found to be 40 mrem at breast and 600 mrem at right-hand finger.

Internal contamination of the workers with ^{65}Zn, an induced radionuclide in the acceleration chamber, had been detected already in 1968. The body burden was measured again this year using a body counter. The result expressed in nCi is as follows :

Year \ Worker	K	L	M
1968	8	32	–
1972	14	11	3

11-2. Residual Radiation in the Cyclotron Vault after Deuteron Acceleration

I. Sakamoto, S. Fujita, and T. Karasawa

(1) Half-life, nuclide, and neutron reaction

It is well known that the residual radiation level in the cyclotron vault is higher after deuteron acceleration than after proton, α, and helium-3 acceleration. This high radiation level in the case of deuteron acceleration is due to the residual activities induced by fast neutron reactions or by neutron capture.

During this year, we have investigated the residual radiation level and main radioactive nuclides.

At the point A in Fig. 1, where the area monitor was installed, the decay curve of the residual radiation level was found to consist of three half-life components of 10 ~ 20 min or less, 2 ~ 3 h, and 13 ~ 15 h, regardless of the energy of accelerated deuterons. A typical decay curve is presented in Fig. 2. The nuclides and the types of reactions can be estimated as listed in Table 1 from the viewpoints that (1) their half-lives are close to those observed, (2) the target materials are contained in the cyclotron components and/or in the shielding

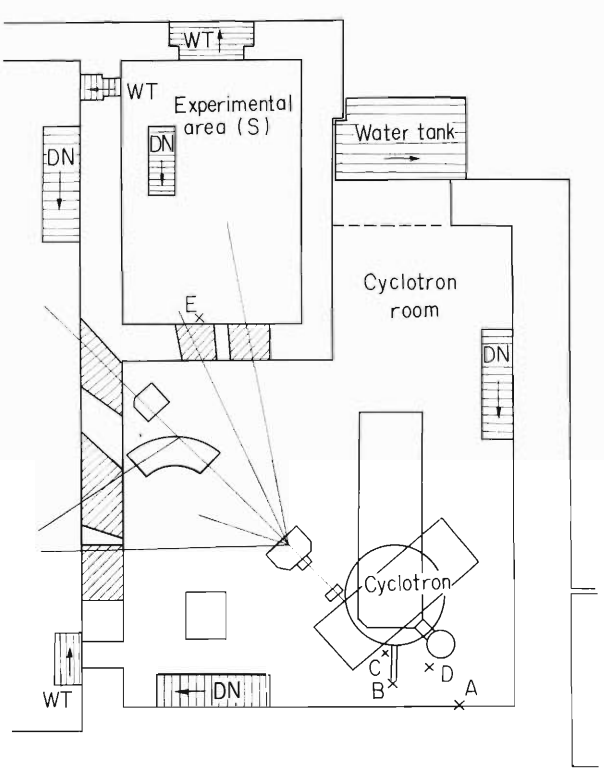

Date: 29 Jan. 1973, E_d 24 MeV, Int. 63μA, Defl. 29μA. Acceleration time: 72 h.

Fig. 1. Layout of the measuring locations.

concrete, and (3) their cross sections of reaction are substantially large. Short-lived activities of less than 30 min are not discussed here.

In fact, the production of these radioactive nuclides was confirmed from the γ-ray spectra obtained with a Ge(Li) detector, which was set up in a small experimental room at the point E in Fig. 1 and was able to detect the γ-ray radiation from the cyclotron vault through the collimater.

Other nuclear reactions which produce the radioactive nuclides in Table 1 are also possible. For example, ^{56}Mn is produced by the ^{59}Co(n, α)^{56}Mn reaction. But the quantity of ^{59}Co in the cyclotron components is far less than ^{56}Fe, only 0.3 % in stainless steel. The electromagnet and the accelerating chamber are made of steel and stainless steel, respectively. Which of the nuclear reactions, ^{56}Fe(n, p)^{56}Mn or ^{55}Mn(n, γ)^{56}Mn, is more contributory for the production of ^{56}Mn? Although the Mn content in the steel is usually about 0.5 % and much

Table 1. Major radioactive nuclides and estimated nuclear reactions.

Radioactive nuclide	Half-life	Estimated reaction	
^{56}Mn	2.6 h	^{56}Fe(n, p)^{56}Mn	^{55}Mn(n, γ)^{56}Mn
^{65}Ni	2.9 h	^{65}Cu(n, p)^{65}Ni	
^{64}Cu	12.8 h	^{63}Cu(n, γ)^{64}Cu	
^{24}Na	15 h	^{23}Na(n, γ)^{24}Na	

Table 2. The cooling time in the case of ^{197m}Hg production.

Date	E_d	Beam intensity		T_a	Radiat. level		Norm. T_c
		Int.	Defl.		(mR/h)	T(h)	
	(MeV)	(μA)	(μA)	(h)			(h)
27, Dec.	20	–	23	1.5	3.3	1	2.2
25, Jan.	22	50	25	1	3.9	1	2.6
1, Feb.	22	–	20	1.5	2.5	0.5	2.5
23, Feb.	24	20	9	1	2.1	0.5	1.7

Int. : Internal beam. Defl.: Deflected beam.

T_a : Acceleration time.

T : The time when radiation at the point A is measured after shutdown.

Norm. T_c : Normalized cooling time. It is calculated so that the residual radiation level at the point C decays to 10 mR/h after shutdown of operation at the irradiation intensity of 30 μA.

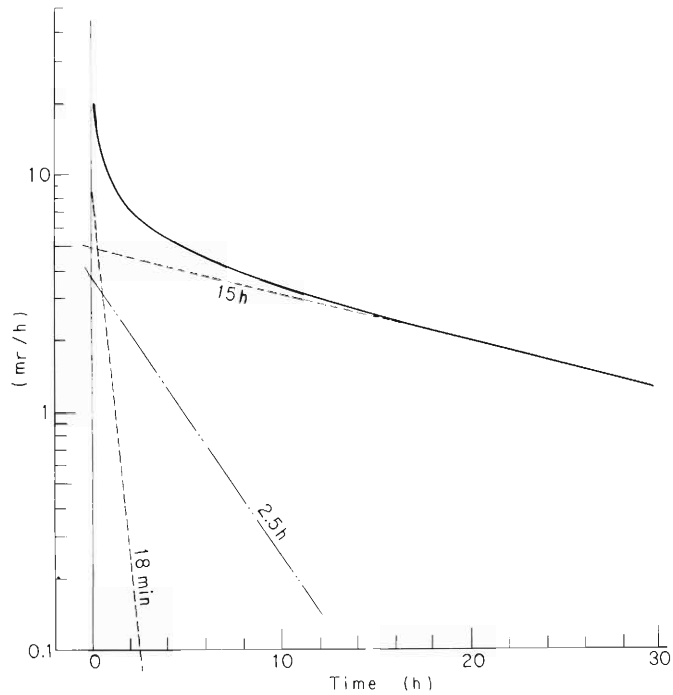

Fig. 2. Decay curve.

smaller than that of Fe, the cross section of the neutron capture is much larger than that of the (n, p) reaction. At present, we can not solve this problem.

In the earlier stage of this study, two types of reactions, (^{23}Na(n,γ)^{24}Na and ^{27}Al(n, α)^{24}Na), were supposed to contribute to the production of ^{24}Na. Aluminium and sodium are contained about 5 % and 2 % respectively in concrete of the shielding wall around the cyclotron vault. For the determination of major reactions to produce ^{24}Na, samples of pure aluminium and sodium chloride were exposed to deuteron-induced neutrons in the cyclotron vault and then the induced activity of ^{24}Na was measured. Considering the activity induced in the samples and the contents in the concrete, it is concluded that ^{24}Na is produced mainly by the ^{23}Na (n, γ)^{24}Na reaction.

Copper is used for both the resonator (dee and liner) in the accelerating chamber and the exciting coil of the electromagnet. For quantitative comparison of the activities induced, ^{64}Cu and ^{24}Na, we used a portable NaI scintillation counter with a special collimator. This set-up was sensitive only for forward direction and positioned between the cyclotron and the shielding wall at the point D in Fig. 1. The γ-rays from ^{24}Na were found to emit predominantly from the shielding wall and the 0.511 MeV γ-rays of positron annihilation from ^{64}Cu originated from the cyclotron. Considering the energy of γ-rays emitted by ^{24}Na was higher than that by ^{64}Cu, the exposure dose at that point seemed to consist of nearly equal parts due to ^{24}Na and ^{64}Cu.

(2) Cooling period for safety

The distribution of the residual radiation level near the cyclotron was measured as a

function of the time after shutdown of acceleration. The radiation level of each point is affected by several factors : energy of deuteron, intensity of beam, period of acceleration time, efficiency of beam extraction, and position of bombarded target.

If these factors are kept constant, we could determine the cooling period, after which persons are allowed to enter the cyclotron vault. Measured radiation levels and normalized cooling time are shown in Table 2. In this case, the target position was at the No. 2 beam course and the factors affecting the residual radiation were kept nearly constant except beam intensity. The normalized cooling periods were calculated so that the residual radiation level at the point C in Fig. 1 decays to 10 mR/h after the operation has been stopped after continued irradiation at 30 μA beam intensity. If the beam intensity is higher, the cooling period should be increased.

12. A NEW MACHINE

12-1. Specifications of Variable Frequency Linac

M. Odera

Main specifications of the linac are briefly shown in Table 1, in which energy gain per charge, power consumption, number of drift tubes, and required field gradient of drift tube quadrupole magnets at each stage are given.

The injector is composed of a high-voltage generator rated at 500 kV and stabilized to 10^{-3}, a metallic cage on high-voltage insulators housing a heavy ion source, a charge snalyzing magnet, telemetering and control equipments, various power supplies, and a motor generator driven by an insulating rod from the ground, an accelerating column, beam focusing elements, slit systems, switching and steering magnets, and devices for beam diagnosis such as emittance and phase measuring probes.

The Wideröe cavities are of a quarter wave coaxial resonator type and change of resonant frequency is possible. High-voltage end of center conductor is loaded with drift tubes. Quadrupole magnets are provided in drift tubes at ground potential. Tubes at ground and

Table 1. Specifications of the Linac.

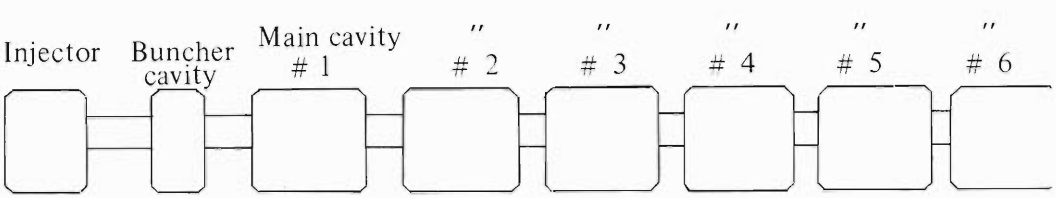

	Injector	Buncher cavity	Main cavity # 1	" # 2	" # 3	" # 4	" # 5	" # 6
Energy gain per charge (MeV)	0.5	–	3.2	4.0	3.8	3.1	3.3	2.8
Rf power (kW)	–	1	60	80	100	120	130	140
Number of drift tubes	–	–	21	19	15	11	11	9
Maximum gradient of quadrupoles (kG/cm)	–	–	7	3	1.5	1.2	1.0	0.8

radiofrequency high voltage are arranged alternately with axes in line and the voltage developed between the tubes accelerates ions. Tube length is determined so that ions travel in it for a half period π of rf. However, for the first several drift tubes of cavity # 1, tube length of 3π has to be adopted to make field gradients of quadrupoles within technically possible limit. Use of this length results in the relatively small effective shunt impedance of the # 1 cavity. The impedance is defined by

$$\frac{(\text{Effective voltage gain/unit length})^2}{\text{power loss/unit length}}$$

and represents efficiency of the accelerating system. If it is possible to use length of π for all the tubes the voltage gain of cavity # 1 would be larger than 4 MV.

A vacuum system comprising of cryopumps and turbo-molecular pumps will maintain the pressure in the cavities below 10^{-6} Torr. The reason for choosing the above system is to secure a clean oil-free vacuum as well as a low pressure. The contemporary progress of cryotechnology seems to allow fulfilment of this aim with relatively low cost.

The most important technique critical to this project is that of the high-power radiofrequency exciter system. The power indicated in Table 1 must be supplied to each cavity for frequencies between 20 and 50 MHz. The amplitude should be regulated and the relative phase be controlled. Detectors necessary to those instrumentation must have wide-band applicability.

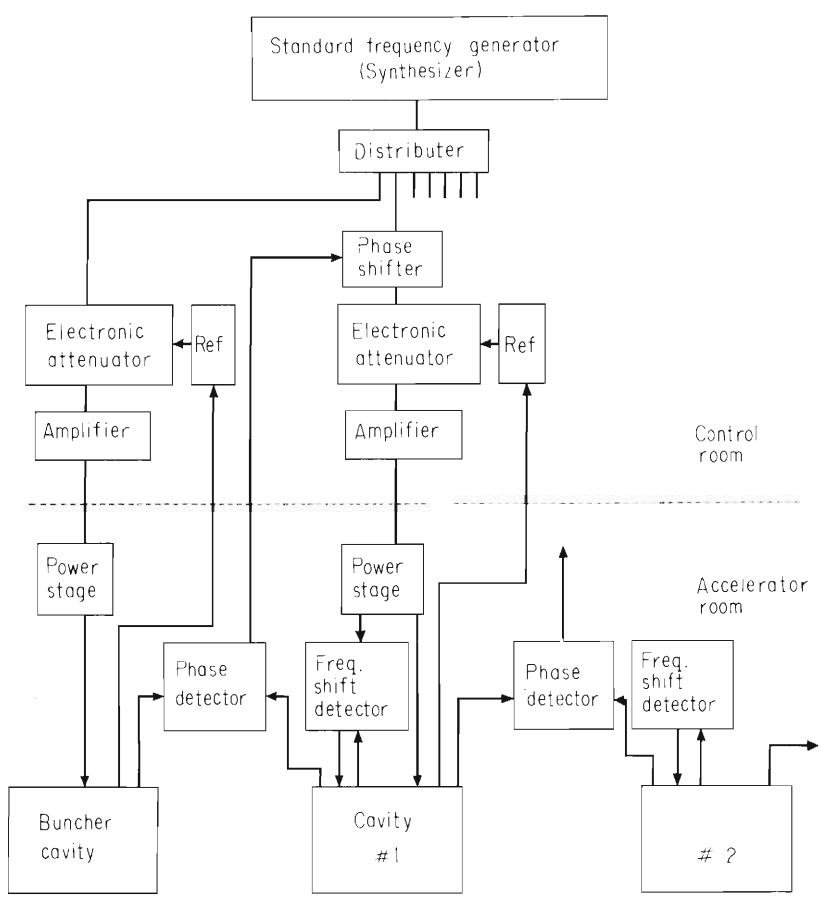

Fig. 1. Block diagram of the radiofrequency system.

Drift of resonant frequency will be detected by comparing the phase of cavity voltage and the exciter current. Figure 1 is a block diagram of the radiofrequency system.

Tuning of the whole accelerator system will be made by observing beam characteristics as emittance or phase bunching. Suitable detecting probes may be installed at various places. When the parameters are determined by the initial testing run the prescription of operation will be prepared. For a while, a small computer will memorize this prescription together with an interpolation formula and give a table of parameters according to operator's request. We hope to be able to expand gradually the role of computer in future. The control equipments have to be designed to allow this expansion.

12-2. The Variable Frequency Linac Project

Results of Measurements on Model Cavity 1

M. Odera, T. Tonuma, M. Hemmi, and Y. Chiba

As our variable frequency linac has no predecessor, several developmental works must be made by ourselves. Here the results of measurements on Model 1 of accelerating structure which was reported previously[1] are described.

The resonant frequency spectra, field distribution of several modes, and its change according to the cavity shape were investigated. The results substantiate the design aim of the linac. The frequency spectra are simple and discrimination of wanted modes from unwanted ones seems easy as was anticipated. Fig. 1 is an example of resonant frequency spectrum. Separation of the first higher mode f_1 and the lowest frequency f_0 is more than 10 MHz. Compare this value with that of the Alvarez type where separation less than 100 kHz is seen at times. In that case, an abrupt change of beam load or a small change of dimensions of some part is apt to excite unwanted modes. Stabilization of a field pattern of the Alvarez cavity needs several devices as well as machining of high precision.

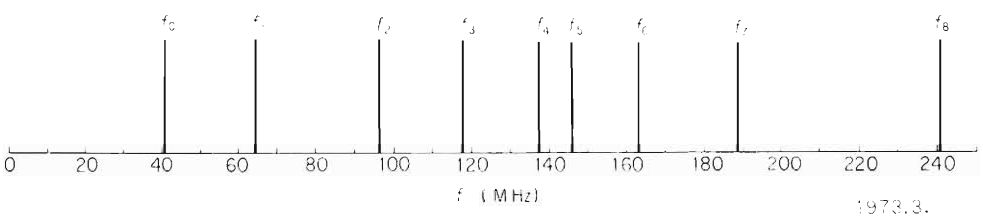

Fig. 1. Resonant frequency spectrum of Model cavity 1.

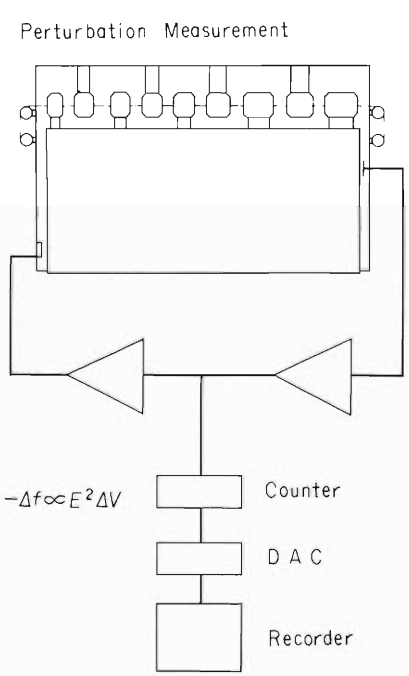

Fig. 2. Method of measurement of field distribution by perturbation. Frequency shift is converted by a digital to analogue converter to a voltage signal and fed to a recorder.

Figure 2 is an illustration of the method of measurement of field distribution by a perturbation technique. A small brass sphere is drawn through the axis of drift tube hole with a Nylon cord. The sphere perturbs the electric field between drift tubes and causes a small change of resonant frequency Δf. Slater's relation allows one to know the strength of field E from this shift. It can be written as $\Delta f \propto E^2 \Delta V$, where ΔV is the volume of the sphere, which must be small enough to make the perturbation approximation good. Maximum Δf is of the order of 1 kHz for resonant frequency of around 50 MHz. To obtain detailed distribution between gaps the oscillator must be stable at 10^{-7} at least for 5 min which is the time the sphere travels 10 cm. The stability was attained by a phase-tuned oscillator scheme using a tuned-amplifier and exclusion of external vibration caused by heavy vehicles on the street about 50 m distant. Figure 3 is a distribution for f_0, Fig. 4 for f_1, and Fig. 5 for f_2. There are distinct differences in the figures. By choosing a suitable feeding point unwanted modes can be easily suppressed. These distributions are essentially constant against frequency variation by a shorting plane. Small change of the relative distribution was seen by use of capacity compensators near drift tubes. Improvement of this structure is in progress.

Table 1 shows transit time factors T_0 calculated from the measured field distribution. Voltage gain in each gap is given by $V_0 T_0 \cos\phi_S$, where V_0 is the potential difference between neighboring drift tubes and ϕ_S is the phase of synchronous particles.

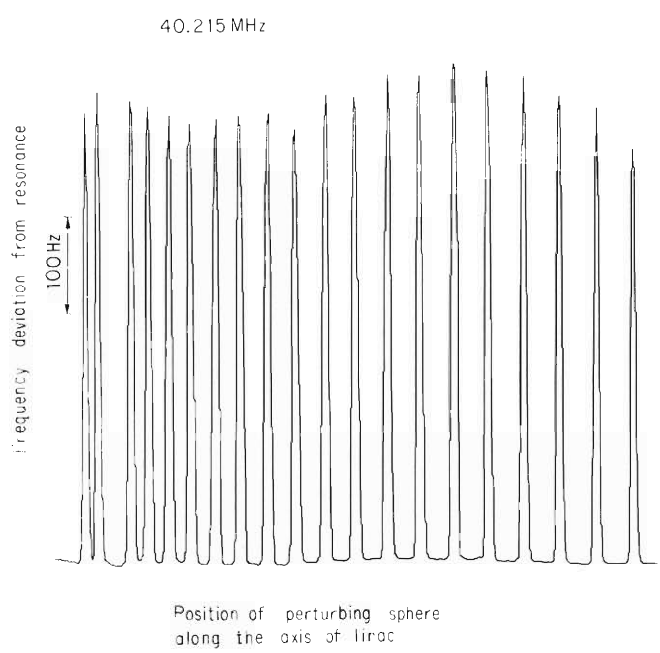

Fig. 3. Field distribution of the lowest mode. Really, this is the distribution of frequency shift and the abscissa is proportional to square of field strength. Representations are the same as in Fig. 4 and Fig. 5.

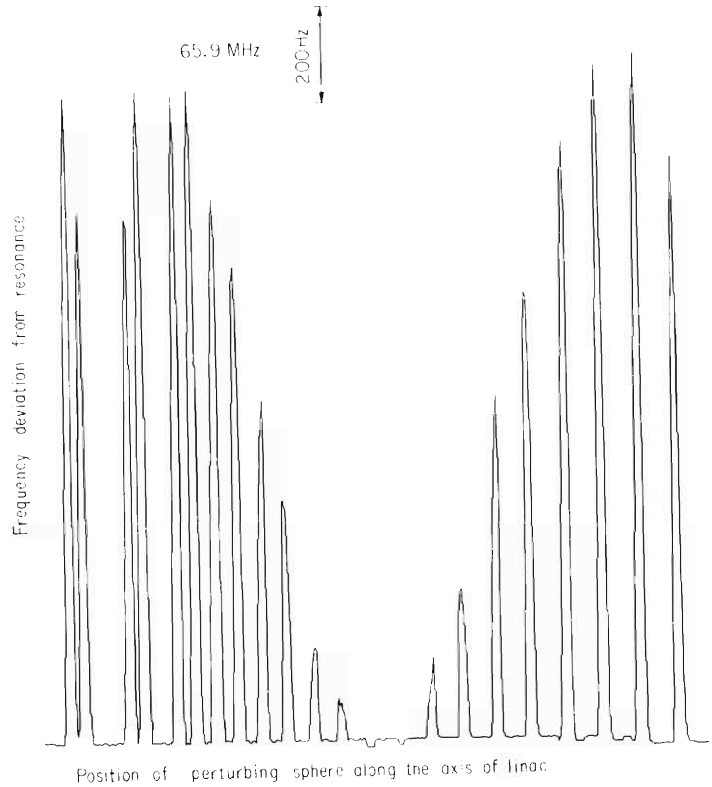

Fig. 4. Field distribution of the first higher mode f_1.

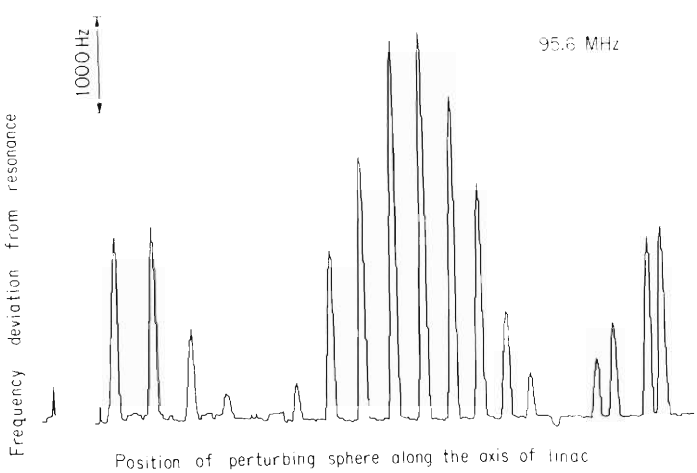

Fig. 5. Field distribution of the second higher mode f_2.

Table 1. Transit time factors T_0 at accelerating gaps determined from measured field distribution.

Gap number	1	2	3	4	5	6	7	8
T_0	0.800	0.830	0.865	0.880	0.895	0.910	0.920	0.930

Gap number	9	10	11	12	13	14	15	16
T_0	0.935	0.940	0.945	0.950	0.955	0.960	0.963	0.966

Reference

1) M. Odera : IPCR Cyclotron Progr. Rep., 6, 16 (1972).

12-3. The Variable Frequency Linac Project

Orbit Dynamics: Radial Acceptance

T. Tonuma, F. Yoshida, and M. Odera

A suitable value of injector voltage was discussed previously and 500 kV was chosen as a compromise between requirements of orbit dynamics and economy.[1] Figure 1 shows magnetic field gradients of quadrupole magnets, which are provided in drift tubes, necessary for focusing ions when an ion beam enters the linac after having been accelerated by a voltage of 500 kV. The field gradients from 1st to 7th tubes have been estimated under the conditions that each drift tube at high voltage potential as well as earth potential has a quadrupole magnet and the tube length is determined so that ions travel in it for one and a half period, 3π, of rf

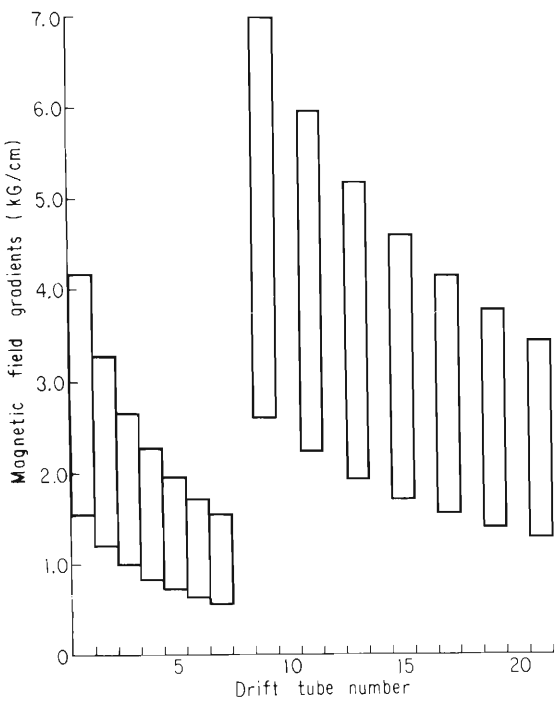

EV number used is $1.5 \times 10^4 kV^2/cm$, the gaps between drift tubes are 3 cm, and $\Psi_S = -25°$ for synchronous particles. Upper limit is for m/e = 22, f = 18.5 MHz and lower limit for m/e = 3, f = 50 MHz.

Fig. 1. Magnetic field gradients necessary for focusing of beams at injector voltage of 500kV.

field to make field gradients of quadrupoles within a technically possible limit. The condition is effective to have a large radial phase acceptance. In the previous report, the field gradients were calculated assuming quadrupoles being installed only in the drift tubes at earth potential.[1] The radial acceptance in that case was much smaller than in the present configuration. The field gradients after the 8th drift tube have been calculated assuming that only drift tube at earth potential are provided with quadrupole magnets and the tube length is chosen to be a half period π of rf.

Figure 2 shows radial acceptance of the first cavity in the x- and y-directions by use of magnetic field gradients shown in Fig. 1. The aperture of a drift tube is 20 mm. The different shape of the acceptance between x- and y-directions comes from the fact that the first quadrupole magnet is divergent in the x-directions and convergent in the y-direction. Both radial phase acceptances are, however, about 70 ~ 80 mm-mrad.

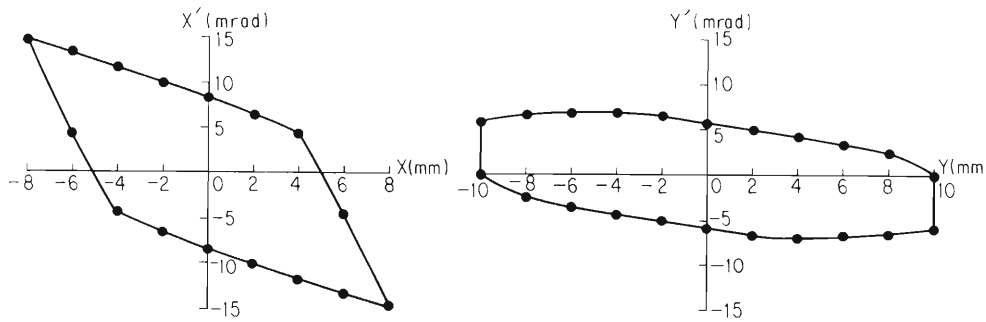

Fig. 2. Radial acceptance.

Reference

1) F. Yoshida, T. Tonuma, and M. Odera : to be submitted to the Reports of IPCR (in Japanese) a part of which was given in IPCR Cyclotron Progr. Rep., 6, 18 (1972).

12-4. The Variable Frequency Linac Project

Orbit Dynamics: Phase Oscillation and Energy Resolution

F. Yoshida, T. Tonuma, and M. Odera

One can follow the phase oscillation of an ion which is injected at an initial phase Ψ_1 different from synchronous phase Ψ_S and then passes through each drift tube. When the phase of Ψ_S ion becomes $\Psi_S + \pi$ by passing through one section, that of Ψ_1 ion will be $\Psi_1 + \pi + \Delta\Psi_1$ as shown in Fig. 1. The phase shift $\Delta\Psi_1$ in the first section is expressed by $\Delta\Psi_1/\pi = (L_2 - L_2')/L_2$, where L_2 is the distance which the synchronous particle travels in a half period and L_2' is that of Ψ_1 ion. These distances can be written in terms of an injection energy E_0, a voltage V_0

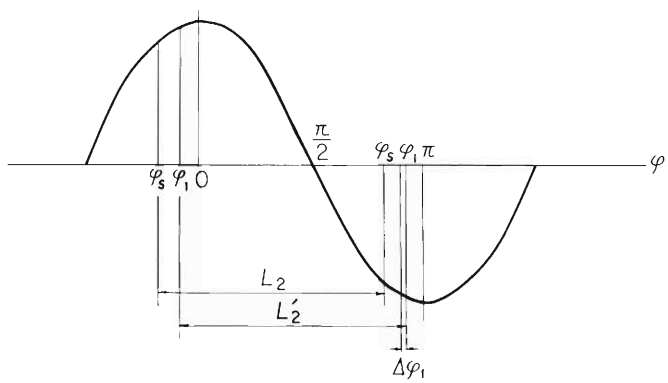

Fig. 1. Diagram used in iterative calculations.

between adjacent drift tusbes, a transit time factor T_0, and a constant κ as follows:

$$L_2 = \kappa \sqrt{E_0 + V_{01} T_{01} \cos\Psi_S}$$

$$L_2' = \kappa \sqrt{E_0 + V_{01} T_{01} \cos\Psi_1} \quad .$$

Use of these relations gives

$$\Delta\Psi_1 = \left(1 - \sqrt{\frac{E_0 + V_{01} T_{01} \cos\Psi_S}{E_0 + V_{01} T_{01} \cos\Psi_1}} \right) \times \pi \ (\text{in } 3\pi \text{ mode}, \times 3) \quad .$$

By renaming $\Psi_1 + \Delta\Psi_1$ as Ψ_2, the phase shift caused by a transit of the ion to the next section is $\Delta\Psi_2$. Then,

$$\Delta\Psi_2 = \left(1 - \frac{L_3'}{L_3} \right) \times \pi \ (\text{in } 3\pi \text{ mode}, \times 3)$$

$$L_3 = \kappa \sqrt{E_0 + V_{01} T_{01} \cos\Psi_S + V_{02} T_{02} \cos\Psi_S}$$

$$L_3' = \kappa \sqrt{E_0 + V_{01} T_{01} \cos\Psi_1 + V_{02} T_{02} \cos\Psi_2} \quad ,$$

and by iteration

$$\Delta\Psi_{n-1} = \left(1 - \frac{L_n'}{L_n} \right) \times \pi \text{ (in } 3\pi \text{ mode, x 3)}$$

$$L_n = \kappa \sqrt{E_0 + V_{01} T_{01} \cos\Psi_3 + \cdots\cdots + V_{0n-1} T_{0n-1} \cos\Psi_s}$$

$$L_n' = \kappa \sqrt{E_0 + V_{01} T_{01} \cos\Psi_1 + \cdots\cdots + V_{0n-1} T_{0n-1} \cos\Psi_{n-1}}$$

The relation of Ψ_n with $(E_n - E_s)/E_s$ is shown in Fig. 2. E_s is the energy of synchronous particle and E_n is that of an arbitrary ion, and the figures show examples of the result of step-by-step calculation starting from two extreme initial conditions. Parameters used in the calculations are tabulated in Table 1. It can be seen from Fig. 2 that the phase oscillations are strongly damped as acceleration proceeds and the energy resolution at the exit of the linac is about ± 0.2 %. However, the calculation does not include factors such as alignment errors, voltage fluctuation or phase excursion of the radiofrequency system, and Fig. 2 should be taken as giving a lower limit of the quantities concerned.

Table 1. Linac parameters used in calculations.

Cavity	# 1	# 2	# 3	# 4	# 5	# 6
Gap (cm)	3.0	5.0	7.0	9.0	10.0	11.0
V_0 (kV)	200	210	320	360	380	400
Number of section	21	19	15	11	11	9
Transit time factor T_0	0.90	0.92	0.94	0.95	0.95	0.95
Total L(m)	3.47	3.63	3.73	3.19	3.55	3.16

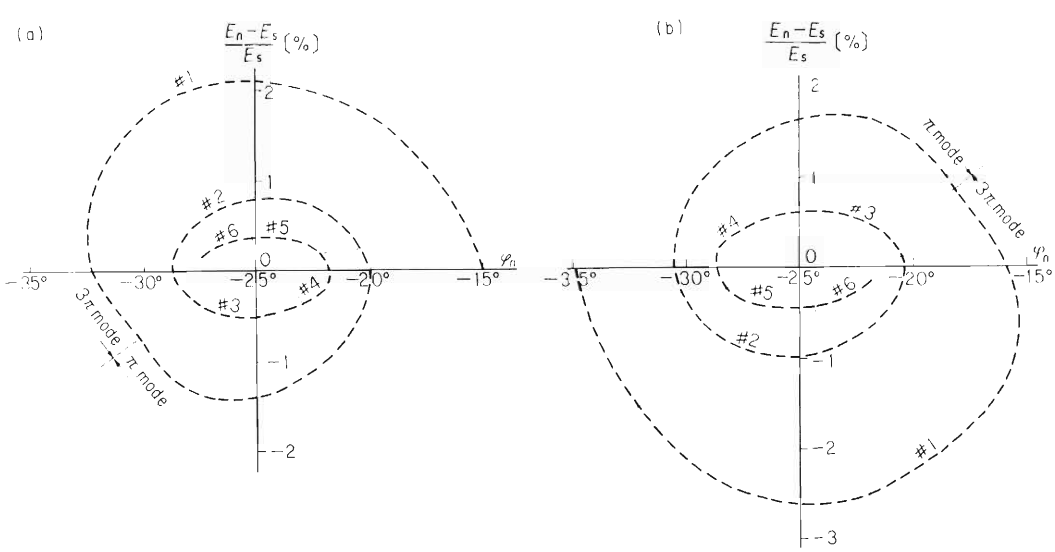

Fig. 2. The relation of Ψ_n with $(E_n - E_s)/E_s$. Calculations of (a) and (b) were carried out with $\Psi_1 = -15°$ and $-35°$ respectively for a synchronous phase $\Psi_s = -25°$.

12-5. Two Examples of Heavy-Ion Cyclotron with External Injection Provision

M. Odera and H. Kamitsubo

It was pointed out by K. Matsuda[1] that an externally injected cyclotron using stripping phenomenon has several desirable characteristics. Table 1 shows the most probable charge states of several ions charge-stripped through media of suitable thickness. The magnetic rigidity of the ions before and after their charge is stripped is compared assuming the initial charge to be that produced by a conventional ion source. A large reduction of rigidity can be seen. Figure 1 taken from Ref. 1) shows a characteristically slow increase of rigidity against large change of energy of heavy ions. These table and figure indicate a possibility of acceleration of heavy ions of large mass to moderate energies by a cyclotron of modest size. Here two examples of design along this scheme are presented.

Table 1. Most probable charge states of after stripping at 1 MeV/nucleon.

Ion specie	O - 16	Ar-40	Kr-84		Xe-132	
Charge before stripping	4	6	8		9	
Magnetic rigidity (kG·cm)	576	960	1510		2110	
Stripper	gas	gas	gas	solid	gas	solid
Charge after stripping	8	12	15	20	17	26
Magnetic rigidity (kG·cm)	288	480	806	605	1100	730

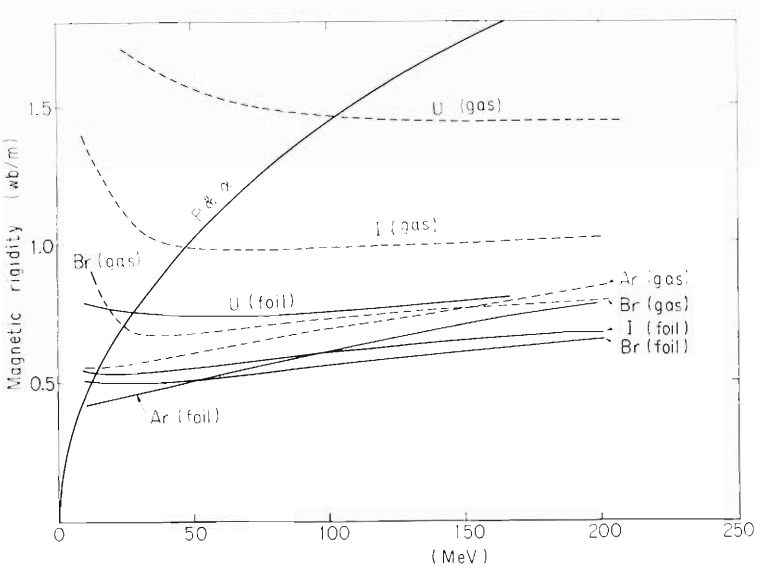

Fig. 1. Magnetic rigidity of ions stripped of charge at the energies indicated.

(1) A linac-injected sector-focused cyclotron

The proposed variable-frequency linac[2] has the characteristics suitable for a heavy ion injector. Energy per nucleon of ions accelerated is larger than 1 MeV and a large increase of the number of charges can be expected by the stripping process. Also, the intensity of beam is moderate. External injection of heavy ions into a sector-focused cyclotron by a linac was first realized in 1971 by the ALICE system in the research institute of University of Paris at Orsay.[3] Particles are injected along the valley of magnet pole and the injection orbit is converted into acceleration orbit by use of an abrupt change of the orbit radius by charge stripping. The scheme is shown in Fig. 2. Table 2 shows an example of parameters of a

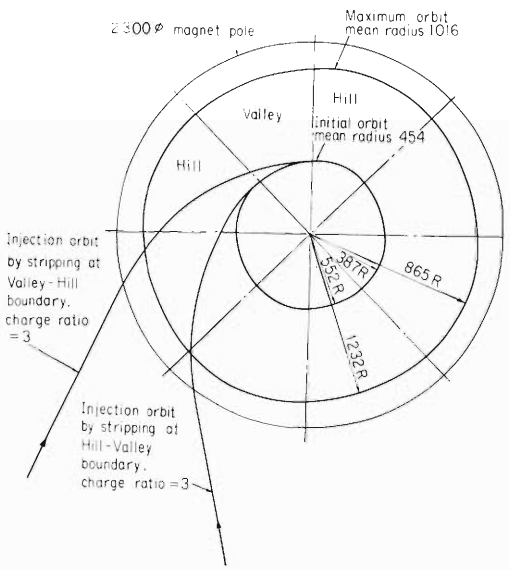

Fig. 2.
Conversion of an injection orbit to an acceleration orbit by stripping of charge at certain radius of a sector-focused cyclotron.

Table 2. An example of parameters of a linac-sector focused cyclotron combination.

Ion species	Ar-40	Kr-84	Xe-132
Injection energy (MeV)	120	160	180
Linac frequency(MHz)	33.5	26.7	22.6
Charge before stripping	6	8	9
Charge after foil stripper	18	24	27
Ratio of charge	3.0	3.0	3.0
Magnetic rigidity (kG·cm) at injection	555	696	820
Initial orbit radius(cm)	45.4	45.4	45.4
Mean field(kG)	12.2	15.4	18.0
Circulating frequency (MHz) of ion	8.38	6.68	5.65
Harmonic number	4	4	4
Maximum orbit radius(cm)	101.6	101.6	101.6
Final energy (MeV)	600	800	900

possible linac-injected s.f. cyclotron system. Conversion of the present cyclotron into the sector-focused type of this size is feasible.

(2) A linac-injected separate-sector cyclotron

The separate-sector cyclotron was originally invented to make external injection and extraction of beam easy.[4] This type is very suitable for an externally injected heavy ion cyclotron. The simplest four-sector type is shown schematically in Fig. 3. Accelerating electrodes can be installed in free sectors where no obstacle is present. Structure of cavity effective to generate a large accelerating voltage can be adopted. Orbit at injection is simple and charge-changing between narrow magnetic gap is not required. While the foil strippers must be used in the above-mentioned s.f. cyclotron scheme between magnetic gap, the well-known fragility of foil under intense heavy ion bombardment presents a problem which is not easy to be solved. There is no such a difficulty in case of the separate-sector cyclotron, where a gas stripper can be used before injection into the accelerating chamber. However, the most probable charge state is considerably smaller for gas strippers than for foils. Larger magnetic rigidity is required in price of simpler structure and easier operation.

Table 3 shows some parameters of this scheme. Turn-separations at the initial and exist orbit in the region free of magnet are large enough to allow good injection and extraction efficiency. This, together with the use of stripper at a suitable place outside of the main accelerator system greatly simplifies operation and guarantees moderate beam intensity. When the energies same with those of Table 2 are required, the weight of magnet can be reduced to 600 ton as shown in parenthesis.

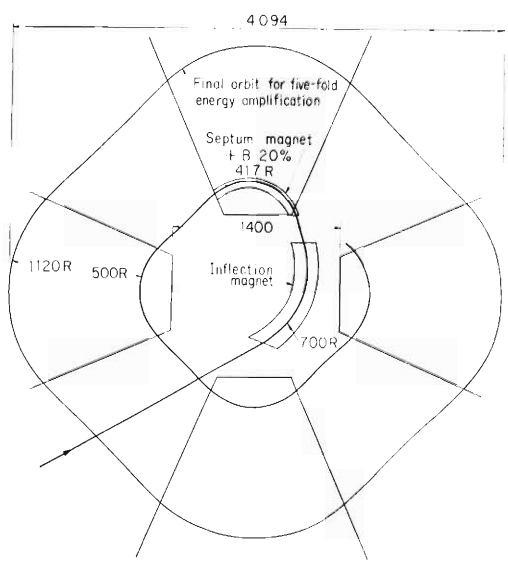

Fig. 3. A four-magnet separate-sector cyclotron and an injection scheme.

Table 3. Parameters of a linac-injected separate four-sector cyclotron.

Ion species	Ar-40	Kr-84	Xe-132	He-3
Injection energy (MeV)	120	160	180	20
Linac frequency (MHz)	33.5	26.7	22.6	50
Charge after stripping	16	20	24	2
Magnetic rigidity at injection (kG·cm)	623	834	924	558
Width of magnet (degree)	47	–	–	–
Gap of magnet (cm)	6	–	–	–
Initial orbit radius (cm)	50	–	–	–
Initial mean radius (cm)	91	–	–	–
Magnetic field (kG)	12.5	16.7	18.5	11.2
Weight of magnet (ton)	1400 (600)	–	–	–
Circulating frequency of ion (MHz)	4.19	3.34	2.83	6.25
Harmonic number	8	–	–	–
Number of accelerating electrodes	2	–	–	–
Width of electrodes (degree)	22.5	–	–	–
Voltage gain per turn (MV)	1	–	–	–
Orbit separation at injection (cm)	3	–	–	–
Orbit separation at extraction (cm)	1.2 (1.6)	–	–	–
Maximum orbit radius (cm)	150 (112)	–	–	–
Maximum mean radius (cm)	273 (204)	–	–	–
Maximum energy (MeV)	1080 (600)	1440 (800)	1620 (900)	180 (100)

Numbers in ( ) are values when the maximum energies same with those of Table 2 are required.

References

1) K. Matsuda : Sci. Papers I.P.C.R., 66, 33 (1972).

2) M. Odera and T. Tonuma : AIP Proc. No. 9, Cyclotrons - 1972, (Eds. J. J. Burgerjon and A. Strathdee), Vancouver, Canada, p. 283, (1972) ; M. Odera : IPCR Cyclotron Progr. Rep., 4, 24 (1970) ; M. Odera and H. Kamitsubo : ibid., 6, 15 (1972).

3) A. Cabrespine and M. Lefort : Nucl. Instr. Methods, 97, 29 (1971).

4) M. M. Gordon : Ann. Phys., 50, 571 (1968) ; Nucl. Instr. Methods, 58, 245 (1968).

13. LIST OF PUBLICATIONS

1) F. Akiha, T. Aburai, T. Nozaki, and Y. Murakami : "Yield of ^{52}Fe for the Reactions of ^{3}He and α on Chromium", Radiochim. Acta, 18, 108 (1972).
2) F. Ambe and S. Ambe : "Chemical Effects of Neutron-Induced Nuclear Reactions in Halates and Related Compounds IV. The (n. γ) and (n, 2n) Reactions in Chlorates", Radiochim. Acta, in press.
3) S. Ambe, F. Ambe, and N. Saito : "The Oxidation States of ^{119}Sb after the EC Decay of ^{119m}Te in TeO_2 and H_6TeO_6", Radiochim. Acta, in press.
4) F. Ambe and S. Ambe : "Mössbauer Spectroscopic Verification of Two Different States of Impurity ^{119}Sn Atoms in Sb_2Te_3", Phys. Lett., 43A, 399 (1973).
5) K. Hiruta, T. Nomura, T. Inamura, and M. Odera : "Alpha Decay of ^{218}Th, a New Isotope", Phys. Lett., 45B, 244 (1973).
6) Y. Yamazaki, S. Nagamiya, T. Nomura, K. Nakai, and T. Yamazaki : "Magnetic Moment of a Core-Excited Isomeric State in ^{210}Po", Phys. Lett., 44B, 440 (1973).
7) T. Suzuki and C. Hinohara : "The Splitting of the Isospin and Spin-Isospin Dipole Resonances in ^{12}C", Nucl. Phys., A204, 289 (1973).
8) C. L. Lin, S. Yamaji, and H. Yoshida : "Finite-Range Calculation of Two-Nucleon Transfer Reaction", Nucl. Phys., A209, 135 (1973).
9) T. Suzuki : "New Giant Resonances", Nucl. Phys., to be published.
10) T. Suzuki : "Sum Rule Approach for Nuclear Vibrations and Effects of the Core Polarization", Nucl. Phys., to be published.
11) S. Nagamiya, Y. Yamazaki, O. Hashimoto, T. Nomura, K. Nakai, and T. Yamazaki : "Magnetic Moments of the $[\pi h_{9/2}^2]\ 8^+$ States in Po Isotopes and of the $[(\pi h_{9/2}^9)\ 8^+ \otimes \nu p_{1/2}]\ 17/2^-$ State in ^{209}Po", Nucl. Phys., A211, 381 (1973).
12) T. Nomura, K. Hiruta, T. Inamura, and M. Odera : "Ground State Alpha Decays of N=128 Isotones; ^{216}Ra, ^{217}Ac and ^{218}Th", Nucl. Phys., in press.
13) F. Ambe, S. Ambe, and H. Shoji : "Preparation of ^{119}Sb for Mössbauer Spectroscopy of ^{119}Sn", Radiochem. Radioanal. Lett., 15, 349 (1973).
14) N. Akiyama, Y. Yatsurugi, Y. Endo, Z. Imayoshi, and T. Nozaki : "Lowering of Breakdown Voltage of Semiconductor Silicon Due to the Precipitation of Impurity Carbon" Appl. Phys. Lett., 22, 630 (1973).
15) Y. Yatsurugi, N. Akiyama, Y. Endo, and T. Nozaki : "Concentration, Solubility, and Equilibrium Distribution Coefficient of Nitrogen and Oxygen in Semiconductor Silicon", J. Electrochem. Soc, 120, 975 (1973).
16) T. Nomura and K. Hiruta : "A Method of Measuring Alpha Decays in the Nanosecond Range", Nucl. Instr., 108, 61 (1973).
17) T. Suzuki and C. Hinohara : "Sum Rules and the Nonexchange Force", Phys. Rev., to be published.

18) T. Suzuki : "Momentum Transfer Dependence of the Effective Charge for Electro-excitation", Phys. Rev C, to be published.

19) T. Nomura, K. Hiruta, M. Yoshie, and O. Hashimoto : "Alpha Decay of ^{215}Fr", Phys. Rev., to be published.

20) T. Fujisawa, S. Yamaji, K. Matsuda, S. Motonaga, F. Yoshida, H. Sakaguchi, and K. Masui : "The Elastic and Inelastic Scattering of ^{3}He from ^{12}C at 24.0, 29.2, 34.7 and 39.6 MeV", J. Phys. Soc. Japan, 34, 5 (1973).

21) T. Tonuma, I. Kohno, Y. Miyazawa, F. Yoshida, T. Karasawa, T. Takahashi, and S. Konno: "Charge Changing of Energetic Heavy Ions in Gases", J. Phys. Soc. Japan, 34, 148 (1973).

22) S. Yamaji : "The Coupled-Channel Born-Approximation Calculation of the Reaction ^{100}Mo (t, p) ^{102}Mo", J. Phys. Soc. Japan, 34, 298 (1973).

23) C. Gil, K. Nishiyama, T. Nomura, T. Yamazaki, and K. Miyano : "A New Short-Lived Isomer in ^{114}Sb", J. Phys. Soc. Japan, 34, 874 (1973).

24) S. Takeda, S. Yamaji, K. Matsuda, I. Kohno, N. Nakanishi, Y. Awaya, and S. Kusuno : "^{100}Mo (t, p) ^{102}Mo Reaction at 15.8 MeV", J. Phys. Soc. Japan, 34, 1115 (1973).

25) O. Hashimoto, T. Nomura, T. Yamazaki, K. Miyano, and M. Ishihara : "Magnetic Moment of the 8^{+} $[(\nu g_{9/2})^{-2}]$ State in ^{86}Sr", J. Phys. Soc. Japan, 34, Suppl. 259 (1973).

26) O. Hashimoto, A. Sumi, T. Nomura, S. Nagamiya, K. Nakai, and T. Yamazaki : "The g Factor of the 7^{+} Isomeric State in ^{202}Tl", J. Phys. Soc. Japan, 34, Suppl. 269 (1973).

27) S. Nagamiya, Y. Yamazaki, O. Hashimoto, T. Nomura, K. Nakai, and T. Yamazaki : "Magnetic Moments of High-Spin Isomeric States in Po Isotopes", J. Phys. Soc. Japan, 34, Suppl. 283 (1973).

28) Y. Yamazaki, S. Nagamiya, T. Nomura, K. Nakai, and T. Yamazaki : "Magnetic Moment of a Core-Excited Isomeric State in ^{210}Po", J. Phys. Soc. Japan, 34, Suppl. 286 (1973).

29) T. Nomura : On the Violation of the Additivity of the $1f_{7/2}$ Neutron Moments", J. Phys. Soc. Japan, 34, Suppl. 331 (1973).

30) T. Nomura : "Magnetic Moments of the $1f_{7/2}$ Nuclei", J. Phys. Soc. Japan, 34, Suppl. 619 (1973).

31) O. Hashimoto, T. Nomura, T. Yamazaki, K. Miyano, and M. Ishihara : "The g-Factor of the 8^{+} State in ^{86}Sr" J. Phys. Soc. Japan, 35, 337 (1973).

32) N. Shiotani, T. Okada, H. Sekizawa, T. Mizoguchi, and T. Karasawa : "Positron Annihilation in Ferromagnetic Nickel", J. Phys. Soc. Japan, 35, 456 (1973).

33) M. Odera, Y. Chiba, T. Fujisawa, Y. Miyazawa, and O. Terajima : "The Radiofrequency System of the IPCR (RIKEN) Variable Energy Multi-Particle Cyclotron", Sci. Papers I.P.C.R., 67, 90 (1973).

(Papers presented at international meetings)

1) M. Imamura : "Some Aspects of Heavy-Ion Radiolysis", Joint U.S.-Japan Conf. Processes and Intermediates in the Radiat. Chem. of Condensed Phase, Catalina Isl., California, Feb. (1973).
2) H. Kamitsubo, M. Yoshie, I. Kohno, S. Nakajima, I. Yamane, and T. Mikumo : "Reaction Mechanism and Level Density Informations in Multi-Nucleon Transfer Reactions", Intern. Symp. Transfer Reactions Induced by Heavy-Ion, Argonne, March (1973).
3) I. Kohno, H. Kamitsubo, S. Nakajima, I. Yamane, M. Yoshie, and T. Mikumo : "Single and Multi-Nucleon Transfer Reactions on N=28 Nuclei Induced by ^{14}N and ^{12}C", Intern. Symp. Transfer Reactions Induced by Heavy-Ion, Argonne, March (1973).
4) T. Nozaki : "Examination of the ^{18}F Yield for Various Reactions and Synthesis of Some ^{18}F Compounds", U.S.-Japan Cooperative Sci. Semi. on Recent Advances in Radiochem. Tech. and Applications, Oiso, Nov. (1973).
5) F. Ambe : "Mössbauer Emission Spectra of ^{119}Sn after the EC Decay of ^{119}Sb", U.S.-Japan Cooperative Sci. Semi. on Recent Advances in Radiochem. Tech. and Applications, Oiso, Nov. (1973).
6) H. Sekizawa, T. Okada, T. Mizoguchi, T. Karasawa, and N. Shiotani : "Positron Annihilation in Ferromagnetic Nickel", Third Intern. Conf. on Positron Annihilation, Helsinki, Aug. (1973).
7) N. Shiotani, T. Okada, H. Sekizawa, and T. Mizoguchi : "Positron Annihilation in Vanadium and Niobium", Third Intern. Conf. on Positron Annihilation, Helsinki, Aug. (1973).
8) S. Takeda, H. Ohnuma, N. Nakanishi, S. Yamada, and M. Sekiguchi : "P-n Interaction Effect Observed by (dt) Reaction on the Isotone", Proc. Intern. Conf. Nucl. Phys., Munich, 1973, 1, 79 (1973).
9) I. Kohno, H. Kamitsubo, S. Nakajima, M. Yoshie, T. Motobayashi, and T. Mikumo : "Transfer Reactions Induced by ^{14}N and ^{12}C at High Energies", Proc. Intern. Conf. Nucl. Phys., Munich, 1973, 1, 498 (1973).
10) T. Nomura, K. Hiruta, M. Yoshie, and O. Hashimoto : "Angular Distribution and Linear Momenta of Heavy Reaction Products in the ^{209}Bi + ^{12}C Reaction", Proc. Intern. Conf. Nucl. Phys., Munich, 1973, 1, 545 (1973).
11) S. Yamaji, S. Suekane, and K. Harada : "Total Energy Surface for ^{236}U in the Two-Center Shell Model", Proc. Intern. Conf. Nucl. Phys., Munich, 1973, 1, 596 (1973).
12) T. Nomura, K. Hiruta, M. Yoshie, and O. Hashimoto : "In-Beam Alpha Spectroscopy of N=128 Isotones, ^{215}Fr, ^{216}Ra, ^{217}Ac, and ^{218}Th", Proc. Intern. Conf. Nucl. Phys., Munich, 1973, 1, 687 (1973).

14. LIST OF PERSONNEL

Members of the Board

HAGIHARA Hitosi 萩原 仁 (Chairman)
HAMADA Tatsuji 浜田達二
KAMITSUBO Hiromichi 上坪宏道
NAKANE Ryohei 中根良平
NOZAKI Tadashi 野崎 正
ODERA Masatoshi 小寺正俊

Users Committee

HAMADA Tatsuji 浜田達二 (Chairman)
IMAMURA Masashi 今村 昌
KAMITSUBO Hiromichi 上坪宏道
KARASAWA Takashi 唐沢 孝
MATSUYAMA Akira 松山 晃
NOZAKI Tadashi 野崎 正
ODERA Masatoshi 小寺正俊
SAKAIRI Hideo 坂入英雄
SEKIZAWA Hisashi 関沢 尚

Managers of Users Group

HAMADA Tatsuji 浜田達二
NOZAKI Tadashi 野崎 正
ODERA Masatoshi 小寺正俊

Operating Personnel

Machine Group

HEMMI Masatake 逸見政武
INOUE Toshihiko 井上敏彦
MIYAZAWA Yoshitoshi 宮沢佳敏
SHIMAMURA Akira 島村 晃
TONUMA Tadao 戸沼正雄

Operation

FUJITA Shin 藤田 新
IKEGAMI Kumio 池上九三男
KAGEYAMA Tadashi 影山 正
KOHARA Shigeo 小原重夫
NAKAJIMA Hisao 中嶋尚雄
OGIWARA Kiyoshi 荻原 清
TAKEBE Hideki 武部英樹
TERAJIMA Osamu 寺島 為

Scientific and Engineering Personnel

Cyclotron Laboratory

CHIBA Yoshiaki 千葉好明
FUJISAWA Takashi 藤沢高志
FUJITA Jiro 藤田二郎
HEMMI Masatake 逸見政武
INAMURA Takashi 稲村 卓
INOUE Toshihiko 井上敏彦
KAMITSUBO Hiromichi 上坪宏道
KARASAWA Takashi 唐沢 孝
KOHNO Isao 河野 功
MIYAZAWA Yoshitoshi 宮沢佳敏
MOTONAGA Shoshichi 元永昭七
NAKAJIMA Shunji 中島諄二
NAKANISHI Noriyoshi 中西紀喜
NOMURA Toru 野村 亨
ODERA Masatoshi 小寺正俊
SHIMAMURA Akira 島村 晃
TAKEDA Shigeru 竹田 繁
TAKIGAWA Noboru 滝川 昇
TONUMA Tadao 戸沼正雄
TOYAMA Manabu 外山 学
YAMAJI Shuhei 山路修平
YOSHIDA Fusako 吉田房子
WADA Takeshi 和田 雄

(Visitors)

EJIRI Hiroyasu 江尻宏泰 (Univ. of Osaka)
FUJINO Takeo 藤野武夫 (Inst. Nucl. Study, Univ. of Tokyo)
HANAZONO Sakae 花園 栄 (Inst. Nucl. Study, Univ. of Tokyo)
IMANISHI Bunryu 今西文竜 (Nihon Univ.)
KATORI Kenji 鹿取謙二 (Tokyo Univ. of Educ.)
KOIKE Masahiro 小池正宏 (Inst. Nucl. Study, Univ. of Tokyo)
KOYAMA Katsuji 小山勝二 (Inst. Nucl. Study, Univ. of Tokyo)
MIKUMO Takashi 三雲 昂 (Tokyo Univ. of Educ.)
MIYANO Kazumasa 宮野和政 (Dept. Phys., Niigata Univ.)
NAGAMIYA Shoji 永宮正治 (Dept. Phys., Univ. of Tokyo)
NAKAI Koji 中井浩二 (Dept. Phys., Univ. of Tokyo)
NAKAMURA Masanobu 中村正信 (Dept. Phys., Kyoto Univ.)
OHNUMA Hajime 大沼 甫 (Inst. Nucl. Study, Univ. of Tokyo)
SAKAGUCHI Harutaka 坂口治隆 (Dept. Phys., Kyoto Univ.)
SEKIGUCHI Masayuki 関口雅行 (Inst. Nucl. Study, Univ. of Tokyo)
SHIBATA Tokushi 柴田徳志 (Dept. Phys., Univ. of Osaka)
Sprouse, Gene (State Univ. of New York at Stony Brook)
TAGISHI Yoshihiro 田岸義宏 (Dept. Phys., Tokyo Univ. of Educ.)
YAMADA Satoru 山田 聡 (Tokyo Inst. Tech.)
YAMANE Isao 山根 功 (Res. Center Nucl. Sci. and Tech. Univ. of Tokyo)
YAMAZAKI Toshimitsu 山崎敏光 (Dept. Phys., Univ. of Tokyo)
YAZAKI Koichi 矢崎紘一 (Dept. Phys., Univ. of Tokyo)
YOSHIDA Hiroshi 吉田 弘 (Univ. of Osaka)

(Students)

HASHIMOTO Osamu 橋本 治 (Univ. of Tokyo)
HIRUTA Kotaro 蛭田幸太郎 (Tokyo Inst. Tech.)
IKEZOE Hiroshi 池添 博 (Univ. of Tokyo)
KANAI Tatsuaki 金井達明 (Tokyo Univ. of Educ.)
MOTOBAYASHI Tohru 本林 透 (Univ. of Tokyo)
YAMAZAKI Yoshishige 山崎良成 (Univ. of Tokyo)
YOSHIE Morio 吉江森男 (Tokyo Univ. of Educ.)

Radiation Laboratory

AWAYA Yohko 粟屋容子
HASHIZUME Akira 橋爪 朗
KATOU Takeo 加藤武雄
KUMAGAI Hidekazu 熊谷秀和
TAKAHASHI Tan 高橋 旦
HAMADA Tatsuji 浜田達二
IZUMO Koichi 出雲光一
KONNO Satoshi 金野 智
OKANO Masaharu 岡野真治
TENDOW Yoshihiko 天道芳彦

(Visitors)

DOKE Tadayoshi 道家忠義 (Waseda Univ.)
IIO Masahiro 飯尾正宏 (Tokyo Metropol. Jeriatric Hosp.)
NAGAHARA Teruaki 永原照明 (Rikkyo Univ.)
SUZUKI Kazuaki 鈴木一明 (Japan Anal. Chem. Res. Inst.)

Nuclear Analytical Chemistry Laboratory

AMBE Fumitoshi 安部文敏
AMBE Shizuko 安部静子
ARATANI Michi 荒谷美智
IWAMOTO Masako 岩本正子
MAKIDE Yoshihiro 巻出義紘
NOZAKI Tadashi 野崎 正
SAITO Nobufusa 斎藤信房

(Visitors)

AKIYAMA Nobuyuki 秋山信之 (Komatsu Electronic Metals Co., Ltd.)
FUKUSHI Kiyoshi 福士 清 (Nat. Inst. of Radiological Sciences)
HARA Toshihiko 原 敏彦 (Nat. Nakano Chest Hosp.)
IDO Tatsuo 井戸達雄 (Nat. Inst. of Radiological Sciences)
KASIDA Yosihiko 樫田義彦 (Nat. Inst. of Radiological Sciences)
YATSURUGI Yoshifumi 八剣吉文 (Komatsu Electronic Metals Co., Ltd.)

Synthetic Organic Chemistry Laboratory

OHTSUKA Yasuo 大塚晏央
TAHARA Akira 田原 昭

Radiobiology Laboratory

IGARASHI Kazui 五十嵐一戌
MATSUYAMA Akira 松山 晃

(Student)

YATAGAI Fumio 谷田貝文夫 (Graduate Course of Sci. Engg., Waseda Univ.)

Radiation Chemistry Laboratory

IMAMURA Masashi 今村 昌
KIMURA Kazuie 木村一宇
MATSUI Masao 松井正夫

Metal Physics Laboratory

HASIGUTI R. Ryukiti 橋口隆吉
KOYAMA Akio 小山昭雄
SAKAIRI Hideo 坂入英雄
SHIOTANI Nobuhiro 塩谷亘弘
YAGI Eiichi 八木栄一

(Visitors)

ISHINO Shiori 石野 栞 (Univ. of Tokyo)
MISHIMA Yoshitsugu 三島良績 (Univ. of Tokyo)
SHIRAISHI Haruki 白石春樹 (Nat. Res. Inst. for Metals)

Magnetic Materials Laboratory

OKADA Takuya 岡田卓也
SEKIZAWA Hisashi 関沢 尚

(Vistor)

MIZOGUCHI Tadashi 溝口 正 (Gakushuin Univ.)

Radiation Monitoring and Safety Office

KODA Kugao 甲田陸男
SAKAMOTO Ichiro 坂本一郎
USUBA Isao 薄葉 勲

15. LIST OF OUTSIDE USERS AND THEIR THEMES

Description is in the order of theme, energy of particle used, and names of person and institution responsible for the theme. Numbers in parentheses are total beam times and frequency of irradiation in the interval between Nov. 1972 and Oct. 1973. Papers published based on the utilization of the cyclotron by the outside users are tabulated at the end of this chapter.

1) "Study of Effect of Helium Bubbles on the Mechanical behavior of Stainless Steel SUS 32 and 316"
   α −32, 34, 36 MeV
   T. Katou, S. Kawasaki, and T. Furuta
   Japan Atomic Energy Research Inst. (88 h, 7)

2) "Study of Method for Measurement of Helium in an Activated Stainless Steel SUS 316 "
   α −34, 36 MeV
   Y. Wada and K. Tsutsumi
   Power Reactor and Nuclear Fuel Development Corporation, Tokai Works. (24 h, 2)

3) "Production of ^{18}F for Bone Tumor Search"
   ^{3}He −18~28 MeV
   H. Kakehi, Chiba Univ. Hospital
   A. Tsuya, National Cancer Center Res. Inst.
   H. Murayama, Tokyo Medical Univ. (43 h, 16)

4) "Production of ^{43}K for Heart Diagnosis"
   α −26, 29, 30 MeV
   M. Nakamura, and Y. Nose
   Med. Dept., Kyushu Univ. (35 h, 5)

5) "Production of ^{18}F for Bone Tumor Search"
   ^{3}He − 19 MeV
   T. Hara and M. Iio
   Nakano National Hospital (15 h, 5)

6) "Production of ^{47}Sc for Cancer Diagnosis"
   p − 16 MeV
   T. Hara and M. Iio
   Nakano National Hospital (3 h, 1)

7) "Production of ^{197}Hg for Diagnosis of Lung Tumor"
d–22 MeV
T. Hara and M. Iio
Nakano National Hospital (39 h, 13)

8) "Production of ^{123}I and ^{61}Cu"
^{3}He–40, 42 MeV, α–40, 42, 45
Y. Homma and Y. Murakami
Chem. Dept., Tokyo Metropolitan Univ. (36 h, 12)

9) "Extraction of ^{146}Eu from ^{146}Gd"
α–30 MeV
K. Tomura
Inst. for Atomic Energy, Rikkyo Univ. (3 h, 1)

10) "Measurement of Excitation Function for $^{66}Zn(\alpha, n)^{69}Ge$ reaction"
α–20 MeV
M. Furukawa
Chem. Dept., Nagoya Univ. (3 h, 1)

11) "Measurement of Excitation Function for $^{69}Ga(p, n)^{69}Ge$ Reaction"
p–8, 16 MeV
M. Furukawa
Chem. Dept., Nagoya Univ. (6 h, 2)

12) "Production of ^{53}Mn"
d–15, 20 MeV
S. Shibata and S. Umemoto
Chem. Dept., Kyushu Univ. (10 h, 2)

13) "Study of Decay and Level Structure of ^{210}Po"
α–40 MeV
Y. Yamazaki
Phys. Dept., Univ. of Tokyo (21 h, 5)

14) "Measurement of Nuclear Magnetic Moment of ^{210}Po, 6^{+} State"
α–10~40 MeV
T. Yamazaki
Phys. Dept., Univ. of Tokyo (5 h, 1)

15) "Preparation of ^{52}Fe for Diagnostic Use"
^{3}He–40
T. Aburai
Radio-isotope School, Japan Atomic Res. Inst. (4 h, 1)

16) "Measurement of Excitation Function for $^{56}Fe(\alpha, n)^{59}Ni$ reaction"
α–25 MeV
S. Tanaka
Inst. for Nucl. Study, Univ. of Tokyo (5 h, 1)

17) "Simulation of Swelling of Stainless Steel with Cyclotron Irradiation"
α−31
M. Terasawa
Toshiba Res. and Development Center (12 h, 1)

Publications

1. T. Furuta, Y. Ogawa, and R. Nagasaki : "The Effect of Creep Test Temperature on Creep Rupture Properties of α-ray Irradiated AISI 316 Stainless Steel", Iron & Steel, 8, 1117 (1972). (in Japanese)
2. T. Furuta and S. Kawasaki : "Influence of Recrystallization on the High Temperature Embrittlement of Austenitic Stainless Steel Induced by α-Irradiation", J. Nucl. Mat., 47, 102 (1973).
3. T. Furuta, S. Kawasaki, and R. Nagasaki : "The Effect of Cold Working on Creep Rupture Properties for Helium-Injected Austenitic Stainless Steel", J. Nucl. Mat., 47, 65 (1973).

AUTHOR INDEX

AMBE Fumitoshi 安部文敏 105, 132

AMBE Shizuko 安部静子 105, 129, 132

ARATANI Michi 荒谷美智 110

AWAYA Yohko 粟屋容子 87, 93

CHIBA Yoshiaki 千葉好明 83, 143

FUJISAWA Takashi 藤沢高志 46, 47

FUJITA Shin 藤田 新 5, 136

FUKUSHI Kiyoshi 福士 清 129

HAMADA Tatsuji 浜田達二 87, 93

HARA Toshihiko 原 敏彦 126

HARADA Kichinosuke 原田吉之助 65

HASHIMOTO Osamu 橋本 治 37, 69, 71, 74, 77

HASHIZUME Akira 橋爪 朗 79, 87, 93

HASIGUTI R. Ryukiti 橋口隆吉 103

HEMMI Masatake 逸見政武 5, 15, 143

HINOHARA Chikara 日野原 力 58, 62

HIRUTA Kotaro 蛭田幸太郎 37, 69, 77

IDO Tatsuo 井戸達雄 129

IGARASHI Kazui 五十嵐一戌 122

IKEGAMI Kumio 池上九三男 5

IKEZOE Hiroshi 池添 博 74

IMAMURA Masashi 今村 昌 112, 114

INOUE Toshihiko 井上敏彦 5

IWAMOTO Akira 岩本 昭 65

IWAMOTO Masako 岩本正子 126

IZUMO Koichi 出雲光一 87, 93

KAGEYAMA Tadashi 影山 正 5, 7

KAMITSUBO Hiromichi 上坪宏道 27, 32, 46, 83, 86, 151

KANAI Tatsuaki 金井達明 46

KARASAWA Takashi 唐沢 孝 7, 103, 112, 114, 126, 136

KASIDA Yosihiko 樫田義彦 129

KATORI Kenji 鹿取謙二 27, 32

KATOU Takeo 加藤武雄 79, 87, 93

KIMURA Kazuie 木村一宇 114

KODA Kugao 甲田陸男 134

KOHARA Shigeo 小原重夫 5

KOHNO Isao 河野 功 17, 27, 32

KOIKE Masahiro 小池正宏 46

KOYAMA Akio 小山昭雄 103

KOYAMA Katsuji 小山勝二 42

KUMAGAI Hidekazu 熊谷秀和 79

MASUI Kuniaki 増井邦明 47

MATSUI Masao 松井正夫 112, 114

MATSUYAMA Akira 松山 晃 117, 122

MIKUMO Takashi 三雲 昂 27, 32

MIYAZAWA Yoshitoshi 宮沢佳敏 5, 7, 10

MIZOGUCHI Tadashi 溝口 正 98, 101

MOTOBAYASHI Tohru 本林 透 27, 32

MOTONAGA Shoshichi 元永昭七 47

NAGAMIYA Shoji 永宮正治 71, 74

NAKAI Koji 中井浩二 71, 74

NAKAJIMA Hisao 中嶋尚雄 5, 14, 15

NAKAJIMA Shunji 中島諄二 22, 27, 32

NAKAMURA Masanobu 中村正信 42

NAKANISHI Noriyoshi 中西紀喜 42

NOMURA Toru 野村亨 37, 39, 69, 77, 83

NOZAKI Tadashi 野崎正 126, 129

ODERA Masatoshi 小寺正俊 139, 143, 147, 149, 151

OGIWARA Kiyoshi 荻原清 5, 10

OHNUMA Hajime 大沼甫 42

OHTSUKA Yasuo 大塚安央 129

OKADA Takuya 岡田卓也 98, 101

OKANO Masaharu 岡野真治 87, 93, 126

RECKNAGEL, EKKEHARD 71

SAITO Nobufusa 斎藤信房 105

SAKAGUCHI Harutaka 坂口治隆 42, 47

SAKAIRI Hideo 坂入英雄 103

SAKAMOTO Ichiro 坂本一郎 134, 136

SEKIZAWA Hisashi 関沢尚 98, 101

SHIMAMURA Akira 島村晏 5

SHIOTANI Nobuhiro 塩谷亘弘 98, 101

SUEKANE Shota 末包昌太 65

SUZUKI Toshio 鈴木敏男 51, 53, 55, 58, 60, 62

TAGISHI Yoshihiro 田岸義宏 46

TAHARA Akira 田原昭 129

TAKAHASHI Tan 高橋旦 87, 93, 117, 122

TAKEDA Shigeru 竹田繁 42, 86

TAKEUCHI Suehiro 竹内末広 42

TENDOW Yoshihiko 天道芳彦 79, 87, 93

TERAJIMA Osamu 寺島為 5

TONUMA Tadao 戸沼正雄 5, 143, 147, 149

USUBA Isao 薄葉勲 134

WADA Takeshi 和田雄 46, 83, 86

YAGI Eiichi 八木栄一 103

YAMADA Satoru 山田聡 42

YAMAJI Shuhei 山路修平 47, 65

YAMAZAKI Toshimitsu 山崎敏光 74

YAMAZAKI Yoshishige 山崎良成 71, 74

YATAGAI Fumio 谷田貝文夫 117, 122

YOSHIDA Fusako 吉田房子 47, 83, 147, 149

YOSHIE Morio 吉江森男 27, 32, 37, 69, 77

IPCR Cyclotron Progress Report

理化学研究所サイクロトロン年次報告 第7巻(1973)

印　刷　昭和49年（1974）3月25日
発　行　昭和49年（1974）3月30日
発行者　理化学研究所
代表者　星野敏雄
351　埼玉県和光市広沢2番1号
電話（0484）62－1111
編集者　理化学研究所サイクロトロン運営委員会
委員長　浜田達二
印刷所　丸星印刷株式会社
101　東京都千代田区
神田神保町1丁目42番地

定価 3,000円

理化学研究所

埼玉県　和光市　広沢